UNIVERSIDAD POLITÉCNICA DE MADRID
Escuela Técnica Superior de Ingenieros Industriales



Contribution of railway systems to frequency control of electric power systems with a multidisciplinary approach

DOCTORAL THESIS

Submitted for the degree of Doctor by:

Jesús Harmodio Araúz Sarmiento
Master of Electrical Engineering

Madrid, 2024





UNIVERSIDAD POLITÉCNICA DE MADRID
Escuela Técnica Superior de Ingenieros Industriales

Doctoral Degree in Electrical and Electronic Engineering

Contribution of railway systems to frequency control of electric power systems with a multidisciplinary approach

DOCTORAL THESIS

Submitted for the degree of Doctor by:

Jesús Harmodio Araúz Sarmiento
Master of Electrical Engineering

Under the supervision of:
Dr. Sergio Martínez González (Supervisor)

Madrid, 2024

Title: Contribution of railway systems to frequency control of electric power systems with a multidisciplinary approach

Author: Jesús Harmodio Araúz Sarmiento

Doctoral Programme: Electrical and Electronic Engineering

Thesis Supervision:

Dr. Sergio Martínez González, Associate Professor, E.T.S.I. Industriales, Universidad Politécnica de Madrid (Supervisor)

External Reviewers:

Thesis Defense Committee:

Thesis Defense Date:

This thesis has been partially supported by the Panamanian Institution Secretaría Nacional de Ciencia, Tecnología e Innovación (SENACYT). Grant Number: 270-2022-107.

Dedicated to my parents and grandparents

Acknowledgement

I extend my gratitude to the professors in the areas of electrical engineering and electrical machines at the Escuela Técnica Superior de Ingenieros Industriales, Technical University of Madrid. Their collective contribution significantly shaped my growth as a researcher. Special thanks to Andrés and Carlos from the electrical engineering area, whose support went beyond technical assistance; they became friends during my time in Madrid.

I express my appreciation to my PhD partner and friend, Donghui Ye, for the valuable knowledge shared and engaging conversations. A heartfelt thank you to Professor Sergio Martinez; words cannot capture the depth of my gratitude. Professor Sergio exceeded my expectations for a PhD advisor, making a profound impact on my academic journey. Thanks for everything.

Acknowledgments extend to those research-related people outside Madrid, particularly my friends at the Energy Lab-IAI-KIT. Their influence not only enhanced my research skills but also contributed to my personal growth. I am thankful to Prof. Dr. Veit Hagenmeyer, Simon Waczowicz, and Friedrich Wiegel for hosting my research stay in Karlsruhe, along with the welcoming individuals I met there. Special thanks to the researchers I met at The Pennsylvania State University, especially Professor Nilanjan Ray Chaudhuri, for broadening my horizons.

My appreciation goes to my flatmates, Petrona and Alfredo, whose company made challenging times more enjoyable. I am profoundly grateful to Francisco and Esperanza for their unparalleled support, making my stay in Madrid a positive experience. I wish I could teleport back to Madrid to continue cherishing moments with Esperanza and Francisco.

Lastly, heartfelt thanks to my parents, siblings, and grandmother for always seeing me as a special person. Their unwavering support and love mean a lot to me.

Abstract

Reducing reliance on fossil fuels due to environmental concerns has driven interest in renewable energy for power generation. Climate change, exacerbated by increased energy consumption, prompts global efforts to address environmental issues, especially in power systems. Integrating renewable sources into grids presents challenges, particularly where high penetration of intermittent resources alters system dynamics. Converter control dynamics significantly impact stability, affecting rotor angle, voltage, and frequency stability. The null inertial response from decoupling prime mover power challenges classical stability problems.

Frequency control in low-inertia grids faces complexity due to renewable energy uncertainty and challenges in estimating system inertia. Intermittent generation complicates synchronous generator dispatch, leading to variations in the rate of change of frequency. Measurement challenges extend to grid-following converters, diminishing monitoring precision. Research explores three main approaches to frequency control: generation-based, transmission-based, and demand-side strategies. The first two have been largely explored, but the last one is considerably less studied.

Demand-side approaches are crucial for efficient energy consumption. Integrating spread and adjustable loads can support power systems in renewable energy integration. Studies show how loads can modulate consumption to better interact with power systems, avoiding grid congestion, mitigating voltage deviation, and reducing frequency fluctuations. This involves adjusting normal signal setpoints to adjust load dynamics to consume without compromising their main objectives but providing some support to grid needs. Any load capable of modifying its consumption without worsening its main activity can be an active contributor. Widely spread loads with increasing usage can play a relevant role in developing demand-side approaches. Railway systems, with growing activity, offer an opportunity to contribute to power system stability. By exploring railway systems for ancillary services, particularly in different types of frequency control, there is potential for synergy between power and railway systems in the ongoing energy transition. As railway systems and urban populations are expected to rise, they should be studied as flexible loads supporting renewable generation integration.

This research aims to assess the potential contribution of railway systems to frequency control. It explores different demand response approaches, their implementation, requirements, and challenges; develops models, assessment methods, and control approaches; and proposes new concepts on the role of railway systems in power systems. Contributions include a methodology for simplifying the coupling between railway systems and distribution grids to estimate surplus regenerative braking energy and assess its injection impact; an approach for enabling trains to contribute to power system inertia and frequency control through their HVAC systems without affecting passenger comfort. This includes modeling proposals to speed up assessments and studies; a low-computational method for tuning frequency control loops using equivalent surface equations to facilitate parametric studies, find local optima, and reduce model multi-variable dependency; and an approach for estimating grid frequency from DC catenary voltage ripple to obtain local signal availability. This work primarily considers urban DC railway systems, but findings can be adapted to other types. Numerical studies show

the theoretical feasibility of the frequency control proposals, and hardware implementation validates them. Railway systems can contribute to frequency control depending on grid events, train technical specifications, thermal behavior, control tuning, and other grid participants' dynamics.

Resumen

Reducir la dependencia a los combustibles fósiles por preocupaciones ambientales ha aumentado el interés por introducir energías renovables en la matriz energética. El Cambio Climático, agravado por el aumento del consumo de energía, impulsa esfuerzos globales para abordar problemas ambientales. La integración de generación renovable en las redes presenta desafíos técnicos, donde la alta penetración de recursos intermitentes altera la dinámica del sistema. La dinámica de los controles de los convertidores electrónicos afecta la estabilidad de ángulo, tensión y frecuencia. La respuesta inercial nula agrava los problemas clásicos de estabilidad. El control de frecuencia en redes de baja inercia es afectado por la incertidumbre del recurso renovable y estimación de la inercia del sistema. La intermitencia complica el despacho de los generadores, ocasionando variaciones de frecuencia. Los retos de medición se extienden a los convertidores que siguen la red, reduciendo la precisión de monitoreo. En el estado del arte se exploran tres enfoques principales para el control de frecuencia: basado en generación, basado en transmisión y basado en consumo. Los dos primeros han sido ampliamente explorados y desarrollados. Sin embargo, el último ha sido menos estudiado. Los enfoques del lado de la demanda son esenciales para un consumo eficiente. La integración de cargas ajustables ayuda a incorporar generación renovable, al cambiar el consumo para interactuar mejor con los sistemas eléctricos. Esto se logra ajustando las consignas de operación para adaptar la dinámica de la demanda, contribuyendo a servicios auxiliares sin comprometer sus objetivos principales. Las crecientes cargas distribuidas desempeñan un papel crucial en los enfoques de la demanda. Los ferrocarriles pueden ayudar a estabilizar sistemas eléctricos al contribuir a los servicios auxiliares de la red, mostrando potencial de sinergia en la transición energética. Esto sugiere que los ferrocarriles pueden estudiarse como cargas flexibles en miras de la integración de generación renovable. El objetivo de esta investigación es evaluar la contribución de los sistemas ferroviarios al control de frecuencia. Esta investigación incluye una exploración de diferentes enfoques de respuesta a la demanda, su implementación actual, los requisitos y desafíos enfrentados para ser aplicados; el desarrollo de modelos, métodos de evaluación, enfoques de control, nuevos conceptos sobre el papel del sistema ferroviario en los sistemas de energía eléctrica; y los resultados de las propuestas basadas en sistemas reales de energía eléctrica y ferroviarios. Algunas de las contribuciones son una metodología para simplificar el acoplamiento de modelos ferroviarios y de redes de distribución, para la estimación del excedente de energía de frenado regenerativo y la evaluación de su inyección; un enfoque para que los trenes contribuyan a la inercia de los sistemas de energía eléctrica y al control de frecuencia primario y secundario, mediante el uso de sus sistemas de aire acondicionado, sin afectar el confort térmico de los pasajeros. Este enfoque incluye modelos para acelerar evaluaciones y estudios; un método de bajo costo computacional para ajustar bucles de control, basado en ecuaciones de superficies. Este facilita hacer estudios paramétricos, la búsqueda de óptimos locales y la reducción de la dependencia multivariable del modelo; y un enfoque para estimar la frecuencia a partir del rizado de la tensión de la catenaria. Este considera ferrocarriles en corriente continua, pero los hallazgos pueden adaptarse a otros tipos. Los estudios muestran la viabilidad teórica de las propuestas de control de frecuencia y la implementación en equipos reales las valida. Los ferrocarriles pueden contribuir al control de frecuencia dependiendo de los eventos, las características técnicas del tren y su comportamiento térmico, el ajuste del control y la dinámica de otros participantes en la red,

entre otros aspectos.

Table of Contents

Acknowledgement v
Abstract vi
Resumen viii
List of Figures xiii
List of Tables xvii
Abbreviations xx

1 Introduction **1**
1.1 Background 1
1.2 Motivation 2
1.3 Objectives 3
1.3.1 Specific objectives 3
1.4 Structure 4

2 Literature review **5**
2.1 Generation-side approaches 5
2.1.1 Based on one renewable generation technology 6
2.1.2 Based on the combination of renewable generation 7
2.2 Load-side approaches 8
2.2.1 Electric vehicle-based approaches 9
2.2.2 Other load-based approaches 10
2.2.3 Railway system-based approaches 13
2.3 Proposal: expansion of railway system-based approaches 14

3 Theoretical framework **17**
3.1 Power systems modeling 17
3.1.1 Phasor-domain 17
3.1.2 Time-domain 19
3.1.3 Load frequency control scheme 21
3.2 Railway systems modeling 21
3.2.1 Kinetic and electrical modeling 21
3.2.2 Thermal modeling 23

4 Contribution of Railway Systems to Power Systems Frequency Control **27**
4.1 Alternative uses of regenerative braking energy 27

4.1.1 Current management of regenerative braking energy 28
4.1.2 Railway simulation methodology 30
4.1.3 Case study 32
Panama Metro Line 1 32
Distribution grid in the PML1 surroundings 35
Railway simulation 38
Impact of injecting the regenerative energy into the distribution grid 44
4.1.4 Conclusions 46
4.2 Contribution of the thermal inertia of trains to the primary frequency control 51
4.2.1 Response to power system disturbances: sudden load shedding 55
4.2.2 Response to power system disturbances: sudden generation unit loss . 56
4.2.3 Response to railway disturbances 57
4.2.4 Response to railway disturbances: different thermal envelopes 58
4.2.5 Response to railway disturbances: two thermal envelopes with different droop control 59
4.2.6 Response to power system disturbances: sudden load shedding and individual train thermal modeling 61
4.2.7 Conclusions 63
4.3 Use of the thermal inertia of trains for providing virtual inertia 65
4.3.1 Case study 1. Non-railway consumption. Response to a sudden load shedding 67
4.3.2 Case study 2. Railway consumption. Response to a sudden load shedding 74
Primary frequency control 74
Virtual inertia control 79
Combined control 81
4.3.3 Case study 3. Railway consumption. Response to a sudden generation losing 82
Primary frequency control 82
Virtual inertia control 84
Combined control 86
4.3.4 Global results comparison 87
Load shedding 87
Generation losing 89
Relative impact index 91
4.3.5 Conclusions 92
4.4 Use of the thermal inertia of trains for relieving renewable generation from frequency control tasks 94
4.4.1 Problem statement 94
Only conventional vs. Partially displaced generation under normal railway consumption 94
4.4.2 Control approach 95
4.4.3 Determining control parameters 97
Normal railway consumption without RG support to frequency control tasks 98
Normal railway consumption with RG support to frequency control tasks 99

4.4.4 Analysis of models . . . 101
Enhancement of frequency performance under normal railway consumption: . . . 103
Enhancement of frequency performance following a load shedding: . . . 104
4.4.5 Experimental validation . . . 107
4.4.6 Conclusions . . . 110
4.5 Local grid frequency estimation in DC railway systems . . . 111
4.5.1 Measurement methodology . . . 111
4.5.2 Computational simulations . . . 112
4.5.3 Offline experimental validation . . . 115
4.5.4 Real-time experimental validation . . . 119
4.5.5 Conclusions . . . 124
4.6 Experimental validation in a real micro-grid . . . 125
4.6.1 Description of the micro-grid . . . 125
4.6.2 Case study: PML1-based railway model in a high-distorted grid . . . 127

5 Conclusions and future works **129**
5.1 Conclusions . . . 129
5.2 Future works . . . 131

References **133**

List of Publications **145**

Characteristics of models **147**
A. Data for Section 4.1 . . . 147
B. Data for Section 4.2 . . . 151
C. Data for Sections 4.3, 4.4 . . . 152
D. Data for Section 4.5 . . . 153

List of Figures

4.1 Overall description of the modeling (DF: dedicated feeder, DG: distribution grid, Inv: inverter, A: number of DFs, B: number of DGs and inverters). . . . 31
4.2 Flow diagram of the coupling approach implementation. 32
4.3 Speed limit versus location. Source: Panama Metro Company. 33
4.4 Slope versus location. Source: Panama Metro Company. 34
4.5 Radius of curvature versus location. Source: Panama Metro Company. . . . 35
4.6 Map of the stations of Line 1 (blue), and substations of ENSA (green) and Naturgy (red). Made on Google Maps. 36
4.7 Daily load profile of the Republic of Panama. 37
4.8 Circulation mesh resulting from the dynamic simulation. 38
4.9 Power characteristic of a train. Simulation result. 39
4.10 Aggregated power consumption obtained from simulation. 42
4.11 Average hourly distribution of energy consumption of PML1 in January 2021. 43
4.12 Phase voltage of distribution substations under different railway extraction scenarios. 48
4.13 Phase voltage variation (V/s) of distribution substations under different railway extraction scenarios. 49
4.14 SCR per substation per railway extraction scenario (RES). The number in brackets indicates the short circuit power of each substation. 50
4.15 Representation of the higher layer of a primary frequency control scheme integrating hydroelectric generators (HG), non-railway consumption, non-frequency dependent (NFD) railway consumption, and frequency-dependent (FD) railway consumption. 51
4.16 FD railway consumption model detail. * denotes those parameters modified by the frequency control. 52
4.17 Considered profiles of speed, acceleration, and position of trains on both tracks. Upper row: profiles for the first train of each track. Lower row: profiles for the second train of each track. 54
4.18 Railway consumption profile. 55
4.19 Railway and power system responses following a sudden load shedding event. 56
4.20 Railway and power system responses following a sudden generation loss event. 57
4.21 Railway and power system responses to normal railway consumption variations. 58
4.22 Railway and power system responses to normal railway consumption variations. Sensitivity to different thermal envelopes of trains. 59

4.23 Railway and power system responses to normal railway consumption variations. Combined sensitivity to thermal configurations and droops. 61
4.24 Railway and power system responses following a sudden load shedding event. Individual train thermal behavior. Null droop control. 62
4.25 Railway and power system responses following a sudden load shedding event. Average train thermal behavior. 63
4.26 Load frequency control responses following a load shedding under different control aggressivity. Primary frequency control. 68
4.27 Load frequency control responses following a load shedding under different control aggressivity. Virtual inertia. 69
4.28 Load frequency control responses following a load shedding under different control aggressivity. The reference case (without frequency control) has been subtracted from each case. Primary frequency control. 70
4.29 Load frequency control responses following a load shedding under different control aggressivity. The reference case (without frequency control) has been subtracted from each case. Virtual inertia. 71
4.30 Combination of primary frequency control and virtual inertia. The reference case (without frequency control) has been subtracted from each case. 72
4.31 Reduction of main metrics with respect to the reference case. 74
4.32 Primary frequency control response following a sudden load shedding. Variables of interest. 76
4.33 Primary frequency control response following a sudden load shedding. Zoom of frequency and rate of change of frequency. 77
4.34 Primary frequency control response following a sudden load shedding. The reference case (without frequency control) has been subtracted from each case. 78
4.35 Virtual inertia control response following a sudden load shedding. The reference case (without frequency control) has been subtracted from each case. 80
4.36 Combination of primary frequency and virtual inertia controls response following a sudden load shedding. The reference case (without frequency control) has been subtracted from each case. 81
4.37 Primary frequency control response following a sudden generation losing. The reference case (without frequency control) has been subtracted from each case. 83
4.38 Virtual inertia control response following a sudden generation losing. The reference case (without frequency control) has been subtracted from each case. 85
4.39 Combination of primary frequency and virtual inertia controls response following a sudden generation losing. The reference case (without frequency control) has been subtracted from each case. 86
4.40 Reduction rates of relevant frequency-related variables following a load shedding. 89
4.41 Reduction rates of relevant frequency-related variables following a generation losing. 90
4.42 Relative impact index (%/p.u.) of relevant frequency-related variables following a load shedding. 91
4.43 Relative impact index (%/p.u.) of relevant frequency-based variables following a generation losing. 92
4.44 Grid frequency performance under different conditions. 95

4.45 Frequency deviations RMS: real vs. fitted. Without RG support and $C_1 = 0$. 98
4.46 Frequency deviations RMS: real vs. fitted. Without RG support and $C_1 \neq 0$. 99
4.47 Frequency deviations RMS: real vs. fitted. With RG support and $C_1 = 0$. . . 100
4.48 Frequency deviations RMS: real vs. fitted. With RG support and $C_1 = 0$. . . 101
4.49 Maximum temperature deviation range without RG support and $C_1 \neq 0$. . . 104
4.50 Frequency deviation RMS reduction following a sudden load shedding. a) RG support: off. C_1=0. b) RG support: off. $C_1 \neq$0. c) RG support: on. C_1=0. d) RG support: on. $C_1 \neq$0. 106
4.51 Maximum temperature deviation range following a sudden load shedding without RG support and $C_1 \neq 0$. 107
4.52 Experimental setup 108
4.53 Experimental results. Frequency and setpoint temperature behavior. 109
4.54 Frequency estimation following sudden frequency steps. 114
4.55 Frequency estimation following a frequency ramp. 114
4.56 Frequency estimation following a sinusoidal frequency fluctuation. 115
4.57 Schematic of the laboratory test-bench. 116
4.58 Laboratory test-bench. 117
4.59 AC phase-to-neutral voltages (magenta, green, and blue) and DC voltage (yellow) recorded with the oscilloscope. 117
4.60 Offline frequency estimation based on real recorded data. 118
4.61 HIL setup schematic. 120
4.62 Real-time frequency estimation in the case of variations in the mechanical torque of the synchronous generator. 121
4.63 Real-time frequency estimation in the case of variations in the railway consumption. 122
4.64 Real-time frequency estimation in the case of simultaneous variations in the torque of the synchronous generator and in the railway consumption. 122
4.65 Railway equivalent consumption profile. 123
4.66 Microgrid overall description: blue, violet, and green lines represent data flow, DC connection, and AC connections, respectively. 126
4.67 Behavior of the AC and DC sides following a sudden load shedding. The "Test time" label records the time after the event. 128

A1 Selected load profile of distribution substations. 150
B1 Bode diagram (magnitude and phase). Stability analysis of the HVAC system frequency-based control. 152
D1 Implementation of ZCD method. 154

List of Tables

4.1 January 2021 PML1 electricity consumption statistical analysis. 41
4.2 Statistical analysis following a load shedding event. Frequency control in the case of non-railway consumption. 73
4.3 Statistical analysis following a load shedding. Frequency control in railway consumption. 88
4.4 Statistical analysis following a generation losing. Frequency control in railway. 89
4.5 Terms of (4.7), goodness of fit, minimum values with different combinations of frequency control and RG support. 102
4.6 Maximum frequency deviation RMS reduction under normal railway consumption. 103

A1 Position of passenger stations referred to the beginning of the line. Those stations marked with * include traction substations. 147
A2 PML1 Rolling stock rated characteristics. 148
A3 Coordinates (North latitude, East longitude) of passenger stations (left) and distribution grid substations (right). 149
B1 Thermal envelope characteristics of trains. 151
C1 Parameters' values and specifications. 152
D1 PLL parameters' values and specifications. 154

Abbreviations

ROCOF Rate of Change of Frequency

PLL Phase-Locked Loop

PSS Power System Stabilizer

PV Photovoltaic

VSG Virtual Synchronous Generator

UFLS Under-Frequency Load Shedding

RS Renewable Sources

DER Distributed Energy Resources

PEC Power Electronic Converters

PANTERA PAN European Technology Energy Research Approach

RD&I Research, Development, and Innovation

DFIG Doubly-Fed Induction Generator

OPPT Optimized Power Point Tracking

MPPT Maximum Power Point Tracking

ASs Ancillary Services

DN Distribution Networks

TS Transmission Systems

AFPID Adaptative Fuzzy Proportional, Integral, and Derivative

SGWO Simplified Grey Wolf Optimization

GWO Grey Wolf Optimization

LFC Load Frequency Control

SWBPS Solar-Wind-Based Power Systems

WTG Wind Turbine Generator

FOPID Fractional-Order Proportional-Integral-Derivate

FPA Flower Pollination Algorithm

IEEE Institute of Electric and Electronic Engineers

MVO Multi-Verse Optimization

MSPS Multi-Source Power System

HVDC High-Voltage Direct Current

SLP Step Load Perturbations

EV Electric Vehicle

VPP Virtual Power Plant

V2G Vehicle-to-Grid

PHIL Power Hardware-in-the-Loop

SEA Specialized Energy Aggregator

ES Electric Spring

SL Smart Load

CIGRE Conseil International des Grands Réseaux Électriques

ESS Energy Storage System

NCL Non-Controlled Load

HVAC Heating, Ventilation, and Air Conditioning

SFC Secondary Frequency Control

EDCPS Energy Direct Current Power Support

MPC Model Predictive Control

PPS Providing Power Support

ASL Aluminum Smelter Load

FRT Fault Ride-Through

CCHT Canadian Centre for Housing Technology

SOC State Of Charge

GSC Grid Support Capacity

DADR Decentralized Active Demand Response

TCL Thermostatically Controlled Load

PSO Particle Swarm Optimization

W-DSO Water Distribution System Operator

DR Demand Response

WDS Water Distribution System

SG Synchronous Machine

IoT Internet of Things

IGBT Insulated Gate Bipolar Transistor

DF Dedicated Feeder

DG Distribution Grid

Inv Inverter

PML1 Panama Metro Line 1

ENSA Elektra Noreste S.A.,

ACSR Aluminum Core Steel Reinforcement

AWG American Wire Gauge

SCR Short-Circuit Ratio

RES Railway Extraction Scenario

HG Hydroelectric Generator

FD Frequency-dependent

NFD Non Frequency-dependent

COP Coefficient Of Performance

PI Proportional-Integral

VAC Ventilation and Air Conditioning

RMS Root Mean Square

PC Primary Control

VI Virtual Inertia

CC Combined Control

DB Dead Band

RG Renewable Generator

HIL Hardware-In-the-Loop

ZCD Zero-Crossing Detection

FLL Frequency-Locked Loop

TPUR Three-Phase Uncontrolled Rectifier

SESCL Smart Energy System Control Laboratory

KIT Karlsruhe Institute of Technology

RCP Rapid Control Prototyping

Chapter 1

Introduction

1.1 Background

The global consensus on reducing humanity's reliance on fossil fuels due to environmental concerns and limited accessibility has prompted a surge in interest in utilizing renewable energy sources for electrical power generation. It is well known that Climate Change has been worsening in the last decades. This has been driven by the normal increase in energy consumption as humanity also increases, and the availability of the used energy resources for achieving an acceptable energy requirement fulfillment, among other factors. Nations have focused many efforts on addressing the current environmental problems from diverse focuses. The focus which drives most research in electrical and electronic engineering is the generation, transmission, operation, and consumption of power systems. Renewable energy sources for electrical power generation have been considered as one of the most effective ways to mitigate the constant deterioration of the environment. Although conventional generation, largely supplied by fossil fuels, still is the most used for electricity generation, it is expected to be notably reduced in less than thirty years [1].

Integrating renewable energy sources into electrical grids presents multifaceted challenges, encompassing political, technical, and social obstacles. Addressing technical challenges involves recognizing that grids with high penetration of intermittent resources and power electronics converters exhibit distinct characteristics from traditional ones [2]. Converter controls, including outer and inner loops and pulse-width modulation, significantly influence dynamics under faults, transients, and steady-state conditions. Notably, the decoupling of the prime mover's power from the grid's electromagnetic power results in a null inertial response, impacting classical stability problems such as rotor angle, voltage, and frequency stability [3].

Rotor angle stability is influenced by power flow changes, displacement of synchronous generators, and the location of converter-based generation, affecting mode shape, damping modes, and modal frequency. Voltage stability may be impacted short and long-term due to converter limitations. Frequency stability faces challenges due to decreased inertia, as converter-based generation lacks intrinsic inertia and primary frequency control. Despite economic considerations limiting power curtailment, converters have demonstrated their ability

to provide frequency control [4].

Navigating frequency control challenges in low-inertia grids becomes complex, especially considering the uncertainty of renewable energy resources and difficulties estimating system inertia. Intermittent generation complicates conventional synchronous generator dispatch, leading to variations in the rate of change of frequency (ROCOF) and affecting inertia estimation. This measurement challenge extends to grid-following converters' phase-locked loop (PLL) functionality, diminishing monitoring and control precision and potentially increasing generation disconnection risks. The dynamics of large conventional generators' displacement, coupled with a reduction in power system stabilizer (PSS) controllers, contribute to a more oscillatory grid behavior [5].

Plenty of research efforts have been oriented toward the comprehensive exploration of various strategies for frequency control within power systems. This extensive body of work categorizes these strategies into three distinctive approaches, each contributing unique insights into power system dynamics. The first and foremost approach delves into the intricacies of generation-based solutions, transcending the conventional boundaries set by both traditional and renewable energy sources. It analyses classical facets inherent to conventional generators, including but not limited to inertial responses, governor reactions, and the inherent constraints due to inertia. Furthermore, this approach probes the current trajectories of emerging technologies such as photovoltaic (PV) and wind generators, exploring contemporary trends. This approach focuses on a spectrum of methodologies encompassing deloading strategies, power curtailment techniques, the dynamics of DC-link capacitors, the influence of delta power variations, and the emulation of inertia. The second exploration approach, the transmission-based approach, considers current cutting-edge solutions. This is based on incorporating technologies such as inducverters and virtual synchronous generators (VSG), coupled to energy storage systems. The latter includes a diverse array of options ranging from pumped hydro, supercapacitors, flywheels, and batteries, to the innovative application of compressed air. Simultaneously, the exploration extends its purview to dynamic thermal rating, adding more sophistication to the transmission-based strategies.

The third approach works through the domain of load-based strategies. This category focuses on load modulation, the strategic integration of energy storage systems, and the application of under-frequency load shedding (UFLS) mechanisms. However, an observation in most of the related research reveals a notable scarcity in the literature concerning the exploration of frequency control demand response strategies, suggesting further scholarly exploration and inquiry [5].

1.2 Motivation

The demand-side approaches have been also considered to address Climate Change from other energy sectors [1]. Achieving more efficient consumption (technology improvement, behavior changes, etc.) is a way to reduce energy generation and the urgency of deploying more renewable generators. As mentioned, the role of demand in current and future power systems has been less explored. Spread and adjustable loads could be considered for supporting power systems to appropriately integrate renewable energy. As civilization grows and improves,

electricity consumption also does. Then, an approach to support the power systems that would increase constantly its contribution is to make load sensitive to the power system operation needs.

At the same time that is expected the world energy outlook to achieve the current objectives toward the reduction of pollution [1], it is also expected passenger and freight railway systems to double their activity. Urban and high-speed are expected to considerably increase around the world since around half of the world's population is settled in urban areas. Railway systems have been considered as an alternative for many transport needs. Railways can reduce the fossil fuel demand by displacing road vehicles, ships, and flights. Also, many large railway systems are committed to electrifying all the tracks, like in India and China [6]. Therefore, providing railway systems with the technical possibility to contribute to the stability of power systems can have beneficial impacts. This means having a widely spread and continuously increasing load in transmission and distribution systems which can contribute in many ways to power systems.

Recently, railway systems have been considered for further objectives than transporting people and merchandise, besides the improvement of their intrinsic behavior toward the optimization of their resources. Some works propose railways for interconnecting different technologies and systems, such as energy storage systems, renewable generators, microgrids, electric vehicles, and even other railway systems [7].

By combining both improvement trajectories, power and railway systems, it is possible to notice the opportunity to develop further research on how railway systems can interact with different technologies and also to support future power systems in the current energetic transition. As the rest of the power systems participants are being adjusted to provide ancillary services, railway systems also would be able to.

1.3 Objectives

The present work is an exploration of how railway systems could support power systems ancillary services, mainly oriented to different types of frequency control. Then, the main objective is to define a theoretical framework for the possibilities of railway systems to behave as a partially controllable load for providing benefits to power systems.

1.3.1 Specific objectives

The main objective involves certain specific objectives:

- Definition of the current State of the Art and Technology of the frequency control load-based strategies within Power Systems.
- Awareness of the role of railway systems in frequency control as in other grid ancillary services.
- Exploration of the railway system consumption behavior to select possible sub-systems and sub-processes as candidates to provide frequency control to power systems.

- Achievement of modeling and assessment methodologies to properly and efficiently describe the interaction between railway systems and power system elements.
- Study of the implications for railway systems to provide primary frequency control. This involves how the chosen sub-systems and/or sub-processes perform while reacting to the grid frequency deviations.
- Study of the possibilities of providing virtual inertia to power systems from railways, combination with primary frequency, and requirements for railway systems to achieve it.
- Analysis of the possibilities of relieving renewable generation from frequency control tasks by means of supporting primary and supplementary frequency control.
- Development of tuning methodologies for the proposed frequency control schemes. This is focused on dealing with railway system multi-scale dynamics as well as on obtaining low-cost and easy-to-implement methods.
- Development of frequency estimation methods to enable DC railway systems to access the instantaneous grid frequency. This way, any consumption connected to the railway system DC side has more possibilities for contributing to the public grid frequency control.

Because of the high diversity of railway systems, this work only considers urban DC railway systems, such as metropolitan ones. It is worth mentioning that all the findings (i.e., controls, concepts, methodologies, and techniques, among others) could be properly adapted to any type and topology or railway system.

1.4 Structure

The present document is organized as follows:

Chapter 2 presents a literature review. This contains an exploration of the techniques to provide frequency control from the generation side as well as the load side. This way, it is possible to notice the current state of development of frequency control provisions, most applied schemes, challenges to be faced, and lack of knowledge related to railway systems. The literature review evidences the contribution of the proposals to the current State of Art and Technology. Chapter 3 shows the different modeling approaches that make it possible to study and experimentally test the proposals. It includes power and railway systems, with their respective sub-systems dynamics. Chapter 4 contains the main content of the present work. It states and explains all the proposals, from the theoretical foundation to the exemplification with case studies based on real systems. Here, the proposed modeling, assessing, frequency estimation, and tuning methodologies, frequency control schemes are shown in detail. Chapter 5.1 gathers the main contributions of the work and establishes the possible future works. The rest of the work is made by references, the list of publications as outcomes of the present research, and an appendix to describe some useful data used during case studies.

Chapter 2

Literature review

As stated, extensive research has been conducted on achieving grid frequency enhancement in low-inertia systems. Most load-side approaches are inspired by well-known techniques applied on the generation-side. Consequently, exploring how conventional and renewable generation provide ancillary services, mainly frequency control, would lead to a better understanding of the possibility of frequency control from loads.

2.1 Generation-side approaches

Conventional generators have been in charge of maintaining an appropriate frequency behavior in power systems. Current and novel research is oriented to the role of renewable generation. Tamrakar et al. [8] provided an overview of the existing methods for implementing virtual inertia, for renewable generations as well as for DC links, examining the current state-of-the-art. It investigates potential approaches for further research and addresses associated challenges. The primary virtual inertia configurations are evaluated and categorized. By reviewing the literature and conducting simulations for selected configurations, it is demonstrated that comparable inertial responses can be attained by correlating the parameters of these setups using time constants and inertia constants, even though there might be slight variations in the exact frequency dynamics. The appropriateness of a particular configuration hinges on the system's control architecture and the desired level of fidelity in replicating synchronous generators' dynamics.

Additionally, new market mechanisms and grid codes are needed for the successful integration of renewable generation [9]. Some authors, such as Gokhale-Welch et al. [10], tried to extract the best practices from worldwide codes to address a technological challenge in a region that lacks appropriate codes. This paper presents a detailed examination of the evolving stability issues in power systems arising from the integration of Renewable Energy Sources (RS) and Distributed Energy Resources (DER) interfaced with Power Electronic Converters (PEC). It particularly focuses on the implications of low inertia and weak system strength conditions. Additionally, the article introduces innovative technologies designed to address these challenges and emphasizes the importance of incorporating suitable techno-economic considerations for their integration into both system and market operations. The complexity

of system services is highlighted as a crucial aspect of ensuring stability in low-carbon grids. The paper also underscores the significance of carefully integrating new grid codes and market mechanisms to fully harness the advantages of emerging technologies during the transition to ultra-low carbon futures. Other authors, such as Carroll et al. [11], concentrated on evaluating existing regulations, codes, and standards to foresee the requirements for updating them. This article centers on an examination of regulations, codes, and standards within the European Union, as undertaken by the PANTERA (PAN European Technology Energy Research Approach) project. It delves into the evolution of Network Codes, using a case study from a research and demonstration project in Ireland. The article emphasizes the potential to advance Research, Development, and Innovation (RD&I) in smart grids by leveraging the collective understanding of insights provided by the PANTERA platform.

Most of the proposals include photovoltaic plants, wind farms, energy storage systems, and a combination of some of these.

2.1.1 Based on one renewable generation technology

Ochoa and Martinez [12] introduced an approach for examining frequency dynamics in large-scale power systems with a high degree of wind energy integration, utilizing a simplified model for doubly-fed induction generator (DFIG)-based wind turbines. Furthermore, a virtual inertia controller variant of the optimized power point tracking (OPPT) technique is applied to such wind turbines. In this variant, the maximum power point tracking curve is adjusted to induce changes in active power injection based on both grid frequency deviation and its time derivative. The outlined methodology integrates this model into a primary frequency control scheme to assess its interaction with other plants in the power system. Additionally, it is demonstrated that, under actual wind conditions, the proposed OPPT variant effectively smoothens the wind power injected into the grid, consequently mitigating frequency fluctuations.

Ochoa and Martinez [13] introduce a novel approach to tackle the challenges associated with frequency deviations caused by the variable power injection from DFIG-based wind turbines in a vulnerable or isolated power system. The proposed solution involves a frequency-dependent smoothing of wind power. An algorithm is presented, allowing an enhanced shifting of the maximum power point tracking (MPPT) curve through adjustments in the blade pitch angle. This algorithm leverages the combined impact of two frequency control strategies: one utilizing stored kinetic energy with the concept of virtual inertia and the other regulating the captured wind power through blade pitch angle adjustments. The objective of this algorithm is to reduce turbine deload requirements while simultaneously increasing available kinetic energy in the turbine. This leads to a more efficient fast-frequency response with a reduced amount of non-dispatched wind energy.

Pierro et al. [14] demonstrated that the augmented flexibility demand induced by solar energy can be effectively met by a specific type of solar farm known as flexible PV. These facilities can offer ancillary services through proactive generation curtailment and storage power injection, akin to the existing use of secondary reserves. Based on current and anticipated penetration levels, it is determined the required capacity of the flexible PV fleet to reduce the Italian

energy imbalance by 36% compared to its 2016 value, while maintaining curtailment at 6% of the national PV generation. The findings indicate that this reduction can be achieved at dispatching costs equal to or lower than current costs, depending on the solar share. Furthermore, it is observed that optimal solar regulation performance is achieved when flexible PV plants, each with different capacities, are strategically distributed throughout the country. Lastly, it is established that the effectiveness of this proposed strategy for mitigating imbalances is only minimally influenced by year-specific load, wind, PV, and energy price profiles used to size the capacity of the flexible fleet.

Julien et al. [15] introduced a hierarchical control system designed to address the variability of PV power plants while offering ASs to the electric grid, all without the need for additional non-solar resources. Through coordinated management of each inverter within the system, the control system directs the power plant to proactively curtail a small portion of its instantaneous maximum power potential. This curtailment provides the plant with the flexibility to increase production for services such as regulation reserve. The control system is particularly effective in managing to change cloud cover conditions on partially cloudy days. The efficacy of the proposed control system is validated through a case study using one-second resolution solar irradiance data from a site in Hawaii. Furthermore, the proposed hierarchical control system is compared to an alternative control technology from the literature, specifically the grouping control algorithm. The results indicate that the proposed hierarchical control system is more than ten times more effective in reducing generator mileage to support power fluctuations from solar PV power plants.

2.1.2 Based on the combination of renewable generation

Kryonidis et al. [16] provided an overview of crucial Ancillary Services (ASs) oriented towards Distribution Networks (DN) and Transmission Systems (TS) anticipated for implementation in forthcoming power systems. Additionally, it outlines the current advancements in measurement-based analysis techniques, which can play a vital role in enabling the delivery of various Ancillary Services by furnishing real-time essential information about the dynamic performance of the system.

Padhy and Panda [17] recommended an adaptive fuzzy-based proportional, integral, and derivative (AFPID) controller for the frequency regulation of power systems, where the controller's parameters are optimized using a simplified grey wolf optimization (SGWO) method. The simplification in the original grey wolf optimizer (GWO) method involves neglecting the worst category wolves and prioritizing superior wolves throughout the search process. The superiority of the proposed SGWO over GWO is demonstrated in terms of achieving a superior solution with reduced execution time, as illustrated by applying it to unimodal, multimodal, and fixed-dimension benchmark functions. Subsequently, the proposed SGWO technique is applied to fine-tune the AFPID controller for frequency regulation in four power systems: two non-reheat area systems, a two-area system with a reheat turbine, a two-area reheat steam turbine with nonlinearity, and a two-area system with a PV and thermal system. This demonstrates the effectiveness of both the controller and the algorithm in regulating frequency changes.

Ramesh et al. [18] conducted a literature review focusing on the challenges of load frequency control (LFC) in solar-wind-based power systems (SWBPS). The LFC problem in SWBPS is exacerbated by the system's lower inertia and the stochastic characteristics of solar radiation and wind speed, which distinguish it from conventional power systems. The paper explores the contributions of solar generators, wind turbine generators (WTGs), and the roles of energy storage systems, electric vehicles, and controllable loads in addressing LFC issues. Additionally, it provides a comprehensive analysis of advanced control and optimization techniques applied to LFC. Finally, based on the extensive review, the paper introduces a solution where the parameters of a fractional-order proportional-integral-derivative (FOPID) controller are optimized using the flower pollination algorithm (FPA). This proposed technique demonstrates the capability to simultaneously handle inertial, primary, and secondary controls, effectively mitigating frequency-related challenges with a single controller and ensuring that the frequency remains within permissible limits according to IEEE standards.

Rezk et al. [19] introduced a reliable approach utilizing a multi-verse optimization algorithm (MVO) for the design of load frequency control in a multi-interconnected power system that incorporates wind power and PV plants. The proposed method is applied to optimize the control parameters of the LFC in a multi-source power system (MSPS), which includes thermal, gas, and hydropower plants for energy generation. Additionally, the MSPS is integrated with RS. The MVO algorithm is employed to determine the optimal parameters for the controller, addressing both single-area and multi-area MSPS configurations integrated with RS. The scheme involves the use of a High-Voltage Direct Current (HVDC) link in parallel with AC multi-area interconnection tie-lines. The proposed approach demonstrates robust performance in the face of disturbances in loading conditions, variations in system parameters, and step load perturbations (SLP) of varying sizes.

2.2 Load-side approaches

The current technological development allows consumers to adapt their consumption behavior toward the provision of ancillary services. This can be done by making consumption responsive to specific signals (incentives, energy prices, and physical magnitudes, among others). This approach is frequently denominated "demand response" [20]. Just like optimization programs employed for power plants, there is the potential to optimize the demand patterns based on factors such as energy costs/prices, peak hours, pollution, technical constraints in electric grids, consumer preferences, and so forth [21]. Therefore, the incorporation of demand response necessitates a comprehensive examination of load demands, operational constraints within the grid, and interactions with other energy systems, such as heat and/or fuel hubs, microgrids, islanded grids, and so on [22].

In literature are several recent works about demand response strategies. Most of them are oriented to electric vehicles (EV), although there are other kinds of loads that have been studied.

2.2.1 Electric vehicle-based approaches

Yumiki et al. [23] proposed a system-level design for delivering ASs to control electric power grids through the use of in-vehicle batteries, specifically targeted for EVs employed in shared mobility service. The design introduces an architecture facilitating collaboration between transportation and energy management systems, enabling the creation of an autonomous Vehicle-to-Grid (V2G) system aimed at providing multi-objective AS. These objectives include primary frequency control within a transmission grid and voltage amplitude regulation in a distribution grid interconnected with EVs. The design leverages the ordinary differential equation model of distribution voltage, a recently introduced physics-based model, to assess and regulate the spatiotemporal impact of charging/discharging across a large fleet of EVs on a distribution grid. The effectiveness of the autonomous V2G design is assessed through numerical simulations utilizing realistic models of transmission and distribution grids, along with synthetic operation data representing EVs in a shared mobility service. Additionally, a Power Hardware-In-the-Loop (PHIL) test is presented to evaluate the feasibility of the design, considering the inherent latency associated with power, control, and communication equipment.

Ledro et al. [24] explored the impact of wind power fluctuations on an EV fleet, taking into account non-synchronized activation times and discrete modulation of the charging current. The investigation compares the effects of a power-based controller with those of an energy-based controller. The results indicate that the response of a realistic EV fleet has a more pronounced effect on the Virtual Power Plant (VPP) output when a power controller is utilized. The discrete modulation of the EV charging current introduces oscillations that would not be present with a linear modulation. Interestingly, the influence of a non-synchronized EV activation time is minimal for both controllers, suggesting that synchronized activation times can be assumed in similar studies. Despite the mathematical equivalence, the hourly energy production of the VPP when employing a power controller does not align with that of an energy controller.

Blatiak et al. [25] quantified the potential revenue that a commercial EV fleet operator can gain by optimizing both trip scheduling and charging on a day-ahead basis. The optimization allows the fleet to complete trips with user-defined lengths and distances while capitalizing on fluctuating energy and ancillary service prices. The paper introduces a mathematical framework for optimal trip scheduling presented as a mixed-integer linear program. The approach is applied to various scenarios representing the current and future British electricity system. The results reveal that optimal journey start times can increase commercial fleet revenue by up to 38% in summer and 12% in winter. This translates to an additional annual revenue of up to £729 for a single EV in the maintenance fleet. Flexible trip schedules are particularly valuable in the summer, benefiting both the grid and fleet operators by keeping EVs plugged in during peak solar output. Additionally, a fleet of 5000 EVs could lead to carbon savings equivalent to removing one Combined Cycle Gas Turbine from the system. The substantial increase in revenue and carbon savings underscores the potential value of this approach for future applications.

In the event of a post-fault condition, the slow recovery of wind power generation, attributed to the fault ride-through (FRT) control strategy, can lead to substantial frequency deviations

due to the power imbalance between supply and demand. These frequency deviations, in turn, can introduce inaccuracies and instability in the control system governing wind power generation. To leverage the extended parking duration of EVs, a demand-side response is harnessed to provide support to the power grid through load-to-grid technology. Consequently, a coordinated control strategy is devised by Tian et al. [26] for power balancing between wind power and demand-side response. This strategy proves effective in significantly alleviating power imbalances, thereby enhancing overall frequency stability.

The escalating integration of RS and EVs poses substantial challenges to the stability, reliability, and resilience of the electrical grid, given the intermittent nature of RS and the uncertain charging demands of EVs. The utilization of V2G technology holds the potential for significant economic benefits in terms of peak load reduction and frequency control. To assess the efficacy of V2G-based frequency control within a microgrid, Yoo et al. [27] conducted modeling and simulations of primary and secondary frequency controls using both single- and multi-vehicle-based approaches. These simulations leveraged integrated components at the Canadian Centre for Housing Technology (CCHT)-V2G testing facility, employing Matlab/Simulink it validated a single-vehicle-based model by comparing empirical testing with simulations of primary and secondary frequency controls. Subsequently, the validated conceptual model was applied for dynamic phasor simulations involving multi-vehicle-based frequency control. The simulations incorporated a proposed coordinated control algorithm aimed at enhancing frequency stability and supporting the integration of renewables using V2G-capable EVs within a microgrid. This model introduced a decentralized coordination of the state of charge (SOC) and charging schedule for the aggregation of five EVs, each featuring different departure times and SOC management profiles tailored to the preferences of EV drivers. The simulation outcomes demonstrated the effective reduction of frequency deviation in a microgrid with a fleet of 5 EVs engaged in V2B/V2G operations.

Khan et al. [28] addressed the assessment of uncertain capacity and the associated response delay for LFC. Subsequently, a robust mixed H_2/H_∞ controller, based on static output feedback, is adopted for EVs participating in multi-objective LFC alongside Charging Stations. The adopted controller ensures system stability by constraining the frequency and tie-line power to their nominal values, even in the presence of internal and external disturbances, through improved reference tracking for both EVs and CSs. The effectiveness of the mixed H_2/H_∞ controller is demonstrated through case studies involving a single-area and three-area system with EVs, providing a comparison with a sole H_∞ controller. The presented results suggest that both, the EVs and the adopted controller, exhibit effective responses to various scenarios, including load variations, uncertainties in parameters, the impact of dead bands, and time delays in both the controller and EVs aggregator responses.

2.2.2 Other load-based approaches

Alhelou et al. [29] conducted an extensive literature review on LFC. The survey initially delves into the utilized LFC models, classifying them for various power system configurations in both traditional and prospective smart power systems. Additionally, the paper examines and categorizes the suggested control strategies for LFC, grouping them into distinct control categories.

Diaz-Londono et al. [30] introduced a conceptual framework that encompasses diverse types of aggregators, including local specialized energy aggregators (SEAs), network aggregators, demand-side general aggregators, and energy community aggregators. The main focus of this framework is the coordination of SEAs to deliver balancing services to the system operator. Each SEA is responsible for managing a specific load type, allowing for detailed control by leveraging their capabilities, and considering factors such as response time, dynamics, and available flexibility. Also, the inclusion of SEAs enhances user privacy, as only information related to a specific type of user's load is shared with the SEA. The SEA Coordinator engages with the Balancing Service Provider to secure frequency containment, frequency restoration, and replacement reserve services. The work elaborates on the SEA Coordinator's formulation, information exchange protocols, and control operation strategies. The case study showcases the utilization of SEAs for three distinct load types (water booster pressure systems, thermoelectric refrigerators, and electric vehicle charging stations). The results underscore the efficacy of the SEA Coordinator's control algorithm in delivering balancing services at different timings across diverse load types.

Chen et al. [31] explored and assessed the potential for virtual inertia derived from the demand side. The investigation reveals that loads linked with voltage-dependent characteristics, when integrated with Electric Spring (ES) technology, can function as Smart Loads (SL) while operating within the $\pm 5\%$ tolerance range of the AC mains voltage, providing virtual inertia. Adhering to the frequency requirements of the U.K. National Grid, the ES-based SL demonstrates the capability to deliver virtual inertia up to an inertia coefficient of 2.5 s, relative to its load power rating. Through simulation studies conducted on a CIGRE benchmark microgrid with a high-resolution domestic demand model, the efficacy of extracting virtual inertia from SL is substantiated. The calculated inertia coefficient remains approximately 1.3 s for most of the day, contributing to an increase of 0.53 s in the overall system inertia coefficient if all domestic loads are transformed into the proposed smart loads.

Yang et al. [32] suggested a decentralized virtual inertial control framework utilizing model predictive control for addressing low inertia challenges in a DC microgrid. Initially, a predictive model for the bidirectional full-bridge DC/DC converter of the Energy Storage System (ESS) is presented. The model predictive control is then employed for optimizing the virtual capacitance during system operation within the virtual inertia control framework. In the event of a disturbance, the virtual capacitance increases to mitigate rapid changes in the DC bus voltage. Conversely, during stability restoration, the virtual capacitance is reduced to facilitate a swift stabilization process. Subsequently, a consensus algorithm based on distributed control is introduced, defining the Non-Controlled Load (NCL) voltage deviation rate. This algorithm achieves equilibrium among NCL voltage deviations, preventing significant voltage imbalances in any specific NCL. Additionally, the small-signal model of the proposed control method is developed, and the impact of the controller on small-signal stability is elucidated through eigenvalue analysis.

Bao et al. [33] introduced a strategy for secondary frequency control (SFC) in industrial power grids, enabling them to deliver emergency HVDC power support (EDCPS) to a system in need through a voltage source converter (VSC) HVDC link. The proposed architecture employs multiple model predictive control (MPC) controllers with periodic communication, aiming to

optimize EDCPS capacity while minimizing adverse impacts on the providing power support (PPS) system. Additionally, a VPP model, encompassing aluminum smelter loads (ASLs) and a significant share of wind power, is established for the PPS system. Enhanced flexibility and controllability of the VPP are achieved through demand response from the ASLs. The impact of wind power uncertainty is addressed through chance constraints. Simulation results, utilizing data from an actual industrial power grid in Inner Mongolia, China, validate the effectiveness of the proposed strategy. The simulation also examines the DC voltage of the VSCs and the DC in the potlines of the ASLs.

Some studies demonstrate the possible contribution to grid ancillary services of thermo-fluidic loads, which regulate the consumption of their motors (pumps, fans, and compressors) based on the dynamics of the systems considered.

Benysek et al. [34] introduced the original stochastic decentralized active demand response (DADR) system in the form of a control algorithm ready for application. Simulation investigations have verified that the proposed stochastic DADR solution, due to its high dynamic response in managing disturbance phenomena, can be employed in both primary and secondary LFC in electrical power systems. The numerical testing of the algorithm's applicability for controlling refrigerators has been conducted with various system parameters. Numerical evaluations confirm the fulfillment of all assumed DADR system requirements, including high dynamic response, "soft" operation, fair share in service, and minimization of degradation in the comfort of use of DADR-controlled devices.

Chen et al. [35] established an aggregated air conditioner model to guide residential air conditioners in participating in power grid operations. This model describes the correlation among total power consumption, external environmental conditions, and indoor temperatures. Additionally, they developed a demand response potential model based on the quantity and duration of demand response, quantitatively assessing the effects of outdoor temperature, indoor temperature adjustments, and the number of air conditioners involved in the response. Finally, the accuracy of both the aggregated model and demand response potential model was verified through numerical simulations.

Eissa et al. [36] introduced a novel technique for wide-area frequency control. Instead of disconnecting power system loads, this control scheme relies on managing thermal conditioning loads and involves distributed multi-agents across the wide-area system. For the success of this technique, it is essential to incorporate an advanced measurement system, leveraging cutting-edge communication technologies, and implement a strong and reliable control algorithm. The Matlab software is used to simulate the wide-area frequency control model. The effectiveness of the control technique is evaluated by introducing various types of disturbances to the new control model.

Chen et al. [37] introduced a scheduling strategy for the aggregator of thermostatically controlled loads (TCLs). It leverages demand-side response technology to regulate the frequency in multi-area interconnected power systems. The approach includes an optimal FOPID controller, which is designed using the particle swarm optimization (PSO) algorithm. The controller aims to suppress regional frequency deviations. Additionally, simulation experiments are conducted in two-area interconnected power systems to validate the effectiveness of both

the FOPID controller and the TCL aggregator scheduling strategy.

Oikkonomou et al. [38] presented a comprehensive framework aimed at optimizing the involvement of water distribution system operators (W-DSOs) in demand response (DR) and frequency regulation markets. The framework considers the combined flexibility offered by variable frequency pumps and water tanks, while also accounting for the underlying hydraulic constraints within water distribution systems (WDSs). The proposed framework comprises two optimization models. The first-step model focuses on minimizing the W-DSO's water procurement cost by optimizing the operation of water pumps and tanks. The second-step model optimizes DR and frequency regulation offers by adjusting the operation of water pumps and tanks. The goal is to maximize the W-DSO's profit from providing these services. To ensure service availability, the model considers the interdependence and compatibility of DR load reduction, load recovery, and frequency regulation services. Additionally, the proposed models incorporate detailed formulations of water distribution networks, including hydraulic constraints, to ensure successful service delivery to power systems. Nonlinear terms in the WDS constraints are linearized, converting the proposed models into instances of mixed-integer linear programming problems. The model's effectiveness is demonstrated using a 15-node WDS, including ancillary service and energy prices from the California Independent System Operator, revealing significant profit opportunities for W-DSOs in the DR and frequency regulation markets.

Toward aggregating demand-side resources for frequency regulation, Chen et al. [39] employed a risk-averse multi-armed bandit learning method to understand user behaviors and introduced a novel aggregation strategy for residential heating, ventilation, and air conditioning (HVAC) systems to enhance the dependability of secondary frequency regulation. In comparison to conventional methods, simulation results demonstrate superior performance in secondary frequency regulation with fewer user selections and opt-outs. Moreover, the proposed approach exhibits increased resilience to random and evolving user behaviors.

2.2.3 Railway system-based approaches

Many authors concluded about the little amount of research on frequency control demand response approaches. According to the possible contribution of railway systems to frequency control, little low-related research is found. To the best of the author's knowledge, only one group of authors has been studying it:

He et al. [40] introduced the incorporation of electrified railways into the power system to enhance frequency regulation, particularly in scenarios with high renewable energy penetration. The authors establish a novel framework for frequency regulation that encompasses day-ahead capacity estimation, dispatch of frequency control parameters, and real-time response for electrified railways to contribute to primary frequency control. Detailed motion equations for electric trains operating under regulation are formulated. To meet frequency regulation requirements while ensuring punctual arrival, a multi-train joint response strategy is proposed, aiming to coordinate different electric trains for primary frequency control. The frequency regulation capacity estimation and frequency control power dispatch problems are formulated based on this multi-train joint response strategy. A unique sequential cutting-plane algorithm

is developed to linearly relax the nonlinear capacity estimation problem and power dispatch problem, incorporating ordinary differential equation constraints. The algorithm iteratively tightens the relaxation area, enhancing solution optimality with desirable efficiency.

He et al. [41] introduced an innovative adaptive frequency control approach based on laxity to seamlessly integrate frequency control into train operations. This method allows electric trains to offer rapid frequency response support to the power system while adhering to the predetermined train timetable. The authors develop an online trajectory optimization model that considers realistic track gradients and speed limits. This model aims to correct deviations in the guidance curve and generate power references for frequency response. The concept of "laxity" is newly defined to quantify the flexibility that a train can contribute to frequency response. Subsequently, an adaptive droop controller is designed based on the train's laxity to deliver an appropriate frequency response in line with the current train state without compromising arrival time commitments.

He et al. [42] introduced a novel hierarchical method for coordinating trains and regulating trajectories to assess and provide Grid Support Capacity (GSC) from electrified railways. Considering the analysis of mechanical energy consumption during train operations, an energy-oriented train operation model is suggested to circumvent the nonlinear differential dynamics associated with large-scale train coordination. Subsequently, the aggregation and disaggregation of trains for grid support are formulated as linear and convex quadratic programming problems, respectively. In order to closely follow the reference power and improve the practicality of train operations, a novel iterative discretization method is introduced to generate accurate reference trajectories. Additionally, a sliding mode controller with disturbance-bound adaption is developed to address modeling errors and disturbances when implementing GSC in real-world scenarios.

2.3 Proposal: expansion of railway system-based approaches

According to the authors of [40]–[42], extensive positive contributions could be obtained. However, this approach requires updating the speed profile of trains and implementing high-computational cost optimization algorithms that are not intuitively implementable. This could be challenging for some real railway systems where the circulation of trains is normally monitored and adjusted by local drivers. Urban and suburban railway systems with no long enough trajectories can also increase the implementation difficulty. Also, the comfort of passengers could be negatively impacted by the changes in acceleration. Therefore, an alternative way of allowing railways to contribute to frequency control is proposed to be explored. This also considers analyzing the requirements for combining different frequency controls in a single load. As noticed in 2.2, it is not common to combine virtual inertia, primary and supplementary frequency control schemes in demand-response approaches. Then, This work also approaches this situation within the railway system context.

As known, railway systems are composed of many subsystems (e.g. HVAC systems, lighting, and communication, among others) that can be controlled to support grid frequency control

tasks. Although the total auxiliary consumption is much smaller than the motion consumption of trains, the accumulative contribution can partially support grid frequency control tasks. This way, railway systems, along with other frequency-responsive grid participants, can maintain frequency stability.

Depending on the topology of railway systems, many HVAC systems can be found in trains and other infrastructure, such as passenger stations. Modifying the operation of HVAC systems would impact in a much more negligible way the overall comfort of passengers. The previous literature review exposed the reliability of using thermo-fluidic consumption, as HVAC, to provide frequency control to some extent. Therefore, for the first time, adjusting the operation of onboard HVAC systems of trains is proposed as a way to enable railway systems to contribute to grid frequency control without risking the main objective of railways. This study requires the proper consideration of railway dynamics and its impact on the performance of the frequency control schemes to be proposed. It is worth mentioning that this approach would work in DC railways as in AC railways. Using existing railway components reduces the need for new ones to provide new services. This is, no storage, generators, or extra electronic converters are needed to change the equivalent railway consumption perceived by the grid. Contrary to conventional approaches that demand new equipment to be installed, the proposal is also inspired by reducing the overall cost of enabling grid participants to support ancillary services. In DC railway systems, can represent larger benefits due to the unidirectional power flow through traction substations. Otherwise, the installation of new DC/AC converters is necessary.

Chapter 3

Theoretical framework

Assessing the impact of trains on the frequency performance of electric power systems involves considering the dynamics of grid elements, and the dynamics of railway systems. Due to the scope of the present work, the kinetics and thermodynamics of trains should be sufficiently described. To achieve this, it is essential to model both systems cohesively. Then, both systems can interact in a frequency-oriented framework.

3.1 Power systems modeling

During the development of the present work, different phenomena are needed to be studied. To properly employ the available computational resources, and to simplify results analysis, three modeling styles are adopted. The phasor-domain model, Section 3.1.1, used in [43], is applied to study voltage variations and fluctuations due to load consumption variation in grids with high inertia. The load frequency control scheme, Section 3.1.3, used in [44]–[47], is applied to study an equivalent grid frequency behavior. The time-domain model, Section 3.1.2, used in [48], is applied to study a deeper grid frequency behavior. All modeling styles are used to represent three main elements: generators, lines, and loads. Therefore, only these are described. Other elements, such as transformers [49] and power electronics [50] could be added to the modeling methodology. However, it is not necessary for the type of studies carried out in this work.

3.1.1 Phasor-domain

For steady-state analysis, this approach fits the most of possible study requirements. The operation voltage can be modeled as in (3.1). This may represent a synchronous generator, a grid-forming converter, or any kind of arrangement of elements that can impose voltage on a grid. U, I, and Z stand for voltage, current, and impedance, respectively. The subscripts Ta, Tb, and Tc represent the phases a, b, and c in the transmitting point of a voltage source. The subscripts $a0$, $b0$, and $c0$ represent the generated voltage in each phase before the voltage drops across the impedance of each phase. Using this voltage source topology it is possible to emulate unbalanced voltage sources, by setting $a0$, $b0$, and $c0$ voltages and/or impedances

with different values. The current in the transmitting point of the voltage source is mainly defined by loads.

$$\begin{cases} \underline{U}_{Ta} = \underline{U}_{a0} - \underline{Z}_a \underline{I}_{Ta} \\ \underline{U}_{Tb} = \underline{U}_{b0} - \underline{Z}_b \underline{I}_{Tb} \\ \underline{U}_{Tc} = \underline{U}_{c0} - \underline{Z}_c \underline{I}_{Tc} \end{cases} \tag{3.1}$$

The equivalent voltage source is connected to the load by means of lines. Railway systems have many topologies and can be specifically modeled depending on the study scope. High-speed railways are usually connected to transmission lines, whereas urban systems (such as metros, monorails, and trams) can be supplied by dedicated feeders of a distribution grid. Therefore, lines can be modeled as transmission lines [49] or distribution lines [51]. Equation (3.2) represents the relation between line currents and phase to neutral voltages of a x phase in the transmitting ($\underline{U}_{Rx}$, $\underline{I}_{Rx}$) and receiving ($\underline{U}_{Tx}$, $\underline{I}_{Tx}$) points of a transmission line. l represents the length of the line. γ is the propagation constant which is the root of the product of the series impedance per length unit times the parallel admittance per length unit. Z_c is the characteristic impedance which is the root of the quotient between the series impedance per length unit and the parallel admittance per length unit.

$$\begin{bmatrix} \underline{U}_{Rx} \\ \underline{I}_{Rx} \end{bmatrix} = \begin{bmatrix} \cosh \gamma l & -Z_c \sinh \gamma l \\ -\frac{\sinh \gamma l}{Z_c} & \cosh \gamma l \end{bmatrix} \cdot \begin{bmatrix} \underline{U}_{Tx} \\ \underline{I}_{Tx} \end{bmatrix} \tag{3.2}$$

For distribution lines (3.3) is used. Here, the influence of the neutral grounded conductor and common asymmetric are considered. $[U_{Diag}]$ is a ones diagonal matrix. $[\underline{Z}_{abc}]$ and $[\underline{Y}_{abc}]$ are the impedance and admittance matrix, calculated as in (3.4) and (3.6), respectively.

$$\begin{bmatrix} [\underline{U}_{Rabc}] \\ [\underline{I}_{Rabc}] \end{bmatrix} = \begin{bmatrix} [U_{\text{Diag}}] + 0.5[\underline{Z}_{abc}][\underline{Y}_{abc}] & -[\underline{Z}_{abc}] \\ -\left([\underline{Y}_{abc}] + 0.25[\underline{Y}_{abc}][\underline{Z}_{abc}][\underline{Y}_{abc}]\right) & [U_{\text{Diag}}] + 0.5[\underline{Z}_{abc}][\underline{Y}_{abc}] \end{bmatrix} \cdot \begin{bmatrix} [\underline{U}_{Tabc}] \\ [\underline{I}_{Tabc}] \end{bmatrix} \tag{3.3}$$

Equation (3.4) shows the calculations of self impedances for x phase, and the mutual between x and k phases. Here: j is the imaginary number, μ_0 is the magnetic permeability in vacuum, GMR_x represents the geometric mean radio a the phase x, D_{xk} represents the distance between x and k phases, ρ represents the ground resistivity, f is the frequency, and $R_x^{'}$ is the conductor resistance [43].

$$\begin{cases} \underline{Z}_{xx} = R_x^{'} + 0.0015836f + j\omega\frac{\mu_0}{2\pi}\left(\ln\frac{1}{GMR_x} + 7.6786 + 0.5\ln\frac{\rho}{f}\right) & \text{,self impedances} \\ \underline{Z}_{xk} = 0.0015836f + j\omega\frac{\mu_0}{2\pi}\left(\ln\frac{1}{D_{xk}} + 7.6786 + 0.5\ln\frac{\rho}{f}\right) & \text{,mutual impedances} \end{cases} \tag{3.4}$$

The distribution line admittance first requires the calculation of the potential coefficient matrix, $[P_{abc}]$, as shown in (3.5). Here, ϵ is the permittivity, S_{xx} is the distance between phase x and its image phase; S_{xk} is the distance between phase x and the image phase k; and q_x

and q_k is the charge of phases x and k, respectively. P_{xx} and P_{xk} are the self and mutual potential coefficients which define $[P_{abc}]$ in (3.6) [43].

$$\frac{1}{2\pi\epsilon}\left(q_x \ln\frac{S_{xx}}{GMR_x} + q_k \ln\frac{S_{xk}}{D_{xk}}\right) = q_x P_{xx} + q_k P_{xk} \tag{3.5}$$

$$[\underline{Y}_{abc}] = j\omega[P_{abc}]^{-1} \tag{3.6}$$

Loads are commonly modeled as current sources. Depending on load behavior, the current may have one or a mix of the topologies shown in (3.7). Equation (3.7) defines the $\underline{I}_R$, needed for calculation in (3.2) and (3.3), of the phase x. For constant power loads, it is required the phase apparent power, $\underline{S}_x$. For constant impedance loads, the phase equivalent load impedance, $\underline{Z}_{Lx}$, is used instead. For constant current loads is required the module of the phase apparent power, S_x and the load angle, θ_{S_x}. In the latter, $\theta_{U_{Rx}}$ stands for the voltage phase angle. Besides the load type selected, any profile can be developed to represent many consumption situations. This can be done by controlling and/or adjusting $\underline{S}_x$, $\underline{Z}_{Lx}$, S_x, and θ_{S_x}.

$$\begin{cases} \underline{I}_{Rx} = \left(\frac{\underline{S}_x}{\underline{U}_{Rx}}\right)^* & \text{,constant power loads} \\ \underline{I}_{Rx} = \frac{\underline{U}_{Rx}}{\underline{Z}_{Lx}} & \text{,constant impedance loads} \\ \underline{I}_{Rx} = \frac{S_x}{U_{Rx}} \angle\left(\theta_{U_{Rx}} - \theta_{S_x}\right) & \text{,constant current loads} \end{cases} \tag{3.7}$$

3.1.2 Time-domain

Among the described grid elements in Section 3.1.1, the distribution and transmission lines keep the same modeling. Because of the scope of the studies, some operative situations, that would influence the transient characteristics of lines, can be disregarded. The effects of temperature, precipitation, and wind, among other atmospheric phenomena, are neglected. Then, impedance does not change over time.

The voltage can be obtained by modeling a voltage source, like (3.1), but considering the frequency variation over time. Equation (3.8) represents same dynamic as (3.1) but including $f(t)$ and $\Delta\theta$. The first term allows to emulate mathematically any frequency variation, and the second one to achieve different phase shifts.

$$\begin{cases} U_{Ta}(t) = U_{a0}(t)\sin(2\pi f(t)t + \Delta\theta) - Z_a I_{Ta}(t) \\ U_{Tb}(t) = U_{b0}(t)\sin(2\pi f(t)t - 2\pi/3 + \Delta\theta) - Z_b I_{Tb}(t) \\ U_{Tc}(t) = U_{c0}(t)\sin(2\pi f(t)t + 2\pi/3 + \Delta\theta) - Z_c I_{Tc}(t) \end{cases} \tag{3.8}$$

For obtaining more realistic dynamics, (3.9) can be applied [52]. Here, the dynamics of the stator, rotor, and damping windings of a synchronous machine (SG) are considered. The vector $[V_{SG}]$ contains the dq axis voltages of the stator, rotor, and excitation. The excitation system can be modeled in many ways depending on the topology of the generator. Some recommended practices for excitation systems modeling can be found in [53]. The diagonal matrix $[R]$ represents the resistance of the windings in the dq axis. $[i]$ is the current vector.

The matrix $[L]$ contains the mutual and self-inductance of windings in the dq axis. $[W]$ is the rotor speed ($2\pi f$) matrix, which depending on the rotor type (salient or round pole) has a different size. The frequency behavior is modeled by (3.10). The frequency variation depends on the synchronous frequency (f_s), mechanical power (P_m) injected by the prime mover by means of the coupling shaft, electrical power (P_e) developed by the SG, and the inertia constant (H) of the overall set. In (3.10) the superscript $p.u.$ means each variable is in *per unit*.

$$[V_{SG}] = [R][i] + \frac{d([L][i])}{dt} + [W]([L][i]) \tag{3.9}$$

$$\frac{df^{p.u.}}{dt} = \frac{f_s{}^{p.u.}\left(P_m{}^{p.u.} - P_e{}^{p.u.}\right)}{2H} \tag{3.10}$$

The prime mover of a SG is normally a hydroelectric turbine (hydro. turb.), steam turbine, gas turbine, or diesel engine (diesel eng.), where each system has its specific dynamics and auxiliary subsystems. These are commonly simplified and expressed as transfer functions in the Laplace domain. Equation (3.11) shows the variation of mechanical power ($\Delta P_m^{p.u.}$) due to the variation in gates/valves opening ($\Delta Op^{p.u.}$) [54]. τ, F, and s stand for the time constant, power fraction, and the Laplace operator. The subscripts hp, rh, ch, c, v, f, cd, and w refer to high-pressure, re-heater, and main inlet volume in steam turbines; combustion in diesel engines; valve, fuel supply, and compressor discharge in gas turbines; and water flow path in the hydraulic turbines; respectively. Some speed controller implementations for each prime mover can be found in [54]–[56].

$$\frac{\Delta P_m^{p.u.}}{\Delta Op^{p.u.}} = \begin{cases} \frac{1+F_{hp}\tau_{rh}s}{(1+\tau_{ch}s)(1+\tau_{rh}s)} & \text{, steam turb.} \\ e^{-\tau_c s} & \text{, diesel egn.} \\ \frac{1}{(1+\tau_v s)(1+\tau_f s)(1+\tau_{cd}s)} & \text{, gas turb.} \\ \frac{1-\tau_w s}{1+0.5\tau_w s} & \text{, hydro. turb.} \end{cases} \tag{3.11}$$

The load modeling techniques have been widely developed. [57] presents an extensive literature review about models for studying transients in power systems, considering different load behavior. Although many load models for time-domain studies can be implemented, by adapting (3.7) to time-domain it is possible to emulate common consumption situations. By Euler complex number theory, (3.7) can be adjusted as in (3.12). This equation is exemplified by using the monophase apparent power, $\underline{S}_x$, of the phase x, but it can be also applied to the other load types exposed in (3.7). The resulting power or impedance equations would interact with the voltage waveforms in the receiving points of lines (3.2)(3.3), to provide the circulating currents.

$$S_x(t) = \Im\left[|\underline{S}_x| e^{j(2\pi f t + \arg(\underline{S}_x))}\right] = |\underline{S}_x| \sin\left(2\pi f t + \arg(\underline{S}_x)\right) \tag{3.12}$$

3.1.3 Load frequency control scheme

This modeling methodology lumps the effect of the considered dynamics of each system into "power vs. frequency" transfer functions. It is an accurate method that reduces computational cost and the complexity of models. Many authors have used it for assessing the integration of renewable generation into power systems [17], [19], [58] and the possibilities of implementing demand response algorithms [28], [34]. Equation (3.13) represents the evolution of the equivalent grid frequency deviation ($\Delta f_{eq}(s)$) due to a load power consumption deviation ($\Delta P_L(s)$) in a grid with n conventional generators and one frequency deviation sensitive controllable load ($L_c(s)$). D_{eq} is the equivalent damping factor. H_ξ, w_ξ, and $G_\xi(s)$ are the inertia coefficient, the energy dispatch percentage presence, and the controlled dynamics of the ξ^{th} conventional generator, respectively. $G_\xi(s)$ includes the physical dynamics as well as the speed regulator. $\Delta P_L(s)$ can be used to represent power consumption/injection variations due to any circumstance. $L_c(s)$ can be expanded to include frequency-based load dynamics, either controllable or uncontrollable. Equation (3.11) and the characteristics of generators can be introduced to solve (3.13). It is worth mentioning that converter-based generation can be also considered in (3.13). However, because of the lack of electromagnetic coupled in most types of renewable generation, it can only contribute to frequency control tasks by means of $G_\xi(s)$.

$$\Delta f_{eq}(s) = -\frac{(2\pi)^{-1}\Delta P_L(s)}{2s\left(\sum_{\xi=1}^{n} H_\xi w_\xi\right) + D_{eq} + L_c(s) - \sum_{\xi=1}^{n} w_\xi G_\xi(s)} \tag{3.13}$$

3.2 Railway systems modeling

The assessment of the possibilities of providing frequency control from railways requires coherent modeling. [59] describes the most known railway systems, including their dynamics, electrification systems, control, and operation, among other aspects. The dynamic foundations are approximately the same among the types of power systems. However, the electrification system may present considerable differences. The present work is focused on modeling DC railway systems used as urban transport systems.

3.2.1 Kinetic and electrical modeling

Modeling DC railway systems is a well-known technique. Current models, besides the appropriate description of mechanical and electric phenomena, allow the integration of renewable generation, energy storage systems, and multi-train optimization algorithms, among other improvements [60]–[63]. The following equations, (3.14)-(3.21), intend to consider in a flexible way the most relevant dynamics that define the kinetic power consumption of a single train [43]. The train speed, v, mostly determines most of them.

Equation (3.14), Davis equation, describes the drag force, where: A relates the train mass, B the interaction between rail and wheels, and C the aerodynamic behavior. These parameters are unique for each train model and describe the effect of lubrication, bearing operation, bogies, pantographs dynamic interaction, etc. Equation (3.15) defines the resistance force

due to track slope. m is the train mass, g is the gravity acceleration, and ang_{slope} is the slope angle. Equation (3.16) defines the resistance force because of the relation between train length (L_{train}) and the radius of curvature (R). Here, ang_d is the deflection angle. Equation (3.17) defines the resistance force caused by the circulation through a tunnel of L_{tunnel} length. Then, the sum of all the previous resistance forces defines the mechanical force (F_{mec}) the motors of the train should overcome (3.18). Finally, the resultant electrical consumption is defined by (3.19): a is the train acceleration; η_{tot} is the total energy conversion efficiency; γ, which can be zero or one, adjusted the efficiency depending whether train is tracking of braking; $P_{elec.aux}$ is the power consumption on non-specified auxiliary consumption's (e.g., lights, communications, controls, etc.), and P_{HVAC} is the consumption of the HVAC systems.

$$F_{Davis} = A + B\,v + C\,v^2 \tag{3.14}$$

$$F_{slope} = m\,g\,\sin(ang_{slope}) \tag{3.15}$$

$$F_{curve} = \begin{cases} \frac{0.6\,m\,g}{R}\,, R \leq L_{train} \\ \frac{0.0105\,m\,g\,ang_d}{L_{train}}\,, R > L_{train} \end{cases} \tag{3.16}$$

$$F_{tunnel} = 1.3 \cdot 10^{-7} L_{tunnel}\,m\,g \tag{3.17}$$

$$F_{mec} = F_{Davis} + F_{slope} + F_{curve} + F_{tunnel} \tag{3.18}$$

$$P_{elec.total} = \frac{v\,(m\,a + F_{mec})}{{\eta_{tot}}^{\gamma}} + P_{elec.aux} + P_{HVAC} \tag{3.19}$$

Depending on the modeling implementation, the exact power consumption profile (3.19) can be obtained in different ways. Many review works used the train speed (v) as the input signal, and, subsequently, the other terms previously introduced are calculated. This implementation speeds up computational simulations and reduces the implementation time, making it flexible and suitable for many kinds of studies. Other studies require to include the train motion controls, as well as assess the mechanical performance of the electrification system (contact lines, feeder, rails), used to control (3.18) by means of (3.20) and (3.21). Here, the instantaneous balance between resistance forces (3.18) and developed forces produces train speed and acceleration. In (3.20): $F_{tract/max}$ is the maximum traction force, v_{lim} is the traction speed limit, $K_{tract/lim}$ is the coefficient which relates forces to speed when the speed limit has been exceed, and v_{max} is the technical maximum circulation speed. In (3.21): $F_{brake/max}$ is the maximum braking force, $v_{lim@brake}$ is the braking speed limit, and $K_{brake/lim}$ is the coefficient which relates forces to speed when the speed limit has been exceed.

$$F_{tract} = \begin{cases} F_{tract/max} & , v \leq v_{lim} \\ F_{tract/max} - (v - v_{lim})K_{tract/lim} & , v_{lim} < v \leq v_{max} \end{cases} \tag{3.20}$$

$$F_{brake} = \begin{cases} F_{brake/max} & , v \leq v_{lim@brake} \\ F_{brake/max} - (v - v_{lim@brake})K_{brake/lim} & , v_{lim@brake} < v \end{cases} \tag{3.21}$$

Before employing the aforementioned equations, it is essential to establish the discretization of the railway layout, striking a balance between accuracy and computational efficiency. It

is recommended to discretize the layout with a minimum of one point at each alteration in the radius of curvature, slope, or speed limit. Following this, the solution for each discretized segment of the rail, as described in [63], [64], will yield profiles over time for forces, speed, acceleration, electric power, voltage, and current at every point and for every train. Additionally, the circulation parameters must be defined, (number of trains and the headway). Consequently, the actual power required by traction substations, as a function of time, can be determined.

Once the power setpoint is defined, it can be traduced to electrical power by means of the aforementioned equations, (3.7)(3.12), where trains are modeled as current sources. The electrification system can also be modeled with equations for voltage sources (3.1)(3.8) and lines (3.2)(3.3), but adjusting them according to the DC voltage and the DC behavior of electrification system conductors.

The traction substation, commonly composed of a step-down transformer and a rectifier can be modeled as in [49] and [50], respectively. Depending on system topology, the traction substation can be formed by mono-phase transformers and rectifiers, for each phase, or three-phase ones. Then, the traction substation can be modeled as a unidirectional DC voltage source rule by (3.22) for phase-domain studies. Here, U_{DC} is the average value on the rectifier DC side, U_{LN} is the line to neutral voltage. U_{LL} is the line-to-line voltage, X_{in} is the reactance in the rectifier input (e.g. transformer windings), and I_{DC} is the circulating current in the rectifier DC side. For time-domain studies, the railway consumption and the traction substation can be lumped into one system and is modeled as a load (3.7)(3.12). This neglects the dynamics of diodes and, therefore, the injection of harmonics into the grid. For including the harmonics effect and the dynamics of diodes should be included in the voltage source modeling [50].

$$U_{DC} = \begin{cases} \frac{2\sqrt{2}}{\pi} U_{LN} - \frac{2}{\pi} X_{in} I_{DC} & \text{, mono-phase rectifiers} \\ \frac{3\sqrt{2}}{\pi} U_{LL} - \frac{3}{\pi} X_{in} I_{DC} & \text{, three-phase rectifiers} \end{cases} \tag{3.22}$$

3.2.2 Thermal modeling

Due to the overall conceptual proposal, an appropriate train thermal modeling is required. As not affecting the main activities of railway systems is an assessment constraint, the thermal comfort of passengers should be secured. However, since the work is on the provision of frequency control, extensive thermal modeling may not be completely necessary for a sufficiently accurate evaluation. Many authors have modeled different railway systems towards specific objectives: [65] studied low-cooling strategies for underground railways, [66] analyzed the impact of climate change on thermal discomfort in underground railways, [67] studied refrigerant alternatives for energy savings in high-speed trains, [68] estimated the heat capacity and transfer of trains, [69] optimized the ventilation design of high-speed train cabins, and [70] simulated the operation of HVAC systems in DC railways, among others. Therefore, to obtain a flexible, simple, easy-implementable, and easy-understandable, a one-dimensional lumped thermal model is developed. The model allows to study bidirectional heat flow over one dimension and represents many thermal subsystems by reduced subsystems while obtaining

enough thermal behavior similarity.

Equation (3.23) represents the thermal behavior of inner air. This model lumps the inner air masses dynamics of every wagon and relates the HVAC system electrical consumption (P_{HVAC}) to the thermal system by means of the average coefficient of performance COP_{mean}. This is, instead of modeling each wagon independently, all air masses are aggregated into one point. Equation (3.24) represents the thermal model of the train body. It mainly represents the mass of bogies, mechanical joints, floor, motors, encapsulated components, and any other metal-based element. In both, (TM), the product UA, T, and $\dot{Q}$ represent the thermal mass, the product between the transmittance and the related heat transfer surface, temperature, and heat gains, respectively. The subscripts a, t, and o refer to inner air, train body, and outside air, respectively. Then, terms with both subscripts, such as $U_{at}A_{at}$, refer to the interaction between both thermal systems. The heat gains represent any heat transferred to the system. These can be the heat of passengers, radiation, heat exchange during the opening of doors, and infiltration gains, among others. In (3.23), the term $\dot{Q}_k$ is the k^{th} heat gain in a system with q heat gains. Similarly, in (3.24) the term $\dot{Q}_l$ is the l^{th} heat gain in a system with p heat gains.

$$\frac{dT_a}{dt} = \frac{U_{ta}A_{ta}}{(TM)_a}(T_t - T_a) + \frac{U_{oa}A_{oa}}{(TM)_a}(T_o - T_a) + \frac{\sum_{k=1}^{q}\dot{Q}_k - (COP_{mean})P_{HVAC}}{(TM)_a} \tag{3.23}$$

$$\frac{dT_t}{dt} = \frac{U_{at}A_{at}}{(TM)_t}(T_a - T_t) + \frac{\sum_{l=1}^{p}\dot{Q}_l}{(TM)_t} \tag{3.24}$$

The train thermal model could be easily expanded to a more detailed one. Instead of combining the mass of furniture and cabin surrounding structure to air mass, each element could be modeled individually. Identically with the train body elements. This would provide many more differential equations that increase the computational cost and the thermal behavior modeling. However, as checked in the literature, even long-term contributions from thermal systems to ancillary services do not risk thermal comfort or own system operation constraints. Hence, more granularity does not add relevant accuracy to the assessment of the contribution of the HVAC system to grid frequency control.

Equation (3.25) defines the electrical power consumption of the HVAC system due to the difference between setpoint temperature (T_{set}) and inner air temperature, injected airflow ($\dot{V}$), air specific heat at constant pressure (C_p), and air density (ρ). This is a simplified model that takes into account the energy in the injected airflow. The injected air temperature is considered equal to the setpoint temperature. If desired, the density and specific heat at constant pressure could be defined as a function of inner air temperature. Also, further details could be added to model the intrinsic dynamics of the setpoint temperature. This means, considering the interaction along the rest of the components (heat exchangers, valves, compression stages, and filters, among others) of the thermo-fluidic system. However, since it is well-known that thermal-fluidic dynamics are much slower than electromagnetic transients, such as frequency phenomena, the thermal characteristics would be negligibly affected by the changes in HVAC system operation.

$$P_{HVAC} = \frac{\rho\, C_p\, \dot{V}(T_{set} - T_a)}{COP_{mean}} \tag{3.25}$$

As reviewed, modern HVAC systems are controlled by variable frequency drives. This can be a DC/AC converter that controls the instantaneous consumed power by the motors that drive compressors and bombs. Hence, this model provides mathematical flexibility to study different approaches to change to HVAC system setpoint power. Also, as the transient effect on the thermal system only depends on the thermal inertia reflected in the inner temperature, T_a, the possible impacts on thermal comfort represent the maximum possible ones.

Chapter 4

Contribution of Railway Systems to Power Systems Frequency Control

As mentioned in Chapter 2, the demand response approaches are inspired by well-known frequency control approaches. As many control techniques applied in electric converters pretend to emulate a synchronous machine's behavior, some demand response algorithms do. Then, an exploration across conventional frequency control schemes is carried out.

It is worth mentioning that this work includes two different main focuses on the source of power for frequency control techniques. The first overall focus is on the regenerative braking energy of trains and the second one is on the previously mentioned HVAC systems. Then, the perspectives selected for studying the contribution of railway systems to electric power systems are:

- Injection of the surplus regenerative braking energy of railway systems.
- Contribution of the thermal inertia of trains for providing primary frequency control.
- Combination of primary frequency control and virtual inertia.
- Relieving of renewable generation from frequency tasks.
- Grid frequency estimation from DC catenary measurements.
- Experimental validation in a micro-grid.

The following sections develop each of the previously mentioned perspectives.

4.1 Alternative uses of regenerative braking energy

As stated in Section 1.2, the growth of these extensive transportation systems has encompassed diverse fields of knowledge. Consequently, these systems have drawn attention from scientific studies and technological advancements that adopt various perspectives, including analysis of their impact on the environment and their participation in energy consumption [6]; examination of the electrical supply structure, taking into account the economic and oper-

ational characteristics of traction substation topologies [71]; compatibility among Internet of Things (IoT) systems and smart grids [72], [73]; enhancement of power electronic components employed in providing and regulating the electrical supply for tractor machinery [74]; and investigation of regenerative braking energy to optimize its utilization and administration to enhance overall energy efficiency and stability [75]–[80]; among others.

It is noticeable the relevance of studies related to regenerative braking energy. Many research works take it into account as a way to improve railway efficiency. This is due to the common approach of dissipating the braking energy through resistors instead of properly managing it.

4.1.1 Current management of regenerative braking energy

The strategies for handling braking energy can be categorized into three main groups: coordination of the movement of rolling stock, deployment of energy storage systems, and the integration of electronic converters to enable the reversibility of traction substations.

Approaches centered on rolling stock coordination take into account the behavior of electrical machines and their operational patterns. In this context, a braking train functions as a generator, supplying energy to other trains [78]. Depending on the system, the current coordination of trains, and the operational patterns established throughout the day, potential reductions in grid consumption ranging from 4% to 38.6% have been identified, as indicated by various studies and implementable algorithms (such as genetic algorithms [81], heuristic models [82], etc.).

The integration of energy storage systems stands out as a widely discussed topic in technical literature. On one hand, onboard storage systems have been applied in various metro lines, such as the Madrid and Brussels lines, realizing savings ranging from 18.6% to 35.8% [83], [84]. Similarly, the Paris metro network achieved reductions from 10% to 18%, enabling free-catenary operation [85], [86]. Trams in Nice and Rotterdam also adopted onboard storage systems, as reported in studies [87], [88].

On the other hand, storage systems positioned alongside the catenary have demonstrated the capability to reduce energy consumption by 20% to 30% [78]. Companies like Siemens have implemented supercapacitors in subways in Beijing, Cologne, Madrid, and Toronto to stabilize voltage [89]. The ABB Group and Hitachi have employed supercapacitors and batteries, respectively, for similar purposes in the subways of Hong Kong and Warsaw [90], [91]. Other companies, including GTR System, Vycon, Regen System, and Kinecit Traction Systems, have opted for flywheels in the subways of London, New York, Lyon, and Los Angeles [78], [90], [92]. In all these cases, various types of batteries, supercapacitors, or flywheels are connected to an onboard direct current bus, where the motor controllers are also linked (onboard systems) or connected to the catenary through a rail-side electronic converter (stationary systems).

The third category of techniques for managing braking energy involves the transformation or replacement of traditional unidirectional traction substations with reversible ones. These systems utilize controllable semiconductors, such as thyristors and IGBTs, to enable the reversal of power flow. This can be achieved either by integrating an inverter in parallel with the conventional rectifier or by completely reconfiguring the substation's topology. Commercial

products in this category include Alstom HESOP [93], ABB Enviline TCR and ERS [94], INGEBER by INGETEAM Traction Company [94], and Sitras from Siemens [95]. Irrespective of the chosen configuration, these systems typically operate to facilitate the exchange of regenerated power between trains while minimizing the impact on both the AC and DC side supplies [96], [97].

In summary, the investigation of regenerative braking energy has garnered significant attention, driven by its potential recuperation ranging from 30% to 40%, as indicated by various authors [89], [98]. This percentage depends on the specific design of railway topologies and their geographical layout. Despite the diversity of studies, a common theme is the lack of exploration into the interaction between regenerated energy within the railway system and the surrounding distribution grid. The majority of research tends to focus on optimal operation, exemplified by Jefimowski et al.[99], and the design of hybrid storage systems, as observed in studies by Dutta et al. [98], Lamedica et al. [100], and Wu et al. [101]. Other works compare control techniques in reversible substations for catenary voltage regulation, such as the investigation by Krim et al. [102]. Additionally, studies delve into the design of DC hubs and assess their performance during the integration of distributed generation and various loads, as evidenced by the works of F. Perez [103], Zangiabadi et al. [104], Feng et al. [105], Nasr et al. [106], and Ahmadi et al. [107], where the involvement of electric vehicles in the power supply is a recurring theme. Economic aspects related to distributed generation-based microgrids are explored in works like those by Akbari et al. [108], Şengör et al. [109], and Chen et al. [110]. Furthermore, Feng et al. [105] consider the internal grid of the railway but fail to evaluate the impact of braking energy within this grid or in the broader public grid. The last two groups of papers do acknowledge the existence of a public grid, yet they fall short of presenting models, results, or noteworthy considerations. The final group of papers explores optimal multi-source energy exchange with the public grid but primarily focuses on energy trading, neglecting technical impacts.

It's important to highlight that the existing studies reviewed do not take into account the injection of braking energy into the AC distribution grid encompassing the railway system. Furthermore, these studies notably lack an analysis of the impact of such injection on a non-railway distribution grid. In contrast, the present section proposes a comprehensive methodology for evaluating the interaction between railway regenerative braking energy and distribution grids. This approach relies on intricate models of both the railway and the grid, coupled through the exchanged energy. The primary objective of this methodology is to streamline the conduct of studies on injecting regenerative braking energy into the distribution grid, eliminating the necessity for detailed power electronics modeling.

Once the surplus regenerative braking energy is estimated, different objectives can be studied. This is, determining the available energy is the first step to defining the contribution of railway systems to the ancillary services of the grid. The proposed methodology would facilitate estimating the energy resources toward the provision of frequency control or any other non-conventional railway-to-grid interaction.

4.1.2 Railway simulation methodology

Before exploring any connection scenarios, it is essential to establish the power requirements of the railway. As previously mentioned, an energy-based approach is introduced to link the railway system and the distribution grid. Given the focus on evaluating the impact of railway operations on the distribution grid, the injected regenerative braking power becomes the sole railway variable perceived by the grid. The overall consumption of the railway system can be calculated by summing the temporal power profiles absorbed by all trains. The braking power profile corresponds to the negative portion of the overall profile. Consequently, assuming that all braking energy is fed into an AC circuit, it becomes feasible to aggregate the entire railway system into an equivalent system with one or potentially multiple outputs. Each output manages a proportion of the total regenerative braking energy.

Conversely, adhering to the customary handling of regenerative braking energy, as outlined in previous practices [102], [111], [112], the regeneration experienced by the grid can be represented as a negative constant power load, as shown in (3.7). While (3.7) is broad in its application, standard operational practice typically avoids reactive power injection/consumption, except in cases requiring voltage-reactive regulation. Additionally, if considering inverter efficiency, the power can be adjusted based on any efficiency criteria chosen by the user (e.g., constant, operation range-based, etc.). This allows the expression of the injected power as a function of other operational parameters.

On the other hand, the volume of data required for describing an entire circulation (comprising the number of trains and headway) will be contingent on the size of the considered system and the chosen circulation setup. Various studies have depicted multi-train operations with different levels of detail and focus. For instance, Nasr et al. [106] simulated circulations lasting between 2 hours 23 minutes and 5 hours 50 minutes without providing detailed information about the railway system. Capasso et al. [61] studied a circulation involving 2 trains between 2 substations over 1000 seconds. Zangiabadi et al. [104] energetically simulated an entire day with various circulations, while Alnuman et al. [62] considered a section between 3 substations with 6 trains over 1800 seconds.

The desired outcome from the railway model simulation is the total power profile during a specific period. This profile enables the separate calculation of absorbed energy and regenerated energy, facilitating a comparison of actual energy consumption values, which is essential for model calibration. Additionally, a circulation mesh depicting the displacement of trains over time is necessary to validate dynamic behavior. If other data are available, such as mechanical forces, catenary voltages, etc., they could also be utilized for validation. Concerning the grid, the variation of voltage, current, power, and total energy can be computed at each point of interest. Given the potentially large volume of data generated (thousands of values per parameter, per node, and phase), a descriptive statistical approach is recommended.

In conclusion, the proposed methodology allows for the development of various types of studies. Potential voltage-oriented studies include assessing how the impact on voltage varies with different injection characteristics, comparing the coupling of the railway to the distribution substation bars through new circuits or to branches distributing energy to consumption areas, and calculating voltage variations in multiple scenarios to study phenomena like

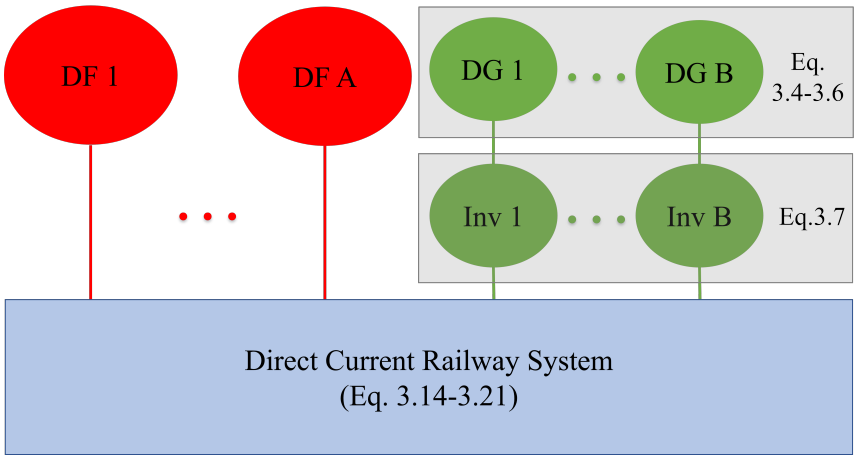


Figure 4.1: Overall description of the modeling (DF: dedicated feeder, DG: distribution grid, Inv: inverter, A: number of DFs, B: number of DGs and inverters).

"flicker". Current-oriented studies could involve evaluating grid efficiency based on injection characteristics and managing grid unbalance and circulating neutral currents.

Ultimately, with the developed model, it becomes feasible to examine how grid magnitudes vary depending on available regenerative braking power and the selected coupling topology. The effectiveness and scope of the proposed methodology are determined by the objectives of the specific case study.

Fig. 4.1 and Fig. 4.2 summarize the proposed methodology. The first shows the relation among the equations used for modeling and the latter how both systems, railway and surrounding distribution grid, are coupled. Also, it established the steps for creating, testing, and coupling both systems. The lowest part of Fig. 4.2 indicates several possible outputs that can be obtained from this methodology.

The calculation involves determining the railway consumption, but the assessment of the impact of its injection into the surrounding distribution grids focuses solely on regenerative energy. Typically, the railway receives power from dedicated feeders that operate independently of other distribution grids. The specifics of the physical connection for extracting braking energy from the railway are not explicitly defined. This connection can occur from various points along the catenary or through an internal AC circuit, contingent on the topology of the system.

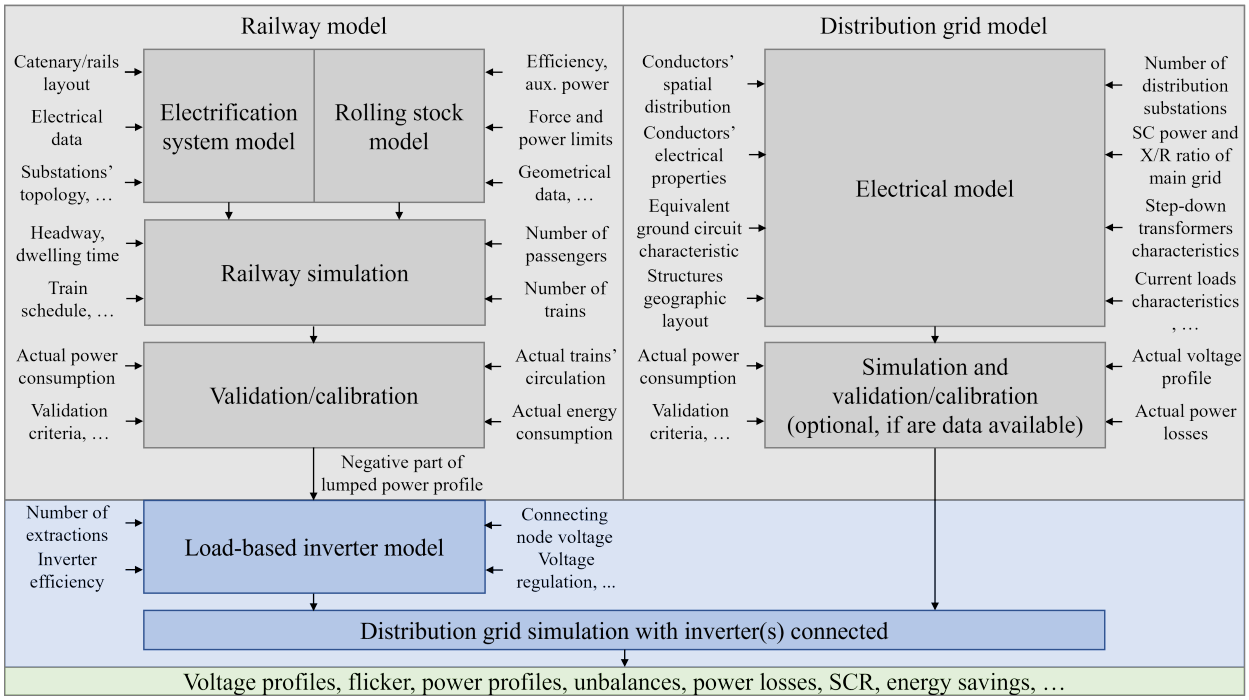


Figure 4.2: Flow diagram of the coupling approach implementation.

4.1.3 Case study

As an illustration of implementing the suggested methodology, this section introduces a case study that explores the interaction between Panama Metro Line 1 (PML1) and the adjacent distribution grid.

Panama Metro Line 1

The implementation of the model takes place within the Matlab application developed by the Department of Mechanical Engineering at the Technical University of Madrid. This application has been widely utilized in railway and academic studies. Real data from the electrification system and rolling stock of PML1 is essential to validate the results. The comparison of simulated outcomes with actual measured energy consumption serves as a validation method.

PML1 commenced its operations on April 6^{th}, 2014. The metro system comprises 14 passenger stations and 8 traction substations equipped with 3.15 MW three-phase diode rectifiers and 3.5 MW, 13.2/1.177 kV transformers, enabling the attainment of 1500 V in both tracks. The first and last substations feature two rectifiers in parallel with transformers of varying configurations to mitigate harmonics. The electrification system is designed to operate with up to 11 electrically isolated sections, including a workshop section, in the event of faults or emergencies. Depending on specific circumstances, trains can be unilaterally or bilaterally powered.

The entirety of PML1 receives power through two connections to the public grid, situated at

kilometer points (pk) 0.091 and 7.782. These connections feed an internal 13.2 kV circuit that distributes AC power to each traction substation (refer to Table A1). It is crucial to note that these connections serve exclusively for railway feeding purposes, ensuring no interaction with other distribution circuits.

The headway on PML1 is set at 120 seconds during peak hours, accommodating 27 trains, and extends to 250 seconds during off-peak hours, involving 14 trains. The metro line encompasses both underground and elevated sections, utilizing rigid and flexible catenary systems in tracks and workshops, respectively. The rolling stock, specifically the Alstom Metropolis 9000 series, comprises trains with either 3 or 5 electric car units, boasting maximum capacities of 800 and 1000 passengers per train, respectively. The dwelling time at passenger stations fluctuates between 20 and 30 seconds, the operational speed is maintained at 32 km/h, the rolling stock's maximum speed reaches 80 km/h, and the maximum slope is recorded at 35 mm/m.

In addition to details regarding the locations of passenger stations and traction substations, knowledge of the rail layout characteristics is essential as they impact the total mechanical resistance force. For this specific case study, the Panama Metro Company has supplied comprehensive blueprints, discretized at intervals of 10 meters to strike a balance between resolution and simplicity. From the blueprints, the profiles of speed limit (Fig. 4.3), slope (Fig. 4.4), and radius of curvature (Fig. 4.5) can be obtained. This information is used to solve (3.14)-(3.18).

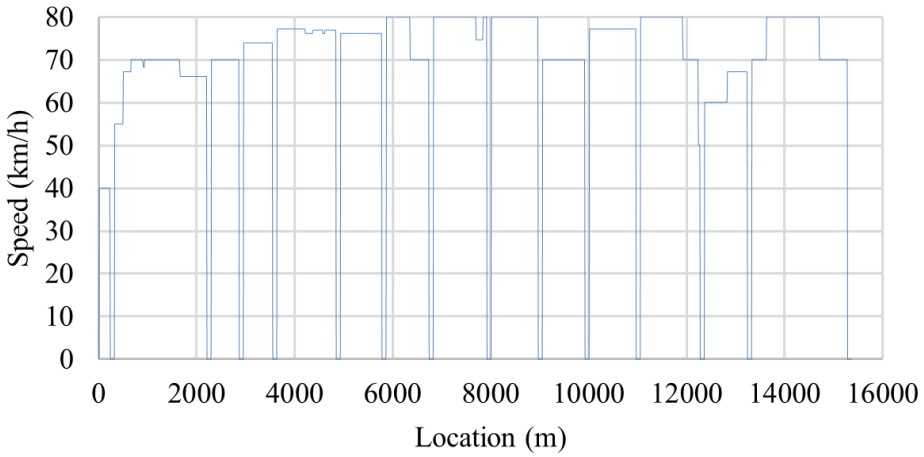


Figure 4.3: Speed limit versus location. Source: Panama Metro Company.

For solving (3.19)-(3.21), the characteristics included in Table A2 are used. It is important to note that, instead of relying on nominal values as presented in Table A2, the use of measured or specifically chosen values is an option, dependent on data availability and the objectives of the study. Utilizing selected values allows for the assessment of various railway scenarios. When the railway system operates under conditions deviating from nominal, employing measured values, if accessible, yields more realistic outcomes.

The catenary can be modeled with varying degrees of detail, ranging from an electromechanical perspective (for studies involving pantograph-catenary dynamic interaction) to an

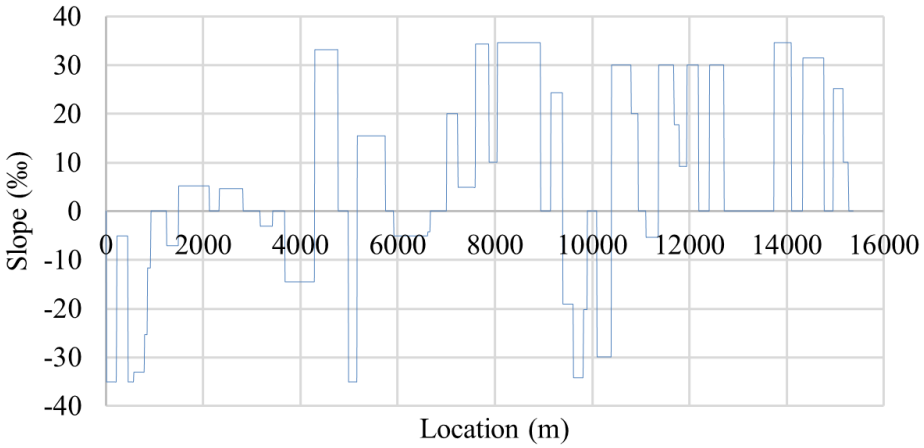


Figure 4.4: Slope versus location. Source: Panama Metro Company.

electrical approach. In this context, the latter is considered, wherein the contact wire-catenary configuration is depicted as a variable conductance proportional to the distance between the train and the traction substation. The contact wire section measures 107 mm^2 of BC 1007 type by EN 50149 standard [113], featuring an electrical resistance of 0.177 Ohm/km at 20 °C. It has a maximum capacity of 592 A at 10 °C and 393 A at 40 °C. The rigid catenary has a copper equivalent section of 1400 mm^2, constructed from a 6106 T5 alloy, with a maximum capacity of 4000 A. The rails exhibit a resistance of less than 0.04 Ohm/km and a width of 1435 mm. The rated operating DC voltage is 1500 V, with permissible variations ranging from 1080 V to 1800 V.

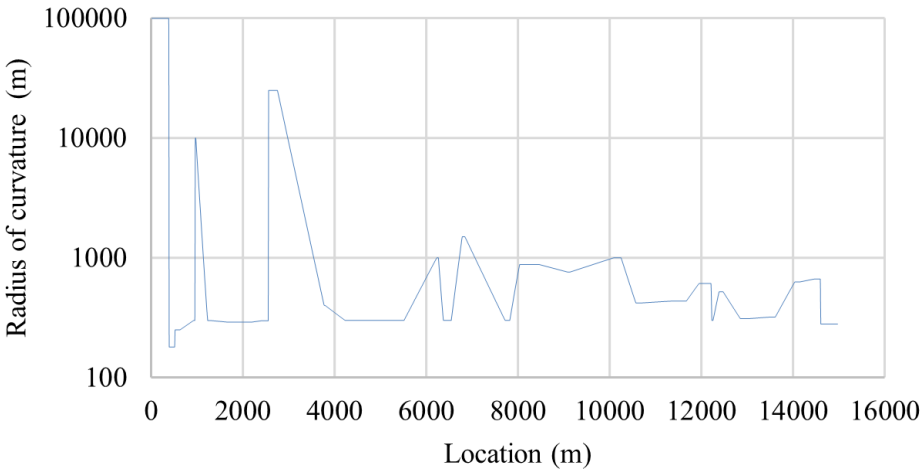


Figure 4.5: Radius of curvature versus location. Source: Panama Metro Company.

Distribution grid in the PML1 surroundings

Two electricity distribution companies, Naturgy and ENSA, are responsible for supplying energy to the vicinity of PML1. Consequently, the substations and branches of both companies near the railway are taken into account. The location of passenger stations and grid substations is illustrated in Figure 4.6, and the details are provided in Table A3. Notably, the injection of excess regenerative braking energy could potentially occur from any passenger station to nearly any distribution grid circuit or substation. As per the topologies outlined in [7], drawing power from the catenary is technologically viable at almost every point, enabling connections to the distribution grid from any location between the blue markers on Figure 4.6. However, for this case study, only the blue markers will be considered as feasible connection points. Assuming adequate available space for installing the inverter to extract surplus regenerative braking energy, this approach eliminates the need for constructing new extensive civil infrastructure.

The configuration of grid lines and substations is detailed in [114], [115]. Distribution substations receive power from various 115 kV transmission lines, where the voltage is subsequently reduced to 13.2 kV for supplying poly-phase and single-phase consumptions. While most circuits are structured in a ring topology, they are operated radially, featuring ACSR conductors ranging from 795 AWG to 1/0 AWG, with 477 AWG being the most prevalent. The overhead lines exhibit diverse conductor topologies. For modeling purposes, a vertical layout of 477 AWG conductors with 48" spacing has been chosen, mounted on poles measuring 12 to 14 meters, and varying in lengths from 1 km to 7 km. The substations' capacity ranges from 146 MVA to 196 MVA for Naturgy substations and from 50 MVA to 100 MVA for ENSA ones.

Access to records of distribution grid power flows is imperative for defining the load profile of substations or branches. In cases where this information is unavailable, an estimation can be derived from alternative data sources. In this study, for instance, the typical load profile

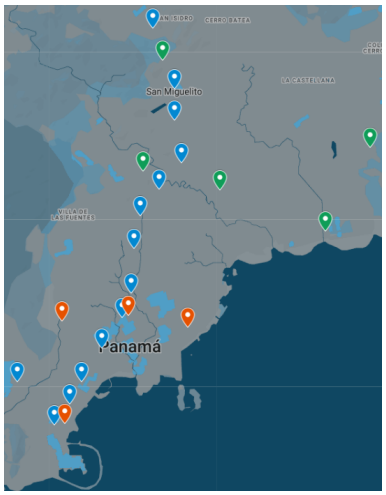


Figure 4.6: Map of the stations of Line 1 (blue), and substations of ENSA (green) and Naturgy (red). Made on Google Maps.

of the Republic of Panama has been utilized (Fig. 4.7), as actual power flow data for each distribution substation is not accessible. Given that the Republic of Panama's economy is centered around services and commerce, and the distribution grid adjacent to PML1 serves residential, commercial, and small industrial areas, using the Panamanian global load profile as an approximation for local profiles is reasonably suitable. Nevertheless, only the periods of the resulting power profile aligning with the injected braking power profile during the railway peak hours will be considered.

The impedance and admittance matrices are derived from equations (3.4), (3.5), and (3.6), incorporating the distribution grid data such as topologies and distances. Appendix A. encompasses per-unit length matrices for the designated base distribution line employed in the modeling process, as previously outlined. Additionally, utilizing the rated power of substations and the load profile depicted in Fig. 4.7, the load profile of each distribution substation can be generated (Fig. A1).

The regenerated power can be introduced into the distribution grid either at its substations or directly into certain nearby feeders. The choice between these alternatives hinges on factors such as territorial availability, facility capacity, the composition of the railway electrification system, and the amount of injectable power. However, the extent of available technical information will delineate the range of feasible studies. In cases where comprehensive details about the railway system and the electrical grid are accessible, it is advisable to assess only those scenarios that are realistic and/or economically viable. Conversely, in situations where detailed information is lacking, it would be prudent to examine a broader spectrum of scenarios to identify overarching behaviors and probabilistic trends.

The integration of the railway system model with the distribution grid model requires careful selection of connection points based on the geographical alignment of the railway route, as previously discussed, and the robustness of the distribution grid at potential connection buses, typically determined by the short-circuit ratio (SCR) (4.2). The SCR is the ratio of injected power (P_{in}) to short-circuit power (S_{cc}). The short-circuit power at a node "N" is

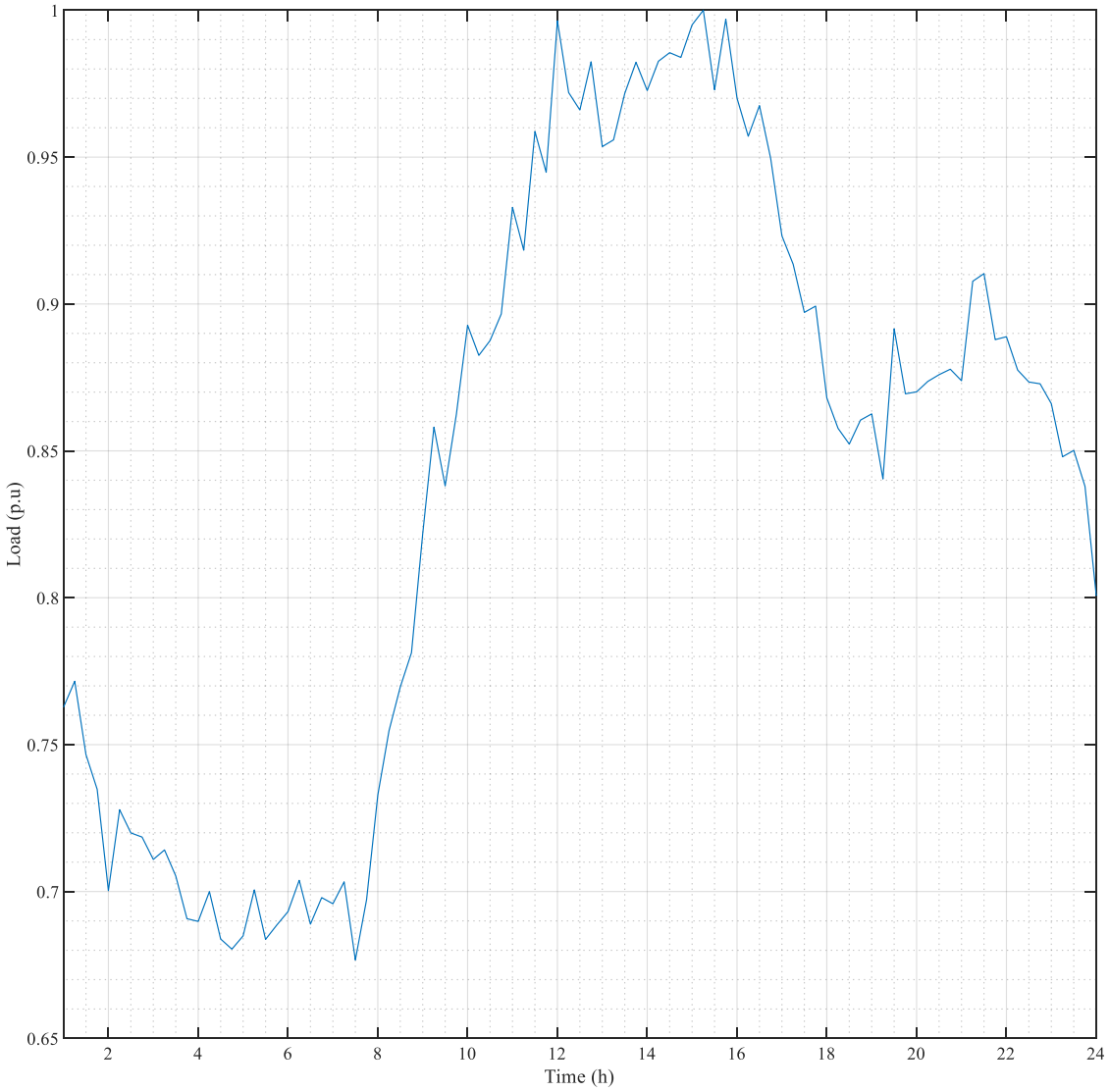


Figure 4.7: Daily load profile of the Republic of Panama.

defined by (4.1), where: $\underline{I}_{cc}$ represents the short-circuit current, $\underline{U}$ is the pre-fault voltage, Z_x is the equivalent impedance observed from the fault point at the x phase. Equation (4.1) underscores that grid strength is primarily influenced by the pre-fault voltage, typically close to the rated voltage. Although voltage variations are generally minimal within a defined voltage level, impedance exerts a more substantial influence.

$$\underline{S}_{cc_N} = \sum_{x=1}^{3} \left(\underline{U}_x \underline{I}_{cc_x}{}^*\right)_N = \sum_{x=1}^{3} \left(\frac{{U_x}^2}{Z_x}\right)_N \tag{4.1}$$

$$SCR(\%) = 100 \frac{P_{in_N}}{S_{cc_N}} \tag{4.2}$$

Railway simulation

As an illustration of the potential outcomes achievable through the proposed methodology, this section conducts simulations of the railway during peak hours, focusing on the most demanding scenario. It is important to note that the simulation results may exhibit variations from the actual values of PML1, necessitating a comparative analysis to evaluate the model's reliability for energetic simulations.

Verification of an appropriate dynamic behavior involves examining the circulation mesh (Fig. 4.8). This mesh comprises 54 curves staggered by 120 s, corresponding to the headway during peak hours on PML1. Each curve depicts the location of a train as a function of time, with 14 constant location zones representing the 14 passenger stations, each with a dwelling time ranging from 20 s to 30 s. The results reveal a train circulation time of approximately 26 minutes, aligning with the typical operational duration of the Panama Metro company.

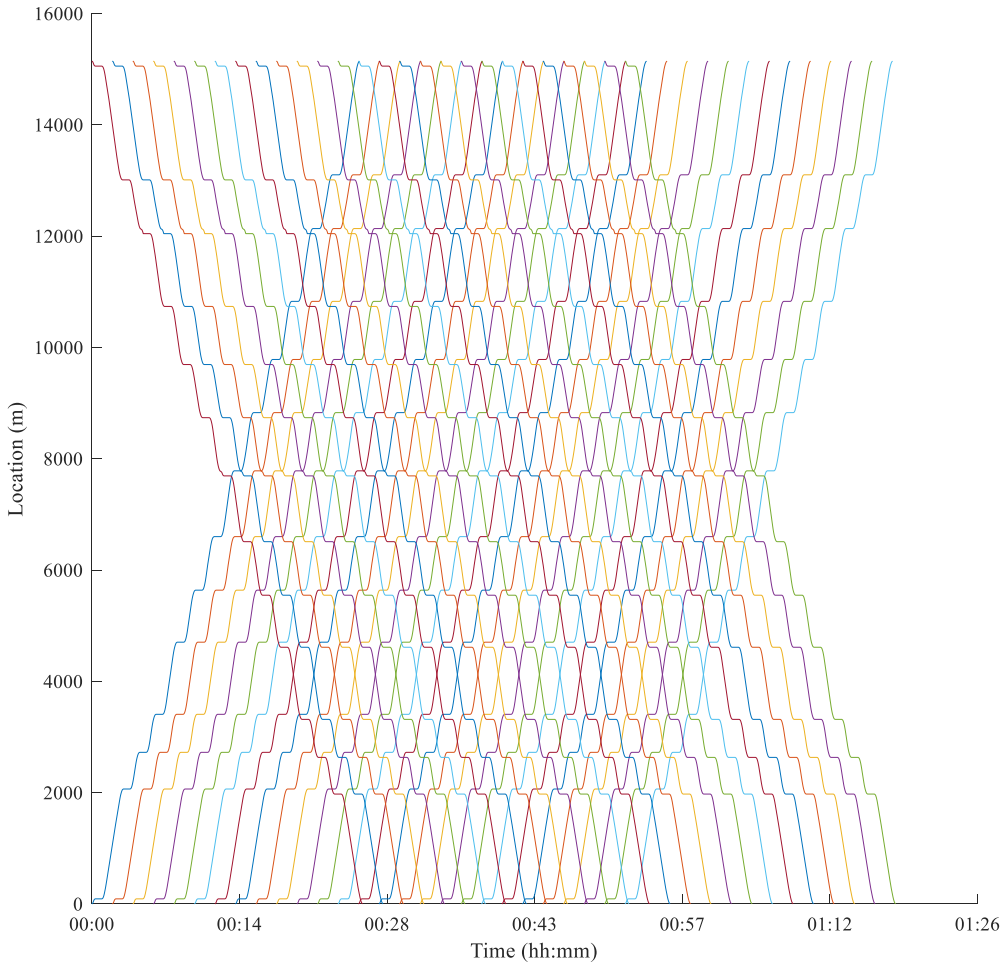


Figure 4.8: Circulation mesh resulting from the dynamic simulation.

Fig. 4.9 illustrates the power absorption characteristics of a single train throughout its journey. The speed profile serves as the primary input for calculating the results depicted in Fig. 4.9. In this instance, the speed profile has been provided by the railway company. However, various types of speed profiles can be employed based on the simulation objectives, such as the sizing

of traction substations, catenary feeders, etc. It is crucial to note that not the entire quantity of negative power can be directly extracted from the railway system. The circulation mesh (Fig. 4.8) reveals periods of high train coincidence (from 00:14 to 01:05, approximately), during which a significant surplus of regenerative energy is not anticipated. This observation is also applicable at the commencement and conclusion of the circulation mesh, owing to the limited number of trains in operation during those intervals.

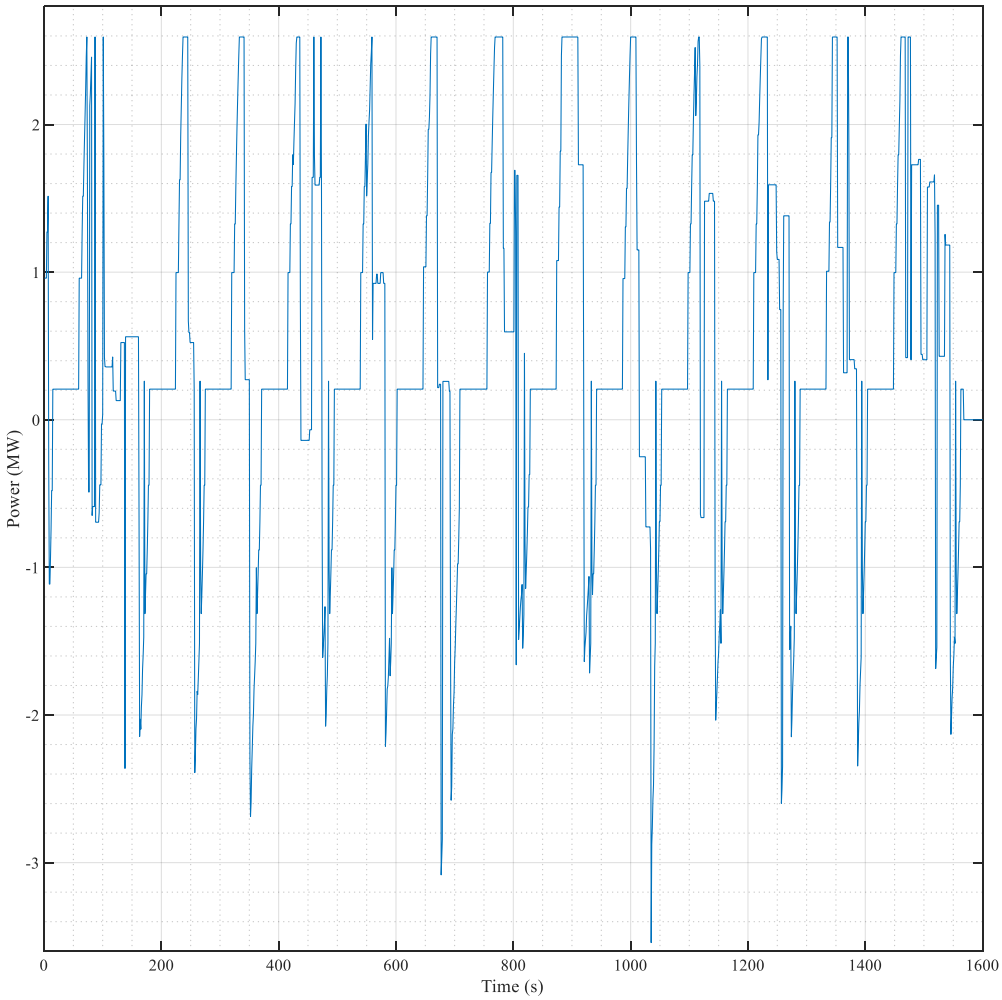


Figure 4.9: Power characteristic of a train. Simulation result.

The primary emphasis of the current investigation lies outside the railway system, with the pertinent information being the power perceived by the grid. In response to this requirement, a power equivalence process is undertaken, wherein the powers of all trains are grouped to derive the overall power profile during circulation. This aggregation is performed by consolidating the profile depicted in Fig. 4.9, taking into account the number of trains and the coordination illustrated in Fig. 4.8. Fig. 4.10 portrays the equivalent railway power consumption profile, where negative values indicate a net surplus of regenerative braking power, while positive values correspond to net power consumption.

To validate the simulation outcomes, a comparison is conducted with actual values of railway

consumption. Fig. 4.11 delineates the average daily profile of real railway energy consumption, aiding in identifying potential peak hours. Table 4.1 shows a statistical analysis of these hours, revealing a considerable dispersion of data. Daily consumption exhibits rapid variations and proves challenging to predict accurately, contributing to the difficulty in conducting precise simulations. This evidences the scarcity of comparative studies featuring simulated models validated against real consumption data in the literature.

Table 4.1: January 2021 PML1 electricity consumption statistical analysis.

Day hour	Feeder Name	Average (MWh)	Maximum (MWh)	Std. deviation (MWh)
7	LAN	2.6699	4.1388	1.4865
7	CMA	2.8517	4.1390	1.2027
8	LAN	2.6144	3.9832	1.4233
8	CMA	3.1135	4.5398	1.2145
17	LAN	2.6933	4.1166	1.4613
17	CMA	3.4424	4.8167	1.1904
18	LAN	2.6618	4.3622	1.5097
18	CMA	3.2671	4.7847	1.1504

The average hourly energy consumption during a simulated peak hour can be calculated by integrating the positive segment of the combined power consumption of all trains (depicted in the central plot of Fig. 4.10) over one period of the profile in the central part (e.g., between $t = 2050$ s and $t = 2167$ s in Fig. 4.10), divided by the duration of the considered period. This result (9.3286 MWh) can be compared with the sum of the maximum consumption of both feeders in Table 4.1 (9.1469 MWh at hour 18), adjusted for non-traction consumption. The non-traction consumption can be inferred from the constant consumption observed in the early hours of the day (ranging from 1.37 MWh to 1.43 MWh in Fig. 4.11). The deviation between the simulated and real energy measurements falls within the range of 20.0% to 20.9%. Nevertheless, it's crucial to note that the validation data used represents the energy consumption during the COVID-19 crisis in the Republic of Panama. The Railway Company reported unpredictable variations in passenger demand due to sanitary restrictions, leading to changes in the number of trains and schedules. If the alteration in circulation hours is considered (from 18 h to 16 h) and applied as an incremental factor to the maximum consumption of both feeders, an adjusted energy consumption of 10.29 MWh is obtained. With this adjustment, the deviation between the simulated and real energy measurements narrows to a range of 4.3% to 5.3%.

Applications commonly used for electric, dynamic, and energetic railway models tolerate maximum deviations of 30% (in substation power, energy consumption, etc.) for safe dimensioning purposes. The obtained deviation falls well below this limit, signifying that the model is suitable for estimating energy consumption. More detailed insights could be derived with the availability of power data, in addition to energy and train circulation data.

In summary, given that the positive segment of the combined power consumption of all trains, acquired through the proposed energy-based approach (central plot of Fig. 4.10), exhibits an acceptable deviation from real values, it can be inferred that the negative segment (lower plot of Fig. 4.10) is also reliable. Therefore, the latter power profile can effectively represent the surplus, typically dissipated, railway regenerative braking energy.

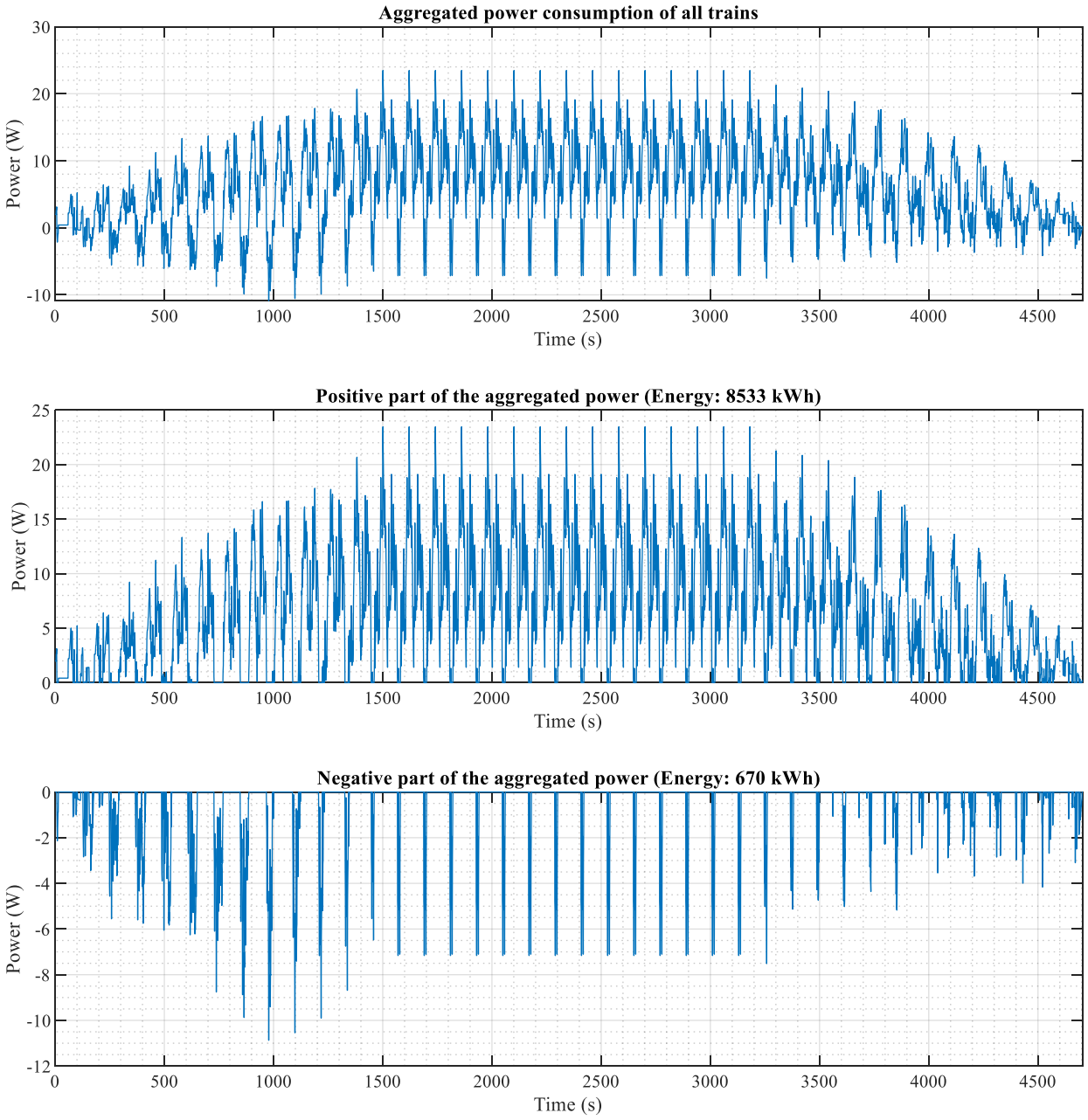


Figure 4.10: Aggregated power consumption obtained from simulation.

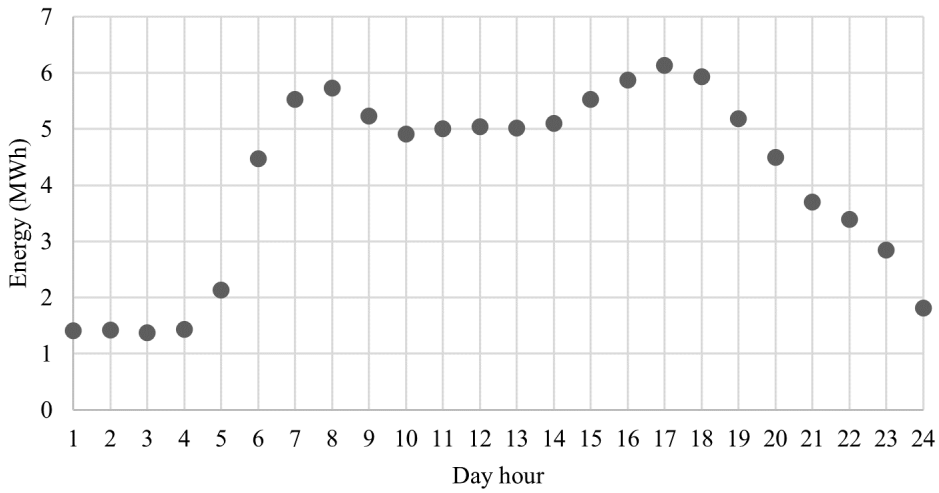


Figure 4.11: Average hourly distribution of energy consumption of PML1 in January 2021.

Impact of injecting the regenerative energy into the distribution grid

The simulation conducted in this section utilized Matlab/Simulink, employing the *Specialized Power Systems* package in "phasor" mode with a time step of 0.05 s, which optimizes computational efficiency by neglecting electrical transients. The simulations were executed on a computer equipped with a sixth-generation i7 processor featuring 4 cores at 2.50 GHz and 8.00 GB RAM, rendering this methodology applicable to most computers.

It's crucial to note that this study is confined to considering the injection of all regenerated energy without specifying how and where it is extracted. These aspects have been extensively explored in existing literature [100], [116]–[118], recognizing that regenerated energy is not generated in a single location, and its transport along the catenary can escalate losses and lead to overvoltage. The placement of multiple extracting devices along the catenary can indeed enhance the potential for energy extraction but at a higher economic cost, a facet beyond the scope of this work. The ensuing results are based on the assumption that all devices extract an equal amount of energy, strategically placed at passenger stations, leveraging their existing infrastructure in areas of high economic and residential concentration.

To evaluate the impact of regenerative braking energy injection (lower plot of Fig. 4.10) into the distribution grid, it could be analyzed the voltage profile of the involved distribution substations. As previously outlined, only passenger stations are considered as feasible extraction points for surplus regenerative braking energy. Consequently, with 9 distribution substations and 14 passenger stations (as depicted in Table A3), there are 126 potential combinations. However, not all are practically viable due to unknown topographical and urbanistic information. To refine the simulation and obtain realistic and meaningful results, the distances from distribution substations to passenger stations are calculated using Table A3 coordinates. By applying an economic criterion based on the proportional relation between circuit length and cost, distances exceeding 3 km are discarded. The filtered results reveal that among the 9 distribution substations, only 2 have longer distances (Llano Bonito and Costa del Este). Apart from distribution substation selection, the number of injections from the railway must be determined, considering scenarios with 2 to 7 injections for study purposes. Each scenario involves partitioning the railway layout into sections equal to the number of injections. For each section, the shortest distance between each passenger station and distribution substations is chosen as the circuit line for simulation. For instance, in the "6 injection scenario," the railway line is divided into 6 parts, each encompassing 2 or 3 passenger stations. Applying this method across the 6 scenarios considers only connections to 5 distribution substations (Monte Oscuro, Tinajitas, Santa Maria, Centro Bancario, and Marañon).

While these scenarios are grounded in realistic and plausible implementations, it's important to acknowledge that if new circuits are constructed to link the railway line to distribution substations, they can also supply new loads. Consequently, not all the surplus regenerative braking energy would reach the distribution substation. Conversely, these new circuits could be utilized to supply the railway from more points than the current two, potentially altering both the grid impact and railway performance. Although these considerations, including energy hubs, renewable energies, and storage systems, are pertinent, they fall outside the scope of this case study but remain analyzable with the presented methodology.

Fig. 4.12 depicts the phase voltage profiles of distribution substations in scenarios with varying numbers of railway extractions. The label "Railway extractions" denotes the number of extractions along the railway line, not the injections received by distribution substations. While all curves share a similar shape dictated by the typical load profile, they exhibit different levels of "noise," reflecting the injection of regenerative braking energy at different rates. Notably, "Tinajitas" and "Centro Bancario" are the distribution substations consistently involved in all scenarios due to their proximity to the railway line. The results for other distribution substations enable a comparison of voltage profiles with and without regenerative braking energy injections. All voltage profiles adhere to Panamanian regulations for electrical installations, with 0.95 p.u. $<$ U $<$ 1.05 p.u., [119]. However, each injection scenario introduces a ripple, influenced by the strength of the distribution substation and the injected power amount. For instance, in the 2-extraction scenario, both "Tinajitas" and "Centro Bancario" receive half of the total regenerative braking energy. Nevertheless, "Tinajitas" exhibits a ripple approximately 1.3 times higher than that of "Centro Bancario" since "Tinajitas" short-circuit power is roughly 1.3 times lower than that of "Centro Bancario." The ripple diminishes proportionally with the number of railway extractions since the same available power is divided into more parts. This is evident in the results for "Monte Oscuro," "Santa Maria," and "Tinajitas," which receive only one railway injection during all their rippled responses. The impact on "Tinajitas" is particularly pronounced, receiving fractions of regenerative braking energy ranging from 1/2 to 1/7.

Concerning the magnitude of voltage fluctuations, while the integration is acceptable, it would be beneficial to delve into the previously observed ripple. Calculating the rate of voltage change per substation per scenario can provide valuable insights. Fig. 4.13 illustrates the results, confirming earlier findings regarding "Tinajitas" and "Centro Bancario" in the 2-extraction scenario. The maximum voltage variation in "Tinajitas" is 10.5 V/s, while in "Centro Bancario," it is 8.36 V/s. Fig. 4.13 demonstrates how diminishing the regenerative braking injection into distribution substations mitigates the impact on voltage variations. In "Monte Oscuro" and "Santa Maria," the variations reduce from 3.26 V/s to 2.80 V/s and from 4.08 V/s to 2.91 V/s, respectively. This trend is clearly illustrated in "Tinajitas" results, where the voltage variation decreases from 10.5 V/s to 3.04 V/s, roughly equal to the ratio between injected power among the relevant scenarios.

According to the findings, the relationship between short-circuit power at distribution substations, under the same injection conditions, can be employed to estimate the impact on one substation using the results of another. Similarly, for the same short-circuit value, the impact on a distribution substation with different injection scenarios can be approximated by leveraging the results from another substation and considering the ratio of injected powers between scenarios.

Beyond the noted maximum voltage variations, continuous fluctuations persist during the injection of regenerative braking energy. While frequent values fluctuate between 2 V/s and 5 V/s, it is noteworthy that voltage variation without injections is nearly negligible. Hence, voltage fluctuations might be pertinent for the connection of loads and auxiliary power quality equipment along the distribution circuits.

Conversely, the SCR in different railway extraction scenarios (RES) is depicted in Fig.

4.14. It can be inferred that regenerative braking injection minimally affects SCR values. Injections at a substation reduce the effective load and, consequently, the SCR. For instance, "Tinajitas" SCR, the distribution substation with the lowest short-circuit power, exhibits more variation than others in the considered railway extraction scenarios (fluctuating from 3.4% to 3.8%). The SCRs of "Marañon" and "Centro Bancario," the strongest substations, experience minimal changes. Their SCRs range from 5.4% to 5.0% and from 5.3% to 5.1%, respectively. Furthermore, in "Marañon," 3 RES and 6 RES yield the same SCR, as is the case in "Centro Bancario," where 2 RES and 4 RES share an identical SCR. These outcomes arise from the resulting injections determined by the distance criterion. "Marañon" receives 1/3, 1/4, 2/5, 1/3, and 2/7 of the total regenerative braking energy from 3 RES to 7 RES. Similarly, "Centro Bancario" receives 1/2, 1/3, 1/2, 1/5, 1/6, and 2/7 of the total braking energy from 2 RES to 7 RES. These explanations clarify why, in Fig. 4.13, the orange curve in "Marañon" is identical to the green one and why the violet one has the maximum values. Also, in "Centro Bancario," the blue curve of Fig. 4.13 is identical to the yellow one.

In essence, the various options for injecting regenerative braking energy into the distribution grid exhibit a limited influence on voltage behavior. Moreover, the resultant voltage values adhere to Panamanian regulations (within ± 5% of the nominal value), suggesting that the injection of surplus regenerative energy, following the proposed energy-based approach, is permissible. Nevertheless, voltage fluctuations arising from the injected power profile may hold significance based on specific load requirements. It is crucial to emphasize that the analysis has considered an entire railway peak hour circulation as a worst-case scenario. In standard railway operations, off-peak hour circulations are more frequent, and the number of passengers and trains fluctuates continuously. Consequently, working with lower regenerative braking power is more typical, resulting in a reduced impact on the grid.

4.1.4 Conclusions

The proposed methodology distinguishes itself through its meticulous modeling of both the railway and distribution grid systems, emphasizing their interaction through regenerative braking energy. An energy-centric approach is advocated to interlink these systems, involving the union of individual train profiles. This method facilitates the estimation of total railway consumption and maximum regenerative braking energy, acknowledging that the exact retrievable braking energy depends on operational factors and the location of extraction equipment, a facet that can be scrutinized in greater detail, encompassing converter topologies, control methods, and allocation strategies.

Notably, the proposed methodology is computationally efficient, enabling fast analysis of the distribution grid's impact by considering specific railway system parameters, such as train circulation, characteristics, and electrification system attributes. The case study indicates that subdividing regenerative braking energy injection mitigates the distribution grid's impact and aligns with existing literature suggesting enhanced surplus braking energy recovery. Employing multiple extraction points, from the railway system to distinct distribution grid coupling locations, contributes to reduced voltage fluctuations and variations. While temporary load relief marginally enhances the SCR, the ripple amplitude reduction is influenced by the injection split, rather than the frequency, which relies on train circulation attributes such as

headway and dwelling time.

Additionally, the proposed methodology facilitates a simplified modeling of railways within microgrids. This simplification enables a more accessible evaluation of the interaction between distribution grids and railway-based microgrids, as the energy-centric approach furnishes an equivalent and highly representative constant power load. Depending on user resources and objectives, analyzing interactions between diverse DC railway systems and different grids becomes feasible.

These results are published in [43].

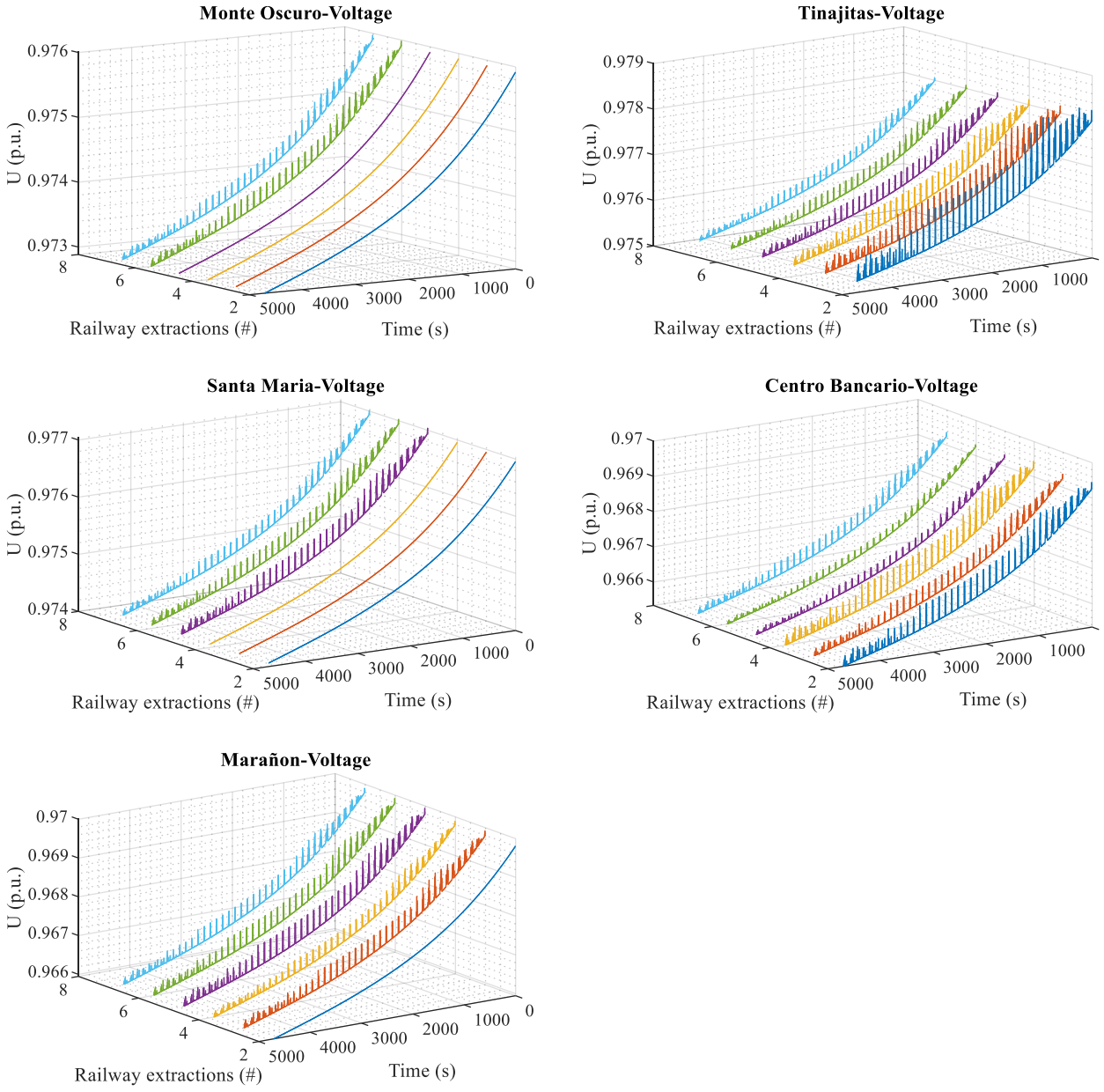


Figure 4.12: Phase voltage of distribution substations under different railway extraction scenarios.

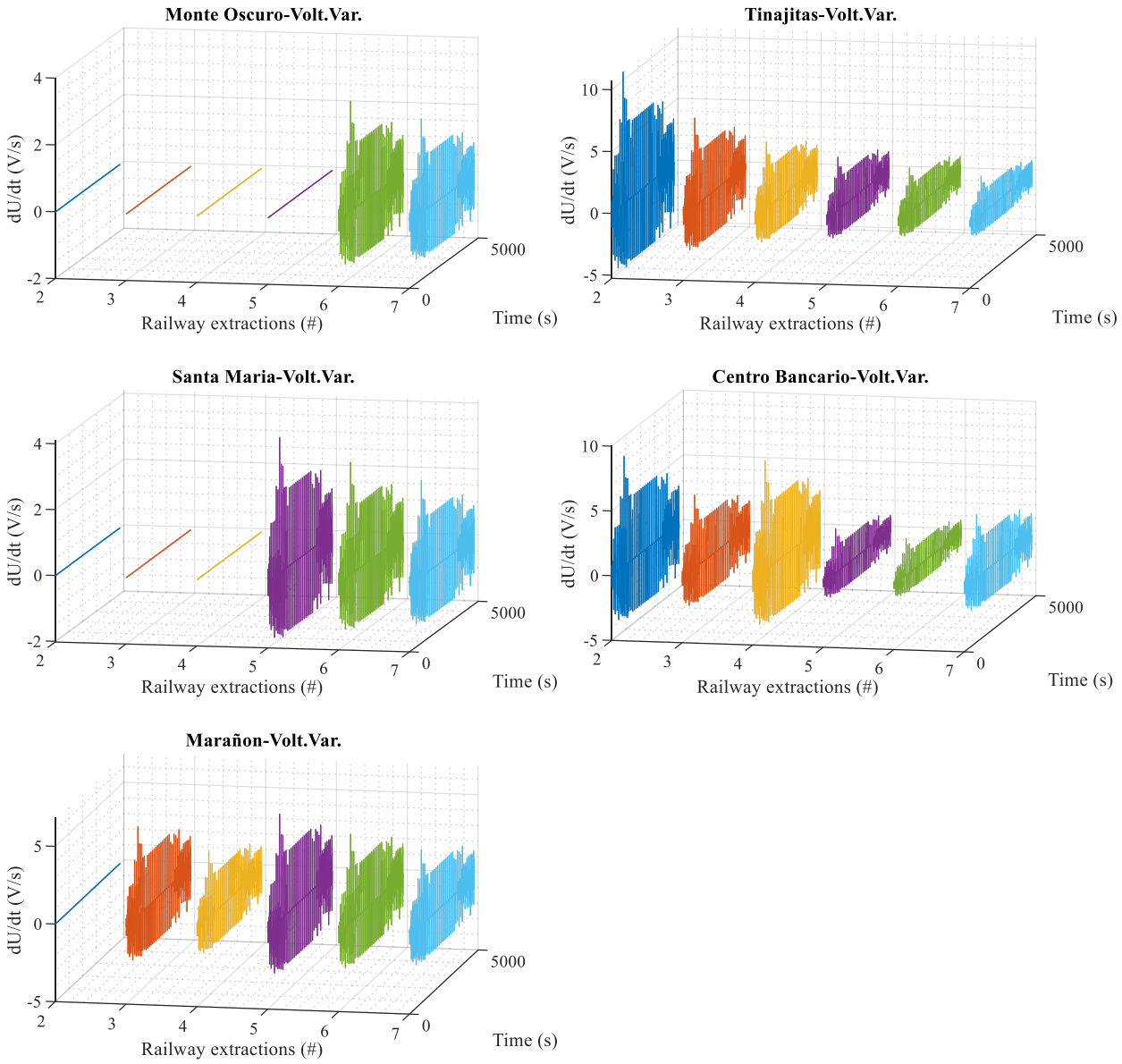


Figure 4.13: Phase voltage variation (V/s) of distribution substations under different railway extraction scenarios.

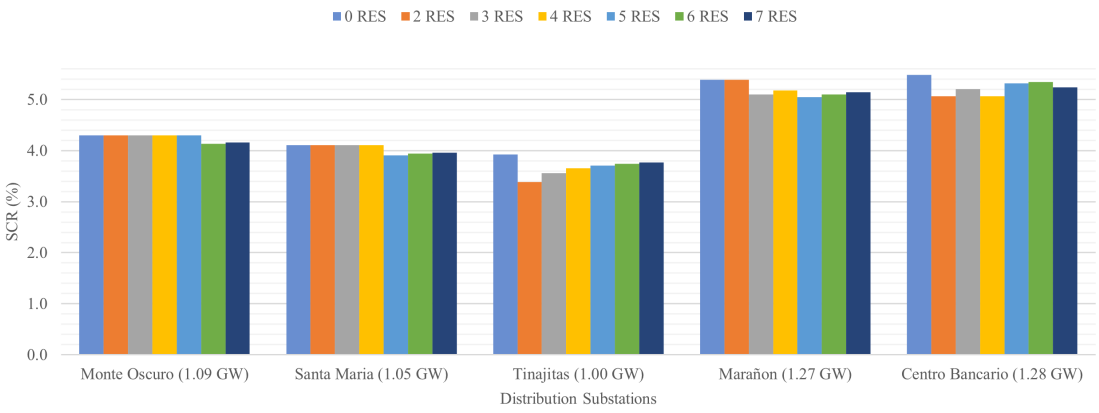


Figure 4.14: SCR per substation per railway extraction scenario (RES). The number in brackets indicates the short circuit power of each substation.

4.2 Contribution of the thermal inertia of trains to the primary frequency control

Fig. 4.15 shows the general modeling scheme. It represents the coupling between the electrical and thermal dynamics. The HG blocks are modeled by (3.11). The power system, simply represented by a single green block, is modeled by (3.13). The railway consumption blocks are modeled by (3.14)-(3.19). The load variations observed by the grid are modeled by the railway model, and, similarly, the power plants in the electric system are simulated using two 180 MW hydroelectric groups. Following several approaches [56], [54], the power system dynamics are characterized by a droop of 5%, a gate time constant of 0.2 s, a transient droop of 4%, and a water time constant of 1 s, with a base power of 180 MW. The inertia of 4.0 s is chosen as a representative value for both hydroelectric power plants, and a typical load damping factor of 1% is applied. The block labeled "FD railway consumption" encompasses subsystems essential for characterizing the HVAC system's reaction to frequency deviations. The typical response of the HVAC system depends on the thermal envelope of the railway and the HVAC system's inherent configuration. The input "Railway data" defines the requisite specifications. Furthermore, deviations in grid frequency have the potential to alter the supplied heat power by adjusting specific operational parameters of the HVAC system. The extent to which frequency deviations influence the operation may vary depending on the intricacy of the HVAC system model. Equation (3.25) simplifies this relationship, indicating that the injected air flow and its temperature are the sole parameters subject to modification.

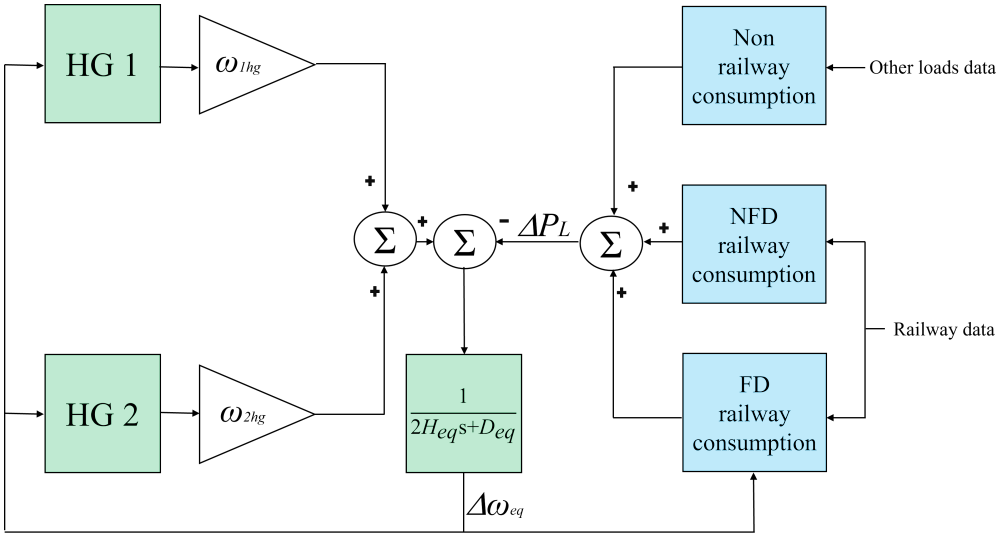


Figure 4.15: Representation of the higher layer of a primary frequency control scheme integrating hydroelectric generators (HG), non-railway consumption, non-frequency dependent (NFD) railway consumption, and frequency-dependent (FD) railway consumption.

Fig. 4.16 clarifies the interaction among (3.14)-(3.19) to define the coupling between thermal dynamics and grid frequency behavior. In this assessment, (4.3) is used to update the setpoint temperature (T_{set}). In Fig. B1 is tested the stability of the proposed method. Thus, in the presence of positive frequency deviations, likely induced by abrupt load shedding or

increased generation, the HVAC system adjusts its setpoint temperature downward, leading to an increase in power consumption. Conversely, negative frequency deviations, resulting from sudden load spikes or generation losses, prompt a reduction in power consumption by the HVAC system. To ensure an appropriate droop value, it is crucial to consider that the interaction between the railway and the power system must adhere to specific standard criteria. As outlined in the standard [120], the maximum allowable frequency deviation is set at 800 mHz, with a maximum quasi-steady state deviation of 180 mHz. Considering permissible temperature (± 2.5°C) and frequency (800 mHz) bands, a value of D_{th} =3.125°C/Hz has been selected for the droop. The droop factor, denoted as k_{th}, allows for the adjustment of droop control aggressiveness for analytical purposes. The output heat power is aimed to maintain a neutral temperature (T_N) of 26°C in trains. Additionally, a dead band of 17 mHz has been incorporated [121].

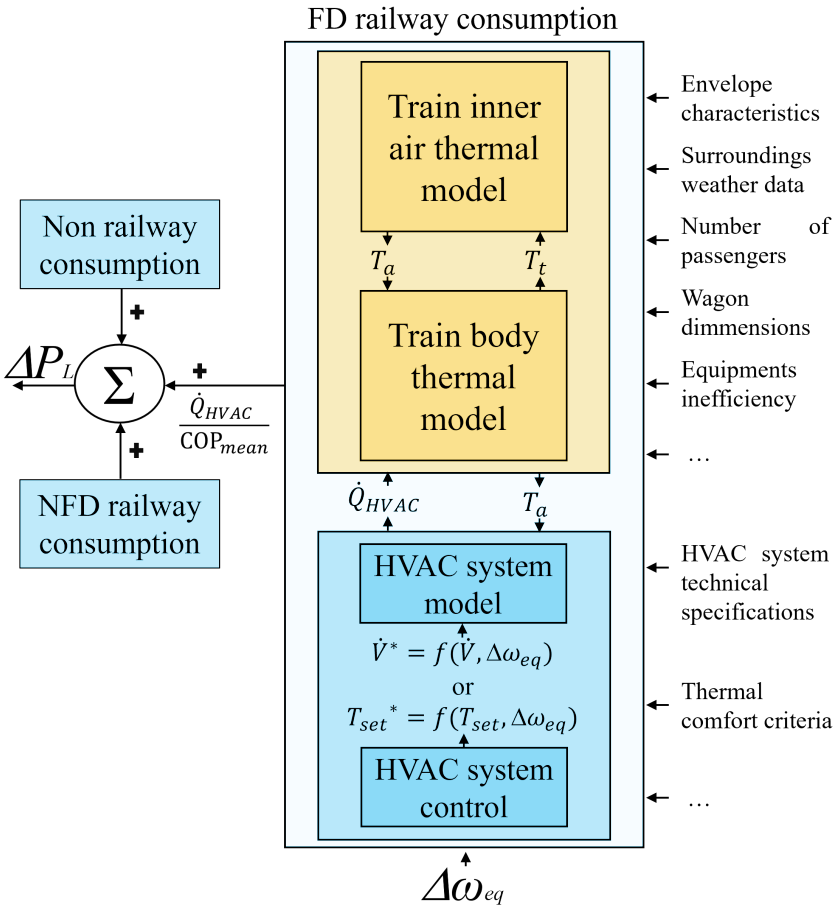


Figure 4.16: FD railway consumption model detail. * denotes those parameters modified by the frequency control.

$$T_{set} = T_N - \Delta f_{eq}\, D_{th}\, k_D \tag{4.3}$$

Concerning the thermal characteristics of the train, the study by Hofstädter et al. [68] is

utilized to explore various thermal configurations and their impact on primary frequency control. Consequently, the terms in (3.23)-(3.25) are straightforwardly derived. Moreover, the characteristics of PML1 trains and climate data are employed to determine heat gains. This involves considering factors such as train geometry, maximum Panamanian solar irradiance ($1000\ \mathrm{W}/m^2$), occupancy relative to the maximum permissible train weight, etc. The convective coefficients' variation due to train speed is neglected. The thermal comfort zone, based on a Panamanian neutral temperature of 26 °C [122], ranges from 23.5 °C to 28.5 °C. Each passenger contributes a thermal load of 116.3 W, and the HVAC system operates exclusively in cooling mode due to Panama's climate. The HVAC system, characterized as an inverter-based class, has a continuously variable motor speed. An average coefficient of performance (COP) of 3.4 is considered [67]. In (3.25), the HVAC system is modeled, but without accounting for technical limitations that might depend on the capacities of blowers, compressors, and motors, among other components. Therefore, the continuous adjustments made by the drivers to maintain comfort conditions are disregarded. Instead, a proportional-integral (PI) controller is employed to minimize temperature deviations. The output of this controller, in conjunction with the characteristics of injected air, defines the HVAC heat power (3.25).

For a highly precise model, detailed information about the railway layout, including slope, speed, and radius of curvature profiles, is essential. However, incorporating such profiles could significantly complicate the model construction without providing substantial insights into the assessment of the railway's contribution to frequency control. To streamline computational efforts, the model assumes a null slope and infinite curvature. Additionally, mechanical phenomena, such as pantograph-contact wire interactions and wheel-rails interactions, are disregarded due to their minimal impact on the study. Consequently, the speed profile becomes the primary determinant of train consumption in solving (3.19).

To address (3.19), a standard circulation of PML1 is employed, as depicted in Fig. 4.17. This circulation considers rated dwelling times and headways. The resulting run is replicated to simulate train transits across five passenger stations and three traction substations. Since the primary frequency control time frame is significantly shorter compared to train dynamics, the model focuses resources on the frequency response study. Therefore, an equivalent circulation involving only two trains per track is considered. Fig. 4.17 illustrates the speed, acceleration, and displacement profiles of trains on both tracks, highlighting a headway of 120 seconds and a dwelling time of 30 seconds. Moreover, the three traction substations are fed by the same public grid feeder, allowing the grid to observe the totalized power consumption of the railway system.

By utilizing the running profiles illustrated in Fig. 4.17, the railway characteristics previously described, and (3.14)-(3.19), the power profile depicted in Fig. 4.18 is derived. This profile reveals a railway peak power consumption of approximately 18 MW, indicating a 5% penetration of railway power compared to the installed capacity [123].

To investigate the interaction between the railway and the power system, six subcases have been defined. Some subcases examine the response to abrupt losses of loads and generation in the power system, while others assess how railways face frequency deviations caused by their consumption and thermal characteristics. The models for the railway and power system are implemented in Matlab/Simulink, utilizing a discrete mode with a time step of 16.67 ms. All

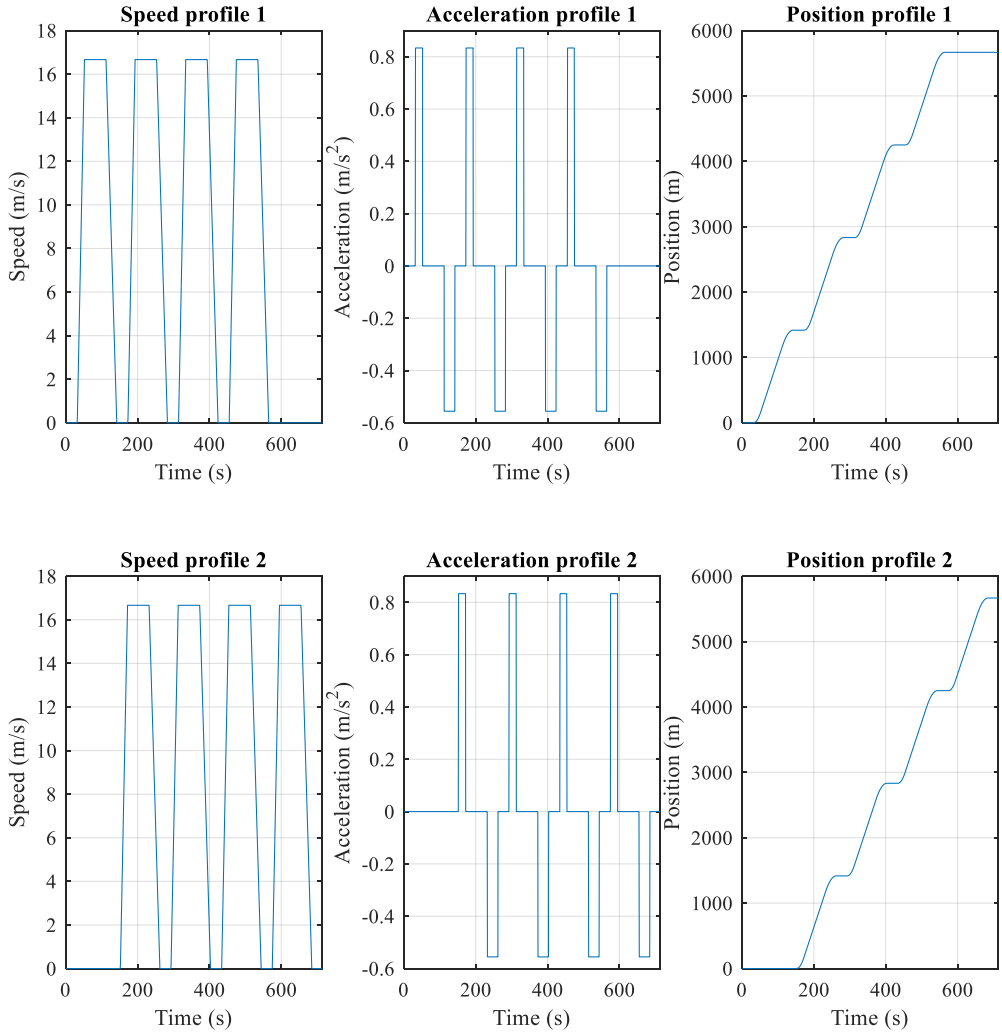


Figure 4.17: Considered profiles of speed, acceleration, and position of trains on both tracks. Upper row: profiles for the first train of each track. Lower row: profiles for the second train of each track.

results are presented in the context of a 60 Hz system, considering an outside temperature ranging from 35 °C to 38 °C to reflect critical days in the Panamanian climate [124].

In the subsequent subcases, the figures illustrate grid frequency, ROCOF, air train temperature, heat power supplied by the HVAC system, and the load observed by the grid. For the sake of modeling efficiency, the thermal behavior of each train is assumed to be identical, except in Section 4.2.6 where diverse thermal states of trains are considered. The 11^{th} thermal envelope configuration detailed in Hofstädter et al. [68] is adopted, except in Sections 4.2.4 (Response to railway disturbances: different thermal envelopes) and 4.2.5 (Response to railway disturbances: two thermal envelopes with different droop control) where multiple configurations are explored.

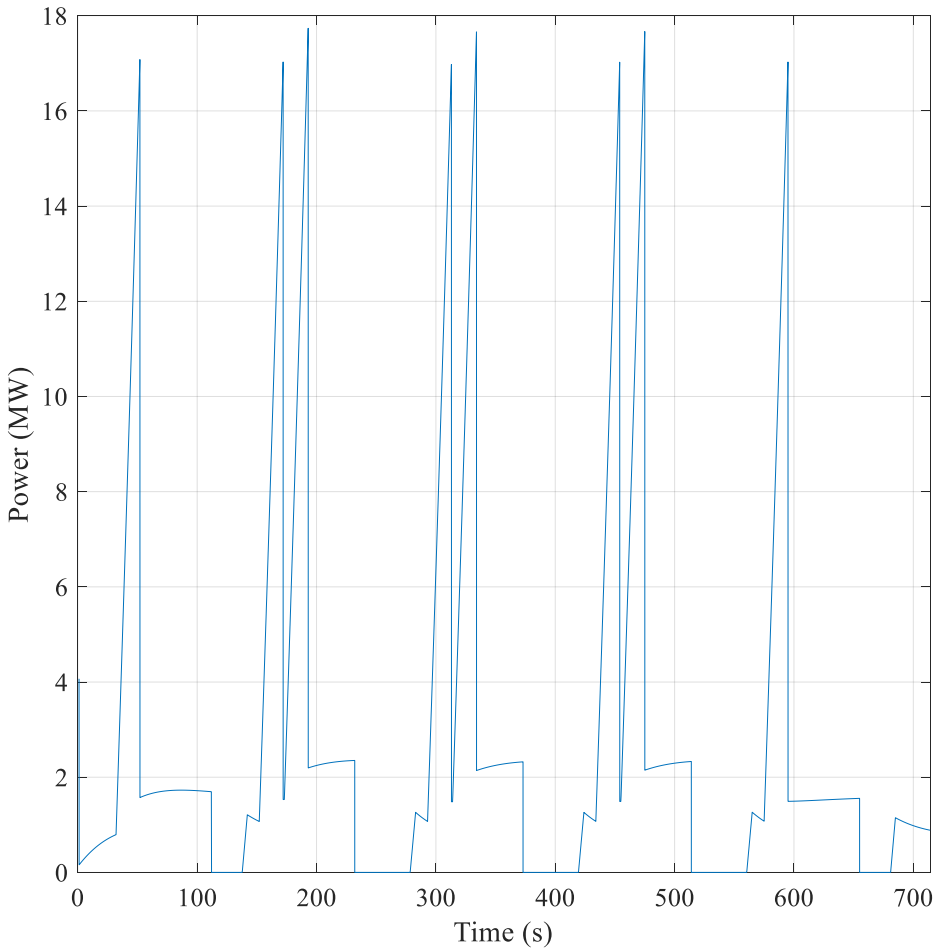


Figure 4.18: Railway consumption profile.

4.2.1 Response to power system disturbances: sudden load shedding

Fig. 4.19 depicts the responses to a 0.1 p.u. load shedding in the power system, considering different droop factors. These factors enable the evaluation of the system response ranging from 0% (indicating no contribution of trains to frequency control) to 500% of the standard droop value, D_{th}. As anticipated, higher droop values lead to faster frequency control and a reduction in maximum deviations. The droop set to 500% achieved a maximum frequency deviation reduction of 16.5 mHz compared to the 0% case, with negligible ROCOF variations among cases. These outcomes are attained by nearly tripling the heat power, resulting in temperature deviations ranging from 0.05 °C to 0.23 °C, which do not compromise passenger comfort.

As observed in Fig. 4.19, the behavior of all cases follows a similar pattern. When the load shedding event occurs, the droop control adjusts the temperature setpoint to contribute to frequency control. Once the power plant speed controller effectively manages the event, the train controllers cease their participation, and each HVAC system returns to its normal operation. However, cases with more aggressive droop control maintain a noticeable temperature

deviation that gradually corrects itself through the HVAC system's normal operation (not shown in Fig. 4.19). The role of thermal inertia is evident in the temperature behavior, where deviations are minimal despite significant variations in heat power.

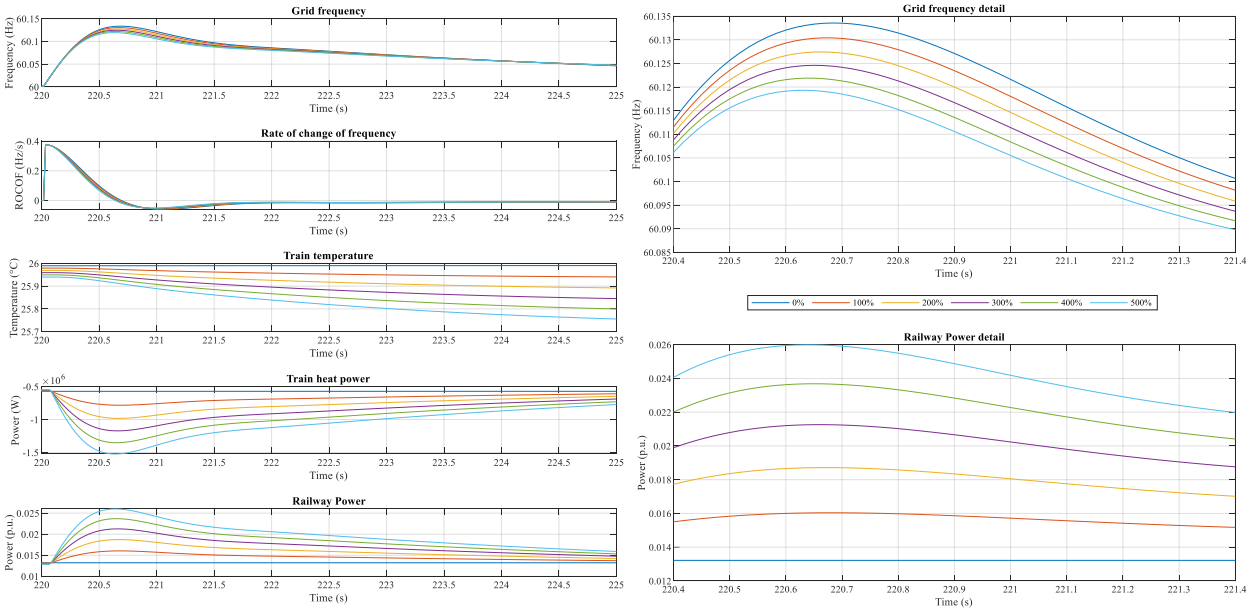


Figure 4.19: Railway and power system responses following a sudden load shedding event.

4.2.2 Response to power system disturbances: sudden generation unit loss

A power plant with an inertia constant of 2.0 s and a power capacity of 0.1 p.u. experiences a sudden disconnection at $t = 220$ s. This event leads to a reduction in grid frequency and a decrease in the capacity for frequency stabilization, given the simultaneous reduction in the equivalent system inertia. Fig. 4.20 illustrates this scenario, highlighting the advantages of employing more aggressive droop settings. The ROCOF variations across cases are minimal. The maximum frequency deviation reduction is 9.6 mHz compared to the case with 0% droop. However, the reductions in droop at 400% and 300% are also 9.6 mHz since, in these scenarios, the consumption reduction has reached the lower limit, i.e., a consumption of 0 W. Consequently, the benefits of using higher droop factors are constrained by the operational range of the HVAC system. This is evident in the "Train heat power" and "Railway power" plots, where certain curves reach a constant power zone defined by other auxiliary consumptions. As a result, the delivered heat rate is affected, and temperatures remain closely aligned. Consequently, a temperature deviation ranging between -0.05 °C and 0.12 °C is observed during the event, which is lower than in the previous case.

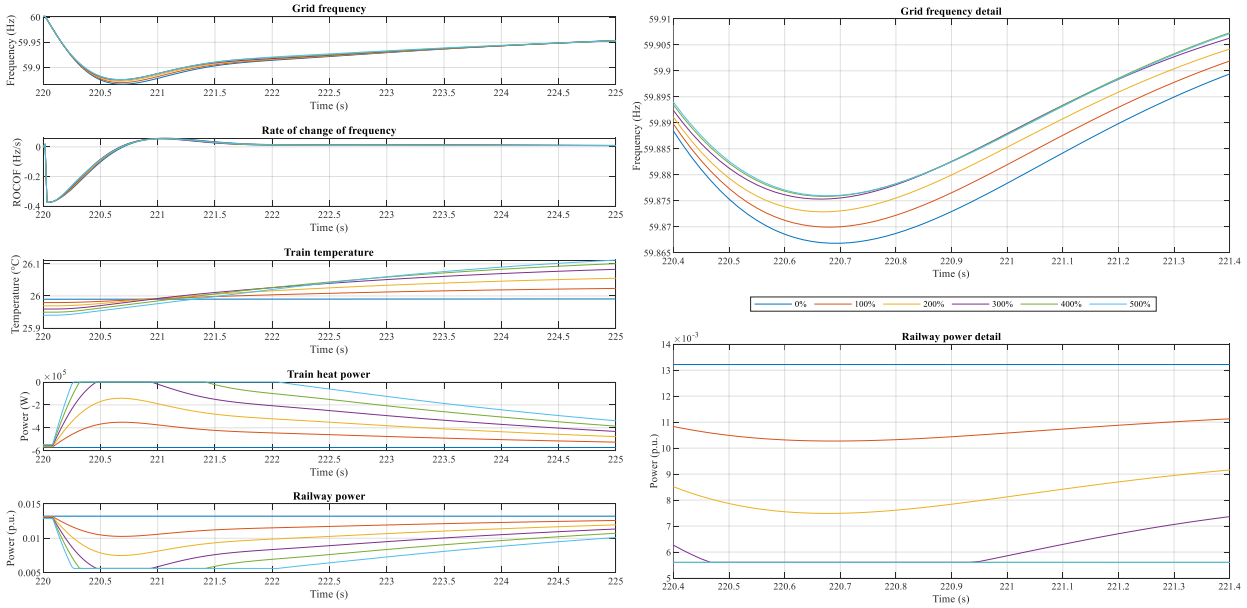


Figure 4.20: Railway and power system responses following a sudden generation loss event.

4.2.3 Response to railway disturbances

The power system can experience disturbances that affect the frequency, as outlined in Sections 4.2.1 (Response to power system disturbances: sudden load shedding) and 4.2.2 (Response to power system disturbances: sudden generation unit loss). However, the normal fluctuations in train consumption, as depicted in Fig. 4.18, also influence power system frequency. The proposed control technique plays a role in mitigating these frequency variations. For instance, the left part of Fig. 4.21 illustrates the behavior of relevant variables in the period from t = 311 s to t = 317 s. As depicted in Fig. 4.18, railway consumption experiences a sudden drop at t = 311 s, decreasing from 17 MW to 1.5 MW, followed by a ramp increase from t = 313 s onward. The right part of Fig. 4.21 provides a close-up view of the system frequency and railway power curves, revealing a maximum frequency deviation reduction of 11.8 mHz compared to the case with 0% droop. Since disturbances are smaller than those in Section 4.2.1, the reductions are correspondingly smaller. Nevertheless, higher droops still contribute to improved frequency control.

Regarding thermal behavior, it's noteworthy that the temperature deviation ranges from -0.02 °C to 0.08 °C among droop cases. This aligns with the delivered heat power, which is lower than in Section 4.2.1. In the initial 311 seconds, numerous load and frequency variations occurred, leading to a diverse thermal evolution in each case. This explains why, at the beginning of the period shown in Fig. 4.21, temperatures differ, but due to the same frequency disturbance, all temperatures evolve similarly.

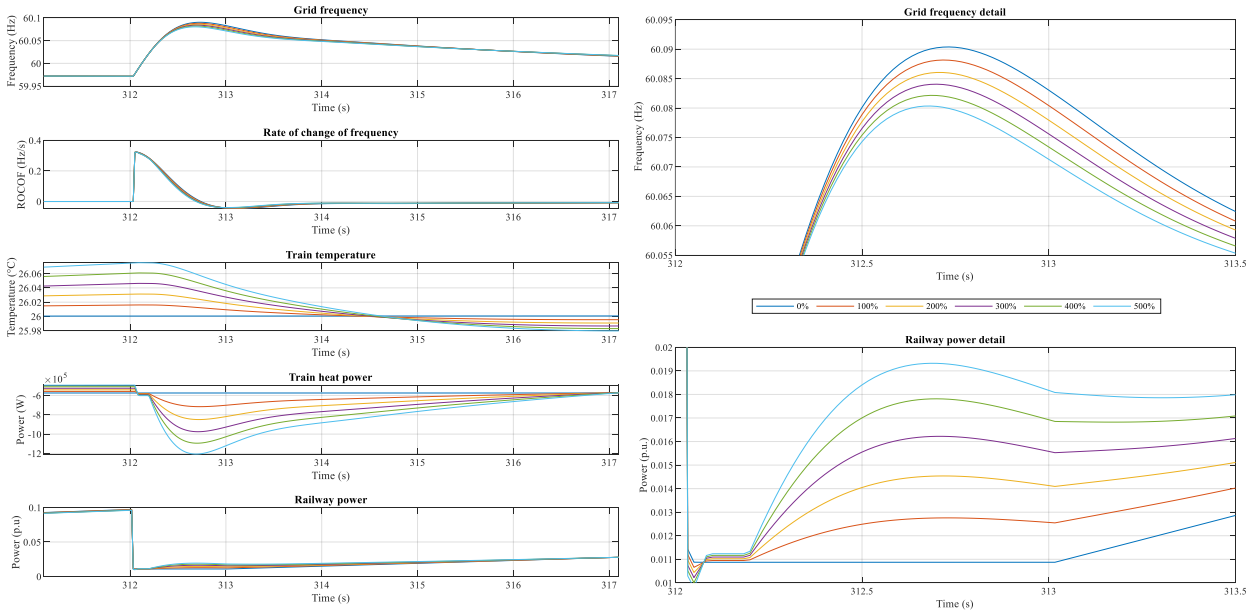


Figure 4.21: Railway and power system responses to normal railway consumption variations.

4.2.4 Response to railway disturbances: different thermal envelopes

This subsection explores the impact of the proposed frequency control strategy on passenger thermal comfort, taking into account the thermal characteristics of different trains. To achieve this, the aggressiveness of the frequency controller is set at 300%, and thirteen distinct trains are evaluated based on their thermal behaviors, as defined in Hofstädter et al. [68]. The parameters in (3.23), (3.24) detailed in [68], include values described in Table B1 (where $TM_t = C_{veh}$, $TM_a = C$, $U_{ao} = k$ and $U_{at}A_{at} = k_{veh}$). Utilizing these equations streamlines the investigation of thermal inertia's influence on grid frequency control without requiring an exhaustive description of train envelopes.

Fig. 4.22 provides a detailed view of the variables of interest during the same period as in Section 4.2.3. Notably, the variation in train thermal characteristics has minimal impact on power system frequency behavior under the same control scheme and load conditions. Conversely, significant differences are observed in the thermal behaviors of trains. Considering the configuration with the least effective frequency control, Main 1 (Ma1), a temperature difference ranging from -0.02 °C to 0.31 °C is identified in the period shown in Fig. 4.22, compared to the configuration with the most effective frequency control, Regio 2 (R2). The train heat power curves also illustrate these performance disparities.

These differences can be explained by examining the parameters in Table B1. The term U_{ao} influences the heat gains between inside and outside air temperatures, and all U_{ao} terms exhibit similar magnitudes. On the other hand, U_{at}, A_{at}, TM_t, and TM_a present noticeable differences among configurations. However, the temperature difference between the inside air and the train body is inherently small, making the influence of $U_{at}A_{at}$ relatively insignificant. The inertia of the train body varies within one order of magnitude among configurations, also not exerting a substantial impact. Consequently, Main 1 (Ma1) exhibits the least favorable

thermal behavior due to its low air and train body thermal inertia and the highest value of $U_{at}A_{at}$, leading to the highest heat gains but with limited capacity to manage them. This clarifies why Main 1 (Ma1) delivers the lowest heat power, as the HVAC system requires less energy to modify the inside air temperature due to the low thermal inertia.

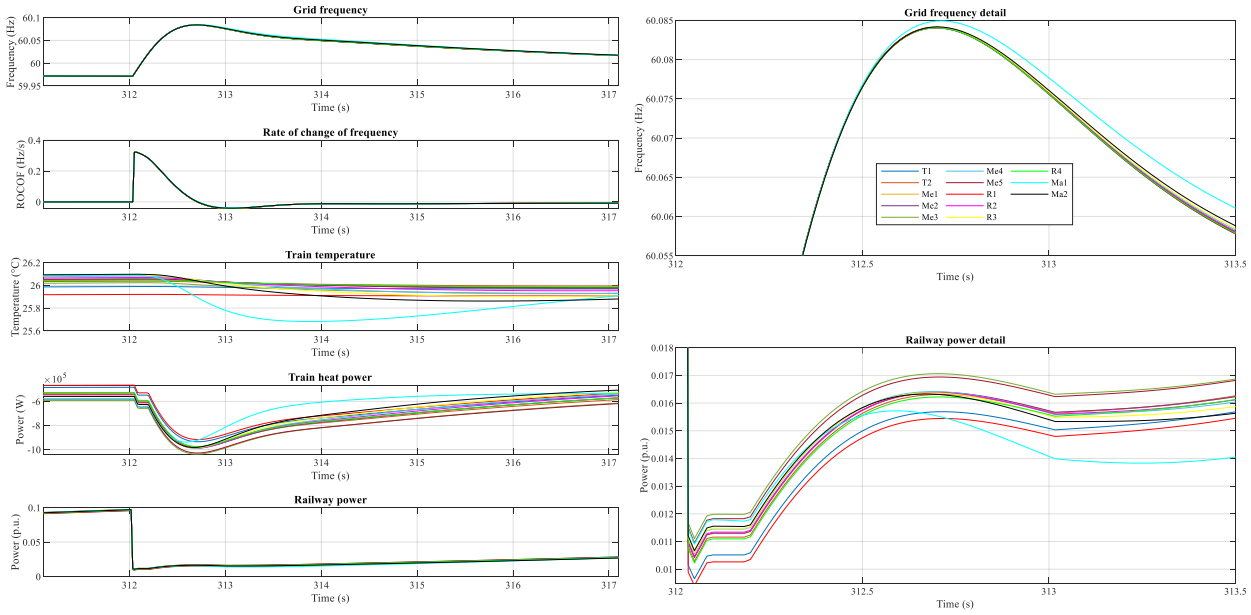


Figure 4.22: Railway and power system responses to normal railway consumption variations. Sensitivity to different thermal envelopes of trains.

In conclusion, it is affirmed that elevated thermal inertia offers increased frequency control opportunities. A higher thermal inertia results in reduced temperature fluctuations, thereby expanding the operational energy range of the HVAC system. As highlighted earlier, this approach relies on the distinction between thermal and frequency dynamics. The slower thermal dynamics enable a more substantial contribution of the railway to frequency control while staying within the confines of passenger comfort.

4.2.5 Response to railway disturbances: two thermal envelopes with different droop control

In Section 4.2.4, diverse thermal configurations were compared under the identical frequency control scheme. According to the outcomes, Regio 2 (R2) demonstrated an average and maximum additional frequency control of 1.1 mHz and 3.0 mHz, respectively, compared to Main 1 (Ma1). Both configurations were subjected to the same 300% droop. This section compares both configurations with varying droops from 300% to 600%. The objective is to observe the extent of frequency control achievable by intensifying control aggressiveness.

Fig. 4.23 illustrates the results of varying thermal characteristics and droop control configurations. Regio 2 (R2) displays minimal temperature variations among droop cases and over time. Due to its substantial thermal inertia, the different droop controls did not result in significant temperature fluctuations, thereby maintaining higher heat power delivery. Notably, in 5

seconds, the temperatures of Regio 2 (R2) decreased by a maximum of 0.22 °C, in contrast to Main 1 (Ma1), where temperatures dropped by more than 0.78 °C, demanding less heat power and electric consumption. Here, thermal inertia primarily determines the range of thermal behavior. Within each thermal configuration, similar trends regarding increased droop control are observed. The higher the droop aggressiveness, the greater the temperature and heat power variations.

In the heat power and railway power behaviors, due to thermal inertia, Regio 2 (R2) consistently maintains higher powers, with little variation among droop cases. In Main 1 (Ma1), lower powers persist after the event, and the thermal behavior of cases tends to be similar. However, during the transient period, between the first two seconds after the action of droop control, the highest thermal inertia and droop coefficients do not seem to individually define the power behavior, which also influences the frequency response. Fig. 4.23 provides a detailed view of the frequency behavior. As observed in previous sections, the highest thermal inertia with the most aggressive droop control (R2–600%) yields the greatest frequency reduction. Similarly, the lowest thermal inertia with the least aggressive droop control (Ma1–300%) results in the lowest frequency deviation reduction. However, some pairs of curves deviate from expectations: "R2-500%" vs. "Ma1-600%", "R2-400%" vs. "Ma1-500%", and "R2-300%" vs. "Ma1-400%". During the transient period, the "R2"-based cases with more aggressive droop control consistently outperform "Ma1"-based cases with less aggressive control, except for the mentioned pairs, where "Ma1"-based cases with higher droop control exhibit temporary superiority. After the transient period, toward the steady-state response, the influence of thermal inertia on curves becomes predominant. This observed behavior suggests that increasing control aggressiveness can transiently compensate for the lack of thermal inertia.

The results demonstrate that an envelope with 8.9 times the thermal inertia, under the same control scheme, can provide an additional maximum reduction of 5.2 mHz in frequency deviations. Furthermore, when extreme cases are compared, "R2-600%" vs. "Ma1-300%", an average and maximum frequency deviation reduction of 2.4 mHz and 8.2 mHz are attained, respectively. This signifies an enhancement in behaviors compared to those in Section 4.2.4.

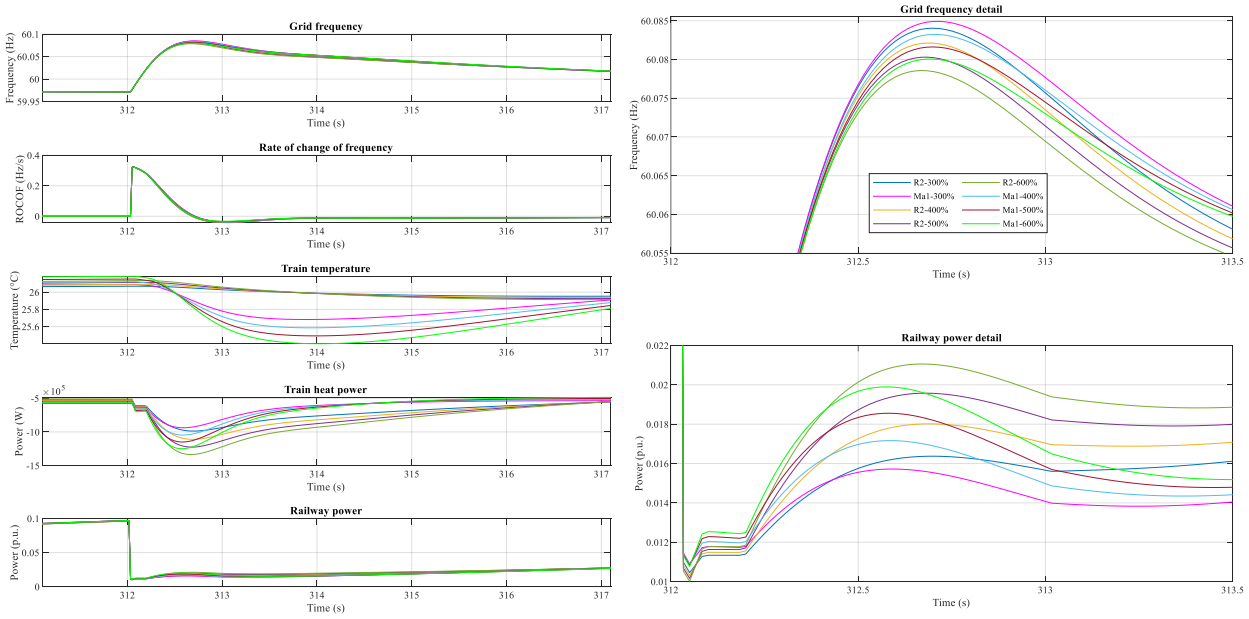


Figure 4.23: Railway and power system responses to normal railway consumption variations. Combined sensitivity to thermal configurations and droops.

4.2.6 Response to power system disturbances: sudden load shedding and individual train thermal modeling

All preceding subsections assumed that all trains shared the same thermal status. This simplification is rational for model simplification to concentrate on grid frequency control. However, it is intriguing to observe how outcomes fluctuate when a higher complexity in the thermal modeling of trains is applied. In this scenario, instead of presuming a representative train thermal behavior to trigger frequency control in all trains, the individual thermal behavior of each train dictates its contribution.

To differentiate the thermal behavior of each train, an update on the solar radiation variation when trains are stationed at passenger stations is considered. Additionally, the trains on each track transport a different number of passengers. Nevertheless, all trains maintain the same thermal configuration. By incorporating headway, dwelling time, and new considerations, a distinct net heat gain is obtained for each train. Fig. 4.24 exhibits the outcomes of individual thermal modeling without the implementation of droop control. As observed, throughout the entire circulation, the temperature remains nearly constant, with a maximum deviation of 0.55 °C. Within the individual temperatures of trains, a deviation band of 0.8 °C to 0.6 °C is identified. Since the temperature behavior of each train is nearly identical, the resulting average temperature curve exhibits minimal differences. The heat power generated by each train illustrates how the thermal requirements of trains vary based on their location (radiation variation) and their track (variation in the number of passengers). Nonetheless, due to the substantial similarity between individual and average temperature responses, it is acceptable to consider the variations in heat power almost negligible.

The same analysis conducted in Section 4.2.1 is replicated, and the outcomes are presented

in Fig. 4.25. In this case, each HVAC system delivers distinct power variations to support frequency control, but the heat power plot represents an average curve. The noteworthy resemblances between Fig. 4.19 and Fig. 4.25 are apparent, as both exhibit a maximum reduction of 16.5 mHz in grid frequency when comparing their responses with 500% droop against 0% droop. Concerning frequency-based events, individual train thermal modeling does not contribute significantly more information.

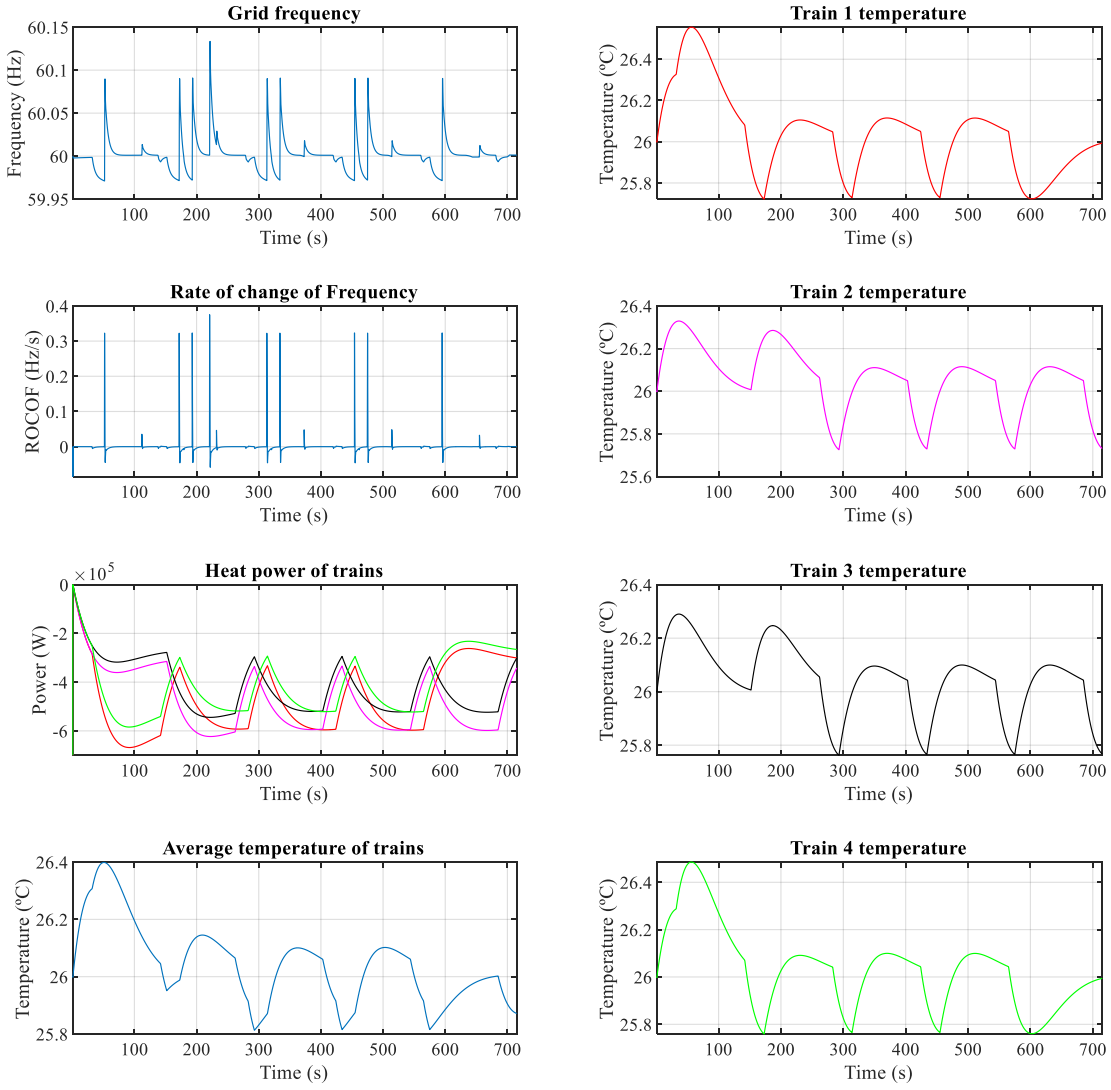


Figure 4.24: Railway and power system responses following a sudden load shedding event. Individual train thermal behavior. Null droop control.

Concerning thermal dynamics, a maximum temperature disparity of 0.2334 °C is identified between different droop cases (Fig. 4.25). In Section 4.2.1, the variation was 0.2352 °C, indicating a negligible distinction of 0.0018 °C between the "representative train-based control" and the "individual train-based control." This suggests that designating a single train as the thermal reference for initiating control is a valid approximation for this type of analysis. Furthermore, for real-time applications involving practical trains, it may also be reasonable

to gauge the thermal condition of one train and employ it to initiate the frequency controls for all trains. However, for an in-depth assessment of thermal comfort in trains, simplifying thermal modeling is not recommended.

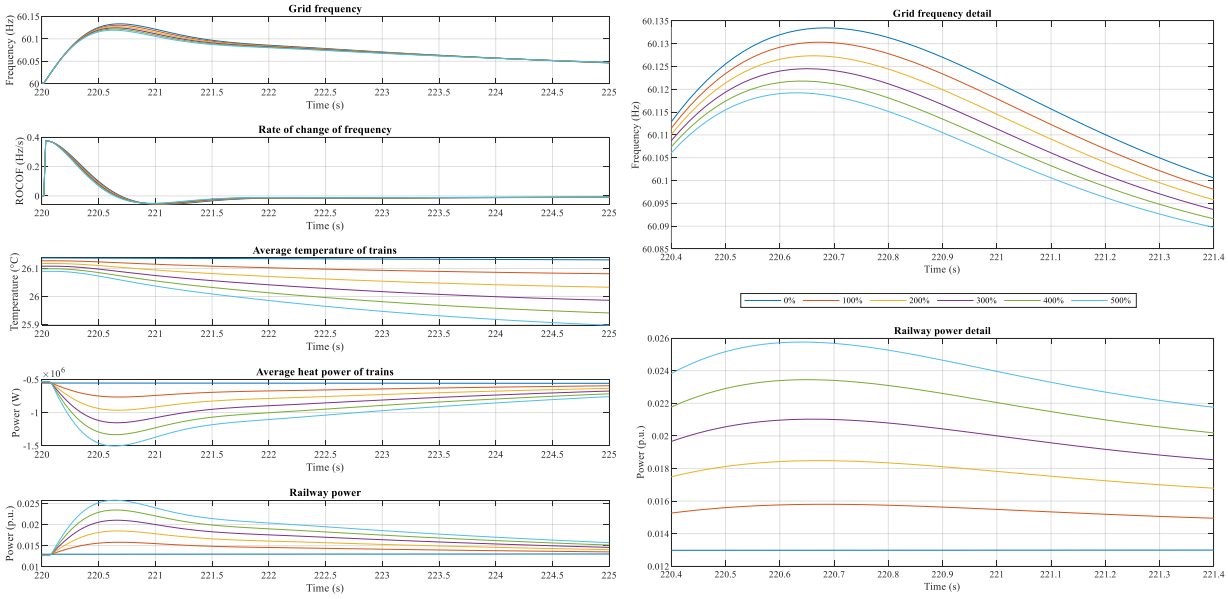


Figure 4.25: Railway and power system responses following a sudden load shedding event. Average train thermal behavior.

4.2.7 Conclusions

The findings illustrate the potential contribution to primary frequency control during external events, including sudden load shedding, generation loss, and power fluctuations resulting from normal railway consumption. The implementation of a droop control system, based on the interplay between grid frequency and the thermal comfort band, showcases the HVAC systems' role in supporting grid frequency without compromising thermal comfort. Across all scenarios, simulation results consistently demonstrated minimal temperature variation during frequency support. The exploration of thermal inertia and droop control aggressiveness in Section 4.2.6 confirms that higher thermal inertias can enhance frequency control, and the robustness of droop control further amplifies these capabilities. Consequently, it is reasonable to assert that this approach holds significant potential for contributing to primary frequency control within the grid.

The conclusions drawn from Section 4.2.6 suggest that employing the thermal behavior of a single train, instead of computing each train's thermal status, yields very similar results in terms of frequency dynamics. However, for studies focused on thermal comfort, the temperature differences between models may be relevant. Thus, while simplifying the multi-train thermal modeling is permissible for frequency control studies, it may not be recommended for thermal comfort assessments.

It is noteworthy that the relative amplitudes of events, railway consumption, and system inertia play a crucial role in defining the railway's contribution to frequency control. Larger

railway systems are expected to offer a more significant contribution. Moreover, with the ongoing integration of more loads and generators into future power systems, each piece of equipment may not contribute significantly, but the aggregate impact on frequency control is expected to be substantial. Therefore, the presented approach is anticipated to play a role in achieving this objective.

The results have successfully demonstrated the technical feasibility of utilizing the thermal inertia of trains to contribute to power system frequency control without disrupting scheduling. However, it is essential to acknowledge the various model simplifications made. The power system model could incorporate more realistic dynamics in energy supply/consumption, while the railway system model, both electrical and thermal, could encompass additional factors such as power converter topologies, HVAC thermal circuit restrictions, occupants' behavior, and multidimensional wagon thermal models, among others. This establishes a foundation for more in-depth analyses, incorporating detailed technical aspects and economic considerations.

These results are published in [44].

4.3 Use of the thermal inertia of trains for providing virtual inertia

As noticed in Section 2.2, the provision of virtual inertia from loads is not widely studied, and even less in railway systems. It is proposed for the first time to provide virtual inertia from railways using auxiliary consumptions, such as HVAC systems. For this contribution proposal, an alternative way to define the injected thermal power is introduced in (4.4). It relies upon the mathematical equivalence of modifying any term in (3.25). This is, adjusting the injected air flow ($\dot{V}$) or the setpoint temperature can represent the same thermal output power under certain setups. Then, an additional output power term can be added ($\dot{Q}^{added}_{HVAC}$) to the heat power setpoint to be managed by the HVAC systems. As shown in [125]–[127] many parameters such as pressure, temperature, and flow, among others, can be adjusted by controlling the speed of the HVAC system motors.

$$\begin{aligned}\rho\, C_p\, \dot{V}\,(T_{set} - T_a) &= \rho\, C_p\, \dot{V}\,(\Delta T + \Delta T(f_{eq})) = \rho\, C_p\, \Delta T\,(\dot{V} + \dot{V}(f_{eq})) \\ &= \frac{P_{HVAC} + P_{HVAC}(f_{eq})}{COP_{mean}} \quad = \dot{Q}_{HVAC} + \dot{Q}^{added}_{HVAC}\end{aligned} \tag{4.4}$$

Hence, in this study, a reduced model of the HVAC system and its control mechanism is employed, capturing the dynamics of its components in a consolidated manner. Certain works delve into the specifics of each element involved in the HVAC thermodynamic cycle [127]. However, such a granular level of detail is unnecessary when aiming to estimate the HVAC system's contribution to frequency control tasks. Naturally, if the focus were on understanding the thermal behavior of each element, more intricate investigations could be conducted by examining the disaggregated dynamics of individual components, as demonstrated in [128]. This approach could provide deeper insights and potentially yield diverse outcomes in terms of HVAC system frequency control.

The additional power term ($\dot{Q}^{added}_{HVAC}$) undergoes proportional variations in response to both frequency deviations and their derivatives, serving the purposes of primary control and virtual inertia [8], [31], [32], [129], [130]. (4.5) outlines the calculation of the added power, where D_p is a parameter correlating the variation in HVAC system power to frequency deviations, D_v is a parameter correlating the HVAC system power variation to the derivative of frequency deviations, and K_p and K_v are coefficients that enable adjustment of the sensitivity of primary control and virtual inertia, respectively. Mathematically, K_p and K_v can also be employed to impose limits on the contribution of each control, facilitating the assessment of their combined effects.

$$\dot{Q}^{added}_{HVAC} = \Delta f\, D_p\, K_p + \frac{d\Delta f}{dt}\, D_v\, K_v \tag{4.5}$$

It is essential to note that (4.5) applies to HVAC systems operating in both cooling and heating modes. In the case of a positive frequency deviation (frequency increase), the control signals an elevation in thermal power, while a negative deviation calls for a reduction. In heating mode, this implies an increase or decrease in heat injection accordingly. Similarly,

cooling mode signifies adjusting the injection of cold air coherently. The injection of hot or cold air is directly associated with electrical power consumption, a magnitude that impacts frequency deviations proportionally.

To illustrate the possibilities of contribution, several case studies are developed. Again, the characteristics of PML1 are considered. Some new data, compared to Section 4.2, are used (Table C1). Also, more detailed information about de ventilation and air conditioning (VAC) systems of PML1 is used. Each train comprises four tractor wagons and one non-tractor wagon. The non-tractor wagon is equipped with two electronic converters primarily responsible for driving the VAC units installed in the train. These two converters collectively have an estimated capacity of 484 kW, with a minimum load threshold set at 96.8 kW. Each wagon is outfitted with two VAC units, each possessing a cooling capacity of 38 kW. Consequently, the overall cooling capacity of the entire train amounts to 380 kW.

To compute the values of D_p and D_v in (4.5), an iterative approach is employed. The process begins by considering the maximum power capacity of the VAC system and the specified frequency limits. Initial values are then adjusted iteratively until reaching a point where the thermal capacity of the VAC system is surpassed. Subsequently, the aggressiveness of each term, whether considered individually or collectively, is fine-tuned using k_p and k_v to examine the control's response. It's important to note that, in this case study, the initial values of these terms were determined as follows: $D_p = \dot{Q}_{HVAC_{max}}/\Delta f_{max}$ and $D_v = \dot{Q}_{HVAC_{max}}/ROCOF_{max}$, where $\dot{Q}_{HVAC_{max}}$ represents the maximum heat power attainable, and $ROCOF_{max}$ is the maximum allowable ROCOF. While optimization algorithms can also be applied to find optimal values based on a specific objective [19], such an approach is not strictly necessary for evaluating the train HVAC system's contribution to frequency control tasks.

As per the specified regulations [120], the permissible maximum frequency deviation stands at ± 0.8 Hz. Additionally, the absolute ROCOF typically falls within the range of 0.1 Hz/s to 1.0 Hz/s [131]. In alignment with the findings in Section 4.2, a more restrictive limit of ± 0.1 Hz/s is chosen for this study. These established limits, coupled with the known maximum thermal power of 380 kW, determine the values of D_p and D_v. Initially set at 475 kW/Hz and 3800 kWs/Hz, iterative adjustments reveal that the first values allowing for the maximum thermal power are 2020 kW/Hz and 551 kWs/Hz.

Two general scenarios are examined: sudden loss of load and sudden loss of generation. The first investigates the loss of an equivalent load amounting to 0.1 p.u. The latter explores the loss of a generation plant equating to 0.1 p.u. with an inertia constant of 2.0 s. Each general scenario encompasses three potential cases: primary control, virtual inertia, and the combination of primary control and virtual inertia. In the first two, K_p and K_v undergo variations from 0% to 100% in increments of 20%. In the latter case, the two controls are combined in the following ratios: (K_p, K_v) = (0.8, 0.2); (0.6, 0.4); (0.4, 0.6); (0.2, 0.8); (1, 1), with each control's contribution restricted to half the remaining capacity of the VAC system after generating the thermal power setpoint exclusively based on (3.25).

4.3.1 Case study 1. Non-railway consumption. Response to a sudden load shedding

A generic case study is presented, excluding the disturbance caused by the railway system on the grid. Essentially, the same model is employed, but without factoring in railway consumption. A load with the equivalent capacity of the two electronic converters of the PML1 trains is considered, operating at half capacity and capable of providing primary frequency control and virtual inertia through (4.5). As in the preceding section, the determination of terms D_p and D_v takes precedence, calculated based on the available power range (0.0012 p.u.) and the specified frequency and rate-of-change limits. Subsequently, diverse values of K_p and K_v are taken into account for performance evaluation.

Figures 4.26 and 4.27 illustrate the progression of frequency, ROCOF, and load power following a sudden load shedding of 0.1 p.u. Figure 4.26 shows the outcomes with exclusive reliance on primary frequency control, while Fig. 4.27 explores the scenario with exclusive virtual inertia. On one hand, the results of primary control exhibit similarities with those found in Section 4.2 and [40], indicating that higher gains lead to increased power consumption from the controlled load, thereby improving frequency control. Additionally, the ROCOF remains relatively stable. On the other hand, virtual inertia is configured to diminish the ROCOF, consequently influencing frequency deviations. It's important to note that since the controlled load's power involved in the control constitutes only a small fraction (0.26%) of the entire electric system's power, the impact of the proposed control might not be easily discerned on the scale used in Figs. 4.26 and 4.27. Nevertheless, this scale provides an overview of the overall behavior, allowing the identification of maximum frequency deviation, particularly around $t = 220.7$ s.

For a more detailed analysis, Fig. 4.28 and Fig. 4.29 utilize the same data as Figs. 4.26 and 4.27 but present the deviations from the reference case. In other words, the values of the case without frequency control have been subtracted from each case with frequency control. Negative values in Fig. 4.28 and Fig. 4.29 indicate reductions, while positive values signify increases. The horizontal blue line represents the baseline case for reference purposes. This visualization aids in observing the effects of both controls. Primary frequency control (Fig. 4.28) primarily influences frequency deviations and the magnitude of load power variations. Conversely, virtual inertia (Fig. 4.29) mainly affects ROCOF and fluctuations in load power. Primary frequency control yields more extended reductions in frequency (first row) and increases in power (third row) compared to virtual inertia. Virtual inertia accelerates the slowing of frequency variation faster than primary frequency control (second row) but requires greater power fluctuation than primary control (third row).

It is important to note that, in certain instances, positive differences in frequency deviations and variations, signifying a deterioration in the load shedding scenario considered, are observed. However, the occurrence of negative differences, indicating an improvement in this scenario, takes place at crucial moments: around the peak frequency deviation (approximately at $t = 220.7$ s) in the case of primary frequency control and just after the disturbance in the case of virtual inertia. Additionally, higher aggressiveness enhances performance in both cases, but it may lead to a faster saturation of VAC systems, aside from temporarily impairing frequency

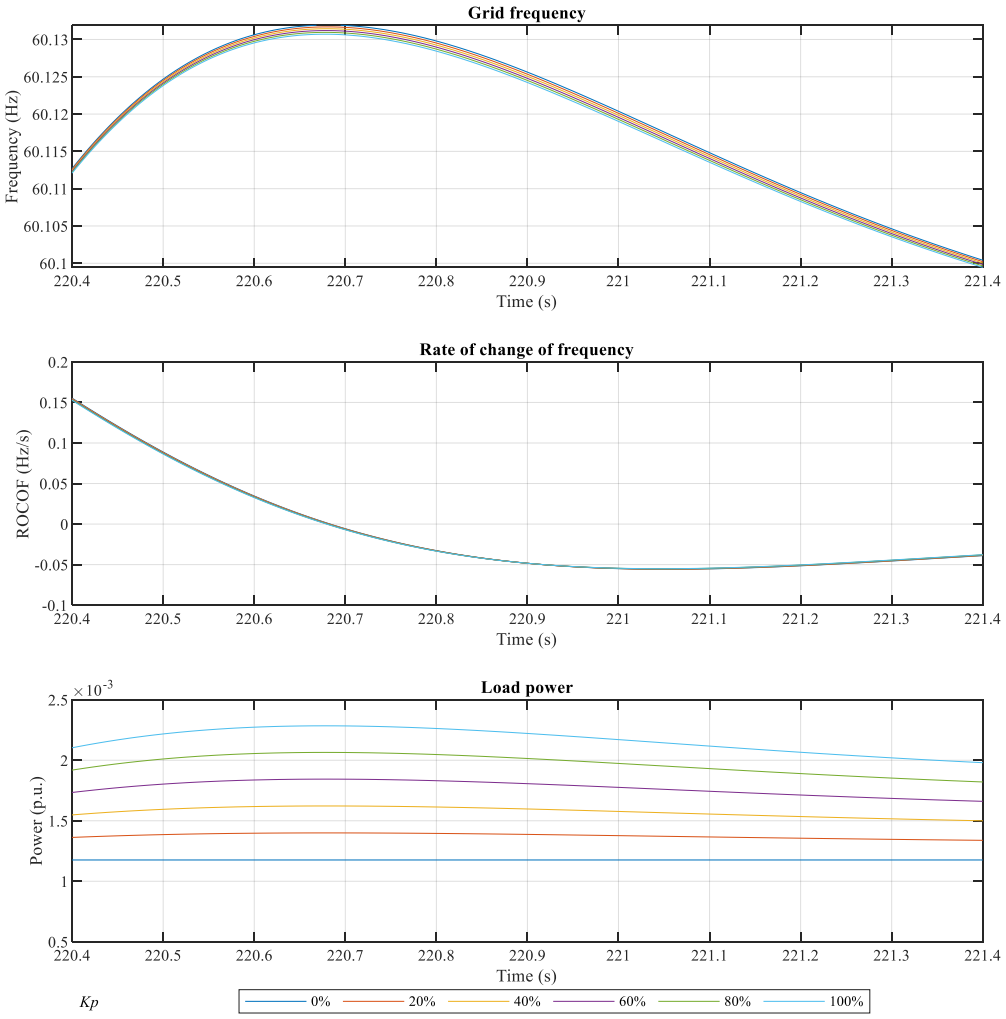


Figure 4.26: Load frequency control responses following a load shedding under different control aggressivity. Primary frequency control.

performance at specific instances.

Fig. 4.30 depicts the outcomes of combining both controls, where each curve corresponds to a pair (K_p, K_v). Similarly, controls with more aggressive virtual inertia tend to saturate and decay more rapidly. Those with high primary control maintain greater contributions once the maximum frequency deviation has passed, unlike those with higher virtual inertia. In summary, a higher weighting of primary frequency control enhances the behavior of frequency deviations, while a higher weighting of virtual inertia improves response speed, consequently reducing the downtime of the VAC system. However, excessive participation in virtual inertia control may harm frequency, saturate the VAC system, and necessitate drastic changes in its operating point.

Beyond the preceding qualitative analysis, Table 4.2 encompasses certain statistics aimed at assessing the performance of controls during the investigated period (from $t = 220$ s to $t = 235$ s): maximum value and root mean square (RMS) of frequency deviation, maximum and

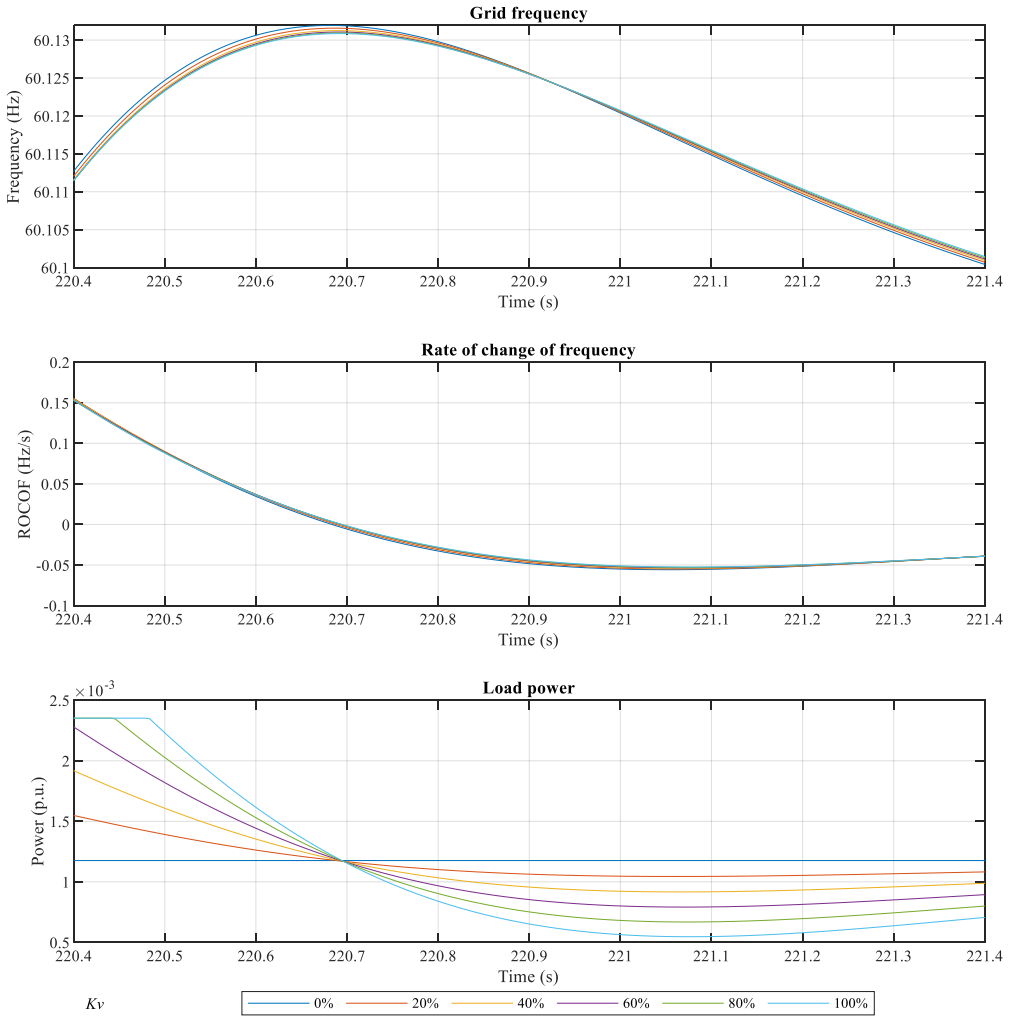


Figure 4.27: Load frequency control responses following a load shedding under different control aggressivity. Virtual inertia.

minimum values and RMS of ROCOF, maximum and minimum values of power and power derivative of the load, and the energy involved. Several conclusions can be readily drawn: the greater the contribution of the controls, the lower the maximum frequency deviations; the minimum frequency deviation remains identical across all cases due to the event's inherent characteristics; the maximum ROCOF is virtually unchanged, given that the system's inertia has not altered significantly and considering the minimal actuation delay of controllers; and higher control gains necessitate more significant energy and power changes.

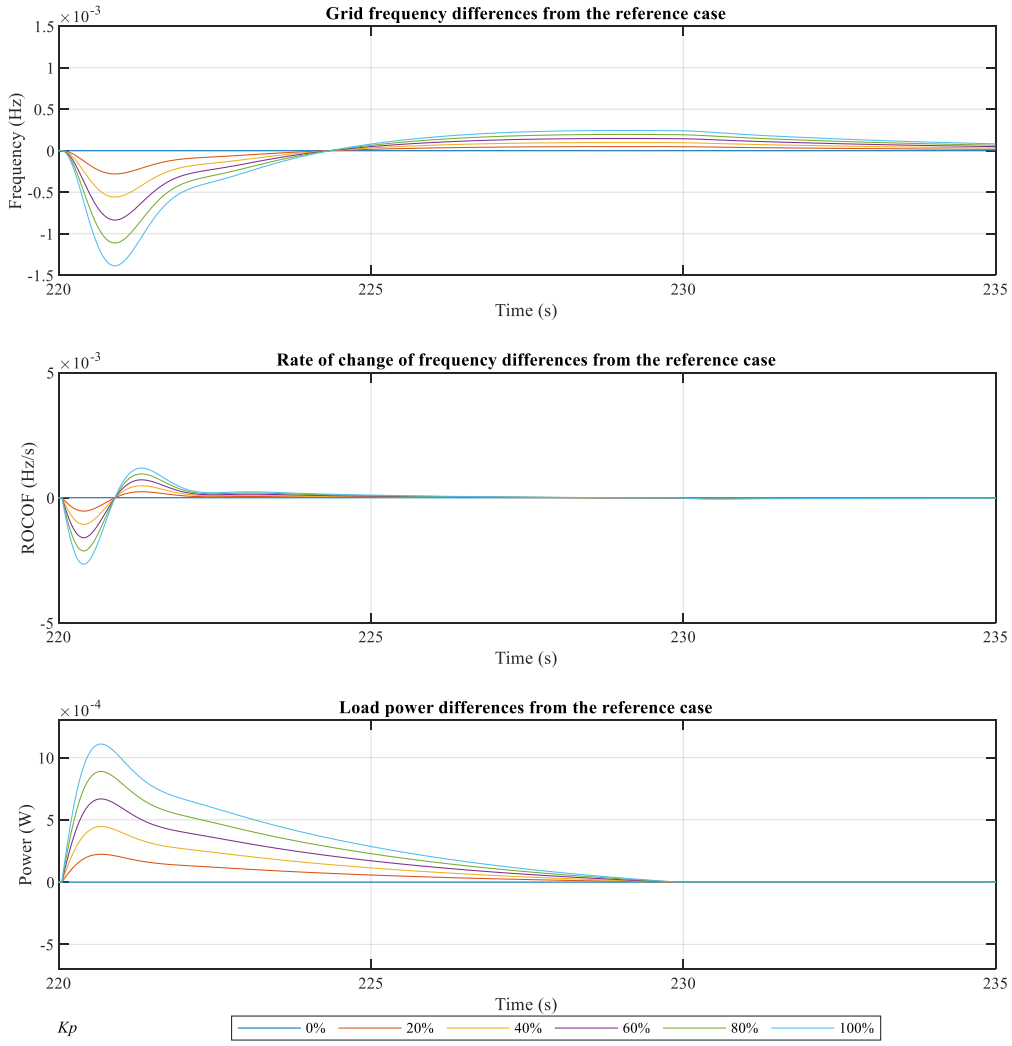


Figure 4.28: Load frequency control responses following a load shedding under different control aggressivity. The reference case (without frequency control) has been subtracted from each case. Primary frequency control.

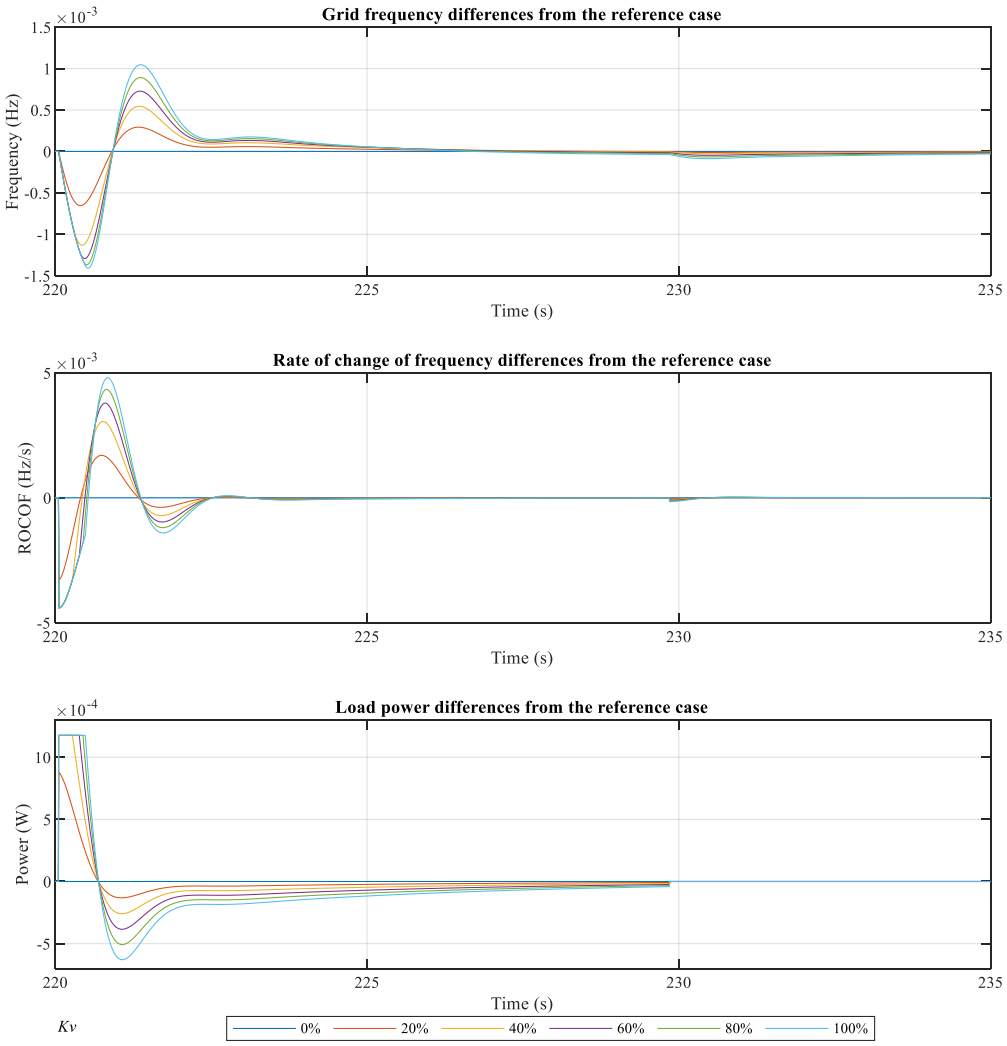


Figure 4.29: Load frequency control responses following a load shedding under different control aggressivity. The reference case (without frequency control) has been subtracted from each case. Virtual inertia.

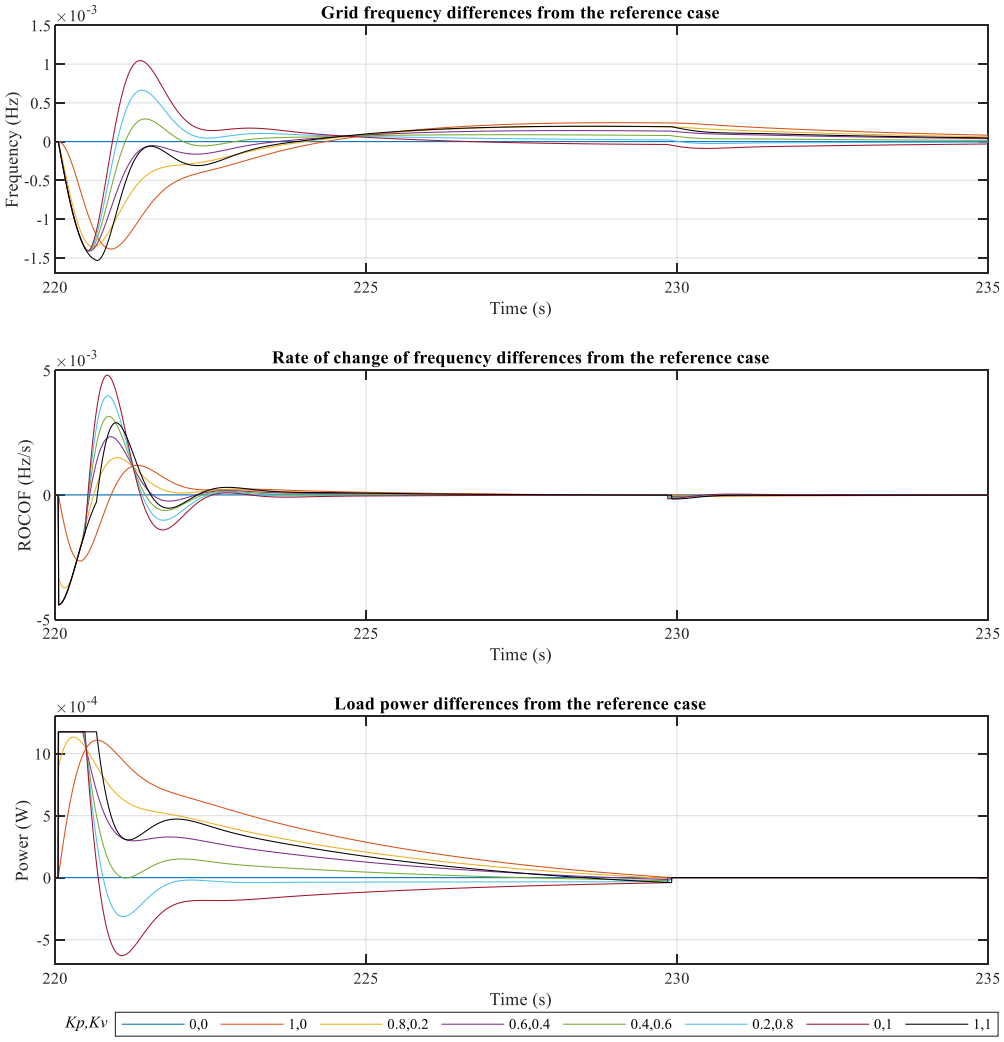


Figure 4.30: Combination of primary frequency control and virtual inertia. The reference case (without frequency control) has been subtracted from each case.

Table 4.2: Statistical analysis following a load shedding event. Frequency control in the case of non-railway consumption.

Cases	Gains (K_p,K_v)	Freq. deviation (mHz)		ROCOF (mHz/s)			Load				
		Max.	RMS	Max.	Min.	RMS	Power extrema (p.u.)		Energy (p.u. s)	Power derivative extrema (p.u.)	
							Max.	Min.		Max.	Min.
Reference (Ref.)	0,0	131.9358	51.3609	375	-55.7522	51.0517	0.001176	0.001176	0.017644	0	0
Primary control (PC)	0.2,0	131.6884	51.3119	375	-55.9899	50.9899	0.001400	0.001759	0.018361	0.0007	-0.0001
	0.4,0	131.4421	51.2631	375	-55.4674	50.9283	0.001622	0.001176	0.019077	0.0014	-0.0002
	0.6,0	131.1965	51.2145	375	-55.3257	50.8671	0.001844	0.001176	0.019793	0.0022	-0.0003
	0.8,0	130.9517	51.1661	375	-55.1848	50.8060	0.002065	0.001176	0.020507	0.0029	-0.0004
	1.0,0	130.7077	51.1179	375	-55.0456	50.7453	0.002285	0.001176	0.021200	0.0036	-0.0005
Virtual inertia (VI)	0,0.2	131.5725	51.3555	375	-54.8368	50.7788	0.002055	0.001044	0.017644	0.1175	-0.0018
	0,0.4	131.2533	51.3539	375	-54.0044	50.5895	0.002352	0.000917	0.017571	0.1866	-0.0035
	0,0.6	131.0644	51.3618	375	-53.3792	50.5321	0.002352	0.000792	0.017374	0.2792	-0.0050
	0,0.8	130.9440	51.3732	375	-52.8714	50.5034	0.002352	0.000688	0.017143	0.2822	-0.0061
	0,1.0	130.8609	51.3864	375	-52.4304	50.4863	0.002352	0.000547	0.016896	0.2822	-0.0071
Combined control (CC)	0.8,0.2	130.5936	51.1608	375	-54.2808	50.5357	0.002309	0.001168	0.020508	0.1203	-0.0009
	0.6,0.4	130.6276	51.2148	375	-53.7569	50.4922	0.002352	0.001160	0.019638	0.1875	-0.0024
	0.4,0.6	130.7033	51.2717	375	-53.3050	50.4893	0.002352	0.001151	0.018727	0.2798	-0.0040
	0.2,0.8	130.7810	51.3289	375	-52.8637	50.4870	0.002352	0.000861	0.017812	0.2822	-0.0056
	1.0,1.0	130.4023	51.1794	375	-52.9846	50.4627	0.002352	0.001135	0.020127	0.2822	-0.0042

Fig. 4.31 compares some of the most relevant characteristics. It is evident that primary control results in lower frequency deviations, while virtual inertia leads to reduced frequency variations. However, primary control entails an increase in net energy consumption, contrary to virtual inertia, which enables a reduction in net consumption. The combination allows the reaping of the benefits of both controls without escalating energy consumption or necessitating abrupt power variations consistently. Based on the results, within the considered scenario, it appears that a blend of virtual inertia with a high emphasis on primary frequency control (K_p, K_v = 0.8,0.2) can deliver the third-lowest frequency RMS and the second-lowest maximum frequency deviation, albeit at nearly 17% higher energy consumption than the reference case.

The following sections analyze the railway consumption profile as illustrated in Section 4.2. The metrics are computed over a multi-train circulation period, during which the power system experiences either a sudden load shedding or a generation loss. Throughout the trains' operation, VAC systems are authorized to participate in frequency control activities using the aforementioned methods.

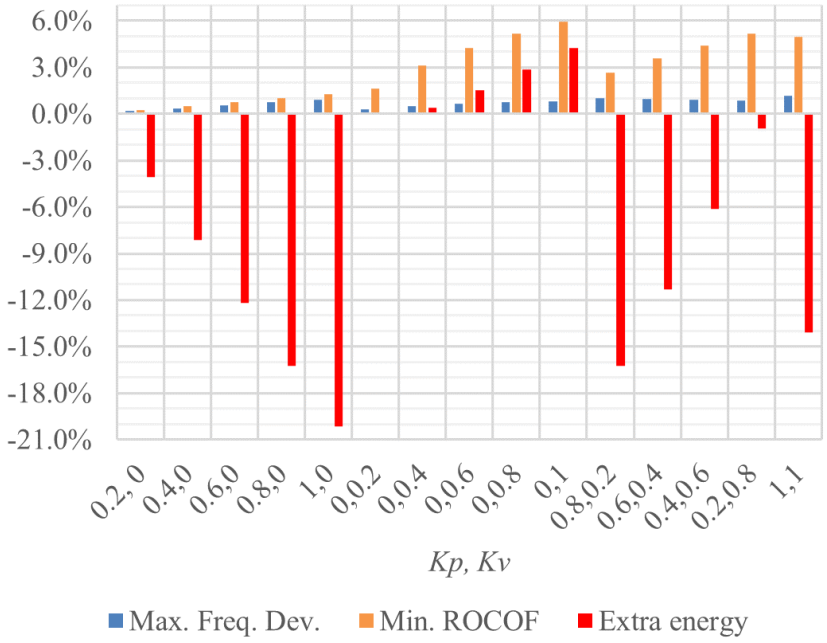


Figure 4.31: Reduction of main metrics with respect to the reference case.

4.3.2 Case study 2. Railway consumption. Response to a sudden load shedding

A segment of the overall railway circulation (from $t = 220$ s to $t = 225$ s) is examined to demonstrate the involvement of railway VAC systems in frequency control. Additionally, the statistics are determined within this specific timeframe to confine the evaluation to the highlighted period.

Primary frequency control

Figs. 4.32 and 4.33 present the absolute outcomes when implementing a control strategy based on instantaneous frequency deviations. Initially, more assertive controls result in more substantial frequency reductions. Moreover, shorter durations to reach peak frequency values, larger increments in thermal power generated by the VAC system, and more significant temperature variations are observed. While aligning the control with instantaneous frequency deviations, there is no direct enhancement in ROCOF behavior, and regardless of control aggressiveness, the alteration in internal temperature remains minimal. These findings align entirely with those reported in Section 4.2, where the potential contribution of trains to primary frequency control tasks, utilizing their thermal inertia and VAC systems, is also examined.

As previously mentioned, the subtraction of results from the reference case (without VAC system involvement in frequency control) enhances the visualization by scaling the figures. Fig. 4.34 presents the same outcomes as Fig. 4.32 but in comparison to the reference case. This representation not only illustrates clearer trends but also facilitates an understanding

of the order of magnitude of variations among cases. Similar to the primary frequency control case in Section 4.3.1, negligible impacts on thermal comfort are observed, regardless of control aggressiveness. Additionally, the effect of thermal inertia becomes evident, with the temperature decreasing by only 0.04°C after nearly five seconds of maximum heat power injection.

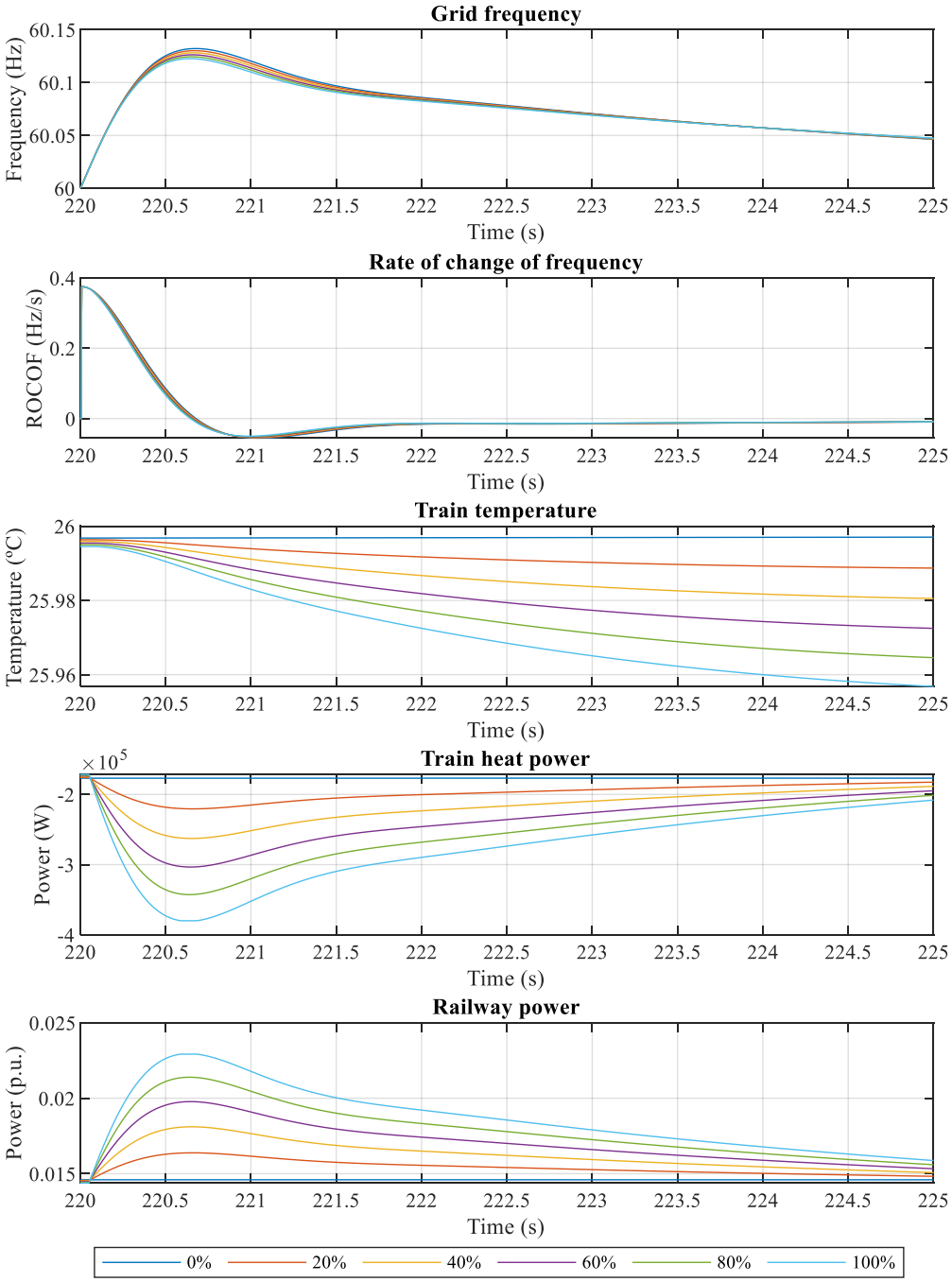


Figure 4.32: Primary frequency control response following a sudden load shedding. Variables of interest.

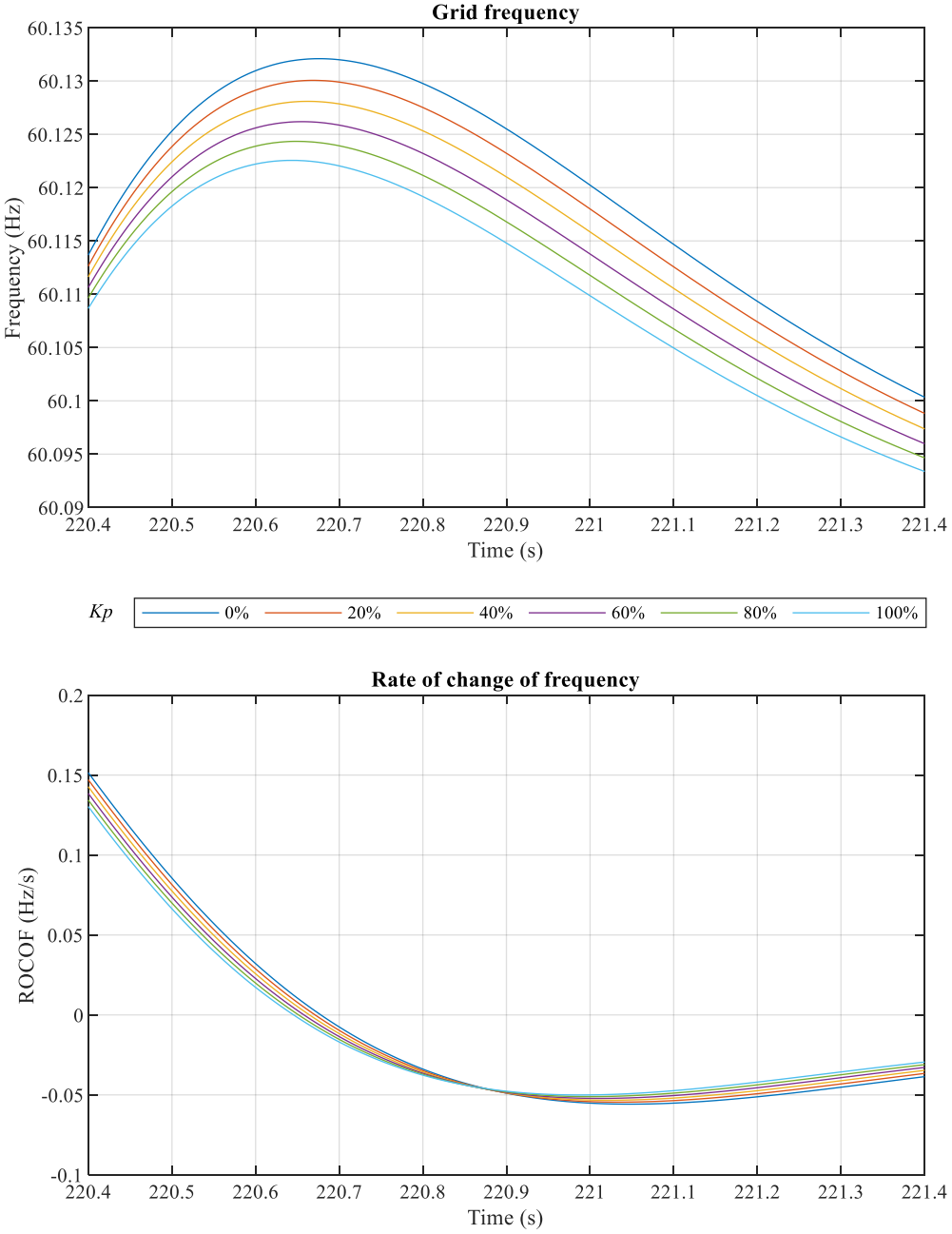


Figure 4.33: Primary frequency control response following a sudden load shedding. Zoom of frequency and rate of change of frequency.

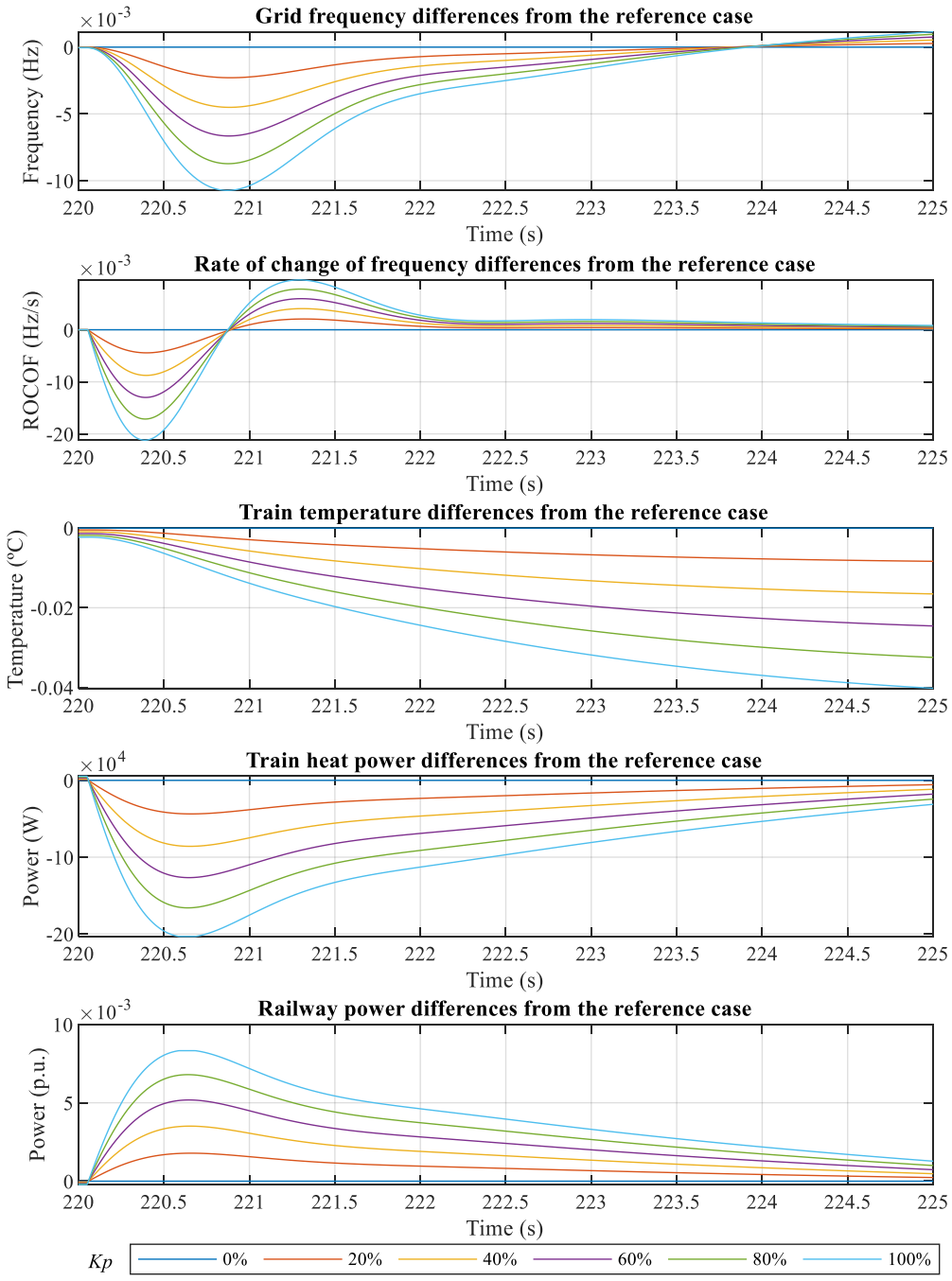


Figure 4.34: Primary frequency control response following a sudden load shedding. The reference case (without frequency control) has been subtracted from each case.

Virtual inertia control

Figure 4.35 depicts the behavior of the variables of interest when implementing virtual inertia control, presented as differences from those of the reference case. It is evident that adjusting VAC electric consumption proportionally to the frequency variation rate also leads to enhancements in grid frequency deviations. However, the benefits are not as pronounced as those observed with primary frequency control. The primary advantage of emulating inertia in frequency control lies in reducing the ROCOF. This necessitates a lower sustained power during the event and results in smaller air temperature variations (thousandths of degrees compared to hundredths of degrees in primary frequency control). Similar to the general study case presented earlier, the maximum ROCOF remains unchanged, although improvements are observed over time. In this scenario, since the control is focused on decreasing the ROCOF, it is important to note that the more aggressive control, while requiring greater power variations, may also have a negative impact on frequency deviation performance over time.

Regarding thermal responses, in the event of a sudden load loss, the thermal power of the VAC system experiences a rapid decrease followed by an increase. The extended duration of the decrease is attributed to the imposed variation rate influenced by the nature of the event. Furthermore, variations in train temperatures are negligible.

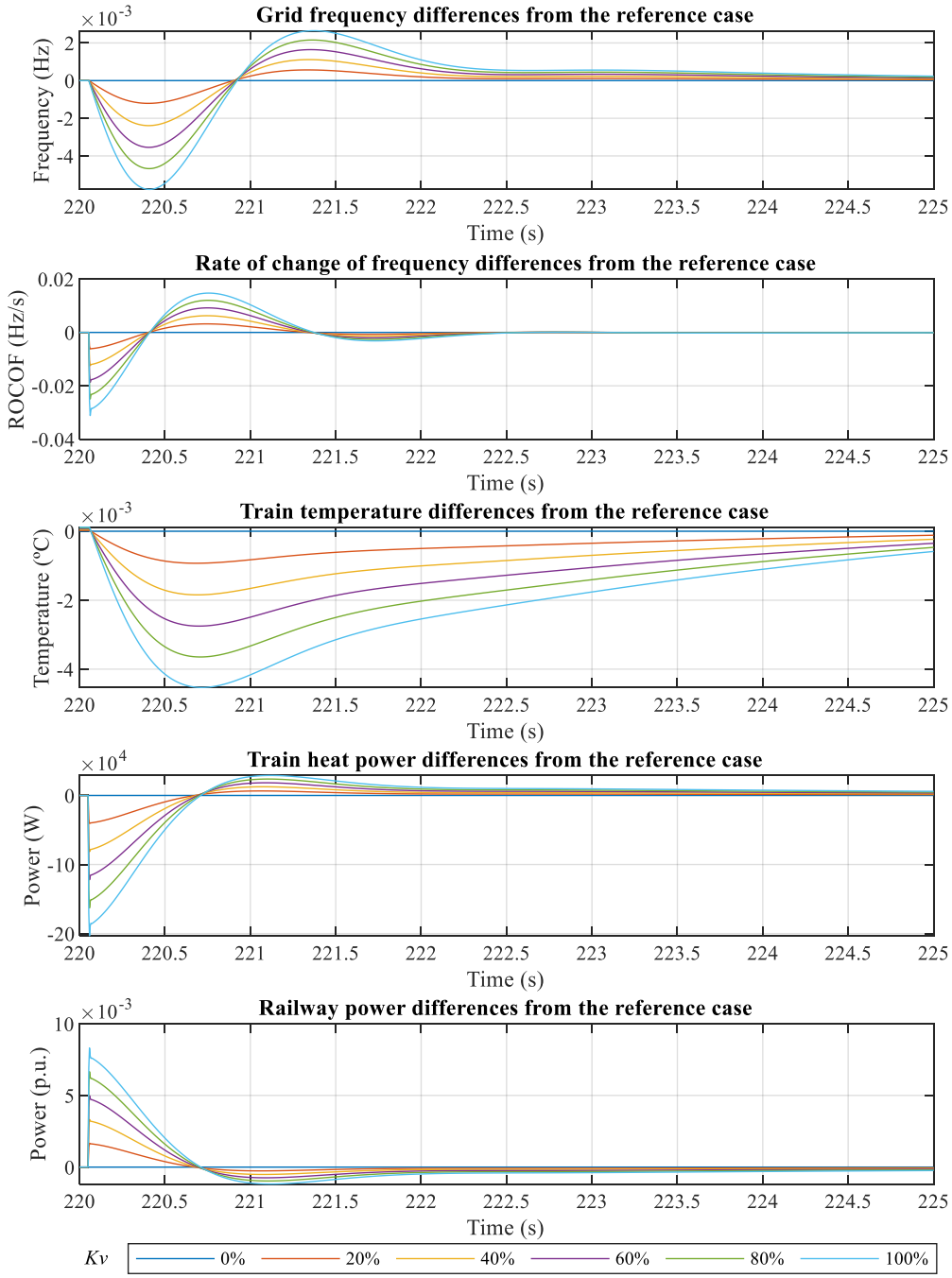


Figure 4.35: Virtual inertia control response following a sudden load shedding. The reference case (without frequency control) has been subtracted from each case.

Combined control

With a combined control, the advantages and limitations of each control are evident, as illustrated in Fig. 4.36. It is noteworthy that none of the cases pose a risk to thermal comfort, but their performances vary significantly in terms of frequency and power. The cases where K_p, K_v = (1,0) and K_p, K_v = (0,1) exhibit the slowest and fastest frequency evolution, respectively, which are correlated with the heat power. The extreme case of K_p, K_v = (1,1), representing an equal contribution from each controller at 100%, ranks as the second-best in minimizing frequency deviations and variations, with an approximately average response time compared to individual responses but with the drawback of power saturation.

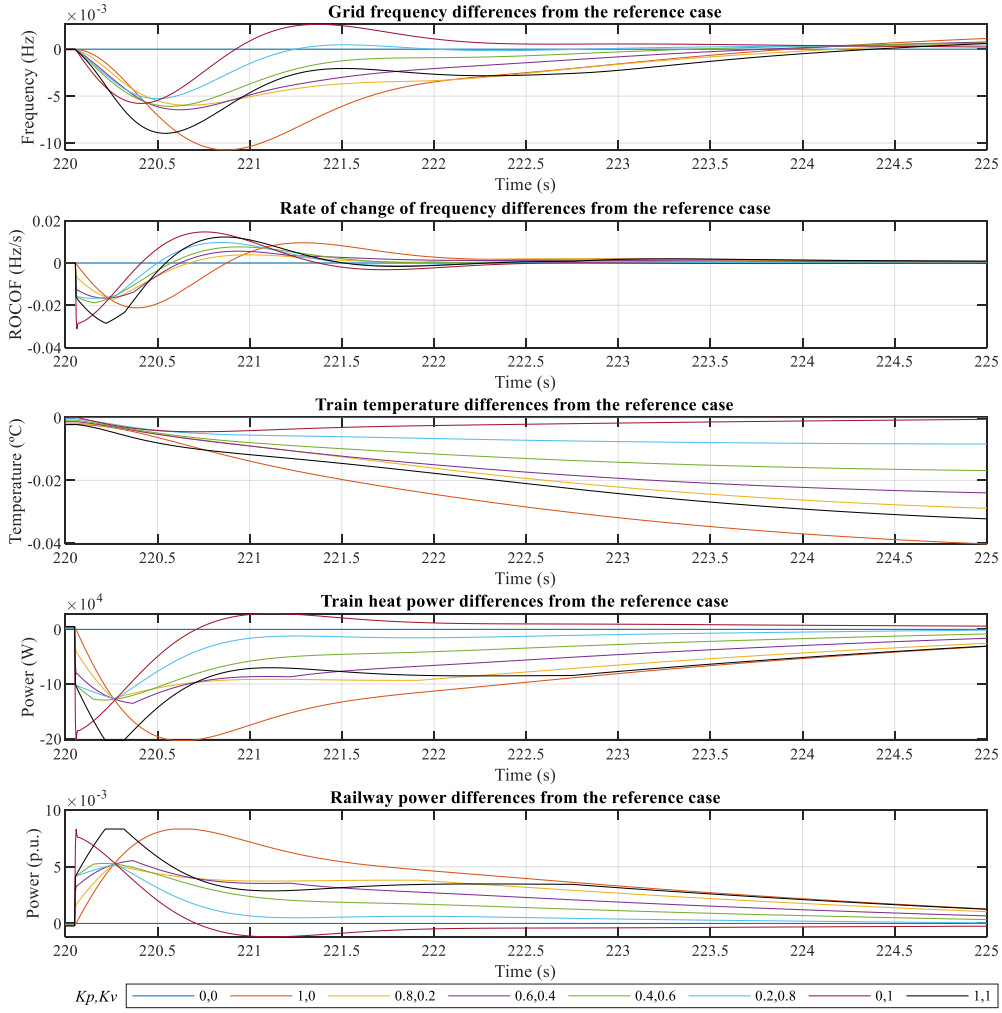


Figure 4.36: Combination of primary frequency and virtual inertia controls response following a sudden load shedding. The reference case (without frequency control) has been subtracted from each case.

Determining the most suitable combination is not evident, as the advantages in terms of frequency and thermal demands exhibit substantial similarities. Examining the chosen cases reveals the acceleration of frequency and power behavior over time with the increase in virtual inertia and the decrease in primary frequency control coefficients.

4.3.3 Case study 3. Railway consumption. Response to a sudden generation losing

The subsequent outcomes were derived using identical procedures as in the prior section. However, this time, a generation loss scenario is examined, maintaining the same event duration and control configurations.

Primary frequency control

Fig. 4.37 illustrates the outcomes of primary frequency control in response to a sudden loss of generation. As the generated power diminishes, there is a corresponding reduction in the thermal power supplied, leading to a decline in the electrical power consumed by the trains. Once again, it is evident how the control action's aggressiveness influences the mitigation of frequency deviations. Similar to findings in Section 4.2, the control response saturates when approaching the technical minimum or maximum of delivered thermal power. The time to reach saturation is inversely related to control aggressiveness. Upon saturation, there are no additional advantages to increasing control aggressiveness, but considerable power demands persist. Additionally, it is observed that saturation aids in sustaining positive differences in frequency deviations, but impacting the typical decline of frequency deviations (first plot) and frequency variations (second plot). In terms of thermal behavior, the limited impact of varying VAC thermal power on thermal comfort is evident. The internal air temperature of the train also exhibits a striking resemblance in cases where frequency control reaches saturation.

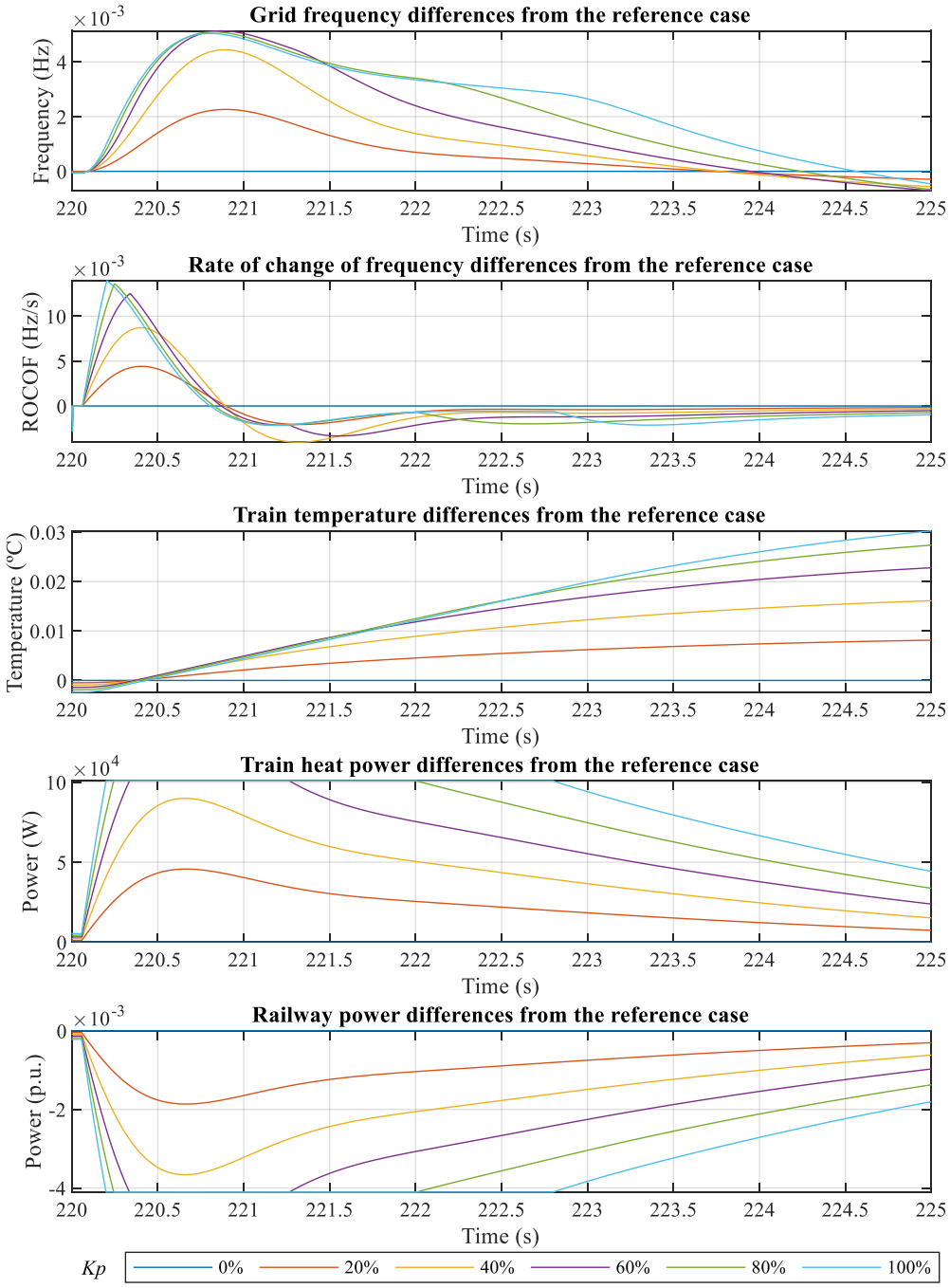


Figure 4.37: Primary frequency control response following a sudden generation losing. The reference case (without frequency control) has been subtracted from each case.

Virtual inertia control

Fig. 4.38 depicts the outcomes of implementing virtual inertia in response to a sudden loss of generation. Similar to the preceding section, it is evident that escalating control aggressiveness does not always result in improved performance regarding system frequency deviations. The ROCOF curve highlights that heightened aggressiveness leads to a reduction in its amplitude. However, given the saturation of heat power, a virtual inertia coefficient of $K_v = 0.6$ would be sufficient to achieve the maximum reduction in ROCOF without necessitating substantial power fluctuations and disrupting the overall frequency behavior.

From a frequency perspective, primary control offers greater advantages than virtual inertia, even though certain responses reached saturation. Nevertheless, virtual inertia control managed to achieve more rapid power changes compared to primary control within the same timeframe, albeit with steeper slopes in the power curves initially. This also implies that internal temperature deviations are negligible.

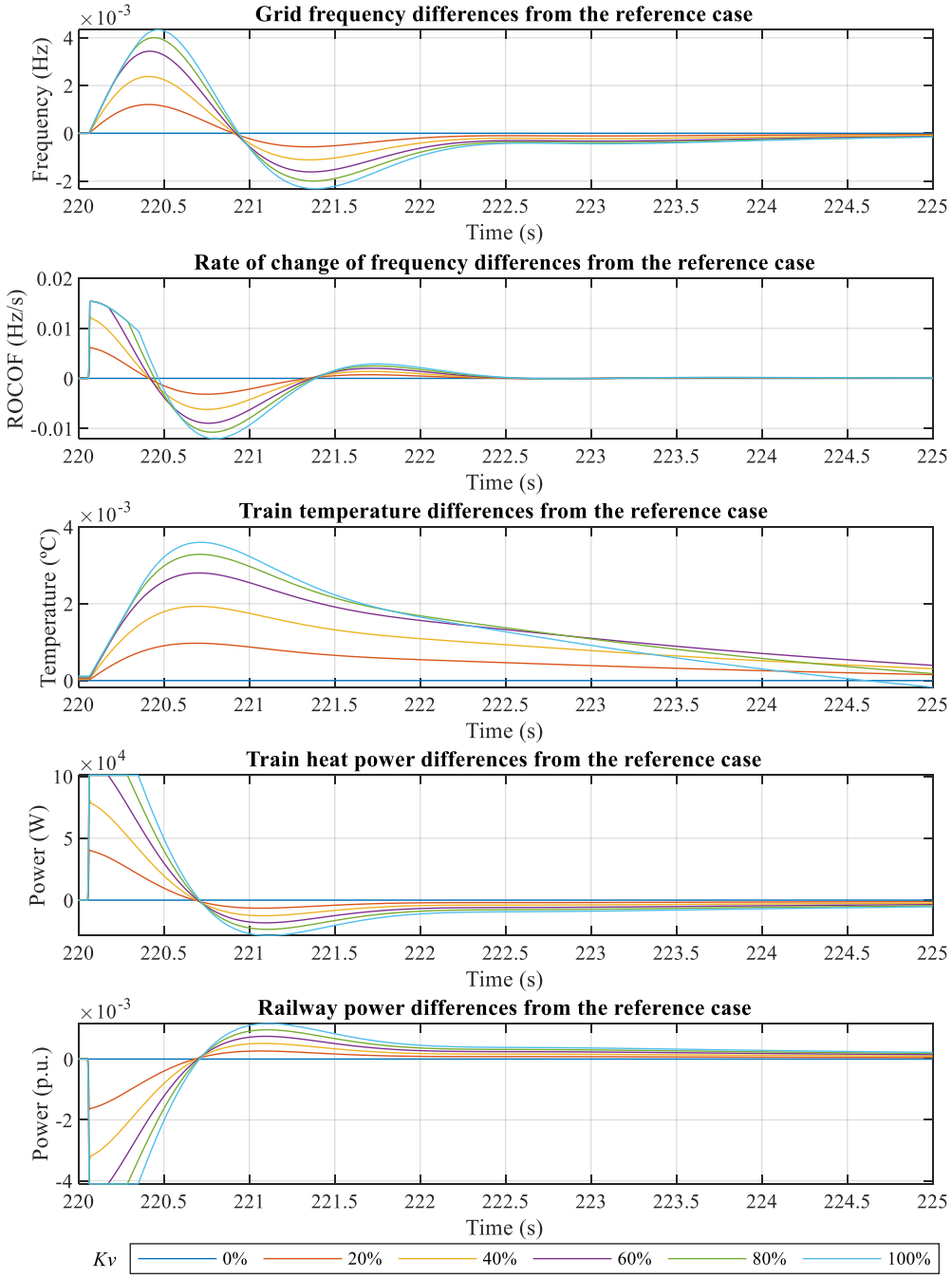


Figure 4.38: Virtual inertia control response following a sudden generation losing. The reference case (without frequency control) has been subtracted from each case.

Combined control

Fig. 4.39 illustrates the outcomes of various combinations of primary control and virtual inertia in response to a sudden generation loss. Irrespective of the control combination, there are consistent advantages in enhancing power system frequency performance. Once again, it is evident that the synergistic benefits of both controls contribute to minimizing frequency deviations and ROCOF, while maintaining less technically demanding thermal power profiles compared to individual control scenarios.

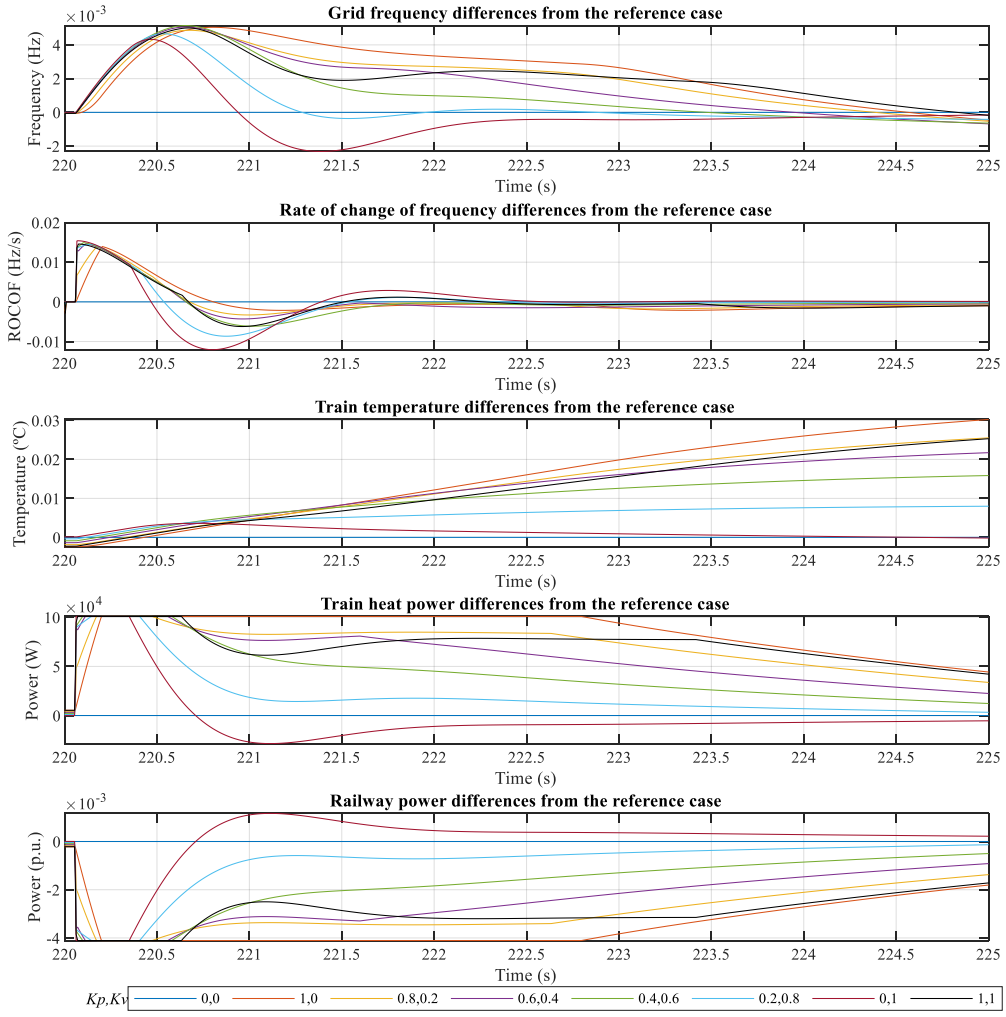


Figure 4.39: Combination of primary frequency and virtual inertia controls response following a sudden generation losing. The reference case (without frequency control) has been subtracted from each case.

Initially, it is evident how the non-combined scenarios, namely K_p, K_v = (1,0), and K_p, K_v = (0,1), establish the boundaries for each plot. Specifically, the K_p, K_v = (1,0) case exhibits a slower response but achieves the most significant mitigation of frequency deviation, whereas the K_p, K_v = (0,1) case shows the opposite trend but allows for faster desaturation.

Given that all cases reached the saturation point, determining the best-performing case is not

straightforward. Nevertheless, the intermediate scenarios, K_p, K_v = (0.6,0.4), and K_p, K_v = (0.4,0.6), appear to strike a reasonable balance between contributing to reductions in frequency deviation and minimizing power variations. This observation suggests the importance of maintaining an equilibrium between primary frequency control and virtual inertia provision. Additionally, the extreme case, K_p, K_v = (1,1), despite experiencing saturation, also exhibits a balanced behavior distinct from other cases. Opting for a well-balanced combination of controls entails fewer technical requirements for VAC equipment and reduced energy consumption while contributing approximately equally to frequency control.

4.3.4 Global results comparison

In addition to analyzing the preceding figures, applying statistical measures to the key variables offers a more precise assessment of the efficacy of each control. This is particularly crucial in cases involving control combinations, as individual responses exhibit similar patterns but vary in speed and amplitude based on control aggressiveness. Consequently, extreme values and RMS values are computed for both frequency deviation and its rate of change, with reference to their assigned limits (60 Hz and 0 Hz/s, respectively). Extrema, energy, and the extrema of the variation rate are also determined for thermal power. For the train's inner air temperature deviation, only the RMS value is calculated, using a baseline of 26°C.

Load shedding

Table 4.3 presents various statistics to assess the impact of primary frequency control, virtual inertia, and their amalgamation in the scenario of sudden load shedding. The trends observed in the graphs are supported by the statistics for primary control, where heightened aggressiveness leads to a reduction in both maximum and minimum deviations. The maximal deviation experiences a more pronounced decrease owing to the load loss event, while the minimal deviation is influenced by the natural consumption of the railway. Additionally, the RMS values clarify the impact of different levels of aggressiveness, showcasing a maximum reduction of 3.8899 mHz.

The influence of primary control on the ROCOF is non-negligible. The maximum ROCOF is determined by the event magnitude and the system's inertia, exhibiting minimal variation. However, the minimum ROCOF experiences more substantial fluctuations due to the altered normal railway consumption triggered by control activation. Nevertheless, the disparity between frequency deviation and ROCOF RMS values remains negligible.

Primary control demonstrates negligible effects on internal temperature. Conversely, in the generated thermal power, increased aggressiveness amplifies the minimum and diminishes the maximum. The elevation in the minimum is attributable to the load loss event, while the reduction in the maximum results from the control's need to track the frequency decrement caused by the train's natural consumption during braking. Similarly, the variation rates of thermal power escalate with control aggressiveness.

Concerning energy consumption, there is a noticeable increase in heightened aggressiveness. As anticipated, greater frequency deviations necessitate increased thermal power injection, leading to augmented energy consumption.

Table 4.3: Statistical analysis following a load shedding. Frequency control in railway consumption.

Gains (K_p,K_v)	Freq. deviation (mHz)			ROCOF (mHz/s)		Thermal power					Temp. deviation (m°C)
						Extrema (MW)		Energy (kWh)	Extrema derivative (MW/s)		RMS
	Max.	Min.	RMS	Min.	RMS	Max.	Min.		Max.	Min.	
Ref.: 0,0	132.096	1.1829	83.1319	-55.7833	87.2959	-0.17684	-0.17687	-0.2458	0	0	3.1
PC: 0.2,0	130.0615	1.1733	82.3146	-54.5329	86.4113	-0.17578	-0.22057	-0.2743	0.0238	-0.1491	8.8
PC: 0.4,0	128.0934	1.1639	81.5181	-53.3368	85.5569	-0.17470	-0.26275	-0.3023	0.0467	-0.2982	14.5
PC: 0.6,0	126.1869	1.1548	80.7415	-52.1922	84.7312	-0.17364	-0.30347	-0.3297	0.0685	-0.4474	20.1
PC: 0.8,0	124.3410	1.1458	79.9839	-51.0955	83.9328	-0.17259	-0.34281	-0.3565	0.0895	-0.5965	25.6
PC: 1.0,0	122.5563	1.1371	79.2450	-50.0596	83.1613	-0.17156	-0.38000	-0.3839	0.1097	-0.7456	30.9
VI: 0,0.2	131.4225	1.1828	83.1178	-54.0550	86.4180	-0.17040	-0.21758	-0.2463	0.1646	-8.1939	3.5
VI: 0,0.4	130.7685	1.1827	83.1043	-52.4121	85.5684	-0.16431	-0.25828	-0.2468	0.6033	-16.3865	4.0
VI: 0,0.6	130.134	1.1826	83.0914	-50.7522	84.7459	-0.15856	-0.29898	-0.2474	1.3161	-24.5778	4.5
VI: 0,0.8	129.5174	1.1824	83.079	-49.3683	73.9492	-0.15312	-0.33968	-0.2479	2.3028	-32.7678	4.9
VI: 0,1.0	128.918	1.1823	83.067	-49.9585	83.1773	-0.14798	-0.38	-0.2484	3.4704	-40.9565	5.4
CC: 0.8,0.2	126.126	1.1457	80.422	-51.9691	83.8376	-0.1726	-0.30256	-0.3436	0.086	-8.4445	22.4
CC: 0.6,0.4	125.7033	1.1545	80.8287	-50.6653	83.2956	-0.17366	-0.31218	-0.3276	0.1701	-16.3962	19.9
CC: 0.4,0.6	126.2488	1.1636	81.4813	-48.621	83.1557	-0.17473	-0.30617	-0.3038	0.1225	-24.4626	15.5
CC: 0.2,0.8	127.6854	1.1729	82.2868	-48.4458	83.6151	-0.17583	-0.30429	-0.2750	0.2316	-24.6239	9.9
CC: 1.0,1.0	123.8752	1.1369	80.1299	-46.3763	81.489	-0.17163	-0.38	-0.3543	0.3843	-25.6061	24.7

The results of implementing virtual inertia confirm its capability to reduce both maximum and minimum frequency deviations, but to a lesser extent than primary control. This is evident in the higher RMS, maximum, and minimum values of frequency deviation compared to the primary control. While virtual inertia contributes to lowering the minimum ROCOF, the RMS value of ROCOF remains identical to that of primary control, providing no additional benefit throughout the train circulation. The impact of virtual inertia on internal temperature is less pronounced than that of primary control, with the RMS value being nearly null and consistent across different levels of control aggressiveness. Similarly, power consumption is approximately equal to the case with no control implemented, but the variation rate of thermal power is considerably higher than with primary control. The application of virtual inertia control requires a high-power variation capacity from VAC equipment, achievable through the activation of compressor motors, fans or ventilators, and circulation pumps, among other devices.

Concerning the combined results of primary and virtual inertia controls, notable improvements are observed across various parameters compared to the reference case. The combined control achieves reductions in maximum frequency deviation up to 8.2208 mHz, in frequency RMS up to 3.00 mHz, and minimum ROCOF up to 9.407 mHz/s. The combination K_p, K_v = (1,1) yields the second-best results for maximum frequency deviation, first for frequency RMS, third for minimum ROCOF, and first for both minimum and RMS values of ROCOF. Additionally, it reduces power fluctuation and temperature deviation RMS.

Fig. 4.40 visually highlights the primary differences in frequency deviations and ROCOF. Primary control directly improves maximum frequency deviations, RMS of frequency, and reduces minimum ROCOF. Virtual inertia decreases maximum frequency deviations and the RMS of ROCOF while primarily improving the minimum ROCOF. Conversely, the combined application of both controls enhances the overall frequency behavior, nearly amalgamating the benefits of individual controls.

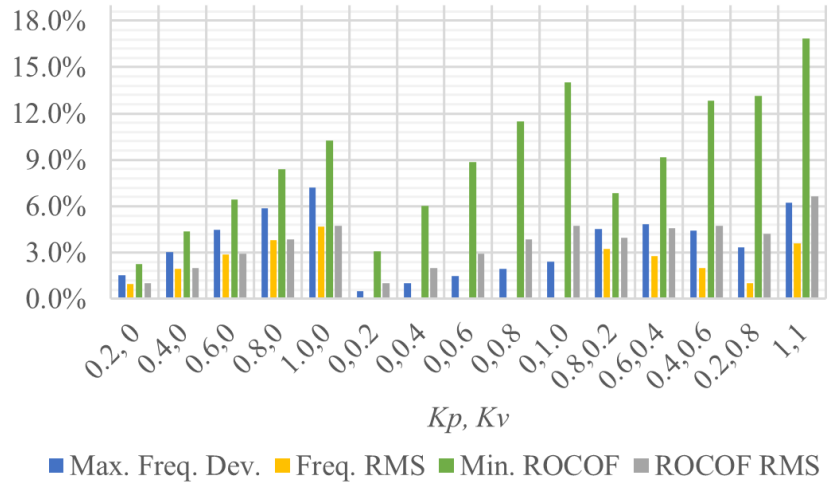


Figure 4.40: Reduction rates of relevant frequency-related variables following a load shedding.

Generation losing

Table 4.4 compiles various statistics to assess the effectiveness of primary control, virtual inertia, and their combination in the event of a sudden loss of generation. The outcomes of primary frequency control align with previous findings. Notably, the degree of control aggressiveness leads to more substantial reductions in both maximum frequency deviation and, consequently, the RMS value. This impact extends to the extrema and RMS of ROCOF, exhibiting similar trends. Additionally, the injection of thermal power, and consequently energy consumption, decreases with escalating control aggressiveness. The extrema of thermal powers, along with their variation rates, also experience an increase. The interior air temperature, while exhibiting minor fluctuations relative to its nominal value, becomes more perceptible with heightened control aggressiveness.

Table 4.4: Statistical analysis following a generation losing. Frequency control in railway.

Gains (K_p,K_v)	Freq. deviation (mHz)			ROCOF (mHz/s)		Thermal power					Temp. deviation (m°C)
						Extrema (MW)		Energy (kWh)	Extrema derivative (MW/s)		
	Max.	Min.	RMS	Max.	RMS	Max.	Min.		Max.	Min.	RMS
Ref.: 0,0	1.4179	-131.792	82.897	72.3071	88.3158	-0.17684	-0.17687	-0.2458	0	0	3.1
PC: 0.2,0	1.4598	-29.787	82.102	71.7121	87.4454	-0.13114	-0.17577	-0.2147	0.1493	-0.0239	3.2
PC: 0.4,0	1.4479	-127.851	81.328	71.1305	86.6067	-0.08694	-0.17469	-0.1841	0.2985	-0.0468	8.3
PC: 0.6,0	1.4363	-126.965	80.725	70.562	86.082	-0.07600	-0.17363	-0.1583	0.4478	-0.06	12.4
PC: 0.8,0	1.425	-126.874	80.353	70.006	85.8614	-0.07600	-0.172557	-0.1401	0.597	-0.0295	14.8
PC: 1.0,0	1.4139	-126.875	80.130	69.4621	85.7473	-0.07600	-0.17154	-0.1279	0.7463	-0.0348	15.9
VI: 0,0.2	1.4718	-131.120	82.883	72.3012	87.4515	-0.13614	-0.18339	-0.2454	8.4306	-0.1701	2.6
VI: 0,0.4	1.4717	-130.469	82.870	72.2953	86.6173	-0.09540	-0.18945	-0.2449	16.8597	-0.6225	2.2
VI: 0,0.6	1.4715	-129.850	82.860	72.2893	85.8888	-0.07600	-0.19518	-0.2447	20.1658	-0.2304	1.9
VI: 0,0.8	1.4714	-129.364	82.871	72.2834	85.54	-0.076	-0.20044	-0.2455	18.8146	-0.3196	1.9
VI: 0,1.0	1.47137	-128.997	82.896	72.2774	85.3459	-0.076	-0.20543	-0.2469	17.4619	-0.396	2.0
CC: 0.8,0.2	1.4248	-126.928	80.547	69.9983	85.4226	-0.0767	-0.17258	-0.1468	8.7289	-0.07	13.4
CC: 0.6,0.4	1.436	-126.750	80.860	70.5475	85.1455	-0.076	-0.17365	-0.1623	16.8539	-0.1927	11.7
CC: 0.4,0.6	1.4475	-126.661	81.363	71.11	84.9949	-0.076	-0.17472	0.1853	16.7537	-0.1302	8.5
CC: 0.2,0.8	1.4592	-127.679	82.110	71.6864	85.1335	-0.076	-0.17582	-0.2156	15.9726	-0.2462	3.5
CC: 1.0,1.0	1.4131	-126.795	80.616	69.4279	85.1499	-0.076	-0.17158	-0.1461	12.7257	-0.2288	12.5

Concerning virtual inertia, it is possible to achieve reductions in the extrema of frequency deviations and their RMS values, although to a lesser extent. Virtual inertia does not exhibit notable benefits in reducing ROCOF extrema but does contribute to a more substantial reduction in ROCOF RMS compared to primary control. The energy consumption and temperature deviation RMS vary minimally with control aggressiveness, mirroring the trends observed in the load shedding scenario. Notably, the aggressiveness of virtual inertia imposes greater variations in the thermal power to be injected.

Combining both controls, specifically comparing cases with the same K_p, K_v, results in greater reductions in the extrema of frequency deviations. Furthermore, it enables lower RMS values of ROCOF compared to the application of each control individually. However, in terms of RMS frequency and energy consumption, the combined controls improve upon the results of virtual inertia but remain similar to those of the primary control. The deviations in internal temperature remain negligible. Once again, the combination of both controls necessitates lower sudden variations in thermal power, although the benefit obtained in this scenario is less pronounced.

Fig. 4.41 illustrates some of the parameters that underwent significant variations among different control combinations in response to sudden generation loss. The selected parameters include the extrema of frequency deviations and the RMS of frequency and ROCOF. As observed previously, virtual inertia applied individually does not yield benefits in any variable compared to the scenarios of individual primary control and the combination of both controls. Individual primary control provides similar reductions in the lower limit of frequency deviations and comparable RMS frequency to the combined control scenario. However, the combination of controls (primary and virtual inertia) yields greater benefits in ROCOF RMS and in reducing the maximum frequency deviations while requiring lower thermal power variations than stand-alone virtual inertia control.

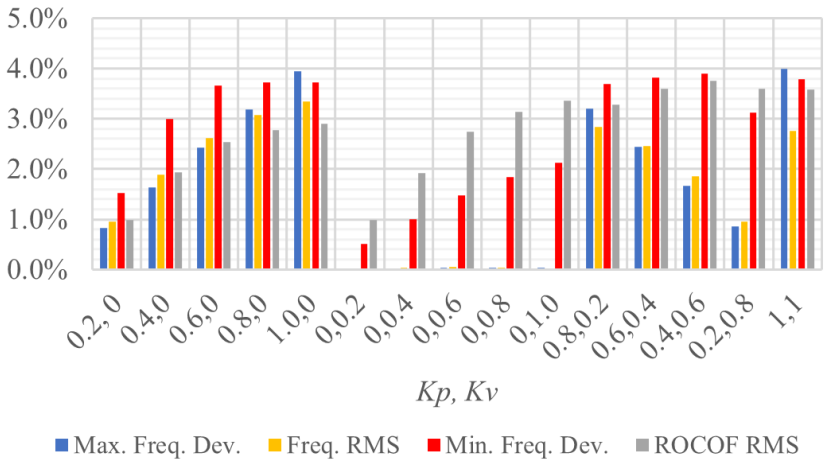


Figure 4.41: Reduction rates of relevant frequency-related variables following a generation losing.

Relative impact index

To better appreciate the influence of trains' VAC systems on frequency control, it is essential to consider the magnitude of the controllable load. In the examined scenario, each train has a maximum power capacity of 0.0013 p.u. available for frequency control functions. Despite variations in the number of trains over time, it can be asserted that a total maximum load of 0.0052 p.u. contributed to the aforementioned benefits in a 2.0 p.u. system (comprising four trains and two generators). The primary aim of this approach is not to independently manage frequency deviations but rather to be one of several contributors. To more accurately evaluate the positive effects of this contribution, this section presents relative results in comparison to the load size. This is achieved by dividing certain key outcomes (percentage reduction) by the total maximum available load (power capacity in p.u.).

Figs. 4.42 and 4.43 illustrate the relative impact index in response to load shedding and generation loss, respectively. In both scenarios, the percentage reductions of RMS frequency and ROCOF are computed. Given the distinct nature of each situation, specific statistics are considered for reduction—maximum frequency deviation in the case of load shedding (Fig. 4.42) and minimum frequency deviation in the case of generation loss (Fig. 4.43).

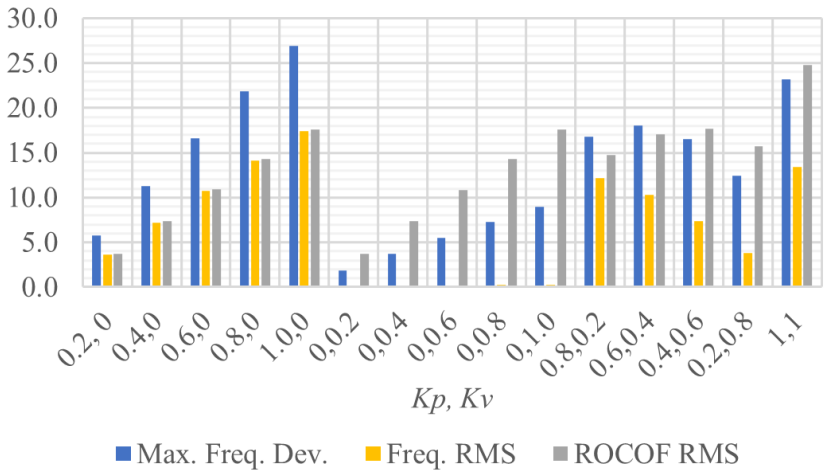


Figure 4.42: Relative impact index (%/p.u.) of relevant frequency-related variables following a load shedding.

The preceding figures illustrate consistent associations, with primary frequency control demonstrating a strong correlation with frequency RMS, and virtual inertia exhibiting a noteworthy connection with ROCOF RMS. Furthermore, the outcomes suggest the substantial reductions that could be achieved if additional loads (up to 1.0 p.u.) implement similar frequency controls. Depending on the controller gains, the enhancement in frequency performance may become even more significant. For instance, in Fig. 18, it is evident that reductions of up to 27%, 17%, and 25% in maximum frequency deviation, frequency RMS, and ROCOF RMS, respectively, could potentially be realized. Similarly, in Fig. 4.43, a maximum feasible reduction of 12%, 14%, and 14% in frequency RMS, minimum frequency deviation, and ROCOF RMS, respectively, is demonstrated.

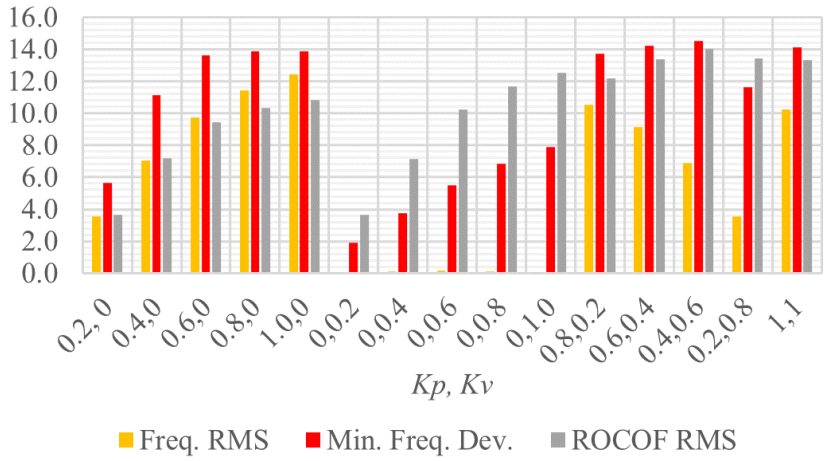


Figure 4.43: Relative impact index (%/p.u.) of relevant frequency-based variables following a generation losing.

4.3.5 Conclusions

The significance of railway contribution to frequency control is largely determined by the relationship between total railway consumption, VAC system fraction, power system characteristics, and the event magnitude. Even a slight relative variation in consumption can positively impact frequency control if the railway, particularly its associated VAC systems, constitutes a substantial load in the instantaneous grid power balance.

The results in the corresponding section illustrate how control actions affect the minimum ROCOF following a load shedding event (with a potential reduction of up to 16.86%) and slightly influence its maximum value following a generation loss event (with a potential reduction of up to 3.98%). These values are contingent on power system inertia, which remains constant, and the instantaneous power balance. In the model, VAC system consumption is significantly smaller than the power involved in events and train traction consumption. Consequently, following a load shedding event, the magnitude of the event defines the maximum ROCOF, while the minimum ROCOF is still determined by normal power consumption (traction and auxiliaries). This clarifies why railway frequency control only enhances the minimum ROCOF. In a generation loss scenario, the event magnitude defines the minimum ROCOF, while the maximum ROCOF is still influenced by normal power consumption (braking and auxiliaries). As braking involves minimal power exchange between the railway and the grid (no injection of regenerative braking energy and auxiliaries' consumption), the impact on frequency performance from varying VAC system consumption is also minimal. In conclusion, the potential benefits of frequency control can vary significantly depending on the type of event in the power system.

The operational status of the VAC system before frequency control activation imposes limitations on its contribution due to operating boundaries. It has been demonstrated that frequency deviations and variations require amounts of thermal power that tend to saturate the VAC system, particularly in the case of generation loss, where the lower limit is frequently

reached. In the event of sudden load shedding, if the VAC is managing a substantial thermal load (passengers, solar radiation, etc.), it is challenging to significantly increase its electrical consumption to mitigate the frequency increase. Similarly, in the case of sudden generation loss, the VAC contribution could be minimal if the preceding instantaneous thermal load is low compared to its rated power. Regardless of the situation, it has been verified that the thermal comfort of passengers is not compromised.

Furthermore, the benefits of implementing these control techniques should account for the technical requirements of the VAC system. In addition to reductions in frequency deviations and ROCOF, there are also decreases in delivered thermal power and, consequently, electrical consumption. However, these benefits necessitate the ability to provide sudden thermal power changes, especially in virtual inertia cases, where reductions of a few millihertz demand variations of several megawatts per second in the VAC system operation. Therefore, the achievable contribution of train VAC systems is also contingent on their operational ranges. Some advantages of combining primary frequency control and virtual inertia, apart from enhancing frequency performance, include reducing technical requirements while achieving better frequency control. This approach can mitigate VAC system fatigue and address other potential issues. It's important to note that controls do not combine linearly, even if the implemented equation suggests so. The action of one control can influence the performance of the other. Thus, an appropriately adaptive combination over time could yield even more benefits. The presented work represents the initial stages of technology readiness.

These results are published in [45].

4.4 Use of the thermal inertia of trains for relieving renewable generation from frequency control tasks

Going beyond the existing research on the contribution of railway systems to inertial and primary frequency control [40], [41], [46] and Sections 4.2 and 4.3, this section introduces a novel approach for these systems to enhance their contribution by incorporating supplementary frequency control. This is achieved through modifications in the operation of on-board HVAC systems of trains, ensuring the continuous circulation of trains and maintaining passengers' thermal comfort without compromise. The proposed approach is also designed to alleviate renewable generation from the responsibility of providing both primary and supplementary frequency control. As an additional contribution, the section presents a methodology for tuning the controllers of railway frequency control, offering a rapid and approximate means of identifying local optimum parameters and minimizing the impact of stochasticity. The efficacy of the proposed demand response approach is evaluated through a numerical study utilizing real train data and considering various scenarios of generation (with or without frequency-responsive renewable generation) and consumption (railway consumption with or without sudden load shedding). Finally, experimental validation is conducted on a Hardware In the Loop (HIL) test-bench to demonstrate the feasibility of the proposed approach in real-time.

4.4.1 Problem statement

As previously indicated, the introduction of renewable generation inherently leads to a reduction in the inertia of power systems. In (3.13), it becomes evident that the equivalent system inertia would decrease with the incorporation of grid-decoupled rotor generation in the energy dispatch. A comprehensive analysis to assess the implications of inertia reduction is conducted in [46]. The following scenarios maintain the same system characteristics as outlined in Section 4.3.

Only conventional vs. Partially displaced generation under normal railway consumption

The configuration of two traditional generators determines the grid frequency performance during regular railway consumption. In this context, maximum, minimum, and RMS frequency deviations of 89.97 mHz, -24.29 mHz, and 15.34 mHz are observed, respectively. Additionally, the maximum, minimum, and RMS ROCOF are recorded as 268.9 mHz/s, -36.90 mHz/s, and 15.56 mHz/s, respectively. This outcome is depicted by the blue line in Fig. 4.44.

Upon replacing one conventional generator with a generic renewable generator in this scenario, alterations occur in the frequency deviations and ROCOF metrics. The maximum, minimum, and RMS values of frequency deviations and ROCOF shift to 179.0 mHz, -47.58 mHz, 30.13 mHz, 537.8 mHz/s, -73.81 mHz/s, and 30.97 mHz/s, respectively. This modification is represented by the orange line in Fig. 4.44.

As a variation of this setup, the renewable generator is permitted to participate in both primary and supplementary frequency control, solely reducing its generation to counteract

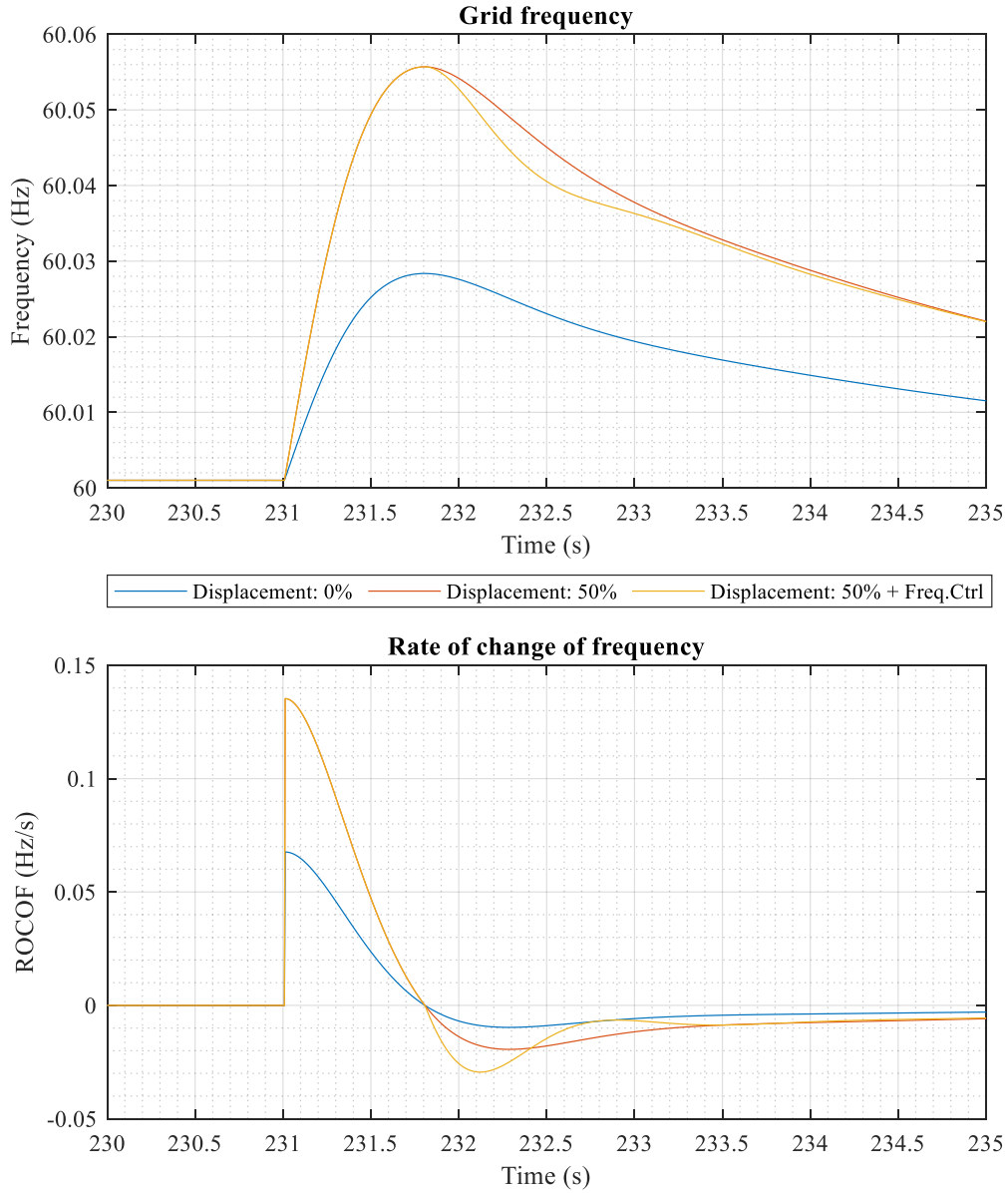


Figure 4.44: Grid frequency performance under different conditions.

positive frequency deviations, aligning with the approach in [46]. Although the frequency deviation and ROCOF extrema remain consistent, the frequency RMS improves to 30.09 mHz, while the ROCOF RMS increases to 30.98 mHz/s. This adjustment is illustrated by the yellow line in Fig. 4.44.

4.4.2 Control approach

The utilization of the thermal inertia inherent in trains, enabling the use of on-board HVAC systems for primary frequency control in power systems, has been previously investigated in [46] and Sections 4.2 and 4.3. The primary focus of this frequency control application is to offload renewable generation from these responsibilities. However, it is crucial that demand

response-based frequency control in railways also includes provisions for supplementary frequency control. In this context, a supplementary frequency control scheme is introduced, along with a method for selecting its parameters. The implementation and effectiveness of this proposal are demonstrated through a case study based on the railway and power systems considered in [46].

In accordance with (3.25) and standard HVAC system control practices [128], various variables can be adjusted to adhere to a specific setpoint. The setpoint temperature (T_{set}) is selected to be modified in response to grid frequency variations. Equation (4.6) presents the proposed frequency control mechanism, altering the instantaneous setpoint temperature of the HVAC systems on trains based on the evolution of grid frequency. This method builds upon the one introduced in [44], incorporating stability analysis findings. The first term denotes primary frequency control, while the last two terms represent supplementary frequency control, with C_1 and C_2 as the respective gains. These gains establish the relationship between equivalent frequency deviation in millihertz (Δf_{eq}) and temperature deviation in Celsius degrees. Unlike power plants, train HVAC systems cannot independently manage steady-state frequency deviations. Therefore, a method to prevent saturation is essential. The function $f(T_a, \Delta f_{eq})$ resets the cumulative frequency deviation based on the inner air temperature and frequency deviation states, resetting when the inner air temperature falls outside the thermal comfort range or when the frequency deviation transitions from a non-zero value to zero. The second term,T_N [122], represents the setpoint temperature during regular HVAC system operation.

$$\begin{aligned} T_{set}(t) = &- C_1 \Delta f_{eq}(t) + T_N \\ &- C_2 \int \Delta f_{eq}(t) dt + C_2 f(T_a, \Delta f_{eq}) \end{aligned} \tag{4.6}$$

It is important to note that each controller is equipped with a dead zone, and these dead zones may not be identical. The dead zone for primary frequency control is selected based on the approach in Section 4.2, which is derived from [121]. This configuration has demonstrated effective performance in previous sections. However, given that supplementary frequency control is anticipated to be activated more frequently than primary frequency control, it can be more susceptible to unpredictable variations in system conditions. As demonstrated in Section 4.1, railway system power consumption is influenced by numerous interconnected variables (e.g., the number of passengers and timetable), making it challenging to tune the control for optimal performance during its typical operational period. To address this challenge, a methodology for determining the parameters of supplementary frequency control is proposed. This approach is designed to assess the impact of the dead band and C_2 on the overall grid frequency performance. Analyzing these two parameters provides a relatively straightforward means of achieving satisfactory outcomes without the need for an extensive analytical process. Additionally, it streamlines supplementary frequency control, making it primarily dependent on just two variables, as opposed to considering all the parameters typically involved in integral control.

4.4.3 Determining control parameters

The methodology commences with the identification of the range values for the supplementary control dead band (DB) and C_2. Subsequently, one or more output variables need to be designated for evaluating frequency performance. Metrics such as RMS, mean, standard deviation, variance, etc., serve as effective indicators of overall performance without being biased by specific grid conditions. The selected statistic is computed for all feasible combinations of DB and C_2 within the specified range and desired granularity. Employing analytical techniques enables the fitting of a surface equation (statistic $= f(DB, C_2)$). The resulting equation facilitates a straightforward analysis of the relationships among variables and their impact on grid frequency performance. This equation can then be utilized to determine the values of the variables that minimize the chosen statistic. These identified values can be employed as appropriate parameters for tuning the railway demand response-based supplementary frequency control. It is important to note that the values derived from the surface equation may vary depending on the mathematical methods used for fitting the surface.

This procedure aims to identify local minima, which also serve as local optima based on the chosen criteria. The objective is not to ascertain global optimum values but rather to identify values that enable optimal frequency performance in various railway consumption scenarios. Given the unpredictable changes in the number of passengers, timetables, and diverse grid conditions, the proposed method outputs values that deliver acceptable frequency performance under such unpredictable circumstances.

The subsequent case studies utilize the DC railway and power system previously introduced. The dead band is varied within the range of 1 mHz to 10 mHz, considering the dead band of the renewable generator relieved from frequency control tasks (1 mHz). The range for C_2 spans from 0.47 °C/Hz to 3.68 °C/Hz, determined as in [45], where a direct iterative method is employed to identify the first value that saturates the heat power. The frequency deviation RMS is chosen as the output variable for assessing frequency performance. To fit the results to a surface, the *Curve Fitting* application of the Matlab Toolbox is utilized. This application allows three-dimensional data fitting using polynomial, interpolant, custom equation, and local regression methods. For the following case studies, a polynomial method, bisquare robustness, second-degree variables, and a linear least squares method are selected (4.7). The system of equations presented in (4.8) is solved for DB and C_2 to identify the variable values that minimize the frequency deviation RMS.

$$\begin{aligned}\Delta f_{eq_{RMS}}(DB, C_2) = p_{00} + p_{10}DB + p_{01}C_2 \\ + p_{20}DB^2 + p_{11}DB\,C_2 + p_{02}C_2^2\end{aligned} \tag{4.7}$$

$$\begin{cases}\frac{\partial(\Delta f_{eq_{RMS}}(DB,C_2))}{\partial DB} = 0 \\ \frac{\partial(\Delta f_{eq_{RMS}}(DB,C_2))}{\partial C_2} = 0\end{cases} \tag{4.8}$$

The subsequent scenarios involve combinations of: (a) the supplementary frequency control proposed in this study, (b) the assistance of renewable generation (RG) in frequency control responsibilities, and (c) the railway-based primary frequency control. The alleviation of RG

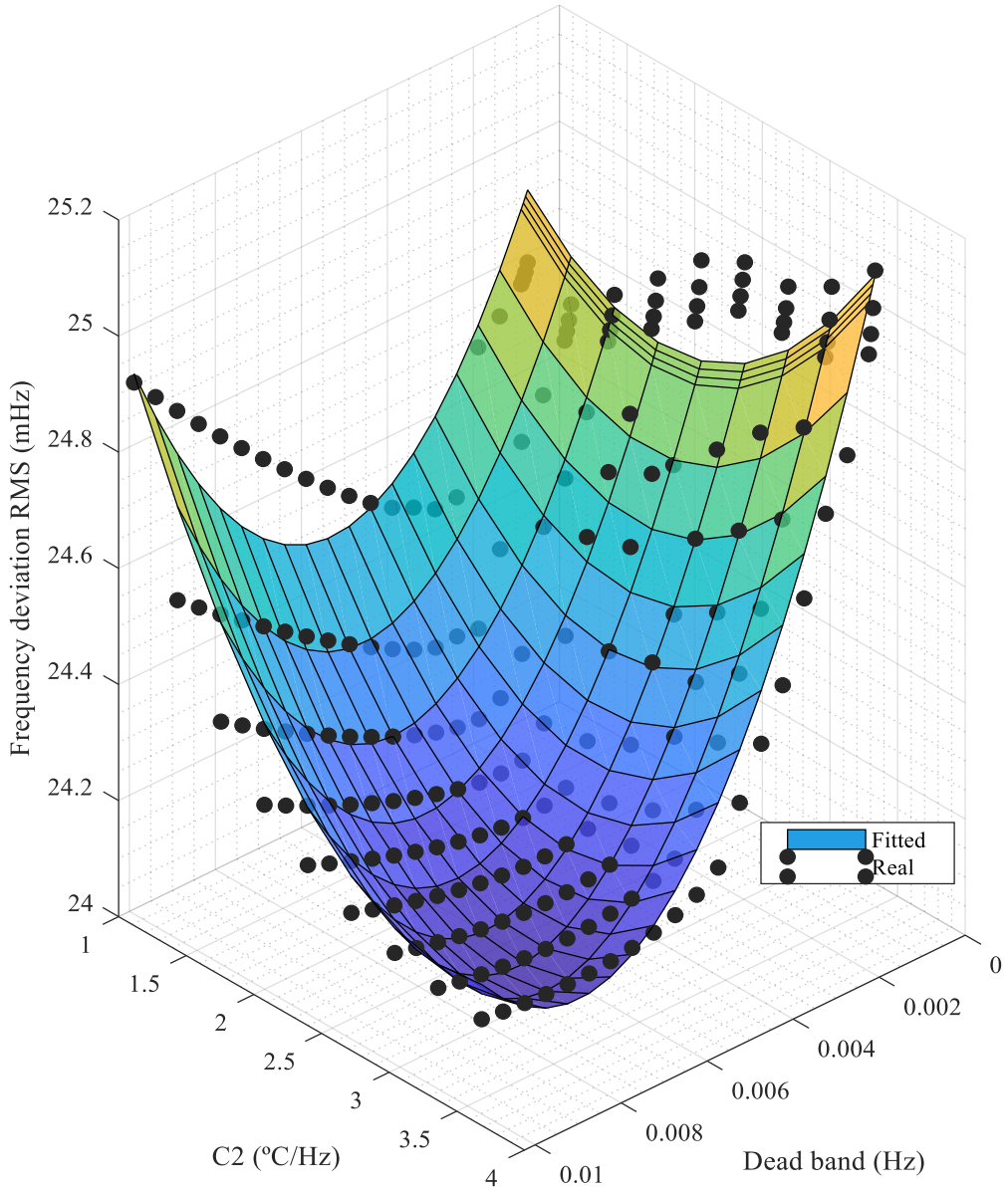


Figure 4.45: Frequency deviations RMS: real vs. fitted. Without RG support and $C_1 = 0$.

from frequency control duties entails the joint implementation of (a) and (c), while maintaining interaction with RG.

Normal railway consumption without RG support to frequency control tasks

Fig. 4.45 compares the actual and the fitted surface depicting frequency deviation RMS in the absence of renewable generation (RG) support and primary frequency control. The obtained surface equation exhibits a commendable fit with a coefficient of determination (R^2) of 0.96. The discrepancies for DB_{min}, $C_{2_{min}}$, and $\Delta f_{eq_{RMS\,min}}$ are 7%, 0%, and -0.36%, respectively.

Fig. 4.46 displays the actual and the fitted surface of frequency deviation RMS in the absence of renewable generation (RG) support but with primary frequency control. The resulting

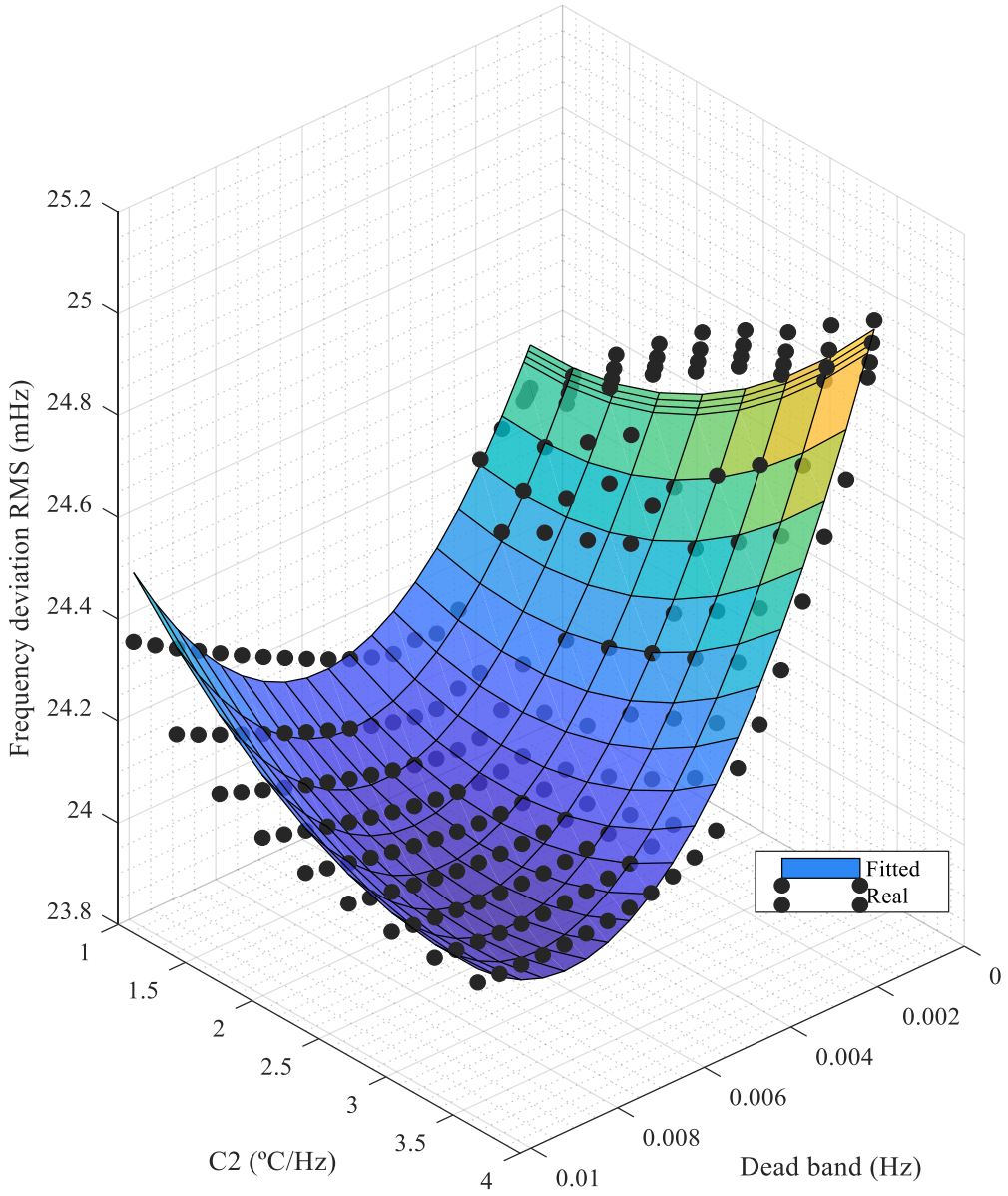


Figure 4.46: Frequency deviations RMS: real vs. fitted. Without RG support and $C_1 \neq 0$.

surface equation exhibits a slightly diminished fit compared to Fig. 4.45 with a coefficient of determination (R^2) of 0.94. The deviations for DB_{min}, $C_{2_{min}}$, and $\Delta f_{eq_{RMS\,min}}$ are 52.6%, 54.8%, and -0.2%, respectively. Despite noticeable fitted deviations, the predicted frequency deviation RMS still aligns with the minimum values.

Normal railway consumption with RG support to frequency control tasks

Fig. 4.47 illustrates the actual and fitted frequency deviation RMS with renewable generation (RG) support but without primary frequency control. The resulting surface equation yields an equivalent fit to Fig. 4.45 ($R^2 = 0.96$), featuring deviations of -6.45%, -9.55%, and -0.34% for DB_{min}, $C_{2_{min}}$, and $\Delta f_{eq_{RMS\,min}}$, respectively. Despite a larger deviation in $C_{2_{min}}$ compared

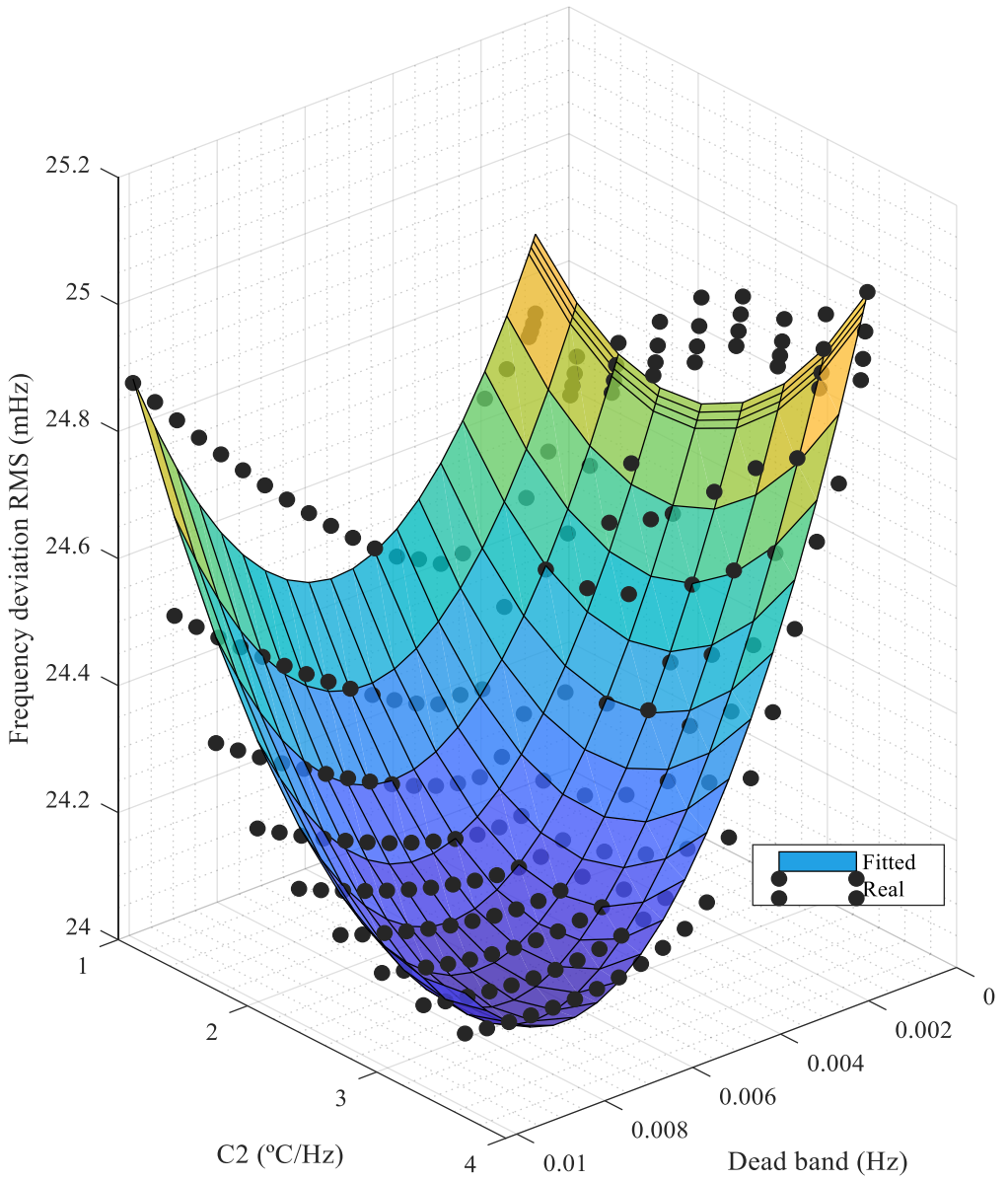


Figure 4.47: Frequency deviations RMS: real vs. fitted. With RG support and $C_1 = 0$.

to the case in Fig. 4.45, the difference in the fitted frequency deviation RMS is smaller.

Fig. 4.48 depicts the actual and fitted frequency deviation RMS with both RG support and primary frequency control. The resulting surface equation mirrors the fit of Fig. 4.46 ($R^2 = 0.94$), showcasing the same DB_{min} and $C_{2_{min}}$, and a slightly improved $\Delta f_{eq_{RMS\,min}}$ (-0.19%).

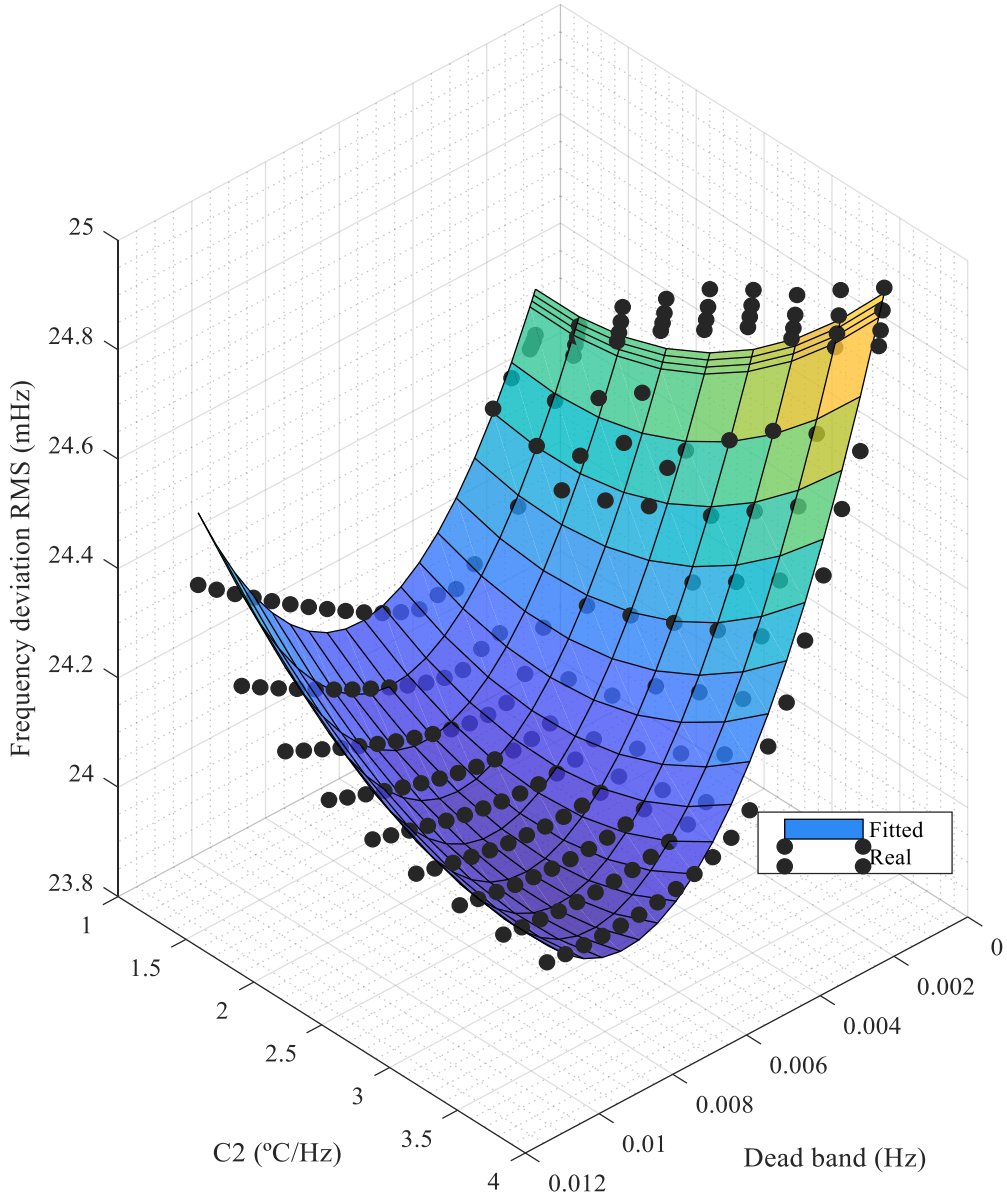


Figure 4.48: Frequency deviations RMS: real vs. fitted. With RG support and $C_1 = 0$.

4.4.4 Analysis of models

Table 4.5 compiles the key values from the preceding section, along with the resultant parameters derived from equation (4.7) for each scenario. The dead band emerges as the most influential variable. Its quadratic terms carry a weight nearly a thousand times greater than the product between this and C_1, and almost a million times more than C_1 and its quadratic term. Consequently, p_{01} and p_{02} could be disregarded if necessary. Consequently, the surface would be defined solely by the linear (p_{10}) and quadratic (p_{20}) terms of the dead band and the relationship between both linear variable terms (p_{11}).

In the preceding section, the addition of primary frequency control noticeably increased the deviation in the fitting. This can be elucidated by Table 4.5. In all cases involving C_1, the

weight of control parameters diminishes. Since the curve-fitting equation does not account for C_1, and its contribution leads to a reduction in $\Delta f_{eq_{RMS}}$, the impact of the other parameters on the overall frequency performance diminishes. This fitting discrepancy is also evident in cases with RG support. However, the reduction in parameter weight is less pronounced. For instance, while p_{02} decreases by 49.22% when incorporating C_1, it only diminishes by 0.22% with RG support consideration. Despite the fitting discrepancies, all C_2 and DB values obtained through fitting align with the zone associated with the least frequency deviation RMS. This underscores the capacity of the supplementary control to yield some of the most substantial frequency deviation reductions, even in conjunction with other contributions to frequency control.

Table 4.5: Terms of (4.7), goodness of fit, minimum values with different combinations of frequency control and RG support.

Case	$p_{00}10^{-2}$	$p_{10}10^{-2}$	$p_{01}10^{-5}$	p_{20}	$p_{11}10^{-2}$	$p_{02}10^{-5}$	R^2	DB_{min} (fitted, real)	$C_{2_{min}}$ (fitted, real)	$\Delta f_{eq_{RMS\,min}}$ (fitted, real)
RG support: off. $C_1 = 0$	2.559	-19.4	-52.46	21	-3.85	13.42	0.96	7.25, 6.75	3.0417, 3.0417	24.084, 24.17
RG support: off. $C_1 \neq 0$	2.488	-19.21	-12.74	19.5	-3.445	6.814	0.94	7.25, 4.75	2.7205, 1.7569	23.99, 24.039
RG support: on. $C_1 = 0$	2.554	-18.89	-53.36	20.41	-3.718	13.39	0.96	7.25, 7.75	3.0417, 3.3628	24.039, 24.12
RG support: on. $C_1 \neq 0$	2.483	-18.72	-13.87	19	-3.336	6.858	0.94	7.25, 4.75	2.7205, 1.7569	23.944, 23.99

The following sections illustrate the advantages of each examined scenario in comparison to the reference scenario, which represents a system devoid of trains contributing to frequency control and lacking RG frequency support. The initial section evaluates the frequency performance under standard railway consumption, while the second one explores the repercussions of abrupt load shedding.

Enhancement of frequency performance under normal railway consumption:

The outcomes from the preceding sections are presented concerning the absolute frequency deviation RMS. The reference case utilized corresponds to the orange line in Fig. 4.44. Table 4.6 consolidates the maximum reduction in frequency deviation RMS for the identical cases outlined in Table 4.5.

Table 4.6: Maximum frequency deviation RMS reduction under normal railway consumption.

Case	Compared to reference case without RG support
RG support: off. $C_1 = 0$	19.79%
RG support: off. $C_1 \neq 0$	20.23%
RG support: on. $C_1 = 0$	19.96%
RG support: on. $C_1 \neq 0$	20.39%

In terms of primary frequency control, the maximum reduction demonstrates a marginal increase of 0.43% in both cases. The support from renewable generation (RG) results in a 0.17% reduction in frequency deviation RMS for both scenarios. Consequently, the cumulative contribution of the proposed supplementary frequency control amounts to 19.79%. Notably, the thermal comfort of passengers remains unaffected. Fig. 4.49 illustrates the range of maximum temperature deviations in the scenario with the most significant railway contribution to frequency control. It is noteworthy that, aside from not surpassing a temperature deviation outside the thermal comfort range, the area with the highest frequency control contribution does not coincide with the region of the most considerable temperature deviations. This implies that the optimal values of dead band and C_1 are not those posing the greatest risk to thermal comfort. Based on the contribution to frequency deviation RMS reduction, it is reasonable to assert that railways can effectively alleviate renewable generation from frequency control duties. However, the significance of each contributor to frequency control fluctuates depending on the magnitude of the frequency event in the grid.

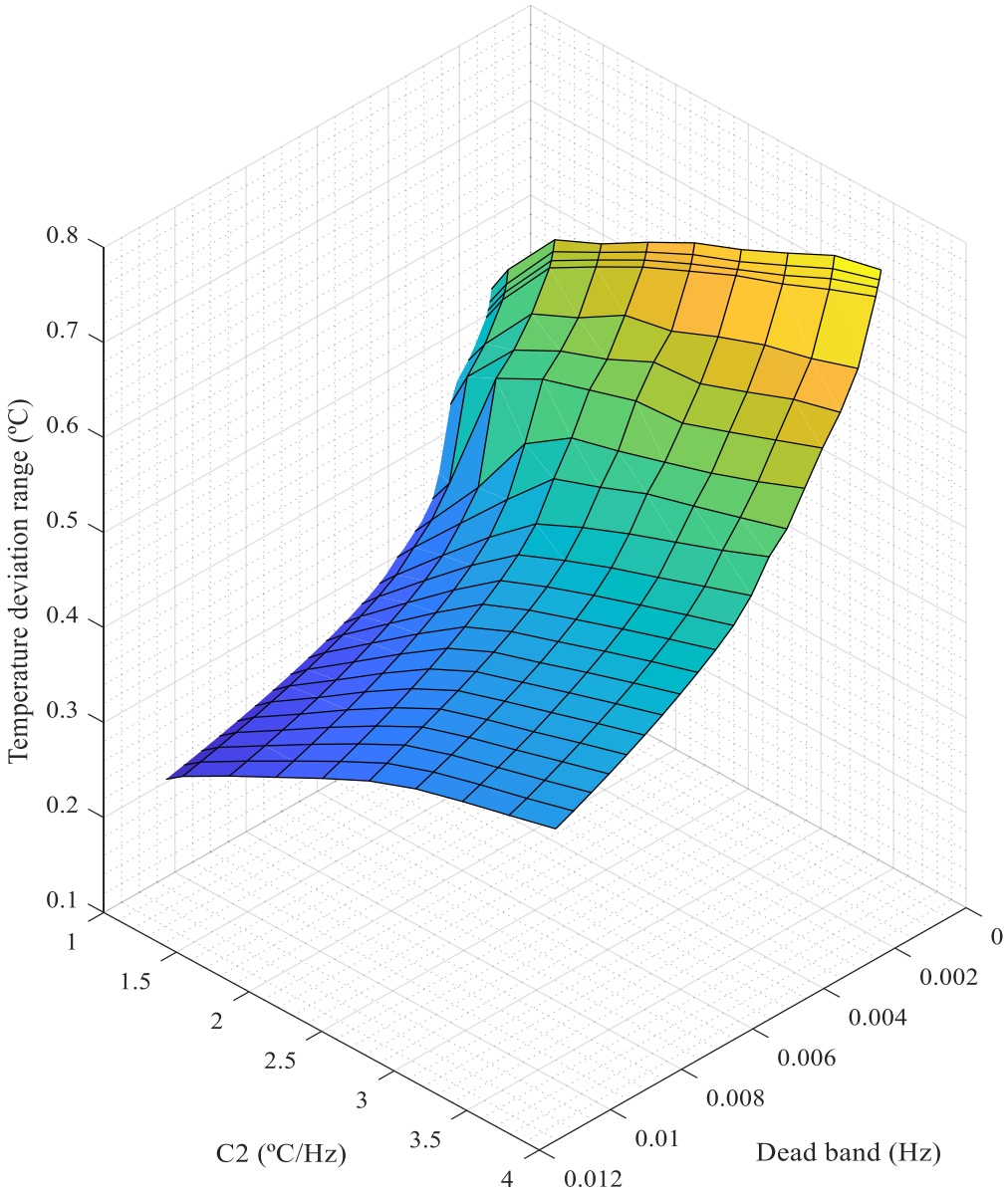


Figure 4.49: Maximum temperature deviation range without RG support and $C_1 \neq 0$.

Enhancement of frequency performance following a load shedding:

To evaluate the advantages of the proposed supplementary frequency control under more demanding scenarios, a sudden load shedding event is considered. The range of variables for the study is determined based on the findings presented in Table 4.5. Fig. 4.50 provides an overview of the reductions in frequency deviation RMS following a sudden load shedding, with subplots illustrating the outcomes for the cases detailed in Table 4.5.

Subplots (a) and (b) of Fig. 4.50 depict the impact of the proposed supplementary frequency control without and with primary frequency control, respectively. Subplot (a) showcases a maximum reduction of almost 13.9%, representing the net contribution of the proposed frequency control. Despite slight discrepancies between the predicted variable values from the

fitted surface (Table 4.5) and the actual maximum reductions, these differences are negligible, hovering around 0.3%. Subplot (b) displays a maximum reduction of approximately 15.2%, encompassing the effect of primary frequency control. In this case, the contribution of primary frequency control is higher than in the previous section, and the predicted values align more closely with the actual results, particularly for the dead band.

Subplots (c) and (d) of Fig. 4.50 illustrate the impact of the proposed supplementary frequency control combined with RG support, without and with primary frequency control, respectively. Both subplots depict more substantial reductions compared to subplots (a) and (b), primarily due to the larger magnitude of the sudden load shedding event. As the event surpasses the frequency control provision capacity of railways, the RG assumes a more crucial role than in the previous section. Consequently, the 51% reduction in frequency deviation RMS is primarily attributed to RG support, with RG handling nearly 40% of the reduction to enhance grid frequency performance. Subplot (d) shows a reduction of 51.7%, signifying a primary frequency control contribution of around 0.7%. Although this contribution is greater than those in the previous section, it is smaller than the previous case due to the interaction with RG support.

Despite the magnitude of the load shedding event, the thermal comfort of passengers remains secure. Fig. 4.51 demonstrates the maximum temperature deviation range based on the chosen control parameters in the scenario without RG support and primary frequency control. Similar to the results in Fig. 4.49, the temperature deviations are negligible but larger due to the event's magnitude. The overall relationship between variables and temperature persists. Notably, the zone with the highest temperature deviation ranges remains sufficiently distant from the zone with the most significant frequency control contributions. This behavior differs from scenarios involving primary frequency control and virtual inertia, such as in Section 4.3, where improved frequency performance brings the system closer to thermal comfort limits.

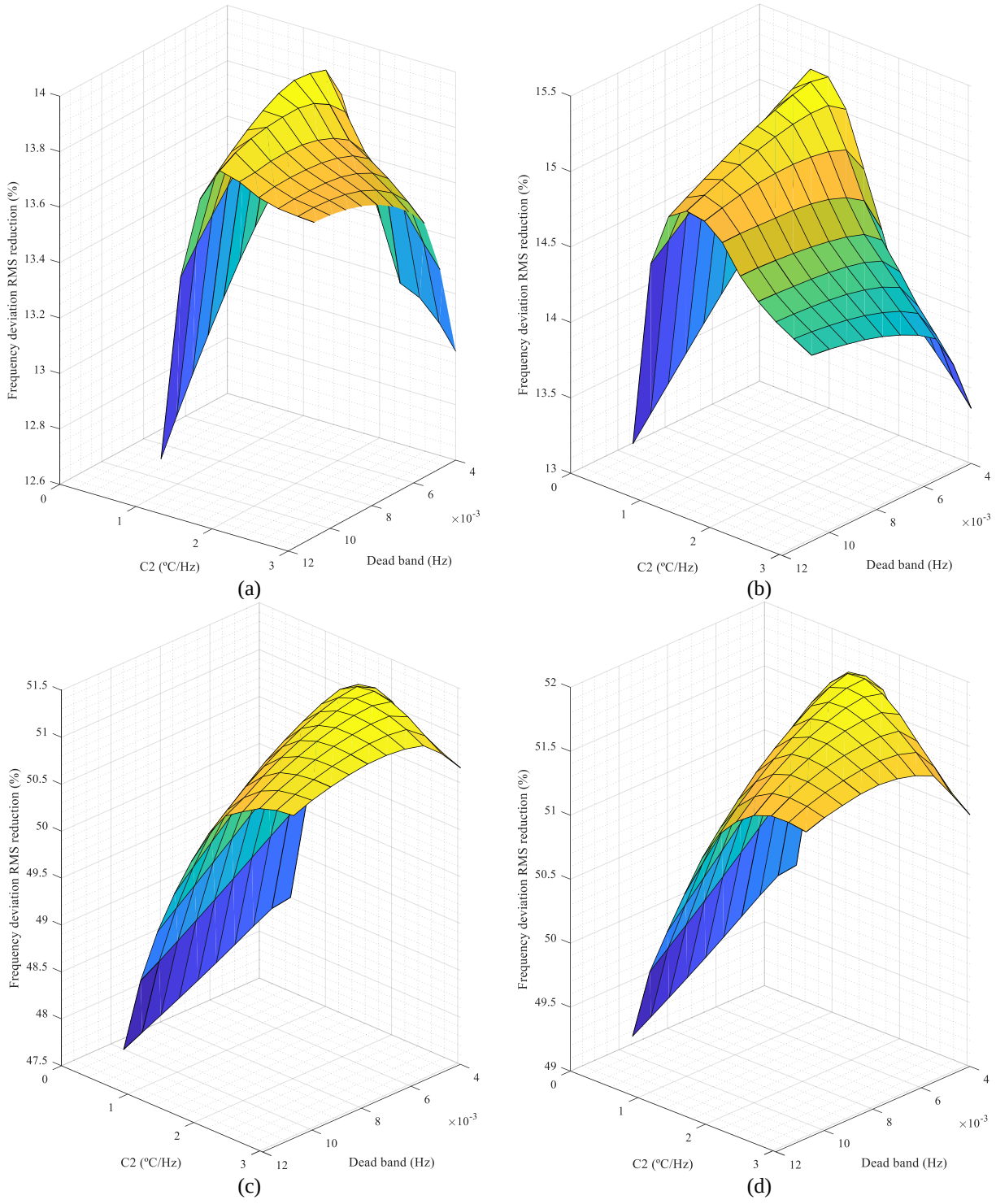


Figure 4.50: Frequency deviation RMS reduction following a sudden load shedding. a) RG support: off. C_1=0. b) RG support: off. $C_1 \neq 0$. c) RG support: on. C_1=0. d) RG support: on. $C_1 \neq 0$.

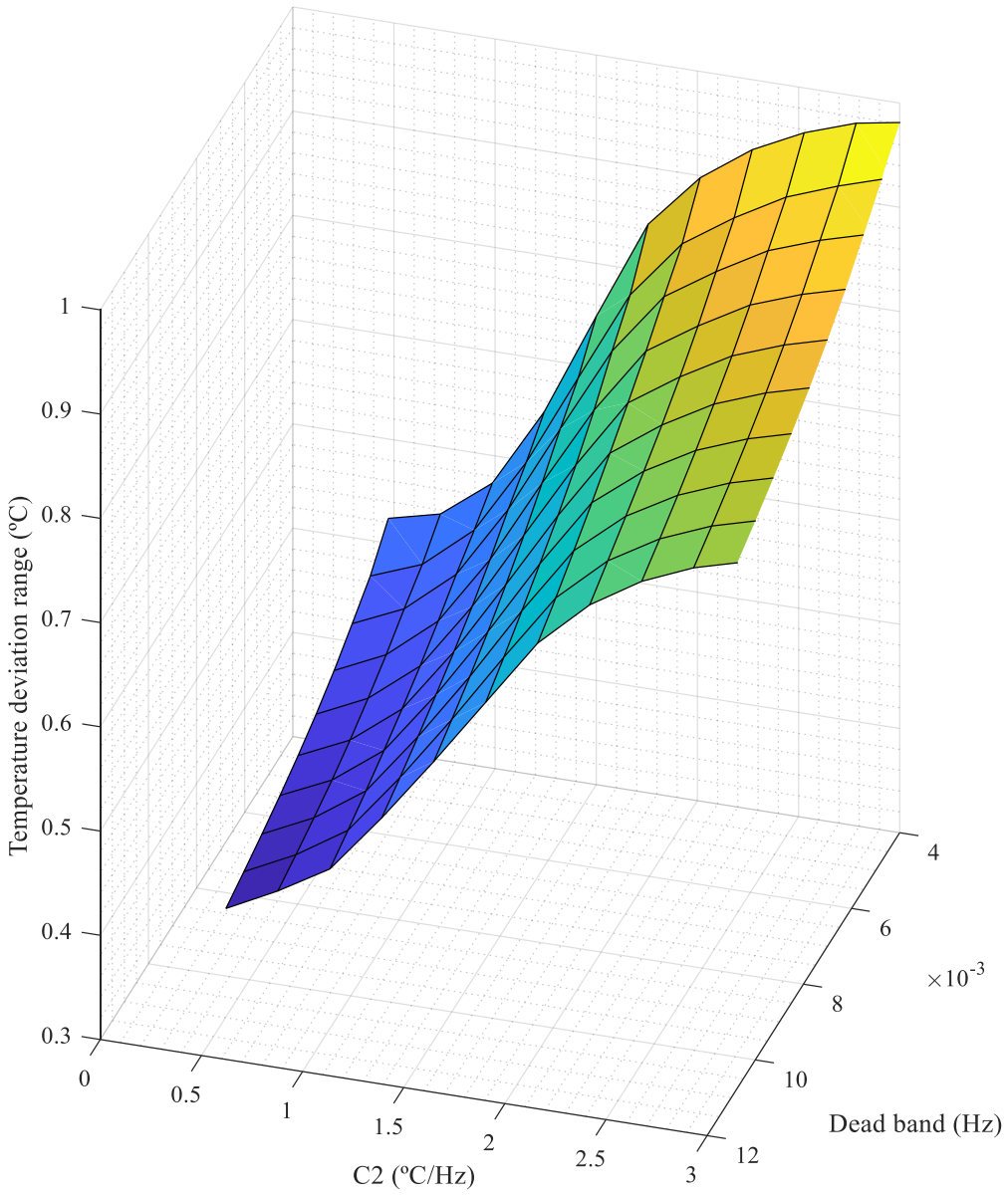


Figure 4.51: Maximum temperature deviation range following a sudden load shedding without RG support and $C_1 \neq 0$.

4.4.5 Experimental validation

The proposed frequency control methodology has undergone experimental validation using the HIL technique. In this approach, the system to be controlled, encompassing the railway system's thermal, electrical, and kinetic dynamics, along with the power system, is separated into distinct devices. These devices communicate asynchronously through analog signals, aiming to emulate realistic noise and delays. Specifically, in this study, the Typhoon HIL 404 real-time simulator is employed to emulate the plant, while the control system, responsible for adjusting the HVAC system's setpoint temperature, is implemented on an Arduino Due microcontroller. Consequently, both components operate in independent real-time systems

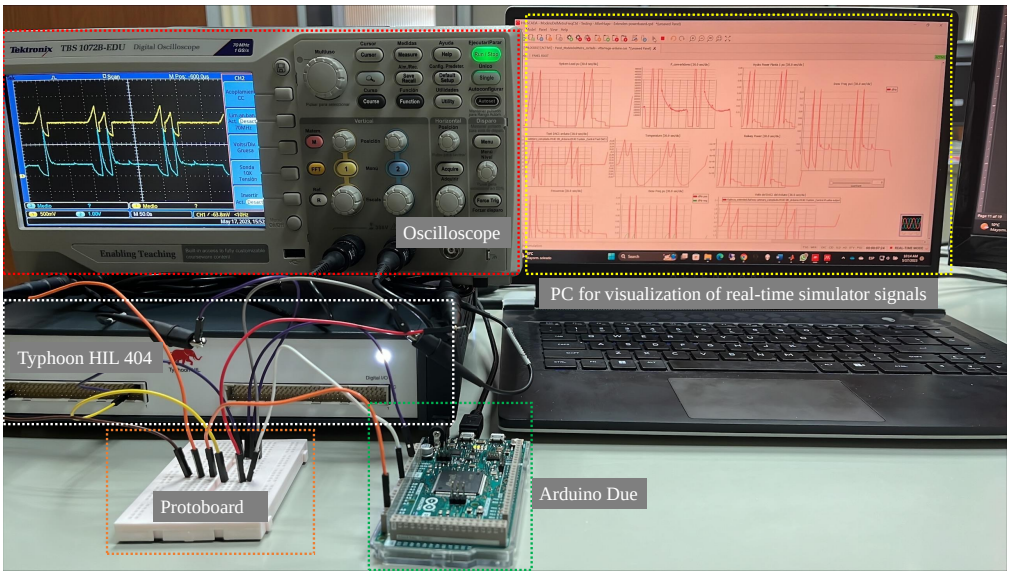


Figure 4.52: Experimental setup

and exchange actual analog frequency and temperature signals.

The experimental setup is illustrated in Fig. 4.52. The Matlab/Simulink programming environment is used to code the Arduino Due, leveraging the *Matlab Support Package for Arduino Hardware*. A protoboard facilitates the measurement of analog signals with an oscilloscope. The PC serves the purpose of visualizing internal real-time simulator signals and displaying relevant scopes on the Typhoon HIL SCADA tool. The Typhoon HIL 404 communicates only two signals with the controller implemented in the Arduino Due (the purple cable representing the common ground). The yellow and white cables transmit the frequency deviation signal from the real-time simulator to the microcontroller, while the orange and brown cables convey the updated HVAC system setpoint temperature from the microcontroller to the real-time simulator.

The experimental validation utilizes the cases presented in Table 4.5, maintaining consistent model characteristics, evaluation period, and the performance metric of frequency deviation RMS. Fig. 4.53 presents the experimental outcomes of key variables, including frequency deviations and the HVAC system setpoint temperature. The upper left plot illustrates a frequency performance comparable to that in [46], with smaller frequency deviation extrema due to the application of frequency control techniques. The evident noise in the signals, in contrast to simulation results, impacts frequency control performance but brings the results closer to reality. Despite the noise and less apparent delays associated with real signals, the proposed control still demonstrates significant benefits.

Comparing the experimental results to those in Table 4.5, for the first through fourth cases, the frequency deviation RMS is 25.76 mHz, 25.66 mHz, 25.75 mHz, and 25.66 mHz, respectively. These values represent a percentage deviation of less than 7% compared to simulation results. The effectiveness order for each case remains consistent. The center-left plot provides a detailed view, showcasing how the case with the least frequency deviation RMS also reduces instantaneous frequency deviations. The lower right plot's details reveal

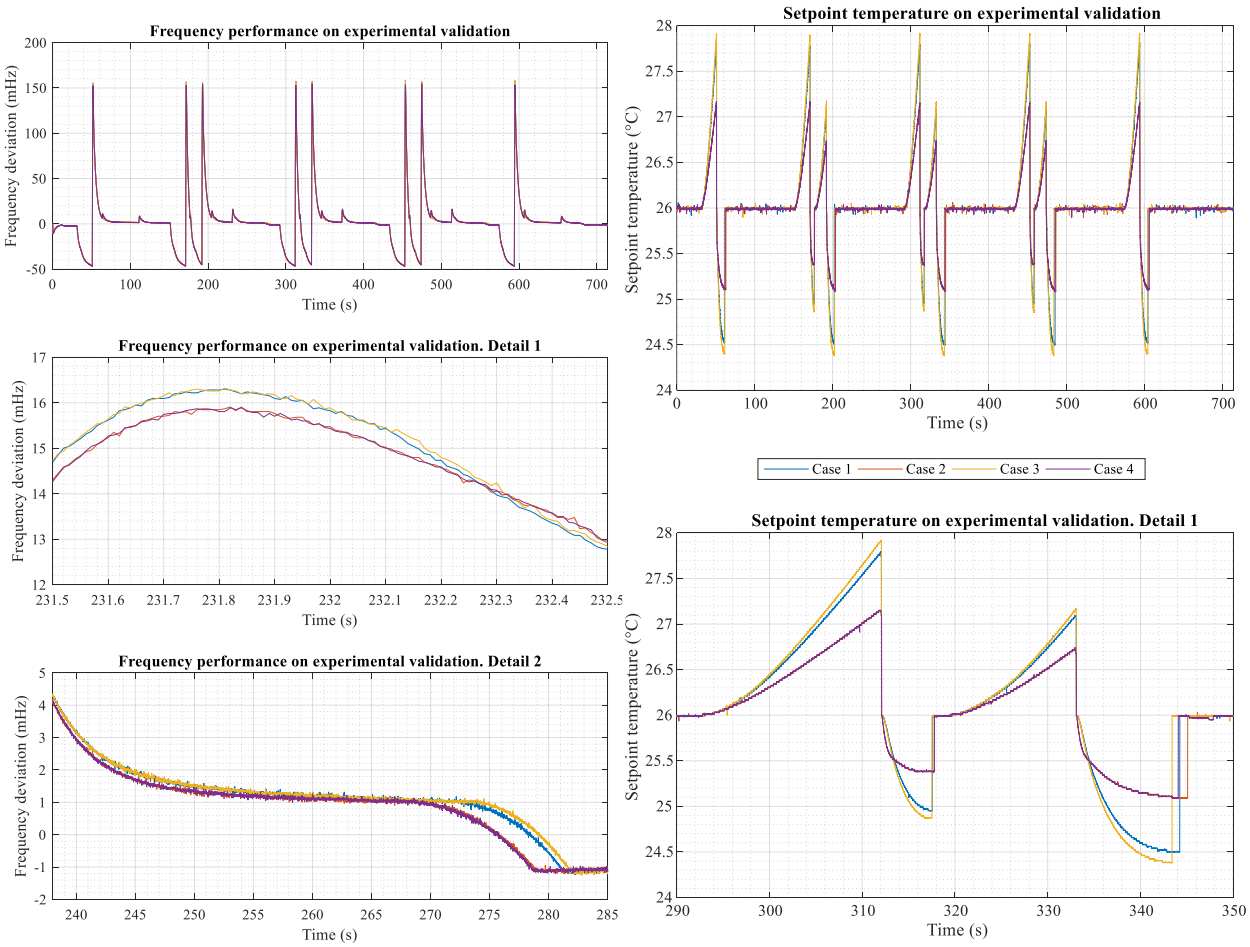


Figure 4.53: Experimental results. Frequency and setpoint temperature behavior.

that higher temperature deviations for updating the setpoint temperature do not always yield the greatest benefit. As observed in simulation results, gains, and dead band values quadratically influence the frequency deviation RMS. This implies that not only the extrema of setpoint temperature are crucial, but also their evolution over time. The lower left plot's details show how the previous temperature behavior defines the frequency performance when all dead bands are activated, indicating that similar setpoint temperatures lead to similar frequency performance.

4.4.6 Conclusions

A method with low computational cost is suggested to expedite controller tuning and assess the impact of different parameters. By fitting initial results to a surface equation, local optimum values can be estimated, variable influence on frequency performance studied, and susceptibility to inherent stochastic railway behavior reduced. The resulting equations exhibit a high goodness of fit ($R^2 \geq 0.94$). The predicted values enable a rapid approximation to local optima, offering satisfactory frequency performance. The fitting outcomes indicate that considering only the dead band may be sufficient for modeling supplementary frequency control in certain applications. This method could be particularly beneficial in situations with low-resolution models, where analytical tuning is challenging due to information scarcity, and in scenarios with high stochasticity. Additionally, the proposed surface equation-based approach allows working with averaged behavior models.

The results illustrate the efficacy of the proposed supplementary frequency control in all examined scenarios. In situations of normal consumption and sudden load shedding, standalone railway-based supplementary frequency control reduces the grid frequency deviation RMS by 19.79% and 13.90%, respectively. Furthermore, incorporating primary frequency control into the demand response strategy yields improved outcomes. For the studied cases under normal consumption and sudden load shedding, it decreases the frequency deviation RMS by 0.43% and 1.3%, respectively. It is acknowledged that the benefits of primary frequency control depend on both its tuning and the severity of events.

Relieving renewable generation from frequency control tasks is feasible under specific conditions. However, when facing considerably large frequency deviations, the proposed railway-based frequency control alone may not suffice. To maintain acceptable frequency performance during significant load events like load shedding, large generators remain essential. The results reveal that renewable generation contributes around 40% frequency deviation RMS reduction, while the proposed supplementary frequency control provides 13.9%. Nevertheless, it is crucial to note that the proposed control primarily aims for partial, not complete, relief of renewable generation from frequency control tasks.

Experimental validation demonstrates the effective functioning of the proposed control under more realistic conditions, even when exposed to noisy and delayed analog signals. This validation underscores the practicality of the proposed control. The proposal is easily implementable, as evidenced by testing on the Arduino Due, a versatile and cost-effective microcontroller. Moreover, since it is designed for integration into existing HVAC system controls, it involves only one analog input and one analog output.

These results are published in [46], [47].

4.5 Local grid frequency estimation in DC railway systems

In DC railway systems, where trains are not directly connected to the main grid, obtaining the frequency deviation signal poses a challenge with the current train topology [132]. This section introduces an approach for the estimation of grid frequency through the analysis of the DC catenary voltage waveform. The DC catenary voltage is already utilized for regulating the voltage received by trains. The main contribution of this section lies in leveraging the correlation between grid frequency and the frequency of DC voltage ripple to derive an estimation of the grid frequency solely from onboard measurements. This estimation can then facilitate the implementation of demand response algorithms in the electrical equipment onboard trains. The intellectual property associated with this concept has been formally asserted by the authors in the Spanish patent [133]. Additionally, the section proposes two methods for achieving this estimation, both of which undergo validation through computational simulations and experimental laboratory tests. One experimental test involves post-processing real analog signals, while the other employs a HIL setup for real-time validation.

4.5.1 Measurement methodology

Frequency measurement and/or estimation of AC signals is well-known. It is possible to find many works on frequency measurement in three-phase grids. Recently, the scientific community has been also focused on single-phase heavily distorted grid systems. Due to the massive integration of renewable energy, even into low-voltage distribution grids, classic techniques may be enhanced to deal with new challenges. In [134] a new method for grid frequency measurement is presented. Based on digital stochastic measurement approaches, finite impulse response filtering, and digital zero-crossing detection (ZCD), the proposed method is capable of getting accurate results with high-distorted signals. [135] also used ZCD logic, along with second-order integrator and digital counter, to propose a few-parameters method to measure AC frequency in heavily distorted systems.[136] proposed a frequency-locked loop (FLL) based on a modified harmonic flag filter and an improved ZCD estimator to provide phase and frequency under high noise and harmonics. [137] disseminated knowledge about modeling and characterization of many types of PLLs. [138] developed four new single-phase PLLs, focused on enhancing accuracy, dynamic response, and disturbance rejection capability. Based on variants of PLLs and to deal with DC bias, a multiple nonlinear harmonic-based frequency estimation is proposed in [139]. [140] proposed a single-phase PLL for amplitude and phase tracking composed by multiple half-cycle filters, a pseudo-rectification stage, and a frequency estimator with online mathematical correction.[141] proposed to combine a third-order PLL with an FLL to provide fast response and precise frequency, phase, and current estimations in isolated microgrids.[142] presented a high-accuracy and strong robustness PLL for grid synchronization which combines high order complex coefficient and moving average filters. No work about analyzing DC grid voltages to assess AC grid behavior could be found. [143] processes DC grid voltages, however, this is done for the primary protection and fault localization.

The present section presents the use of PLL and ZCD approaches as alternatives to estimate

AC grid frequency from DC railway catenary. As noticed in the literature, these approaches require filtering stages. The overall frequency estimation goes as follows: First, a band-pass filter is used to eliminate the DC component and non-desired harmonics from the input signal, the rippled DC railway catenary voltage. Second, a single-phase PLL or ZCD method is applied to the filtered signal. Finally, the estimated frequency is divided by six or twelve, depending on the traction substation topology (six or twelve pulses).

To validate the viability of the frequency estimation approach and assess the efficacy of the proposed methods, three distinct studies were conducted: software simulations (Section 4.5.2), offline experimental validation (Section 4.5.3), and real-time experimental validation (Section 4.5.4). These studies aimed to examine various aspects of implementability. It's important to note that the primary focus was on testing the conceptual framework and the suggested approaches under diverse frequency perturbations and in systems with different characteristics, without delving into the detailed dynamics causing these perturbations. The scheme details and the values of parameters are included in Appendix D..

4.5.2 Computational simulations

A basic railway system was simulated, consisting of a 50 Hz three-phase power system supplying power to both a traction substation and a train. The substation comprises a three-phase double-winding transformer connected in series with a three-phase uncontrolled rectifier (TPUR) equipped with standard capacitive filtering. It's noteworthy to mention that higher filtering capacity results in reduced ripple, making AC frequency estimation more challenging. The catenary and the train were simplified as a resistive load. The power system was modeled as a three-phase voltage source with a controllable frequency, following (4.9):

$$\begin{cases} u_{an}(t) = U_0 \ \sin(2\pi f t) \\ u_{bn}(t) = U_0 \ \sin(2\pi f t - 2\pi/3) \\ u_{cn}(t) = U_0 \ \sin(2\pi f t + 2\pi/3) \end{cases} \tag{4.9}$$

Here, $u_{an}(t)$, $u_{bn}(t)$, and $u_{cn}(t)$ represent the instantaneous phase-to-neutral voltages, and U_0 denotes the voltage amplitude.

To evaluate the capacity of the proposed method in tracking the AC grid frequency based on DC measurements onboard the train, three distinct types of frequency variations have been artificially generated: step changes (4.10), ramp changes (4.11), and sinusoidal fluctuations (4.12).

$$f(t) = \begin{cases} f_0 & , t < t_1 \\ f_0 + F_0 & , t_1 < \ t < t_2 \\ f_0 & , t > t_2 \end{cases} \tag{4.10}$$

$$f(t) = \begin{cases} f_0 & ,t < t_1 \\ f_0 + \frac{F_0(t-t_1)}{t_2-t_1} & ,t_1 \leqq\ t \leqq t_2 \\ f_0 + F_0 & ,t > t_2 \end{cases} \tag{4.11}$$

$$f(t) = \begin{cases} f_0 & ,t < t_1 \\ f_0 + F_0\ \sin(\frac{2\pi(t-t_1)}{t_2-t_1}) & ,t_1 \leqq\ t \leqq t_2 \\ f_0 & ,t > t_2 \end{cases} \tag{4.12}$$

In the provided equations, f_0 represents the rated frequency (specifically, 50 Hz), while t_1 and t_2 denote the initial and final moments of the frequency event, respectively. Additionally, F_0 stands for the amplitude of the frequency event. The blue lines in Fig. 4.54, Fig. 4.55, and Fig. 4.56 (referred to as 'Reference' in each figure legend) illustrate the three scenarios with $t_1 = 1$ s, $t_2 = 3$ s, and $F_0 = 0.8$ Hz. It is important to note that various events, such as short circuits, load shedding, generation loss, intermittent generation, etc., can induce frequency variations in power systems. The synthesized frequency variations in (4.10), (4.11), and (4.12) are designed to mimic some possible and more challenging frequency disturbances that may impact the accuracy of frequency estimation.

In Fig. 4.54, it is evident that the ZCD method excels in achieving highly accurate frequency tracking. The proposed single-phase PLL also demonstrates satisfactory tracking, albeit at a slower pace, with occasional temporary deviations attributed to transient characteristics in its controllers. The ZCD method performs notably well during transitions. In the steady-state regime, the single-phase PLL aligns perfectly with the reference, while the ZCD exhibits periodic deviations ranging from -0.2 mHz to 13 mHz. Both approaches exhibit nearly negligible average estimation deviations (2 mHz and 0 mHz for single-phase PLL and ZCD, respectively). Their standard deviation and RMS of estimation deviation are equivalent, approximately 0.1 Hz and 0.05 Hz, respectively.

In Fig. 4.55, both implementations showcase similar behavior to the reference signal. Given that the ramp represents a gradual variation, the distinctions in their performance are minimal, though the single-phase PLL appears to have a slight advantage. In this case, the single-phase PLL records an average estimation deviation of -0.5 mHz, while the ZCD reports -1.8 mHz. Standard deviation and RMS continue to display very comparable results for both methods, yet the values are considerably smaller than in the step case: around 0.8 mHz and 6.2 mHz for single-phase PLL and ZCD, respectively. The ZCD method retains the same periodic deviation observed in Fig. 4.54 during steady-state conditions.

In Fig. 4.56, where the frequency varies sinusoidally, both implementations successfully achieve smooth frequency tracking. This scenario represents a more realistic depiction of frequency variations in power systems, characterized by non-sudden and fluctuating perturbations. Both methods yield null average estimation deviation for the ZCD and nearly null (-0.1 mHz) for the single-phase PLL. Once again, the standard deviation and RMS metrics for both cases are identical, measuring around 7.3 mHz and 11.8 mHz for single-phase PLL and ZCD, respectively.

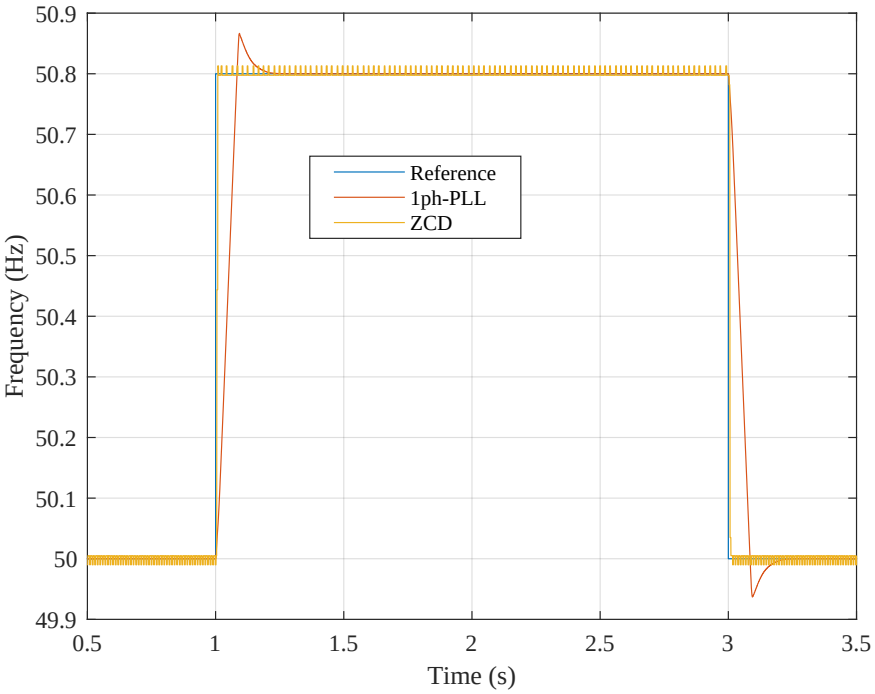


Figure 4.54: Frequency estimation following sudden frequency steps.

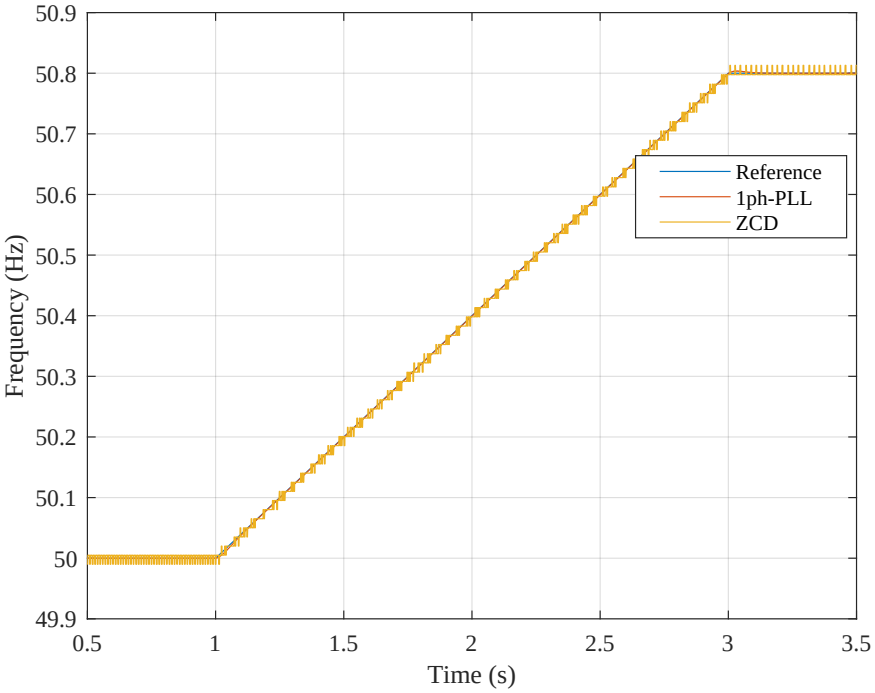


Figure 4.55: Frequency estimation following a frequency ramp.

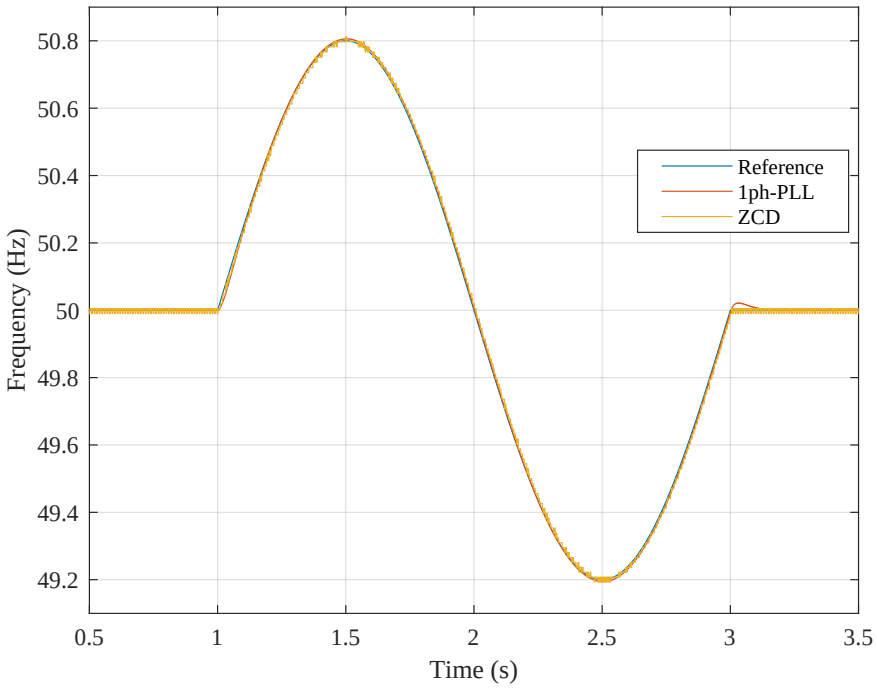


Figure 4.56: Frequency estimation following a sinusoidal frequency fluctuation.

4.5.3 Offline experimental validation

The experimental validation of the proposed method is conducted in a laboratory test-bench, outlined schematically in Fig. 4.57. This setup consists of a basic power system and a simplified railway system.

A visual representation of the setup is provided in Fig. 4.58. The power system emulation involves a genuine synchronous generator (A) and a three-phase resistive load (B, located behind the bench). The generator is powered by a controlled induction motor (C), serving as a surrogate for the prime mover. To achieve this, the induction motor receives power from the main grid, controlled by a variable frequency drive, and is mechanically linked to the generator. The railway system emulation includes a commercial TPUR (D), simulating the traction substation, which supplies power to a DC load (E), representing the train consumption.

The experimental setup is equipped with various measurement and monitoring devices. A four-channel oscilloscope (F) is utilized to capture the three AC phase-to-neutral voltages and the DC voltage, as illustrated in Fig. 4.59. The test-bench produces authentic non-ideal three-phase voltages, resulting in irregular rectified signals. The machines introduce harmonics and imbalance due to factors such as eccentricities, manufacturing defects, and uneven winding distribution. Moreover, the presence of a noisy environment and measurement errors from the oscilloscope contribute additional realism to the recorded data.

Subsequently, these collected data undergo offline post-processing using both the single-phase PLL and ZCD algorithms. Fig. 4.60 illustrates the outcomes of both estimations, wherein

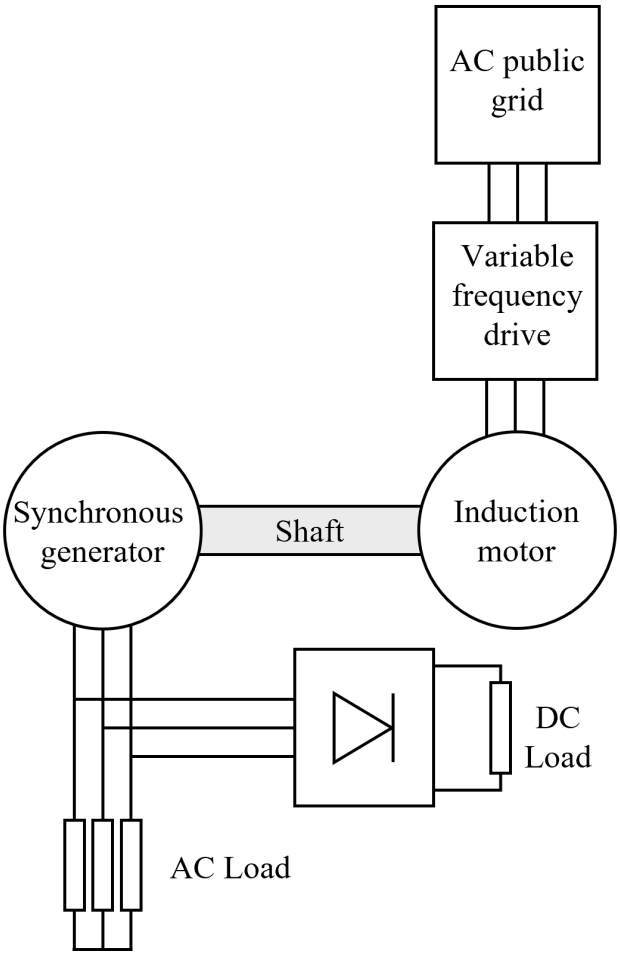


Figure 4.57: Schematic of the laboratory test-bench.

the expected frequency value (depicted by the blue line) is derived from measurements on the AC side (channel two, CH2, in Fig. 4.59).

The single-phase PLL method yields maximum, minimum, average, and RMS frequency deviation values of 16.7 mHz, -7.8 mHz, 1.6 mHz, and 5.9 mHz, respectively. In comparison, the ZCD method shows corresponding values of 27.1 mHz, 13.8 mHz, 20.4 mHz, and 20.6 mHz. It is evident that both approaches exhibit satisfactory performance, even when subjected to noisy and distorted signals. While the single-phase PLL method demonstrates slightly smaller estimation deviations, both methods appear suitable for frequency estimation, facilitating the implementation of demand response strategies.

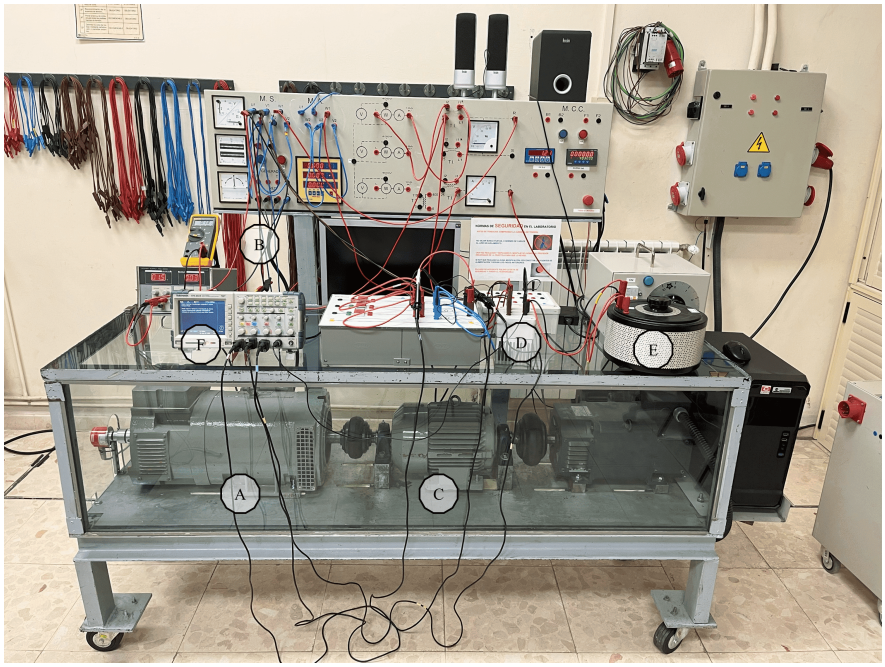


Figure 4.58: Laboratory test-bench.

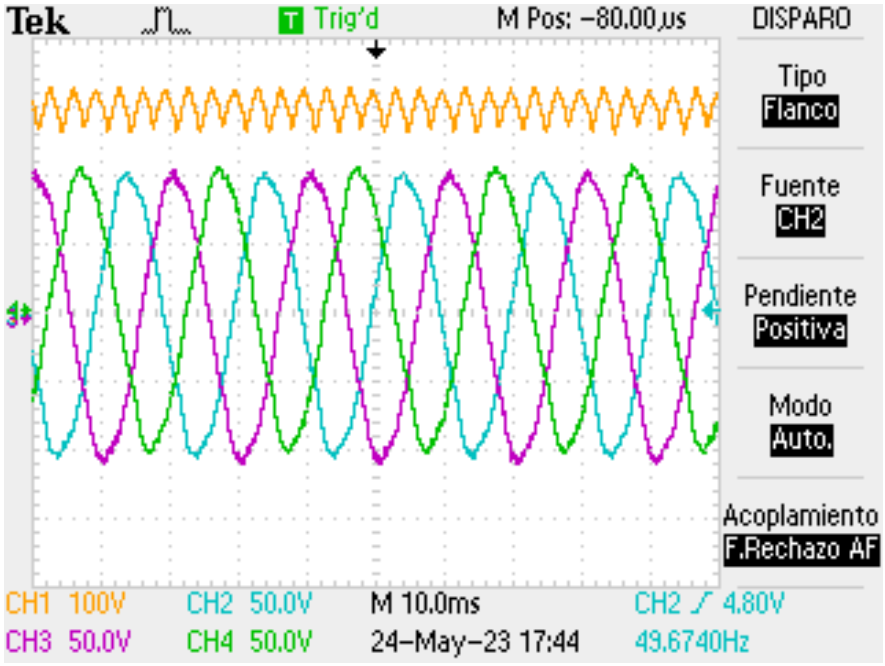


Figure 4.59: AC phase-to-neutral voltages (magenta, green, and blue) and DC voltage (yellow) recorded with the oscilloscope.

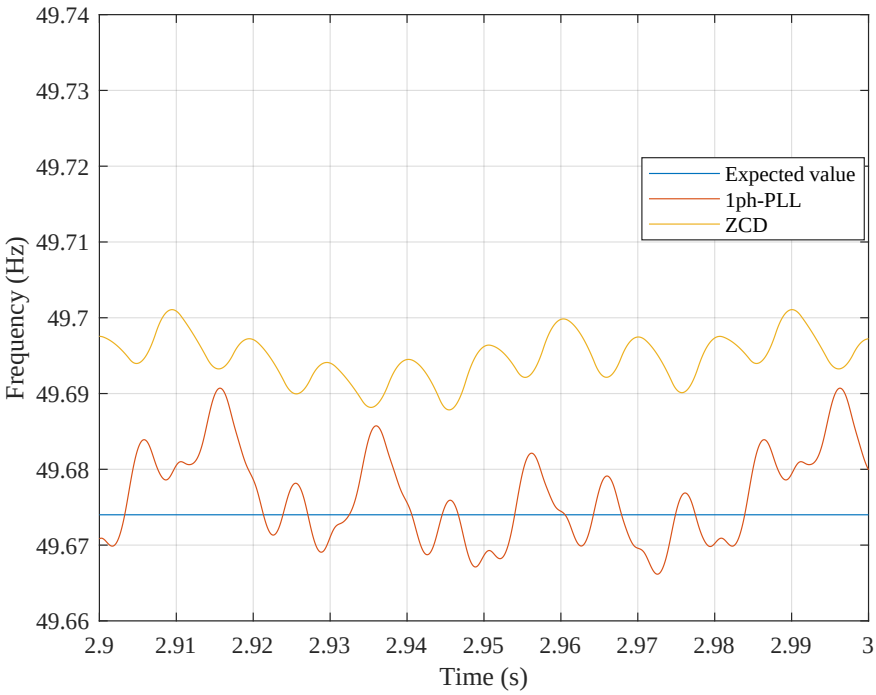


Figure 4.60: Offline frequency estimation based on real recorded data.

4.5.4 Real-time experimental validation

In addition to the investigations conducted in Sections 4.5.2 and 4.5.3, a third study utilizing the HIL technique is performed with a dual purpose. Firstly, it aims to validate the feasibility of implementing the proposed algorithms in real-time, considering their intended application for control purposes. Secondly, the HIL technique offers the advantage of combining the flexibility and sophisticated modeling capabilities of simulation environments, as seen in section 4.5.2, with the availability of physical signals, as observed in section 4.5.3.

HIL techniques enable the assessment of real-time interactions between emulated and real devices asynchronously with actual analog signals [144]. For instance, a complex power system model interacting with a detailed model of a railway system could be implemented in a real-time simulator, referred to as the plant model. One of the plant model's outputs might be the catenary voltage signal observed from a particular train, and the HIL system can generate the corresponding real-time physical analog signal. This signal can be measured using a genuine measurement system, such as an oscilloscope, or it can serve as the input to an external controller where the frequency estimation proposal is integrated into the control algorithm.

In this section, a plant model resembling the one outlined in section 4.5.3 is implemented in a Typhoon HIL 404 real-time simulator. The analog output is recorded using an oscilloscope and is utilized as an input to a frequency estimator, also implemented in the same real-time hardware, as illustrated in Fig. 4.61. To ensure asynchronicity between the plant model and the frequency estimator, besides exchanging only the analog signal, different sample times are employed.

The emulated power system operates at a steady-state frequency of approximately 33 Hz, and its response to three distinct sets of perturbations is examined: variations in the mechanical torque of the synchronous generator (Fig. 4.62), fluctuations in the consumption of the railway system (Fig. 4.63), and the combination of both (Fig. 4.64). In these figures, only the ZCD algorithm is implemented, as it has demonstrated superior frequency tracking compared to the single-phase PLL, as evidenced in earlier sections. It is worth noting that variations in mechanical torque in actual power systems may be triggered by faults, issues with the primary energy source (e.g., gas, water), and load-following, among other common scenarios. Therefore, the frequency perturbations investigated in this subsection aim to evaluate the proposed method's performance under frequently encountered disturbances affecting grid frequency on the AC side.

Fig. 4.65 illustrates the railway consumption profile employed in the earlier tests. This profile is a modified version of the one utilized in Sections 4.2 and 4.3. It simulates the movement of four trains in two directions, passing through three traction substations and five passenger stations. While the profile remains consistent, the specific values are chosen in accordance with the modeling methodology outlined in section 4.5.3.

In figures 4.62, 4.63, and 4.64, the actual frequency evolution, directly derived from the synchronous generator speed, is depicted with a blue line, while the estimated frequency is represented by a red line.

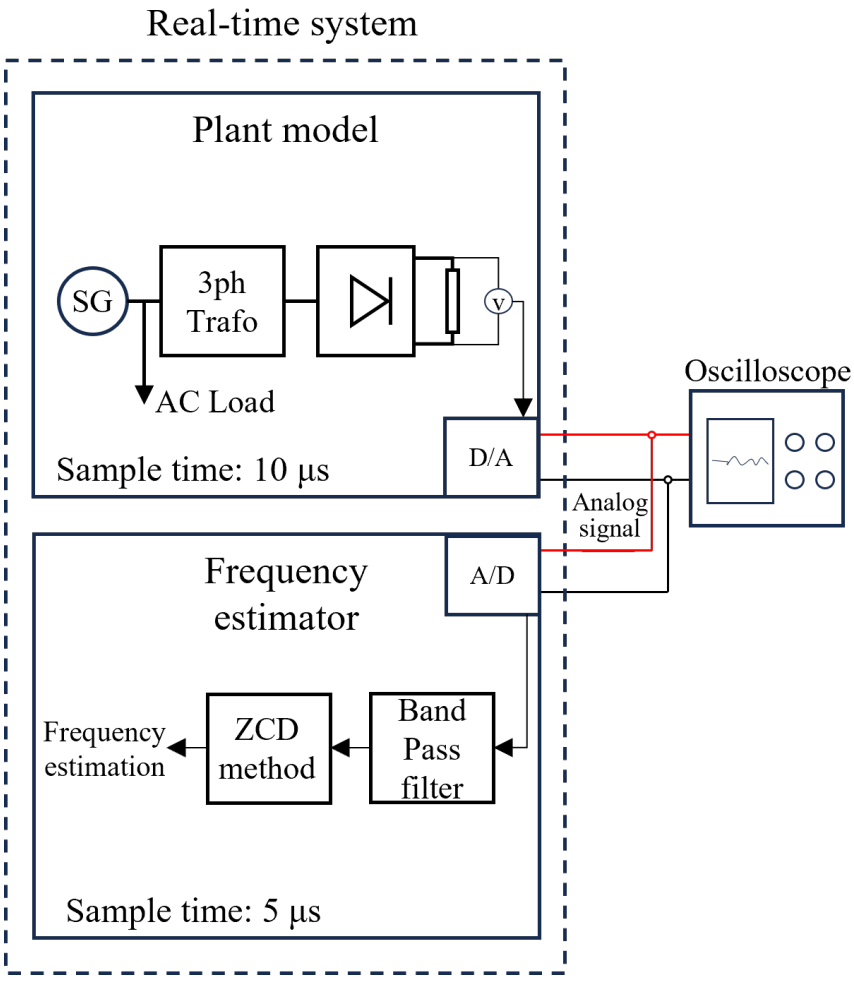


Figure 4.61: HIL setup schematic.

Upon initial observation, it is evident that the frequency estimation approach consistently delivers results with minimal deviations. In the test results shown in Fig. 4.62, where three-stepped torque ramps are applied to the synchronous generator simulating variations in consumption in the power system, the method exhibits a smooth tracking of frequency evolution. The detailed view in Fig. 4.63 and the overall behavior in Fig. 4.64 demonstrate the proposed approach's capability to estimate frequency even under abrupt power variations on the DC side. Some occasional outliers, lasting for a single time step, are primarily attributed to the combined effects of rapid power fluctuations and the computational execution rate. The deviation band, clearly visible in Fig. 4.63, aligns with the order of magnitude of the average and RMS of estimation deviations calculated in section 4.5.2. The influence of noise in the DC voltage signal necessitates a reduction in the calculation time step, leading to an overall increase in computational cost. It is important to note that the frequency estimation output is presented without filtering. The addition of an appropriate filter could enhance the smoothness of the output, making it more suitable for integration into frequency control algorithms.

The results in Fig. 4.62 indicate an average and RMS estimation deviation of approximately

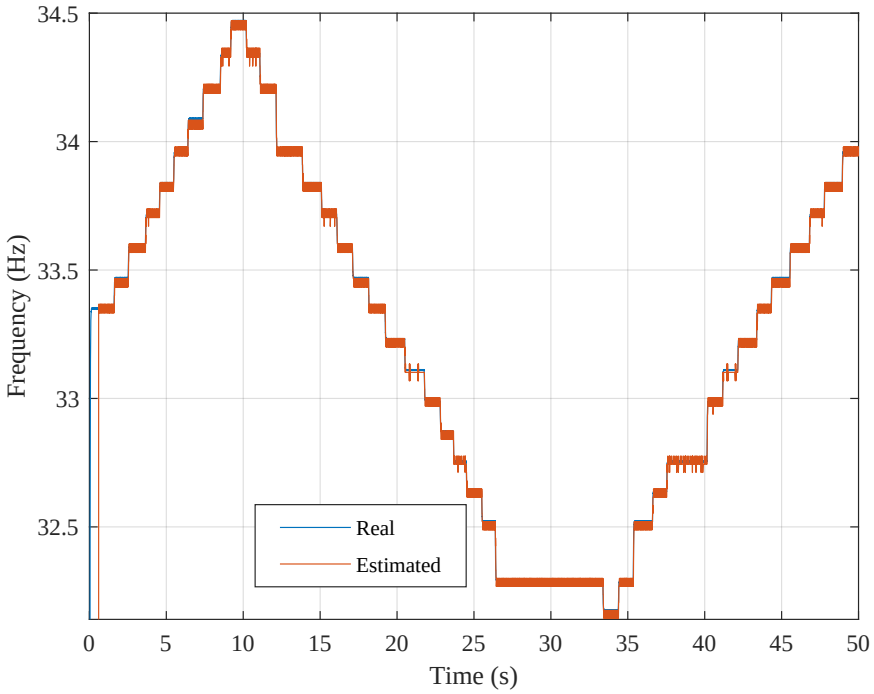


Figure 4.62: Real-time frequency estimation in the case of variations in the mechanical torque of the synchronous generator.

-9 mHz and 18 mHz, respectively. Periods of constant frequency in all scenarios (e.g., between $t = 55$ s and $t = 105$ s in Fig. 4.63) exhibit slightly smaller average and RMS estimation deviations. From $t = 5$ s to $t = 10$ s in Fig. 4.62, these performance indicators worsen to -11 mHz and 20 mHz, respectively. It is noteworthy that, across all scenarios, the overall average estimation deviation remains around -9 mHz. This underscores the feasibility and effectiveness of estimating AC grid frequency from DC voltage, even in noisy scenarios and with varying AC and DC power conditions. Considering that power systems typically allow frequency deviation events of around 1 Hz to trigger frequency controls [120], having an average deviation of 9 mHz still enables accurate tracking of the frequency evolution.

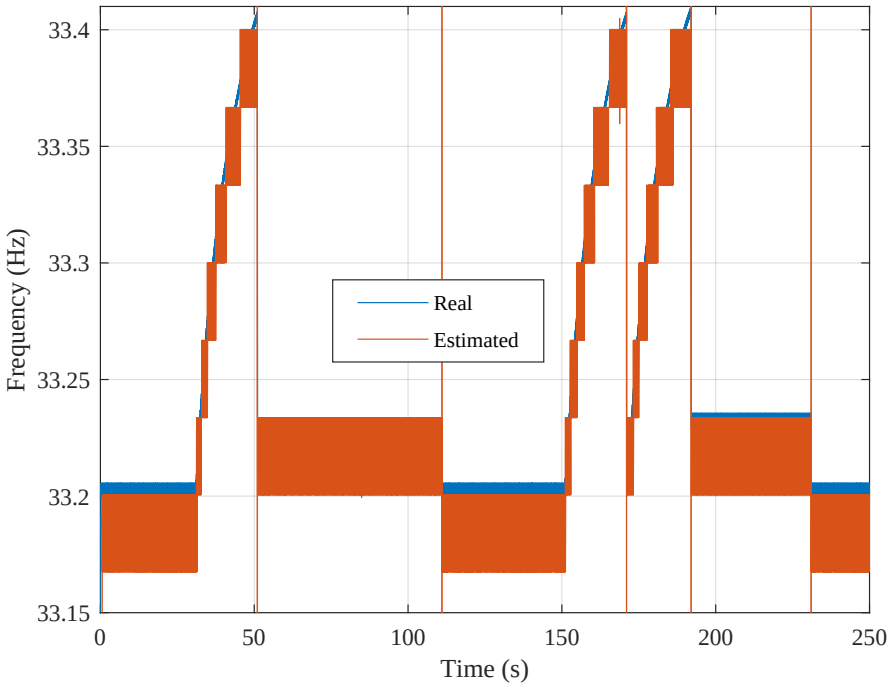


Figure 4.63: Real-time frequency estimation in the case of variations in the railway consumption.

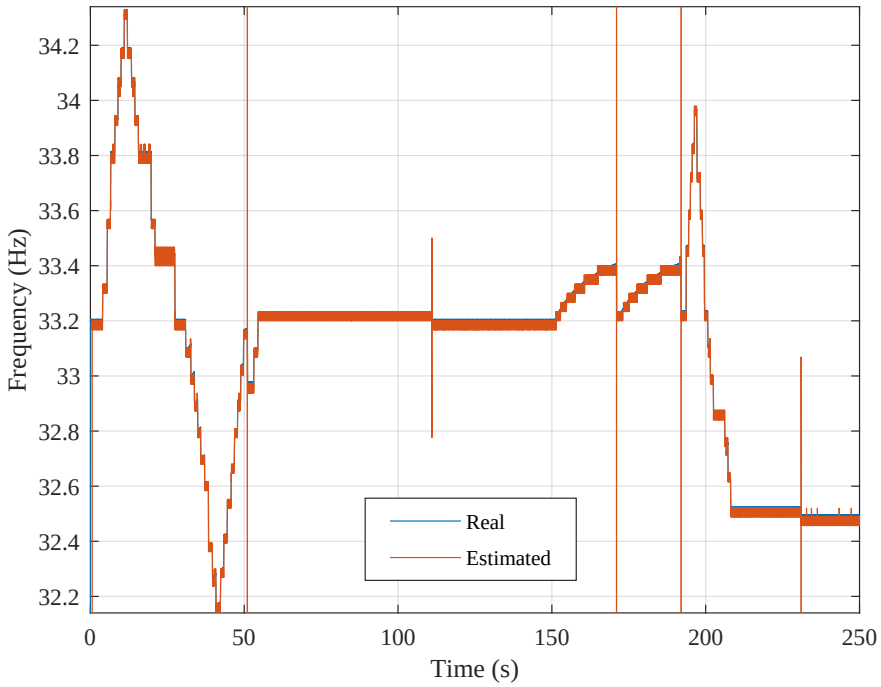


Figure 4.64: Real-time frequency estimation in the case of simultaneous variations in the torque of the synchronous generator and in the railway consumption.

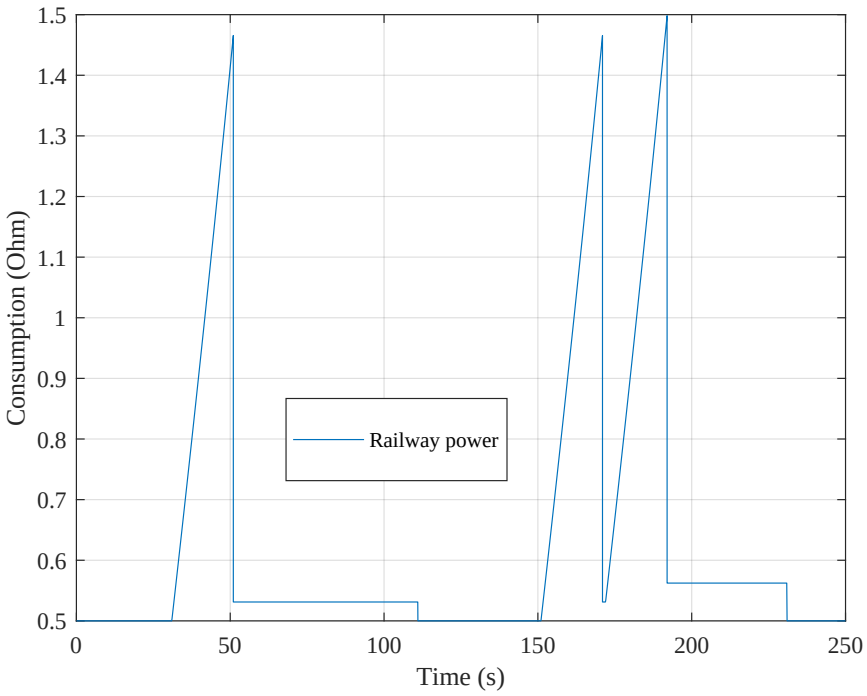


Figure 4.65: Railway equivalent consumption profile.

4.5.5 Conclusions

Loads powered by DC grids, such as trains in DC railway systems, face challenges in accessing the AC grid frequency signal directly. To address this issue, a method is proposed to estimate the AC grid frequency directly for DC railway trains by processing the onboard DC voltage signal. This method leverages the coupling of both sides, AC and DC, in DC railway traction substations.

In addition to introducing this novel concept, two realization approaches are presented. Both methods, based on single-phase PLL and ZCD algorithms, have undergone testing through simulations and experimental validation. The results consistently demonstrate their capability to provide accurate estimates of the AC grid frequency. Section 4.5.2 illustrates how the proposed methods effectively detect and track frequency variations. Section 4.5.3 confirms their suitability for frequency estimation even in the presence of noisy signals, provided adequate filtering stages are implemented. Section 4.5.4 validates their real-time implementability, showcasing acceptable frequency tracking amidst sudden power fluctuations and in the presence of noise. All results underscore the effectiveness of the proposed methods in handling AC-side disturbances of various amplitudes and forms, including scenarios with abrupt changes, as depicted in figures 4.54, 4.62, 4.63, and 4.64.

The implementation of the proposed methods also revealed certain challenges. Both the single-phase PLL and ZCD methods necessitate suitable filtering stages to mitigate the impact of undesired noise and harmonics, which can adversely affect estimation performance. Additionally, the DC component of the rectified signal must be filtered without excessively attenuating the fundamental harmonic component. It is important to note that the single-phase PLL and ZCD methods differ in complexity. Single-phase PLL relies on multiple parameters, and their tuning is non-trivial. In addition to PLL time constants, the method chosen for generating quadrature signals can significantly influence frequency estimation performance. The ZCD method, on the other hand, can be implemented effectively with fewer parameters but requires smaller calculation time steps to achieve less deviated results.

These results are currently under revision (Check the List of Publications).

4.6 Experimental validation in a real micro-grid

Some previous sections include experimental validation, such as Sections 4.4 and 4.5. As noticed in the literature and across the work, experimental validation allows to achieve a more realistic assessment of proposals. So, these can be properly adjusted and deployed in real systems. Previous experimental tests are oriented to test the control under noisy and delayed signals, offline and in real-time. The present section, in addition to providing real-time experimental validation, includes high-power equipment, such as electronic converters, synchronous generators, load, and connection elements. Testing the proposals in a real microgrid is a step further in the development of technologies.

The objective of this preliminary result analysis is to experimentally validate the possibility of contributing to the grid frequency control from a load connected directly to a DC side that is simultaneously fed by the AC grid, which is the overall concept of the present work but oriented to railways.

4.6.1 Description of the micro-grid

For carrying out the experimentation, the facilities of the Smart Energy System Control Laboratory (SESCL) are used. The lab belongs to the Energy Lab infrastructure of the Karlsruhe Institute of Technology (KIT). SESCL is a fully automated, user-oriented research infrastructure designed for controlling and operating smart energy systems within a microgrid testing environment. Its high degree of automation and ability to operate in a grid-disconnected mode enables the study of yet-to-be-developed tools and algorithms for energy technologies and grid control strategies oriented to system stability. SESCL stands out for its fully automated busbar matrix, providing a highly flexible and adjustable microgrid topology. It also offers the capability for load shedding, integration of grid participants, and the ability to change microgrid topology on demand. The infrastructure allows for the control and modification of setpoints and operating parameters of grid participants during runtime. Inspired by real-world events in isolated grids, microgrid islanding serves as a use case to showcase SESCL's capabilities. To create realistic grids for experiments, the laboratory incorporates a variety of energy technology system components, including generators, converters, inverters, PV systems, ESS, HILs, and smart houses. These components can be freely interconnected to form a microgrid with a variable topology, facilitated by a matrix of ten busbars and 424 contactors controlled by a central automation system. The laboratory's design includes both real transmission lines and line replicas, allowing for the representation of the physical behavior of a transmission line. A total of 71 grid participants with various power ratings can be connected to the busbars, supporting realistic experiments in the laboratory setting [145].

Toward the adjustment of the laboratory for PHIL tests, SESCL includes four real-time simulators (all from OPAL-RT: two OP5707 and two OP4510), one microgrid test-bench (OP1420 from OPAL-RT), and two four-quadrant amplifiers (CSU100 2GAMP4 from EGSTON). In the context of the present work, the SESCL facilities are structured as shown in Fig. 4.66. Here, an OP4510 real-time simulator, a CSU100 2GAMP4 EGSTON amplifier, an Imperix RCP, three AC connection points of the AC bus bar, a controllable resistive load, and a natural gas generator are used.

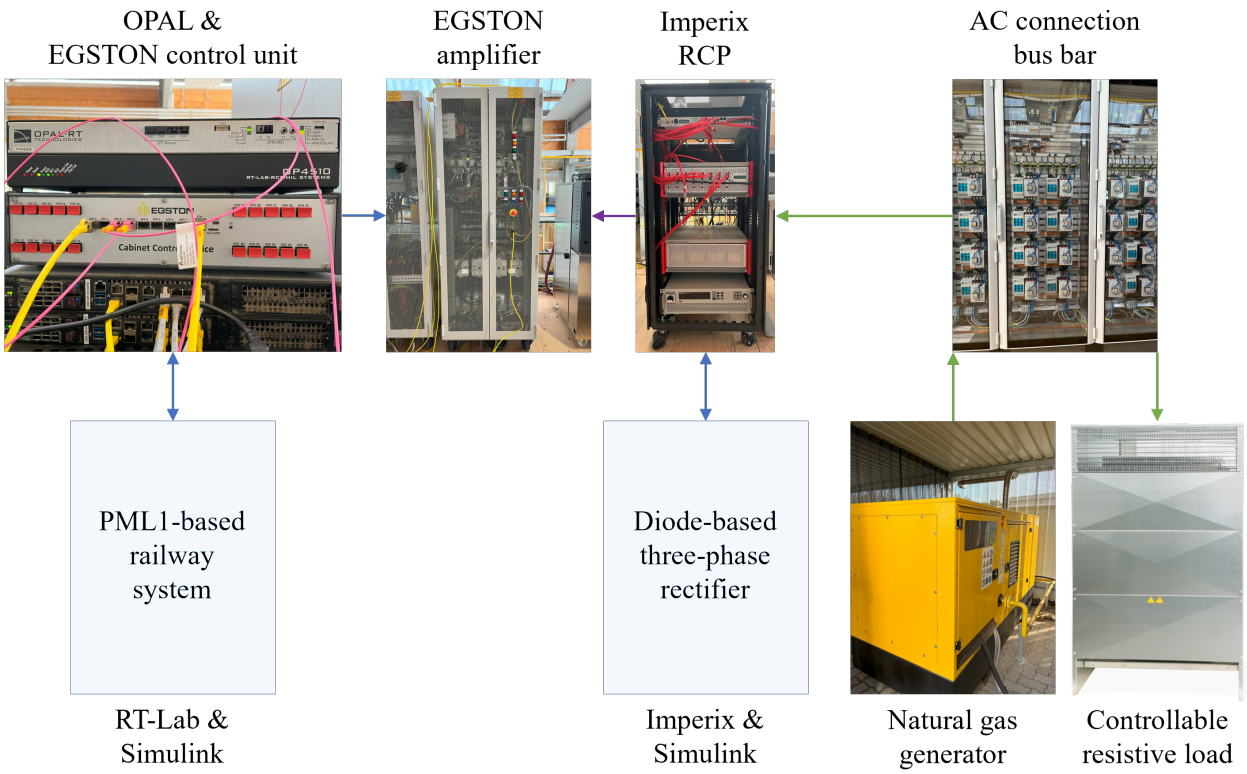


Figure 4.66: Microgrid overall description: blue, violet, and green lines represent data flow, DC connection, and AC connections, respectively.

The OP4510 is a compact and affordable simulator that incorporates OPAL-RT's strengths in high-performance Rapid Control Prototyping (RCP) and HIL systems. It features high-speed connectivity, is open and optimized for power electronics, and provides a cost-effective entry into this technology. Its compact, portable design comes with a substantial number of robust I/O channels.

The CSU100 is a highly adaptable 100kVA emulation and testing system, featuring galvanic isolation and up to six independent four-quadrant power amplifiers. With its capability to operate in predefined AC and DC modes, as well as user-defined HIL-based modes, the CSU100 stands out as the most versatile PHIL test and emulation platform in the current market. Its control options include external HIL systems or EGSTON real-time processors, facilitated through fast fiber-optic or analog interfaces.

The imperix RCP of SESCL is composed of six PEB8024 SiC power modules. Each power module is formed by voltage/current sensors outputs, gate drivers inputs, fault output, board-to-board link, 5 V and 12 V power supply, a cooling fan, DC link terminals, two SiC MOSFETs rated up to 800 V and 24 A.

The natural gas generator is from Feeser Generators (model GM52/NGT-AS). It includes a 4-poles synchronous generator coupled to an engine. The first provides 56 kVA with a power factor of 0.8, standard 230/400 V four wires at 50 Hz, It contains an automatic voltage regulator. The latter has 8 cylinders, an electronic speed control, and a rated output power

of 56.8 kW. The standard rotation speed is 1500 rpm.

4.6.2 Case study: PML1-based railway model in a high-distorted grid

The railway system that has been considered in the development of the present work is considered. The characteristics of trains, the electrification system, and timetables, among other setups, remain. This model is emulated by the OP4510. The frequency control setup and the rated power consumption are tuned accordingly to the equivalent power system. This is, maintaining the same proportions between generation capacity and power consumption, and frequency deviations and HVAC system consumption. The equivalent power system, the microgrid, is formed by the AC connection bus bar, natural gas generator, and controllable load. The generator is set at 50.5 Hz, to evidence the isolated operation, and the speed control setup is the default one. The normal operation of this generator, conceived for emergency supply, established a constant frequency oscillation of ± 0.3 Hz. Considering this operational restriction and previous section results, a dead band of ± 0.309 Hz is selected. The controllable load is 100% resistive. It is used to create a sudden load shedding of around 10 kW that results in a 1.2 Hz maximum frequency deviation. The SiC MOSFETs of the Imperix RCP are permanently inactive so the bypass diodes define the dynamic. Then, providing the behavior of a TPUR. Based on the saturation of P_{HVAC}, as stated in Section 4.3, and on the frequency behavior of the microgrid, the following values are selected for the primary control, supplementary control, and virtual inertia, respectively: 0.1885, 2.2951, and 0.0367. The frequency control schemes are the same as in Sections 4.2, 4.3, and 4.4.

Fig. 4.67 shows the influence of the proposals in the AC grid frequency behavior. The legend shows the ID for each case study. The 00 case represents no provision of frequency control from the on-board HVAC systems. Next, each bundle of 5 consecutive cases represents the control setup multiplied by the following factors: 1.5, 1.00, 0.75, 0.50, and 0.25. The first five cases are for studying the primary frequency control, the second five cases for the supplementary frequency control, and the third five cases for virtual inertia provision.

At a glance, it is evident that, among the different setups, the reduction in frequency deviations and variations is possible. The pointed line is the case without any frequency control. It can be seen how most frequency control setups provide less frequency deviations and closer-to-null ROCOF. As an example of the difference among the responses of controls, it can be pointed out how the supplementary frequency control slows down its response just after the maximum frequency deviation (around Test time = 0.1 s). Since it reacts to the cumulative frequency deviation, it smoothly decreases its response variation when the maximum is reached.

It is worth mentioning that this experimental implementation faced many challenges related to the frequency measurement. The constantly oscillatory behavior of the gas natural generator power output makes the proposed frequency control response less homogeneous than in the previous sections. The effect of these oscillations can be noticed in the upper plot of Fig. 4.67 as the low-frequency behavior of all curves. Also, the "spikes" in the lower plot evidence some measurement errors.

In summary, it is technically possible to implement the proposed frequency controls, even if

exposed to noisy, oscillatory, and unpredictable signals. Every control setup achieves a certain degree of enhancement. Then, a deeper study can suggest better frequency control schemes that can gather the benefits of each frequency control (primary, supplementary, and virtual inertia). Besides this preliminary experimental study, it has been demonstrated the feasibility, reliability, and effectiveness of the proposals in a real microgrid composed by commercial components.

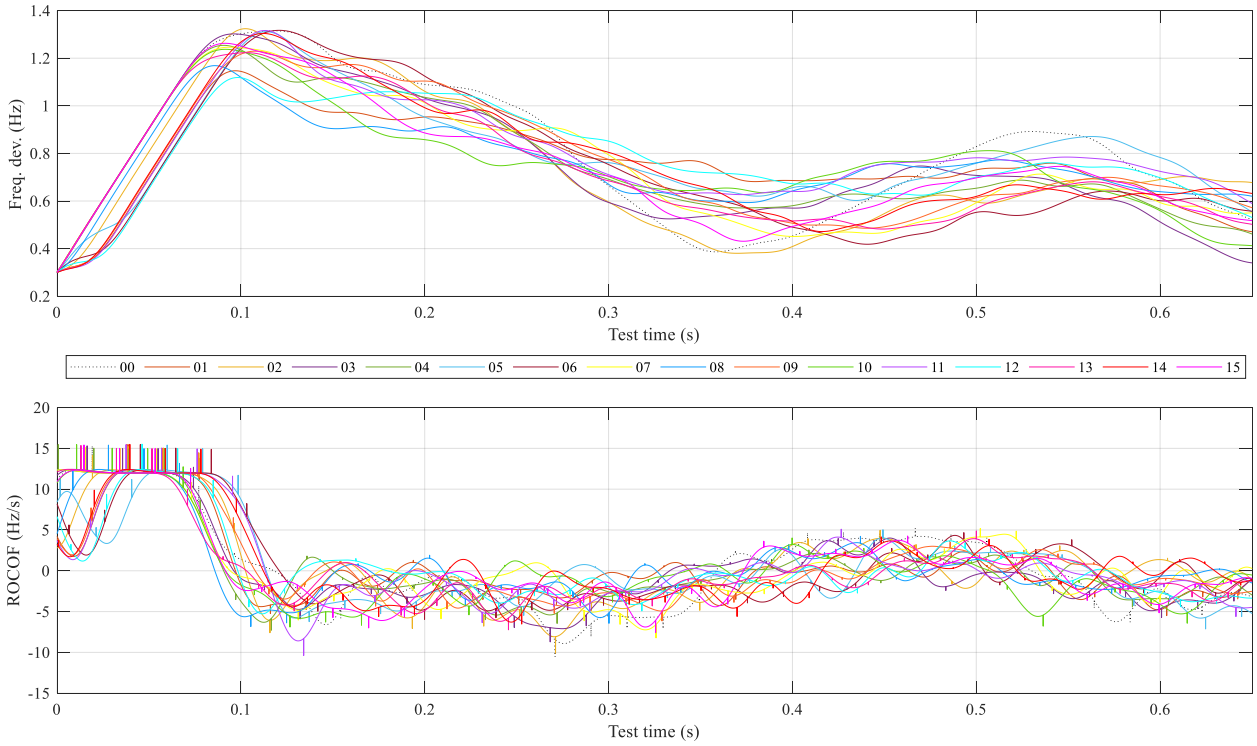


Figure 4.67: Behavior of the AC and DC sides following a sudden load shedding. The "Test time" label records the time after the event.

Chapter 5

Conclusions and future works

From Section 4.1 to Section 4.6, various perspectives have been taken into account to explore the possibilities of the railway system to contribute to grid frequency control. As noticeable, the overall study considers estimation methods, modeling methodologies, new control approaches, and measurement procedures, among other main lines. Then, the main outcomes of each section of Chapter 4 are exposed.

5.1 Conclusions

The present work has explored different aspects to study the possibilities of railway systems to contribute to frequency control in power systems. Without being exhaustive, it has been demonstrated that is possible for the HVAC systems of trains to contribute to frequency control. The results show the effectiveness of providing virtual inertia, and primary and supplementary frequency control. Also, the proposed control can be oriented to relieve renewable generation from frequency control tasks under certain conditions. In addition to frequency control techniques, the work has proposed a way for estimating the grid frequency from the DC catenary of railways. Some experimental validations have been included in the work. Sections 4.4 and 4.5 exposed the results of testing the control proposals and their implementability by using the HIL technique and recorded signals from a test-bench composed of real machines, loads, and a rectifier. Additionally, in the results of Section 4.6 is noticeable that all the frequency control proposals perform appropriately and enhance the grid frequency performance of a real microgrid.

Concerning the injection of surplus energy into the public grid, the proposed methodology models the railway and distribution grid systems meticulously, emphasizing their interaction through regenerative braking energy. An energy-centric approach links these systems, involving the union of individual train profiles, facilitating the estimation of total railway consumption and maximum regenerative braking energy. The method is computationally efficient, enabling fast analysis of the distribution grid's impact by considering specific railway system parameters. Subdividing regenerative braking energy injection mitigates the distribution grid's impact, and employing multiple extraction points contributes to reduced voltage fluctuations. The methodology also simplifies modeling railways within microgrids, enabling an accessible

evaluation of the interaction between distribution grids and railway-based microgrids.

Regarding the first approach to frequency control from the HVAC systems of trains, the findings highlight the potential contribution to primary frequency control, especially during external events like load shedding, generation loss, and power fluctuations from normal railway consumption. Implementing a droop control system based on grid frequency and thermal comfort maintains HVAC support for the grid without compromising thermal comfort. Simulation results consistently show minimal temperature variation during frequency support across all scenarios. Exploring thermal inertia and droop control aggressiveness confirms their positive impact on frequency control. Employing the thermal behavior of a single train, instead of individual trains, yields similar frequency dynamics results, but temperature differences may matter for thermal comfort studies. The railway's contribution to frequency control depends on event amplitudes, system inertia, and railway size, with larger systems expected to have a more significant impact. As power systems integrate more loads and generators, the aggregate impact on frequency control is anticipated to be substantial. The technical feasibility of using train thermal inertia for frequency control is demonstrated, but model simplifications are acknowledged.

The results of the study about the provision of virtual inertia along with primary frequency control demonstrate control actions' impact on minimum ROCOF after load shedding and slightly influence maximum ROCOF after generation loss. Values depend on power system inertia and instantaneous power balance. In load shedding, event magnitude defines maximum ROCOF, and minimum ROCOF is determined by normal power consumption. In generation loss, event magnitude defines minimum ROCOF, and maximum ROCOF is influenced by normal power consumption. Braking minimally affects frequency performance due to minimal power exchange. VAC system's operational status before frequency control activation limits its contribution. Sudden load shedding challenges increase electrical consumption. Regardless, passenger thermal comfort isn't compromised. Implementing control techniques must consider VAC system technical requirements, including reductions in thermal power and electrical consumption. Achievable contributions depend on operational ranges. Combining primary frequency control and virtual inertia offers advantages, including mitigating VAC system fatigue. Controls don't combine linearly; one control's action can influence the other's performance.

For relieving renewable generation from frequency control tasks, a low computational cost method is suggested for tuning the proposed supplementary control. This is done by using a surface equation fitting method to estimate local optimum values and study variable influence on frequency performance. The resulting equations, with high goodness of fit, offer rapid approximation to local optima. Results show the efficacy of railway-based supplementary frequency control, reducing grid frequency deviation RMS in normal consumption and sudden load shedding scenarios. Incorporating primary frequency control into a demand response strategy further improves outcomes. The benefits of primary frequency control depend on tuning and event severity. While renewable generation can relieve frequency control under specific conditions, the proposed railway-based control alone may not suffice during large deviations. Experimental validation on Arduino Due demonstrates effective functioning under realistic conditions, highlighting practicality and ease of implementation into existing HVAC

system controls.

In relation to frequency estimation techniques, a method is proposed for direct AC grid frequency estimation in DC railway trains using the onboard DC voltage signal, leveraging coupling in DC railway traction substations. Two realization approaches, based on single-phase PLL and ZCD algorithms, are presented and validated through simulations and experiments. Results consistently show accurate AC grid frequency estimates. Despite challenges requiring suitable filtering stages, both methods effectively detect and track frequency variations, handle noisy signals, and demonstrate real-time implementability. The single-phase PLL and ZCD methods differ in complexity, with the former requiring non-trivial tuning and the latter offering faster results with fewer parameters.

5.2 Future works

Due to the exploratory nature of the present research work, many possible future works can be developed. Without being exhaustive, some future works are:

- Study of the interaction between diverse converter-interfaced distributed energy resources and the regenerative braking energy toward the provision of multiple grid ancillary services. The study can include modeling different electronic converter topologies and the interaction among their controllers.
- Techno-economic assessment of integrating converter-interfaced distributed energy resources into the DC catenary to enhance the capacity of railway systems to improve their performance and the surrounding grid one. This assessment may include different political frameworks, not currently defined, to establish appropriate alternatives for a wider integration of railway systems to the world's energetic transition. This research topic can explore the current ways of paying power system participants for their contribution, and take it as a reference to take into account the benefits railway systems would be providing.
- Analysis of the impact of the extension of the thermal model of trains on the frequency control performance. This may include the definition of the provision limits by using all the available flexibility provided by the thermal inertia of trains.
- Exploration of the different types of HVAC systems and their implications on the frequency control performance. As known, railway systems can use various HVAC system technologies that can behave differently according to the characteristics of their thermo-fluidic circuits, electric and electronic components, mechanical devices, and embedded controls, among other subsystems. Deeper modeling and analysis would provide useful insights toward a successful real implementation of the proposals.
- Study of the requirements of physical implementation. This is, to analyze the modifications to be done and the possible performance when selecting specific HVAC subsystems to be adjusted to provide frequency control (compressors, ventilators, pumps, valves, electronic components, etc.).
- Study of the combination of all the proposed frequency control schemes. The study

can be oriented to determine optimal combinations, propose new schemes, and develop adaptative controls, among other possible objectives.

- Analysis of possible changes in the proposed frequency control approaches based on the characteristics of the railway systems where they will be implemented. The analysis can consider conventional systems, monorails, high-speed trains, trams, etc. Also, the interaction between the proposals and conventional control loops can suggest new approaches to integrate railway systems as a grid ancillary services supporter.
- Large-scale assessment of the contribution of railway systems to frequency control. The present work modeled an entire metro line and then a part of it. However, it is expected that all the available railways, along with other loads, contribute to frequency control when required. Then, a large-scale study, which considers the model of regional grids, can provide conclusions about the requirements of the proposals to be deployed in real power systems.
- Exploration of different auxiliary consumptions that can also be modified to support grid ancillary services. This work studied on-board HVAC systems. However, other devices, currently or to be installed, can be considered. The exploration may include the compatibility of each device's nature and the ancillary service to be provided.
- Estimation of the degree of fatigue due to the provision of the mentioned ancillary services. Modifying the normal operation of devices may lead them to operations regimes not considered by manufacturers in the design stage. Then, the lifetime can be reduced.

References

[1] IEA, *World energy outlook 2023, license: Cc by 4.0 (report). cc by nc sa 4.0 (annex a)*, 2023.

[2] P. Denholm, D. J. Arent, S. F. Baldwin, *et al.*, "The challenges of achieving a 100% renewable electricity system in the united states", *Joule*, vol. 5, pp. 1331–1352, 6 Jun. 2021. DOI: 10.1016/j.joule.2021.03.028.

[3] J. Shair, H. Li, J. Hu, and X. Xie, "Power system stability issues, classifications and research prospects in the context of high-penetration of renewables and power electronics", *Renewable and Sustainable Energy Reviews*, vol. 145, Jul. 2021. DOI: 10.1016/j.rser.2021.111111.

[4] N. Hatziargyriou, J. Milanovic, C. Rahmann, *et al.*, "Definition and classification of power system stability - revisited & extended", *IEEE Transactions on Power Systems*, vol. 36, pp. 3271–3281, 4 Jul. 2021. DOI: 10.1109/TPWRS.2020.3041774.

[5] M. N. H. Shazon, Nahid-Al-Masood, and A. Jawad, "Frequency control challenges and potential countermeasures in future low-inertia power systems: A review", *Energy Reports*, vol. 8, pp. 6191–6219, Nov. 2022. DOI: 10.1016/j.egyr.2022.04.063.

[6] IEA, *The future of rail. license: Cc by 4.0*, 2023.

[7] M. Brenna, F. Foiadelli, and H. J. Kaleybar, "The evolution of railway power supply systems toward smart microgrids: The concept of the energy hub and integration of distributed energy resources", *IEEE Electrification Magazine*, vol. 8, pp. 12–23, 1 2020. DOI: 10.1109/MELE.2019.2962886.

[8] U. Tamrakar, D. Shrestha, M. Maharjan, B. P. Bhattarai, T. M. Hansen, and R. Tonkoski, "Virtual inertia: Current trends and future directions", *Applied Sciences (Switzerland)*, vol. 7, pp. 1–29, 7 2017. DOI: 10.3390/app7070654.

[9] L. Meegahapola, P. Mancarella, D. Flynn, and R. Moreno, "Power system stability in the transition to a low carbon grid: A techno-economic perspective on challenges and opportunities", *Wiley Interdisciplinary Reviews: Energy and Environment*, vol. 10, pp. 1–27, 5 2021. DOI: 10.1002/wene.399.

[10] C. Gokhale-Welch and S. Stout, *Key considerations for adoption of technical codes and standards for battery energy storage systems in thailand*, 2021.

[11] P. Carroll, A. Nouri, S. Khadem, *et al.*, "Development of network codes to facilitate the energy transition", in *9th International Conference on Smart Grid, icSmartGrid 2021. June 29-July 1*, IEEE, 2021, pp. 63–67. DOI: 10.1109/icSmartGrid52357.2021.9551230.

[12] D. Ochoa and S. Martinez, "Fast-frequency response provided by dfig-wind turbines and its impact on the grid", *IEEE Transactions on Power Systems*, vol. 32, pp. 4002–4011, 5 2017. DOI: 10.1109/TPWRS.2016.2636374.

[13] D. Ochoa and S. Martinez, "Frequency dependent strategy for mitigating wind power fluctuations of a doubly-fed induction generator wind turbine based on virtual inertia control and blade pitch angle regulation", *Renewable Energy*, vol. 128, pp. 108–124, 2018. DOI: 10.1016/j.renene.2018.05.047.

[14] M. Pierro, R. Perez, M. Perez, D. Moser, and C. Cornaro, "Imbalance mitigation strategy via flexible pv ancillary services: The italian case study", *Renewable Energy*, vol. 179, pp. 1694–1705, 2021. DOI: 10.1016/j.renene.2021.07.074.

[15] S. Julien, A. Sajadi, and B. M. S. Hodge, "Hierarchical control of utility-scale solar pv plants for mitigation of generation variability and ancillary service provision", *IEEE Transactions on Sustainable Energy*, vol. 3029, pp. 1–13, c 2022. DOI: 10.1109/TSTE.2022.3149451.

[16] G. C. Kryonidis, E. O. Kontis, T. A. Papadopoulos, *et al.*, "Ancillary services in active distribution networks: A review of technological trends from operational and online analysis perspective", *Renewable and Sustainable Energy Reviews*, vol. 147, p. 111 198, May 2021. DOI: 10.1016/j.rser.2021.111198.

[17] S. Padhy and S. Panda, "Simplified grey wolf optimisation algorithm tuned adaptive fuzzy pid controller for frequency regulation of interconnected power systems", *Protection and Control of Modern Power Systems*, vol. 6, p. 16, 2 2021. DOI: 10.1080/01430750.2021.1874518.

[18] M. Ramesh, A. K. Yadav, and P. K. Pathak, "An extensive review on load frequency control of solar-wind based hybrid renewable energy systems", *Energy Sources, Part A: Recovery, Utilization and Environmental Effects*, vol. 00, pp. 1–25, 00 2021. DOI: 10.1080/15567036.2021.1931564.

[19] H. Rezk, M. A. Mohamed, A. A. Z. Diab, and N. Kanagaraj, "Load frequency control of multi-interconnected renewable energy plants using multi-verse optimizer", *Computer Systems Science and Engineering*, vol. 37, pp. 219–231, 2 2021. DOI: 10.32604/csse.2021.015543.

[20] M. Hussain and Y. Gao, "A review of demand response in an efficient smart grid environment", *Electricity Journal*, vol. 31, pp. 55–63, 5 2018. DOI: 10.1016/j.tej.2018.06.003.

[21] A. R. Jordehi, "Optimisation of demand response in electric power systems, a review", *Renewable and Sustainable Energy Reviews*, vol. 103, pp. 308–319, July 2018 2019. DOI: 10.1016/j.rser.2018.12.054.

[22] W. Huang, N. Zhang, C. Kang, M. Li, and M. Huo, "From demand response to integrated demand response: Review and prospect of research and application", *Protection and Control of Modern Power Systems*, vol. 4, p. 13, 1 2019. DOI: 10.1186/s41601-019-0126-4.

[23] S. Yumiki, Y. Susuki, Y. Oshikubo, *et al.*, "Autonomous vehicle-to-grid design for provision of frequency control ancillary service and distribution voltage regulation", *Sustainable Energy, Grids and Networks*, vol. 30, Jun. 2022. DOI: 10.1016/j.segan.2022.100664.

[24] M. Ledro, L. Calearo, J. M. Zepter, T. Gabderakhmanova, and M. Marinelli, "Influence of realistic ev fleet response with power and energy controllers in an ev-wind virtual power plant", *Sustainable Energy, Grids and Networks*, vol. 31, Sep. 2022. DOI: 10.1016/j.segan.2022.100704.

[25] A. Blatiak, F. Bellizio, L. Badesa, and G. Strbac, "Value of optimal trip and charging scheduling of commercial electric vehicle fleets with vehicle-to-grid in future low inertia systems", *Sustainable Energy, Grids and Networks*, vol. 31, Sep. 2022. DOI: 10.1016/j.segan.2022.100738.

[26] X. Tian, Y. Chi, C. Liu, P. Cheng, and Y. Li, "Power-balancing coordinated control of wind power and demand-side response under post-fault condition", *Journal of Modern Power Systems and Clean Energy*, vol. 10, no. 5, pp. 1207–1215, 2022. DOI: 10.35833/MPCE.2020.000868.

[27] Y. Yoo, Y. Al-Shawesh, and A. Tchagang, "Coordinated control strategy and validation of vehicle-to-grid for frequency control", *Energies*, vol. 14, 9 May 2021. DOI: 10.3390/en14092530.

[28] M. Khan, H. Sun, Y. Xiang, and D. Shi, "Electric vehicles participation in load frequency control based on mixed h2/∞", *International Journal of Electrical Power and Energy Systems*, vol. 125, p. 106 420, March 2020 2021. DOI: 10.1016/j.ijepes.2020.106420.

[29] H. H. Alhelou, M. E. Hamedani-Golshan, R. Zamani, E. Heydarian-Forushani, and P. Siano, "Challenges and opportunities of load frequency control in conventional, modern and future smart power systems: A comprehensive review", *Energies*, vol. 11, p. 35, 10 2018. DOI: 10.3390/en11102497.

[30] C. Diaz-Londono, C. A. Correa-Florez, J. Vuelvas, A. Mazza, F. Ruiz, and G. Chicco, "Coordination of specialised energy aggregators for balancing service provision", *Sustainable Energy, Grids and Networks*, p. 100 817, Dec. 2022. DOI: 10.1016/j.segan.2022.100817.

[31] T. Chen, J. Guo, B. Chaudhuri, and S. Y. Hui, "Virtual inertia from smart loads", *IEEE Transactions on Smart Grid*, vol. 11, pp. 4311–4320, 5 2020. DOI: 10.1109/TSG.2020.2988444.

[32] H. Yang, T. Li, Y. Long, C. L. Chen, and Y. Xiao, "Distributed virtual inertia implementation of multiple electric springs based on model predictive control in dc microgrids", *IEEE Transactions on Industrial Electronics*, vol. 0046, c 2021. DOI: 10.1109/TIE.2021.3130332.

[33] P. Bao, W. Zhang, and Y. Zhang, "Secondary frequency control considering optimized power support from virtual power plant containing aluminum smelter loads through vsc-hvdc link", *Journal of Modern Power Systems and Clean Energy*, vol. 11, no. 1, pp. 355–367, 2023. DOI: 10.35833/MPCE.2021.000072.

[34] G. Benysek, J. Bojarski, R. Smolenski, M. Jarnut, and S. Werminski, "Application of stochastic decentralized active demand response (dadr) system for load frequency control", *IEEE Transactions on Smart Grid*, vol. 9, pp. 1055–1062, 2 2018. DOI: 10.1109/TSG.2016.2574891.

[35] X. Chen, J. Wang, J. Xie, S. Xu, K. Yu, and L. Gan, "Demand response potential evaluation for residential air conditioning loads", *IET Generation, Transmission and Distribution*, vol. 12, pp. 4260–4268, 19 Oct. 2018. DOI: 10.1049/iet-gtd.2018.5299.

[36] M. M. Eissa, A. A. Ali, K. M. Abdel-Latif, and A. F. Al-Kady, "Emergency frequency control by using heavy thermal conditioning loads in commercial buildings at smart grids", *Electric Power Systems Research*, vol. 173, pp. 202–213, Aug. 2019. DOI: 10.1016/j.epsr.2019.04.008.

[37] H. Chen, L. Xiang, L. Lin, and S. Huang, "Fractional-order pid load frequency control for power systems incorporating thermostatically controlled loads", in *Proceedings of 2021 IEEE 4th International Electrical and Energy Conference, CIEEC 2021*, Institute of Electrical and Electronics Engineers Inc., May 2021. DOI: 10.1109/CIEEC50170.2021.9510621.

[38] K. Oikonomou, M. Parvania, and R. Khatami, "Optimal demand response scheduling for water distribution systems", *IEEE Transactions on Industrial Informatics*, vol. 14, pp. 5112–5122, 11 Nov. 2018. DOI: 10.1109/TII.2018.2801334.

[39] X. Chen, Q. Hu, Q. Shi, X. Quan, Z. Wu, and F. Li, "Residential hvac aggregation based on risk-averse multi-armed bandit learning for secondary frequency regulation", *Journal of Modern Power Systems and Clean Energy*, vol. 8, no. 6, pp. 1160–1167, 2020. DOI: 10.35833/MPCE.2020.000573.

[40] Z. He, C. Wan, and Y. Song, "Frequency regulation from electrified railway", *IEEE Transactions on Power Systems*, vol. 8950, pp. 1–18, c 2021. DOI: 10.1109/TPWRS.2021.3119706.

[41] Z. He, C. Wan, and Y. Song, "Adaptive frequency response from electrified railway", *IEEE Transactions on Power Systems*, 2022. DOI: 10.1109/TPWRS.2022.3179369.

[42] Z. He, C. Wan, H. Liu, and P. Ju, "Evaluation of grid support capacity from electrified railways", *IEEE Transactions on Power Systems*, vol. 39, no. 1, pp. 2310–2326, 2024. DOI: 10.1109/TPWRS.2023.3268246.

[43] J. Araúz and S. Martinez, "Methodology for assessing the impact of regenerative braking energy injection of a direct current railway system on the distribution grid", *Electric Power Systems Research*, vol. 220, p. 109 368, Jul. 2023. DOI: 10.1016/j.epsr.2023.109368.

[44] J. Araúz and S. Martinez, "Contribution of the thermal inertia of trains to the primary frequency control of electric power systems", *Sustainable Energy, Grids and Networks*, vol. 34, p. 100 988, Jun. 2023. DOI: 10.1016/j.segan.2022.100988.

[45] J. Araúz and S. Martinez, "Use of the thermal inertia of trains for contributing to primary frequency control and inertia of electric power systems", *IEEE Access*, vol. 11, pp. 57 099–57 116, May 2023. DOI: 10.1109/ACCESS.2023.3279499.

[46] J. Araúz and S. Martinez, "Using the thermal inertia of trains for contributing to primary frequency control in grids with photovoltaic generation", in *2023 IEEE International Conference on Electrical Systems for Aircraft, Railway, Ship Propulsion and Road Vehicles & International Transportation Electrification Conference (ESARS-ITEC), Venice, Italy, 2023, pp. 1-6*, IEEE, Mar. 2023. DOI: 10.1109/ESARS-ITEC57127.2023.10114893.

[47] J. Araúz and S. Martinez, "Using the thermal inertia of trains for contributing to primary and supplementary frequency control in grids with high penetration of renewable generation", *IEEE ACCESS*, vol. 12, pp. 63 271–63 281, May 2024. DOI: 10.1109/ACCESS.2024.3396331.

[48] J. Araúz, S. Martinez, J. C. Serrano, and C. Veganzones, "Ac grid frequency estimation from dc catenary voltage measurements onboard trains", *1*, vol. 1, p. 1, Jan. 1. DOI: 1.

[49] W. Stevenson and J. Grainger, *Power System Analysis*. McGraw-Hill Education, 1994.

[50] N. Mohan, T. M. Undeland, and W. P. Robbins, *Power Electronics: converters, application, and design*, 3rd. John Willey and Sons, Inc., 1997.

[51] W. Kersting and R. Green, "The application of carson´s equation to the steady-state analysis of distribution feeders", in *2011 IEEE/PES Power Systems Conference and Exposition*, IEEE, 2011, pp. 1–6. DOI: 10.1109/PSCE.2011.5772579.

[52] IEEE, *Ieee guide for synchronous generator modeling practices and applications in power system stability analyses. ieee std 1110-2002 (revision of ieee std 1110-1991 [2003])*, 2003.

[53] IEEE, *Recommended practice for excitation system models for power system stability studies," ieee® standard 421.5-1992*, 1992.

[54] P. Kundur, N. Balu, and M. Lauby, *Power system stability and control*. 1994.

[55] M. Asad, S. Martinez, and J. A. Sanchez-Fernandez, "Diesel governor tuning for isolated hybrid power systems", *Electronics*, vol. 12, p. 2487, 2023. DOI: 10.3390/electronics12112487.

[56] D. Ochoa and S. Martinez, *Contribución de los aerogeneradores de velocidad variable al control primario de frecuencia en sistemas de energía eléctrica, doctoral thesis defense*, 2019.

[57] A. Arif, Z. Wang, J. Wang, B. Mather, H. Bashualdo, and D. Zhao, "Load modeling—a review", *IEEE Transactions on Smart Grid*, vol. 9, no. 6, pp. 5986–5999, 2018. DOI: 10.1109/TSG.2017.2700436.

[58] D. Ochoa and S. Martinez, "Proposals for enhancing frequency control in weak and isolated power systems: Application to the wind-diesel power system of san cristobal island-ecuador", *Energies*, vol. 11, p. 25, 4 2018. DOI: 10.3390/en11040910.

[59] F. Kiessling, R. Puschmann, and A. Schmieder, *Contact Lines for Electric Railways: Planning, Design, Implementation*, 1st. Publicis Corporate Publishing, Munich Erlangen, 2001.

[60] S. Su, T. Tang, and Y. Wang, "Evaluation of strategies to reducing traction energy consumption of metro systems using an optimal train control simulation model", *Energies*, vol. 9, pp. 1–19, 2 2016. DOI: 10.3390/en9020105.

[61] A. Capasso, R. Lamedica, A. Ruvio, M. Ceraolo, and G. Lutzemberger, "Modelling and simulation of electric urban transportation systems with energy storage", *EEEIC 2016 - International Conference on Environment and Electrical Engineering*, 2016. DOI: 10.1109/EEEIC.2016.7555480.

[62] H. Alnuman, D. Gladwin, and M. Foster, "Electrical modelling of a dc railway system with multiple trains", *Energies*, vol. 11, 11 2018. DOI: 10.3390/en11113211.

[63] K. Almaksour, Y. Krim, N. Kouassi, *et al.*, "Comparison of dynamic models for a dc railway electrical network including an ac/dc bi-directional power station", *Mathematics and Computers in Simulation*, vol. 184, pp. 244–266, 2021. DOI: 10.1016/j.matcom.2020.05.027.

[64] P. H. Hsi, S. L. Chen, and R. J. Li, "Simulating on-line dynamic voltages of multiple trains under real operating conditions for ac railways", *IEEE Transactions on Power Systems*, vol. 14, pp. 452–459, 2 1999. DOI: 10.1109/59.761865.

[65] J. A. Thompson, G. G. Maidment, and J. F. Missenden, "Modelling low-energy cooling strategies for underground railways", *Applied Energy*, vol. 83, pp. 1152–1162, 10 2006. DOI: 10.1016/j.apenergy.2005.12.001.

[66] K. Jenkins, M. Gilbey, J. Hall, V. Glenis, and C. Kilsby, "Implications of climate change for thermal discomfort on underground railways", *Transportation Research Part D: Transport and Environment*, vol. 30, pp. 1–9, 2014. DOI: 10.1016/j.trd.2014.05.002.

[67] R. Mastrullo, A. W. Mauro, and C. Vellucci, "Refrigerant alternatives for high speed train a/c systems: Energy savings and environmental emissions evaluation under variable ambient conditions", *Energy Procedia*, vol. 101, pp. 280–287, September 2016. DOI: 10.1016/j.egypro.2016.11.036.

[68] R. N. Hofstädter, T. Zero, C. Dullinger, G. Richter, and M. Kozek, "Heat capacity and heat transfer coefficient estimation for a dynamic thermal model of rail vehicles", *Mathematical and Computer Modelling of Dynamical Systems*, vol. 23, pp. 439–452, 5 2017. DOI: 10.1080/13873954.2016.1263670.

[69] N. Li, L. Yang, X. Li, X. Li, J. Tu, and S. C. Cheung, "Multi-objective optimization for designing of high-speed train cabin ventilation system using particle swarm optimization and multi-fidelity kriging", *Building and Environment*, vol. 155, pp. 161–174, March 2019. DOI: 10.1016/j.buildenv.2019.03.021.

[70] S. Istomin and A. Shtraukhman, "Simulation model of the heating and air conditioning system of dc electric trains", in *E3S Web of Conferences*, vol. 135, 2019, p. 9. DOI: 10.1051/e3sconf/201913502018.

[71] D. Serrano-jiménez, L. Abrahamsson, S. Castaño-solís, and J. Sanz-feito, "Electrical power and energy systems electrical railway power supply systems : Current situation and future trends", *Electrical Power and Energy Systems*, vol. 92, pp. 181–192, 2017. DOI: 10.1016/j.ijepes.2017.05.008.

[72] T. Train, J. Feng, J. Xu, W. Liao, and Y. Liu, "Review on the traction system sensor technology of", *Sensors. MDP*, Dc 2017. DOI: 10.3390/s17061356.

[73] P. Fraga-lamas, T. M. Fernández-caramés, and L. Castedo, "Towards the internet of smart trains : A review on industrial iot-connected railways", *Sensors. MDP*, 2017. DOI: 10.3390/s17061457.

[74] H. Hayashiya and K. Kondo, "Recent trends in power electronics applications as solutions in electric railways", *IEEJ Transactions on Electrical and Electronic Engineering*, vol. 15, pp. 632–645, 5 2020. DOI: 10.1002/tee.23121.

[75] S. M. G. Mousavi, F. Faraji, A. Majazi, and K. Al-haddad, "A comprehensive review of flywheel energy storage system technology", *Renewable and Sustainable Energy Reviews*, vol. 67, pp. 477–490, 2017. DOI: 10.1016/j.rser.2016.09.060.

[76] Y. Lu, Y. Zhao, X. Zhao, G. Li, and C. Zhang, "Status analysis of regenerative braking energy utilization equipments in urban rail transit", *2017 IEEE Transportation Electrification Conference and Expo, Asia-Pacific, ITEC Asia-Pacific 2017*, 2017. DOI: 10.1109/ITEC-AP.2017.8080771.

[77] A. Berrueta, A. Ursua, I. S. Martin, A. Eftekhari, and P. Sanchis, "Supercapacitors: Electrical characteristics, modeling, applications, and future trends", *IEEE Access*, vol. 7, pp. 50 869–50 896, 2019. DOI: 10.1109/ACCESS.2019.2908558.

[78] M. Khodaparastan, A. A. Mohamed, and W. Brandauer, "Recuperation of regenerative braking energy in electric rail transit systems", *IEEE Transactions on Intelligent*

Transportation Systems, vol. 20, pp. 2831–2847, 8 2019. DOI: 10.1109/TITS.2018.2886809.

[79] I. Villalba, V. Yepes, P. Martínez, and R. Insa, "A review of modelling and optimisation methods applied to railways energy consumption", *Journal of Cleaner Production*, vol. 222, pp. 152–162, 2019. DOI: 10.1016/j.jclepro.2019.03.037.

[80] J. Zhang, Y. Li, H. Xie, and B. Li, "Urban rail transit energy storage based on regenerative braking energy utilization", *Journal of Physics: Conference Series*, vol. 1549, 4 2020. DOI: 10.1088/1742-6596/1549/4/042053.

[81] A. Nasri, M. F. Moghadam, and H. Mokhtari, "Timetable optimization for maximum usage of regenerative energy of braking in electrical railway systems", in *SPEEDAM 2010*, 2010, pp. 1218–1221. DOI: 10.1109/SPEEDAM.2010.5542099.

[82] D. Fournier, F. Fages, and D. Mulard, "A Greedy Heuristic for Optimizing Metro Regenerative Energy Usage", in *Railways 2014*, J. Pombo, Ed., ser. Proceedings of the Second International Conference on Railway Technology: Research, Development and Maintenance, Ajaccio, France, Apr. 2014. DOI: 10.4203/ccp.104.240.

[83] R. Barrero, X. Tackoen, J. V. Mierlo, V. U. Brussel, and B. Elsene, "Improving energy efficiency in public transport : Stationary supercapacitor based energy storage systems for a metro network", in *IEEE Vehicle Poer and Propulsion Conference*, 2008, pp. 1–8. DOI: 10.1109/vppc.2008.4677491.

[84] R. Barrero, X. Tackoen, and J. van Mierlo, "Stationary or onboard energy storage systems for energy consumption reduction in a metro network", *Proceedings of the Institution of Mechanical Engineers, Part F: Journal of Rail and Rapid Transit*, vol. 224, no. 3, pp. 207–225, 2010. DOI: 10.1243/09544097JRRT322.

[85] A. González-gil, R. Palacin, P. Batty, and J. P. Powel, "Energy-efficient urban rail systems: Strategies for an optimal management of regenerative braking energy", in *Transport Research Arena (TRA) 5th Conference: Transport Solutions from Research to Deployment*, Transportation Research Board, 2014, pp. 374–388.

[86] J. P. Moskowitz and J. L. Cohuau, "Steem: Alstom and ratp experience of supercapacitors in tramway operation", in *2010 IEEE Vehicle Power and Propulsion Conference, VPPC 2010*, IEEE, 2010, pp. 1–5. DOI: 10.1109/VPPC.2010.5729152.

[87] A. González-Gil, R. Palacin, P. Batty, and J. P. Powell, "A systems approach to reduce urban rail energy consumption", *Energy Conversion and Management*, vol. 80, pp. 509–524, 2014. DOI: 10.1016/j.enconman.2014.01.060.

[88] F. Lacôte, "Alstom-future trends in railway transportation", *Japan Railway & Transport Review*, pp. 4–9, December 2005.

[89] Siemens, *Increasing energy efficiency optimized traction. "supply in mass transit systems."* 2011.

[90] A. González-gil, R. Palacin, and P. Batty, "Sustainable urban rail systems: Strategies and technologies for optimal management of regenerative braking energy", *Energy Conversion and Management*, vol. 75, pp. 374–388, 2013. DOI: 10.1016/j.enconman.2013.06.039.

[91] T. Konishi and M. Tobita, "Fixed energy storage technology applied for dc electrified railway (traction power substation)", in *2012 Electrical Systems for Aircraft, Railway and Ship Propulsion*, IEEE, 2012, p. 6. DOI: 10.1109/ESARS.2012.6387438.

[92] F. Castro and G. Thompson, "Saving money every day: La metro subway wayside energy storage substation", in *Proceedings of the 2015 Joint Rail Conference. 2015 Joint Rail Conference. San Jose, California, USA. March 23–26, 2015*, ASME, 2017, pp. 2015–2018. DOI: 10.1115/jrc2015-5691.

[93] D. Cornic, "Efficient recovery of braking energy through a reversible dc substation", in *Electrical Systems for Aircraft, Railway and Ship Propulsion*, IEEE, 2010, p. 9. DOI: 10.1109/ESARS.2010.5665264.

[94] V. Gelman, "Energy savings with reversible thyristor controlled rectifier", in *Proceeding of the 2009 ASME Joint Rail Conference*, IEEE, 2009, pp. 1–6. DOI: 10.1115/jrc2009-63013.

[95] Siemens, *Tci–thyristor controlled inverter for dc traction power supply*, 2018.

[96] Q. Lu, B. He, Z. Gao, *et al.*, "An optimized regulation scheme of improving the effective utilization of the regenerative braking energy of the whole railway line", *Energies*, vol. 12, 21 2019. DOI: 10.3390/en12214166.

[97] F. Hao, G. Zhang, J. Chen, Z. Liu, D. Xu, and Y. Wang, "Optimal voltage regulation and power sharing in traction power systems with reversible converters", *IEEE Transactions on Power Systems*, vol. 35, pp. 2726–2735, 4 2020. DOI: 10.1109/TPWRS.2020.2968108.

[98] O. Dutta, M. Saleh, M. Khodaparastan, and A. Mohamed, "A dual-stage modeling and optimization framework for wayside energy storage in electric rail transit systems", *Energies*, vol. 13, pp. 1–26, 7 2020. DOI: 10.3390/en13071614.

[99] W. Jefimowski, A. Nikitenko, Z. Drążek, and M. Wieczorek, "Stationary supercapacitor energy storage operation algorithm based on neural network learning system", *Bulletin of the Polish Academy of Sciences: Technical Sciences*, vol. 68, pp. 733–738, 4 2020. DOI: 10.24425/bpasts.2020.134176.

[100] R. Lamedica, A. Ruvio, L. Palagi, and N. Mortelliti, "Optimal siting and sizing of wayside energy storage systems in a d.c. railway line", *Energies*, vol. 13, p. 6271, 23 2020. DOI: 10.3390/en13236271.

[101] C. Wu, S. Lu, F. Xue, L. Jiang, and M. Chen, "Optimal sizing of onboard energy storage devices for electrified railway systems", *IEEE Transactions on Transportation Electrification*, vol. 6, pp. 1301–1311, 3 2020. DOI: 10.1109/TTE.2020.2996362.

[102] Y. Krim, K. Almaksour, H. Caron, *et al.*, "Comparative study of two control techniques of regenerative braking power recovering inverter based dc railway substation", in *2020 22nd European Conference on Power Electronics and Applications, EPE 2020 ECCE Europe*, 2020, pp. 1–9. DOI: 10.23919/EPE20ECCEEurope43536.2020.9215770.

[103] F. Perez, *Control of ac/dc microgrids with renewables in the context of smart grids : Including ancillary services and electric mobility, doctoral thesis defense. automatic. université paris-saclay; universidade federal de itajuba. brésil*, 2020.

[104] M. Zangiabadi, Z. Tian, T. Kamel, P. Tricoli, N. Wade, and V. Pickert, "Analysis the impact of energy storage a shared asset between dc railway network and electricity distribution network", in *2021 IEEE International Power and Renewable Energy Conference (IPRECON)*, IEEE, 2021, pp. 1–6. DOI: 10.1109/IPRECON52453.2021.9640788.

[105] C. Feng, Z. Gao, Y. Sun, and P. Chen, "Electric railway smart microgrid system with integration of multiple energy systems and power-quality improvement", *Electric Power Systems Research*, vol. 199, p. 107 459, May 2021. DOI: 10.1016/j.epsr.2021.107459.

[106] S. Nasr, M. Iordache, and M. Petit, "Smart micro-grid integration in dc railway systems", in *IEEE PES Innovative Smart Grid Technologies Conference Europe*, vol. 2015-Janua, 2015, pp. 1–6. DOI: 10.1109/ISGTEurope.2014.7028913.

[107] M. Ahmadi, H. J. Kaleybar, M. Brenna, F. Castelli-Dezza, and M. S. Carmeli, "Integration of distributed energy resources and ev fast-charging infrastructure in high-speed railway systems", *Electronics*, vol. 10, p. 2555, 20 2021. DOI: 10.3390/electronics10202555.

[108] S. Akbari, S. S. Fazel, and S. Jadid, "Optimal operation of a smart railway station based on a multi-energy hub structure considering environmental perspective and regenerative braking utilization", *Energy Science and Engineering*, vol. 9, pp. 1614–1631, 9 2021. DOI: 10.1002/ese3.937.

[109] I. Şengör, H. C. Kiliçkiran, H. Akdemir, B. Kekezoğlu, O. Erdinç, and J. P. Catalão, "Energy management of a smart railway station considering regenerative braking and stochastic behaviour of ess and pv generation", *IEEE Transactions on Sustainable Energy*, vol. 9, pp. 1041–1050, 3 2018. DOI: 10.1109/TSTE.2017.2759105.

[110] M. Chen, Z. Cheng, Y. Liu, Y. Cheng, and Z. Tian, "Multitime-scale optimal dispatch of railway ftpss based on model predictive control", *IEEE Transactions on Transportation Electrification*, vol. 6, pp. 808–820, 2 2020. DOI: 10.1109/TTE.2020.2992693.

[111] M. Khodaparastan and A. Mohamed, "Modeling and simulation of a reversible substation for recuperation of regenerative braking energy in rail transit systems", in *ITEC 2019 - 2019 IEEE Transportation Electrification Conference and Expo*, 2019. DOI: 10.1109/ITEC.2019.8790530.

[112] D. Ramsey, T. Letrouve, A. Bouscayrol, and P. Delarue, "Comparison of energy recovery solutions on a suburban dc railway system", *IEEE Transactions on Transportation Electrification*, vol. 7, pp. 1849–1857, 3 2021. DOI: 10.1109/TTE.2020.3035736.

[113] UNE, *Une-en:50149-2012. railway applications - fixed installations - electric traction - copper and copper alloy grooved contact wires*, 2012.

[114] ENSAGrupoepm, *Normas eléctricas*, 2020.

[115] ENSAGrupoepm, *Subestaciones*, 2020.

[116] H. Xia, H. Chen, Z. Yang, F. Lin, and B. Wang, "Optimal energy management, location and size for stationary energy storage system in a metro line based on genetic algorithm", *energies MDPI*, vol. 8, pp. 11 618–11 640, 10 2015. DOI: 10.3390/en81011618.

[117] V. Calderaro, V. Galdi, G. Graber, and A. Piccolo, "Optimal siting and sizing of stationary supercapacitors in a metro network using pso", in *2015 IEEE International Conference on Industrial Technology (ICIT)*, IEEE, 2015, pp. 2680–2685. DOI: 10.1109/ICIT.2015.7125493.

[118] K. Almaksour, H. Caron, N. Kouassi, *et al.*, "Mutual impact of train regenerative braking and inverter based reversible dc railway substation", in *2019 21st European Conference on Power Electronics and Applications, EPE 2019 ECCE Europe*, 2019. DOI: 10.23919/EPE.2019.8915517.

[119] AutoridadNacionaldelosServiciosPublicos, *Estadisticas*, 2019.

[120] RedElectricadeEspaña, *Establecimiento de la reserva para la regulación frecuencia-potencia. boletín oficial del estado no. 173*, 2006.

[121] R. Quint and D. Ramasubramanian, "Impacts of droop and deadband on generator performance and frequency control", *IEEE Power and Energy Society General Meeting*, vol. January, pp. 1–5, 2018. DOI: 10.1109/PESGM.2017.8274729.

[122] Samsuddin, R. Rahim, B. Hamzah, and R. Mulyadi, "Proposed model of neutral temperature equation for adaptive thermal comfort in student flats units in the tropics", *Civil Engineering and Architecture*, vol. 9, pp. 477–492, 2 2021. DOI: 10.13189/cea.2021.090220.

[123] N.-E. Clausen, *Planning and development of wind farms: Environmental impact and grid connection*, 2013.

[124] J. Araúz, D. Mora, and M. C. Austin, "Assessment of different envelope configurations via optimization analysis and thermal performance indicators: A case study in a tropical climate", *Sustainability (Switzerland)*, vol. 14, p. 20, 4 2022. DOI: 10.3390/su14042013.

[125] S. Williams, M. Short, and T. Crosbie, "On the use of thermal inertia in building stock to leverage decentralised demand side frequency regulation services", *Applied Thermal Engineering*, vol. 133, pp. 97–106, November 2017 2018. DOI: 10.1016/j.applthermaleng.2018.01.035.

[126] E. Trygstad, *R744 hvac unit for nsb flirt trains. norwegian university of science and technology, p = 188*, 2017.

[127] Y. Zhou, H. Bi, H. Wang, Y. Zhao, and B. Lei, "Time-delay characteristics of air-conditioning system for subway trains", *Journal of Building Engineering*, vol. 40, p. 102 731, March 2021. DOI: 10.1016/j.jobe.2021.102731.

[128] I. Beil, I. Hiskens, and S. Backhaus, "Frequency regulation from commercial building hvac demand response", *Proceedings of the IEEE*, vol. 104, pp. 745–757, 4 2016. DOI: 10.1109/JPROC.2016.2520640.

[129] X. Hou, S. Member, Y. Sun, and X. Zhang, "Improvement of frequency regulation in vsg-based ac microgrid via adaptive virtual inertia", *IEEE Transactions on Power Electronics*, vol. 35, pp. 1589–1602, 2 2020. DOI: 10.1109/TPEL.2019.2923734.

[130] M. H. Moradi and F. Amiri, "Virtual inertia control in islanded microgrid by using robust model predictive control (rmpc) with considering the time delay", *Soft Computing*, vol. 25, pp. 6653–6663, 8 2021. DOI: 10.1007/s00500-021-05662-z.

[131] D. Ochoa and S. Martinez, "Frequency control issues in power systems: The effect of high share of wind energy", *IEEE Latin America Transactions*, vol. 16, pp. 1934–1944, 7 2018. DOI: 10.1109/TLA.2018.8447360.

[132] M. Khodaparastan, O. Dutta, M. Saleh, and A. A. Mohamed, "Modeling and simulation of dc electric rail transit systems with wayside energy storage", *IEEE Transactions on Vehicular Technology*, vol. 68, pp. 2218–2228, 3 Mar. 2019. DOI: 10.1109/TVT.2019.2895026.

[133] S. Martinez, J. Araúz, and J. C. Serrano, *Método y sistema de estimación de la frecuencia de una red eléctrica de corriente alterna que alimenta un sistema eléctrico ferroviario de corriente continua, spanish patent p202330595*, Dec. 2023.

[134] A. Radonjic, P. Sovilj, and V. Vujicic, "Stochastic measurement of power grid frequency using a two-bit a/d converter", *IEEE Transactions on Instrumentation and Measurement*, vol. 63, pp. 56–62, 1 2014. DOI: 10.1109/TIM.2013.2277515.

[135] M. Satyanarayana and A. V. R. Teja, "A digital frequency locked loop with minimum computation overhead for heavily distorted single-phase grid systems", *IEEE*

Transactions on Instrumentation and Measurement, vol. 71, pp. 1–13, 4 2022. DOI: 10.1109/TIM.2022.3165273.

[136] M. Satyanarayana and A. V. R. Teja, "Orthogonal signal based single phase fll with minimum computational overhead for adverse grid conditions", *IEEE Journal of Emerging and Selected Topics in Industrial Electronics*, pp. 1–11, 2023. DOI: 10.1109/JESTIE.2023.3299193.

[137] S. Golestan, J. M. Guerrero, J. C. Vasquez, A. M. Abusorrah, and Y. Al-Turki, "All-pass-filter-based pll systems: Linear modeling, analysis, and comparative evaluation", *IEEE Transactions on Power Electronics*, vol. 35, pp. 3558–3572, 4 Apr. 2020. DOI: 10.1109/TPEL.2019.2937936.

[138] S. Gautam, W. Xiao, D. D. C. Lu, H. Ahmed, and J. M. Guerrero, "Development of frequency-fixed all-pass filter-based single-phase phase-locked loop", *IEEE Journal of Emerging and Selected Topics in Power Electronics*, vol. 10, pp. 506–517, 1 Feb. 2022. DOI: 10.1109/JESTPE.2021.3085124.

[139] H. Ahmed, M. Bierhoff, and M. Benbouzid, "Multiple nonlinear harmonic oscillator-based frequency estimation for distorted grid voltage", *IEEE Transactions on Instrumentation and Measurement*, vol. 6, pp. 2817–2825, 4 2020. DOI: 10.1109/TIM.2019.2931065.

[140] A. K. Verma, P. Roncero-Sanchez, H. Ahmed, S. B. Elghali, and T. D. C. Busarello, "A robust half-cycle single-phase prefiltered open-loop frequency estimator for fast tracking of amplitude and phase", *IEEE Transactions on Instrumentation and Measurement*, vol. 71, 2022. DOI: 10.1109/TIM.2021.3129211.

[141] S. Kundu, M. Singh, and A. K. Giri, "Adaptive control approach-based isolated microgrid system with alleviating power quality problems", *Electric Power Components and Systems*, vol. 0, no. 0, pp. 1–16, 2023. DOI: 10.1080/15325008.2023.2239222.

[142] N. Hui, Y. Feng, and X. Han, "Design of a high performance phase-locked loop with dc offset rejection capability under adverse grid condition", *IEEE Access*, vol. 8, pp. 6827–6838, 2020. DOI: 10.1109/ACCESS.2020.2963993.

[143] M. Banafer and S. R. Mohanty, "Traveling wave-based primary protection and fault localization scheme for mtdc grid considering iec 61869-9 measurement standard", *IEEE Transactions on Instrumentation and Measurement*, vol. 72, pp. 1–16, 5 2023. DOI: 10.1109/TIM.2023.3271735.

[144] J. M. Riquelme-Dominguez, F. D. P. García-López, and S. Martinez, "Power ramp-rate control via power regulation for storageless grid-connected photovoltaic systems", *International Journal of Electrical Power and Energy Systems*, vol. 138, Jun. 2022. DOI: 10.1016/j.ijepes.2021.107848.

[145] F. Wiegel, J. Wachter, M. Kyesswa, R. Mikut, S. Waczowicz, and V. Hagenmeyer, "Smart energy system control laboratory – a fully-automated and user-oriented research infrastructure for controlling and operating smart energy systems", *at - Automatisierungstechnik*, vol. 70, no. 12, pp. 1116–1133, 2022. DOI: doi:10.1515/auto-2022-0018.

[146] Mathworks-HelpCenter, *Pll. determine frequency and fundamental component of signal phase angle*, 2003.

List of Publications

Within the previously described results, those with more relevance and theoretical impact have been disseminated in several ways, such as in journals and one international conference.

Journal Publications

J1. **J. Araúz**, S. Martinez "Contribution of the thermal inertia of trains to the primary frequency control of electric power systems". Sustainable Energy, Grids and Networks 2023, 34, 100988. Doi: 10.1016/j.segan.2022.100988.

J2. **J. Araúz**, S. Martinez "Methodology for assessing the impact of regenerative braking energy injection of a direct current railway system on the distribution grid". Electric Power Systems Research 2023, 220, 109368. Doi: 10.1016/j.epsr.2023.109368.

J3. **J. Araúz**, S. Martinez, "Use of the Thermal Inertia of Trains for Contributing to Primary Frequency Control and Inertia of Electric Power Systems," in IEEE Access, vol. 11, pp. 57099-57116, 2023. Doi: 10.1109/ACCESS.2023.3279499.

J4. **J. Araúz**, S. Martinez, "Using the Thermal Inertia of Trains for Contributing to Primary and Supplementary Frequency Control in Grids with High Penetration of Renewable Generation," in IEEE Access, vol. 12, pp. 63271-63281, 2024, Doi: 10.1109/ACCESS.2024.3396331.

J5. **J. Araúz**, S. Martinez, J.C. Serrano, C. Veganzones, "AC Grid Frequency Estimation from DC Catenary Voltage Measurements Onboard Trains," submitted and under review in the IEEE Transactions of Transportation Electrification.

Conference Publication

C1. **J. Araúz**, S. Martinez "Using the Thermal Inertia of Trains for Contributing to Primary Frequency Control in Grids with Photovoltaic Generation," in 2023 IEEE International Conference on Electrical Systems for Aircraft, Railway, Ship Propulsion and Road Vehicles & International Transportation Electrification Conference (ESARS-ITEC), Venice, Italy: IEEE, Mar. 2023. Doi: 10.1109/ESARS-ITEC57127.2023.10114893.

Apart from the mentioned scientific publications, the industrial property regarding some of the thesis developments has been protected with the patent:

P1. S. Martinez, **J. Araúz**, J.C. Serrano, "Método y sistema de estimación de la frecuencia de una red eléctrica de corriente alterna que alimenta un sistema eléctrico ferroviario de corriente continua," Spanish Patent P202330595, December 14, 2023.

Characteristics of models

A. Data for Section 4.1

The matrices exposed in (A1), (A2), and (A3) are obtained by using (3.3), (3.5), and (3.6). The input data is obtained from the official websites of both distribution grid companies, Naturgy and ENSA. Once matrices are obtained, the corresponding values are introduced in the Matlab block for modeling lines.

$$L_{\text{Lines}} = \begin{bmatrix} 1.8 & 0.8 & 0.6 \\ 0.8 & 1.7 & 0.6 \\ 0.6 & 0.6 & 1.6 \end{bmatrix} \text{mH/km} \tag{A1}$$

$$R_{\text{Lines}} = \begin{bmatrix} 159.7 & 43.4 & 44.8 \\ 43.4 & 161.6 & 46.2 \\ 44.8 & 46.2 & 165.7 \end{bmatrix} \text{m}\Omega\text{/km} \tag{A2}$$

$$C_{\text{Lines}} = \begin{bmatrix} 8.477 & -2.537 & -1.192 \\ -2.537 & 9.193 & -2.253 \\ -1.192 & -2.253 & 9.246 \end{bmatrix} \text{nF/km} \tag{A3}$$

The position values from Table A1 are also extracted from the blueprints provided by the Railway Company. Table A1 data is complementary to Figs. 4.3, 4.4, and 4.5.

Table A1: Position of passenger stations referred to the beginning of the line. Those stations marked with * include traction substations.

Stations	Position (km)	Stations	Position (km)
Albrook*	0.091	El Ingenio*	7.782
5 de Mayo*	2.065	12 de Octubre*	8.828
La Loteria	2.724	Pueblo Nuevo	9.783
Santo Tomas*	3.407	San Miguelito*	10.827
Iglesia Del Carmen	4.703	Pan de Azucar	12.135
V. Argentina*	5.638	Los Andes*	13.101
Fernandez de Cordoba	6.600	San Isidro	15.145

Table A2 contains the rated values of trains. These values are provided by the manufacturer, Alstom, to the Railway Company. Although these values represent the maximum operational conditions, the Railway Company does not operate trains at these setpoints.

Table A2: PML1 Rolling stock rated characteristics.

Parameter (letter symbol)	Value (units)	Parameter (letter symbol)	Value (units)
Traction proportionality constant at constant force zone ($K_{tract/lim}$)	3.42 (kNh/km)	Braking proportionality constant at constant force zone ($K_{brake/lim}$)	5.00 (kNh/km)
Maximum deceleration ($a_{brake/max}$)	0.9 (m/s^2)	Train mass (m)	155.875 (ton)
Maximum wheel power ($P_{tract/max}$)	2385.5 (kW)	Total efficiency (η_{tot})	0.9
Maximum braking power ($P_{brake/max}$)	5000 (kW)	A	254.7648 (daN)
Maximum traction force ($F_{tract/max}$)	264.24 (kN)	B	2.16048 (daN/(km/h)
Maximum acceleration ($a_{tract/max}$)	1 (m/s^2)	C	0.059 (daN/(km/h)^2)
Speed at constant force zone (v_{lim})	32.5 (km/h)	Maximum braking force ($F_{brake/max}$)	250 (kN)
Maximum speed (v_{max})	80 (km/h)	Braking limit at constant force zone ($v_{lim@brake}$)	72 (km/h)
Auxiliary service power ($P_{elec.aux.}$)	207.493 (kW)	Train length (L)	86.094 (m)

Table A3 shows the exact location of railway passenger stations and distribution grid substations. The general position is depicted in Fig. 4.6. The power capacity of substations is also provided by the Distribution grid company.

Using Fig. 4.7 and toward the selection of a real but low-variant enough power consumption profile, the profiles for each distribution grid substation are obtained, as shown in Fig. A1.

Table A3: Coordinates (North latitude, East longitude) of passenger stations (left) and distribution grid substations (right).

Stations	Coordinates (°)	Subsations (capacity in MVA)	Coordinates (°)
San Isidro	9.06499, -79.51409	Costa del Este (80)	9.01234, -79.46891
Los Andes	9.04915, -79.50845	Tinajitas (84)	9.05674, -79.51153
Pan de Azucar	9.04104, -79.50833	Monte Oscuro (100)	9.02285, -79.49647
San Miguelito	9.03002, -79.50648	Santa Maria (92)	9.02777, -79.51658
Pueblo Nuevo	49.02328, -79.51253	El Marañon (146)	8.9624, -79.53725
12 de Octubre	9.01639, -79.51732	La Loceria (147)	8.98897, -79.5379
El Ingenio	9.00788, -79.51897	Centro Bancario (196)	8.99036, -79.52035
Fernandez de Cordoba	8.99639, -79.51966	San Francisco (196)	8.9873, -79.50491
V. Argentina	8.98986, -79.52213	Llano Bonito (50)	9.03409, -79.45712
Iglesia Del Carmen	8.98196, -79.52746		
Santo Tomas	8.97322, -79.5328		
La Loteria	8.96753, -79.53578		
5 de Mayo	8.96209, -79.53994		
Albrook	8.97326, -79.54961		

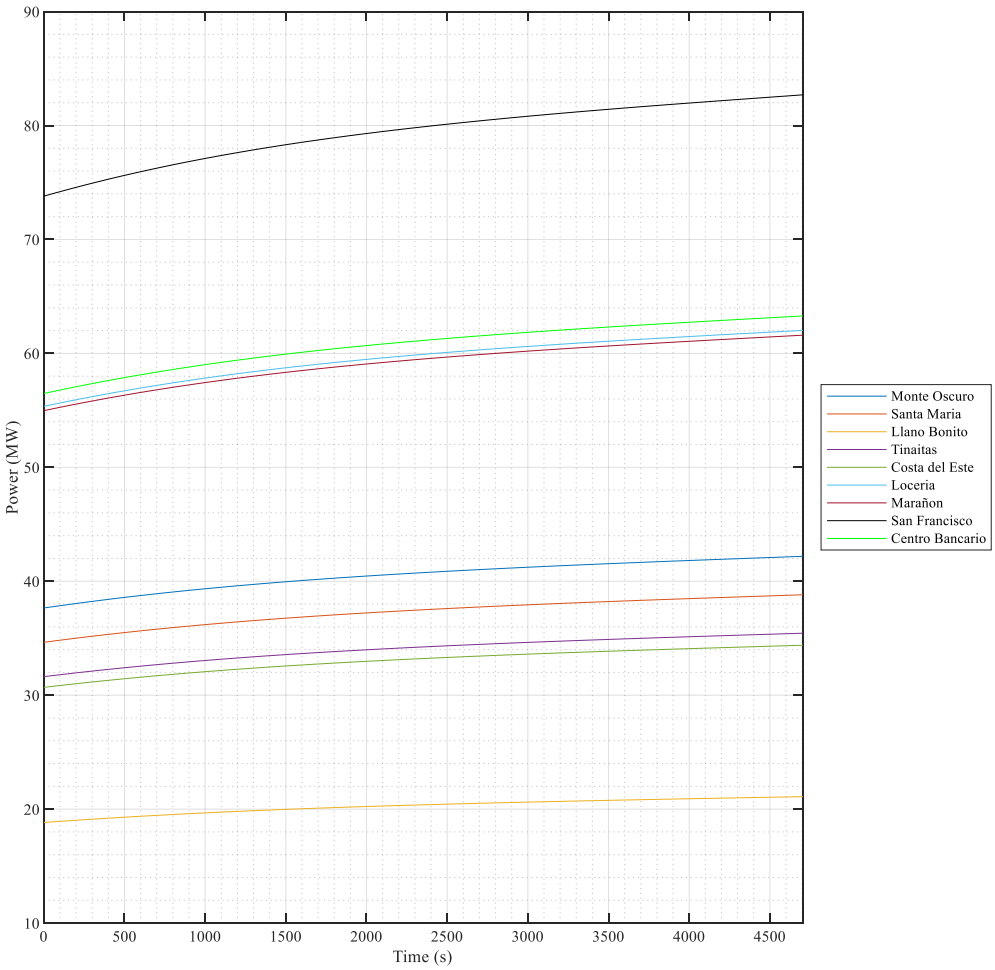


Figure A1: Selected load profile of distribution substations.

B. Data for Section 4.2

Table B1: Thermal envelope characteristics of trains.

Envelope code name	U_{ao} (W/m^2 K)	TM_a (J/K)	$U_{at}A_{at}$ (W/K)	TM_t (J/K)
Tram 1	2.5	$3.0{\cdot}10^7$	246	$1.7{\cdot}10^7$
Tram 2	3.2	$1.8{\cdot}10^7$	974	$1.0{\cdot}10^7$
Metro 1	2.8	$9.4{\cdot}10^6$	464	$1.9{\cdot}10^7$
Metro 2	3.1	$9.2{\cdot}10^6$	199	$9.6{\cdot}10^6$
Metro 3	2.9	$8.0{\cdot}10^6$	47 831	$5.7{\cdot}10^6$
Metro 4	2.4	$4.6{\cdot}10^6$	230	$1.3{\cdot}10^7$
Metro 5	2.9	$1.1{\cdot}10^7$	5 479	$2.3{\cdot}10^7$
Regio 1	1.7	$4.3{\cdot}10^7$	484	$4.6{\cdot}10^6$
Regio 2	1.3	$6.4{\cdot}10^6$	1 366	$3.1{\cdot}10^7$
Regio 3	2.0	$3.6{\cdot}10^6$	217	$1.1{\cdot}10^7$
Regio 4	1.7	$1.3{\cdot}10^7$	907	$3.7{\cdot}10^7$
Main 1	1.4	$7.2{\cdot}10^5$	93 627	$3.9{\cdot}10^6$
Main 2	1.6	$2.6{\cdot}10^6$	564	$2.4{\cdot}10^7$

Fig. B1 validates the stability of the exemplified HVAC system control. Employing the Bode diagram shows the stability of the closed-loop response. The results were obtained for $k_D = 5$. At $k_D = 1$, the gain margins are 14 dB less negative. The outcomes under typical inputs are omitted in this section since the case study encompassed numerous potential scenarios, including step perturbations, and the stability under actual plausible situations has been discussed in the results section. It is crucial to note that the stability margin is contingent upon the type of control implemented and its calibration. The feasibility of deploying the suggested approach may hinge on the specifics of the controls and all the technical details mentioned.

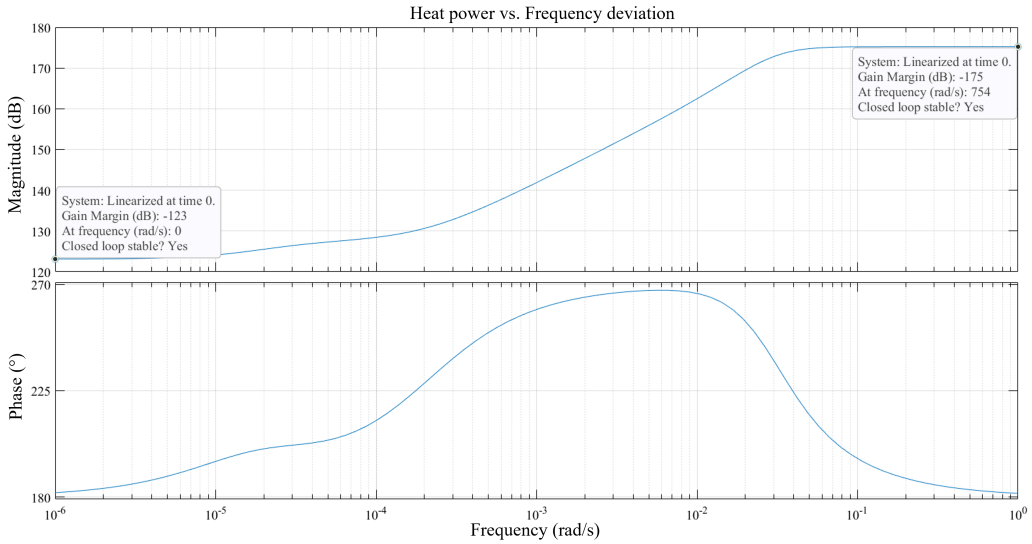


Figure B1: Bode diagram (magnitude and phase). Stability analysis of the HVAC system frequency-based control.

C. Data for Sections 4.3, 4.4

Table C1: Parameters' values and specifications.

Parameters (units)	Values
Generators inertia constant (s)	4.0
Generators dead band (mHz)	± 1
Generators PI controller gains	-20, -5
Load damping factor (%)	1
Base power (MW)	18
Train weight (kg)	204 525
Train power conversion efficiency (%)	95
Davis coefficients (N, Nh/km, Nh^2/km^2)	2 547.648, 21.6048, 3.859
Train length, width, and height (m)	86.094, 2.71, 3.859
Dwelling and headway times (s)	30.0, 120.0
HVAC system PI controller gains	50, 1
HVAC system frequency control dead band (mHz)	± 17
Maximum solar irradiance (W/m^2)	760
Outside air temperature ($°C$)	30

D. Data for Section 4.5

A flexible band-pass filter is employed in Sections 4.5.2, 4.5.3, and 4.5.4, comprising a series connection of a high-pass and a low-pass filter. The transfer function is illustrated in D1. In this representation, T_{hp} and T_{lp} denote the time constants for the high-pass and low-pass filters, respectively, while s signifies the Laplace operator. For each section, $T_{hp} = 1$ ms. In Section 4.5.2, the band-pass filter is configured to operate as a high-pass filter due to the absence of external noise in the input signal. For sections 4.5.3 and 4.5.4, the low-pass filter time constants, T_{lp}, are set to 0.5 ms and 0.18 ms, respectively. These values are chosen to account for the distinct levels of noise in the laboratory test-bench and the HIL setup.

$$H_{bp}(s) = \frac{T_{hp}s}{(1+T_{hp}s)}\frac{1}{(1+T_{lp}s)} = \begin{cases} \dfrac{10^{-3}s}{1+10^{-3}s} & \text{, Section 4.5.2} \\ \dfrac{10^{-3}s}{1+10^{-3}s}\dfrac{1}{1+0.5\cdot 10^{-3}s} & \text{, Section 4.5.3} \\ \dfrac{10^{-3}s}{1+10^{-3}s}\dfrac{1}{1+0.18\cdot 10^{-3}s} & \text{, Section 4.5.4} \end{cases} \tag{D1}$$

The model for the single-phase PLL used in the implementation is selected from the Simulink® library of *SpecializedPowerSystems*. This approach is applied in sections 4.5.2 and 4.5.3. In this model, an internal frequency oscillator is adjusted to maintain a zero phase difference [146]. The configurable parameters include minimum frequency (f_{min}), initial phase (θ_0), initial frequency (f_0), proportional gain (Kp_{pll}), integral gain (Ki_{pll}), derivative gain (Kd_{pll}), time constant for derivative action (T_{da}), maximum rate of change of frequency ($ROCOF_{max-pll}$), and filter cut-off frequency for frequency measurement (f_{cfm}). The values for these parameters are detailed in Table D1. Both setups are fine-tuned through iterations based on the signal behavior.

The ZCD method is depicted in Fig. D1 and is implemented by estimating the AC frequency of the power system through the calculation of periods between two rising edges. After filtering the signal, the catenary DC voltage (V_{dc}), to remove the DC component and non-desired frequencies, undergoes a comparison to zero, activating a rising edge detector. This detector initiates a subsystem that computes the time difference between two instances and utilizes it to derive six times the rated frequency. The blocks with a squared arrow symbolize a delay, where the output corresponds to the previous input value.

Table D1: PLL parameters' values and specifications.

Parameters (symbol)	Section 4.5.2 values	Section 4.5.3 values
Minimum frequency (f_{min})	270	270
Initial phase (θ_0)	0°	0°
Initial frequency (f_0)	300	298.02
Proportional gain (Kp_{pll})	180	2160
Integral gain (Ki_{pll})	3200	32000
Derivative gain (Kd_{pll})	1	1
Time constant for derivative action (T_{da})	$0.1{\cdot}10^{-3}$	$0.1{\cdot}10^{-3}$
Maximum rate of change of frequency ($ROCOF_{max-pll}$)	72	200
Filter cut-off frequency for frequency measurement (f_{cfm})	150	300

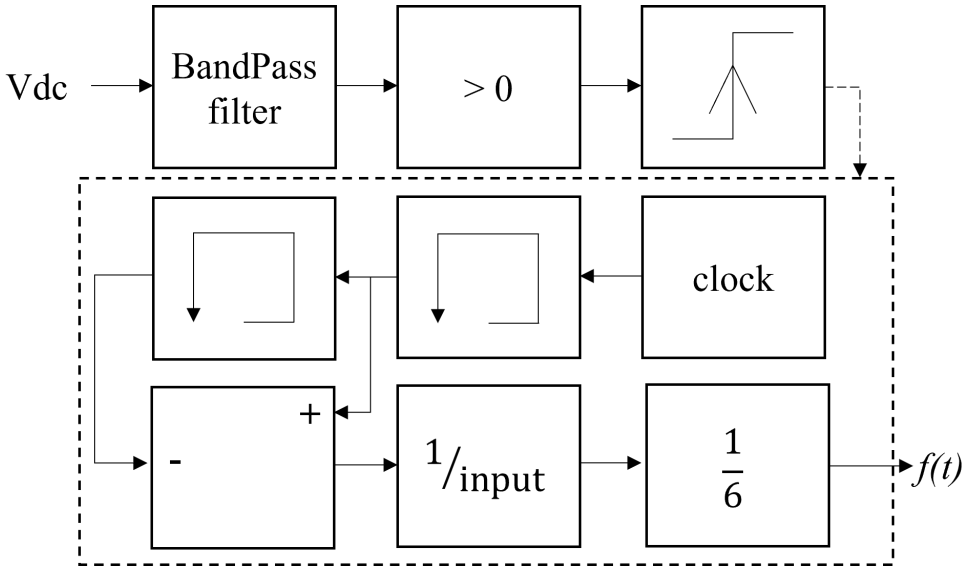


Figure D1: Implementation of ZCD method.